Departamento de Química Inorgánica
Universidad de Sevilla

Multilayer solar selective coatings for high temperature solar applications: From concept to design

Irene Heras Pérez

Sevilla, junio 2016

TESIS DOCTORAL

Directores:

Dr. Ramón Escobar Galindo

Dr. Elena Guillén Rodríguez

Dr. Matthias Krause

Tutor:

Dr. Agustín Rodríguez González-Elipe

ABENGOA RESEARCH

Departamento de Química Inorgánica
Universidad de Sevilla

TESIS DOCTORAL

Multilayer solar selective coatings for high temperature solar applications: From concept to design

Memoria para optar al título de Doctor en *Ciencia y Tecnología de Nuevos Materiales* por la Universidad de Sevilla con Mención Internacional, presentada por:

Irene Heras Pérez

Directores:

Dr. Ramón Escobar Galindo

Dr. Elena Guillén Rodríguez

Dr. Matthias Krause

Tutor:

Dr. Agustín Rodríguez González-Elipe

Sevilla, junio 2016

ABENGOA RESEARCH

CONTENTS

LIST OF ABBREVIATIONS AND ACRONYMS

3D	Three-dimensional
a-C	Amorphous carbon
a-C:H	Hydrogenated amorphous carbon
a-C:MeC	Amorphous carbon metal carbide
AFM	Atomic force microscopy
AM	Air mass
AR	Antireflective
ASTM	American Society for Testing and Materials
BE	Backscattered electrons
BER	Bergman
BF	Bright-Field
BN	Boron nitride
BRU	Bruggeman
BWF	Breit-Wigner-Fano
ccp	Cubic closed-packed
CSP	Concentrating solar plant
CTM	Centre tecnologic de Manresa
CVA	Cathodic vacuum arc
CVD	Chemical vapour deposition
DC / RF MS	Direct current radio frequency magnetron sputtering
DF	Dark-field
DLC	Diamond-like carbon
EBPVD	Electron Beam Physical Vapour Deposition
EDX/EDS	Energy Dispersive X-ray Spectroscopy
EELS	Electron energy loss spectrometry
EMA	Effective medium approximation
ERD	Elastic recoil detection
fcc	Face-centred cubic
FCVA	Filtered cathodic vacuum arc
FFT	Fast Fourier transformation
FIB	Focused ion beam
FL	Fullerene-like
FTIR	Fourier Transform infrared spectroscopy
FWHM	Full width at half maximum
GISAXS	Grazing incidence small angle X-ray scattering
GIXRD	Grazing incidence X-Ray diffraction
GLC	Graphite like carbon
HAADF	High angle annular dark field
hcp	Hexagonal close-packed
hex	Hexagonal simple
HiPIMS	High Power Impulse Magnetron Sputtering
HR-TEM	High-resolution transmission electron microscopy
HZDR	Helmholtz Zentrum Dresden Rossendorf
IBAD	Ion beam assisted deposition
ICMSE	Instituto de ciencia de materiales de Sevilla
IEA	International Energy Agency
IPA	Isopropyl alcohol

IR	Infrared
KKR	Kramers-Kronig relations
LOO	Looyenga
MG	Maxwell Garnett
MS	Magnetron sputtering
nc-graphite	Nanocrystalline graphite
NIR	Near infrared
NMR	Nuclear magnetic resonance
NPs	Nanoparticles
NRA	Nuclear reaction analysis
PACVD	Plasma-assisted chemical vapour deposition
PECVD	Plasma enhanced chemical vapour deposition
PFCVA	Pulsed filtered cathodic vacuum arc
PVD	Physical vapour deposition
RBS	Rutherford backscattering spectroscopy
RMS	Root mean square roughness
RT	Room temperature
SAED	Selected area electron diffraction
SE	Spectroscopic ellipsometry
SEM	Scanning electron microscopy
SHC	Solar Heating and Cooling
SS	Stainless steel
SSC	Solar selective coatings
STEM	Scanning transmission electron microscopy
ta-C	Tetrahedral amorphous carbon
ta-C:H	Hydrogenated tetrahedral amorphous carbon
TBC	Thermal Barrier Coating
TEM	Transmission electron microscopy
TGO	Thermally Grown Oxide
TM	Transition metal
TOF	Time of flight
UV	Ultra-violet
VDOS	Vibrational density of states
VF	Volume fraction
Vis	Visible
XEDS	X-ray energy dispersive spectroscopy
XRD	X-ray diffraction

I. MOTIVATION AND SUMMARY

Increasing the share of renewables in the energy mix has a key function for the security of energy supply and the reduction of greenhouse gas emissions from fossil fuels. The purpose of this thesis is to develop new solar selective coating (SSC) designs for high temperature applications in order to improve the performance of concentration solar power (CSP) plants.

The main part of this thesis has been carried out in the company Abengoa, which is a world leader in the development of CSP plants, but also with the collaboration of other well-recognized academic organizations (Instituto de Ciencia de Materiales de Sevilla-CSIC, Center Tecnologic Manresa and the Helmholtz-Zentrum Dresden - Rossendorf) and the SME Metal Estalki.

The improvement in efficiencies in solar thermal energy plants partially means the increase in the receivers' temperature, reaching up to an average maximum temperature of 650ºC for superheated steam and molten salts receivers. There are several R&D approaches to substitute commercial absorber paints due to the degradation problems they show at high temperatures when exposed to air. The different routes include the development of new solar selective coatings fabricated using physical vapour deposition techniques.

In this thesis, two potential candidates as solar selective coatings were selected: i) carbon–transition metal carbides nanocomposites (a-C:MeC) and ii) aluminium titanium oxynitride ($AlTi(O_xN_{1-x})$) based coatings.

The methodology followed in this thesis contains aspects of very high novelty including optical simulation, coating deposition using cathodic vacuum arc (CVA) and advanced characterization. The computer program CODE was used to simulate the reflectance spectra of the different complete coatings. Simulated reflectance spectra were compared with the measured reflectance of the deposited films to verify the agreement between simulations and experimental results. The simulations allowed predicting the optical properties of solar selective coatings with different thicknesses and with different materials avoiding a try and error approach. Special attention was paid to the simulation of optical constants. The knowledge of the coating microstructure revealed critical for a proper design of solar selective coatings. In this thesis, valuable insight into the most accurate way of simulating nanocomposite materials and oxynitrides is given. Several optical models were evaluated and their appropriateness described in detail. Different SSC stacks were deposited with pulsed filtered cathodic vacuum arc (PFCVA) and non-filtered CVA setup comparing different materials, compositions and thicknesses for each one of the layers that conforms the coating. After the deposition of single layers and complete SSC, the

stacks were characterized employing a wide range of techniques. The optical properties were characterized by UV-Vis-NIR and FT-IR spectrophotometers; the elementary compositions were determined by Rutherford Backscattering Spectroscopy (RBS), Nuclear Reaction Analysis (NRA) and Elastic Recoil Detection (ERD) ion beam techniques; the crystal structure was studied by X-ray diffraction and Raman spectrometry was used to determine the chemical bonding of the carbon atoms; and finally, SEM and HR-TEM were employed to determine the morphology of the deposited thin films. The unique *cluster tool* (sited at HZDR) allowed the *in-situ* characterization of the films performance at high temperature. This novel technique provided a detailed study of the diffusion processes occurring at extreme temperatures in solar selective coatings of interest and the identification of their failure mechanism.

The simulations, depositions and characterizations performed for the two selected candidate materials for SSC are thoroughly described in the following chapters. The introductory **chapter 1** starts with a brief description of the advantages of thin films and coatings versus their bulk counterparts, followed by a summary of physical vapour deposition (PVD) techniques and the main growing mechanisms of thin films. The fundamental principles of the interaction of light with materials are also introduced, in order to get a better understanding of the thin film optical properties. The chapter ends with a summary of the current state of the art of SSC and the mechanisms employed to maximize the absorption of sunlight and to minimize the losses by thermal radiation.

The methodology followed in this thesis for a complete design of solar selective coatings is fully explained in **chapter 2**. The design process starts with the selection of the material that composes each layer in the multilayer stack. Then, the different deposition systems employed are described followed by the complete characterization performed on the deposited thin films. Finally, the thermal treatment tests included in this work to analyse the durability in air at high temperatures and to predict their service lifetime are explained.

Chapter 3 introduces the properties of transition-metal carbides and carbon as the individual components of the nanocomposite (a-C:MeC). Nanocomposite thin films consisting of interstitial metal carbide embedded in an amorphous carbon matrix exhibit a unique combination of properties which makes them very attractive candidates as absorber layer of SSC for thermo-solar applications. In a first step, optical simulation based on literature optical constants was employed for optimizing SSC. After the initial simulation, the selected a-C:MeC candidates were deposited and characterized. Following a thorough analysis of their composition and microstructure, the simulations were feedback with experimental data. The simulated complete coating based on these measured properties provided excellent selective optical selective properties (a>96% and $\varepsilon_{600ºC}$<14%). A complete solar selective coating was deposited and analysed and afterwards, a heating test was performed to study the stability of the coating at high temperature.

Aluminium titanium oxynitrides were selected as candidate materials for SSC on the basis of the state of the art described in the introduction of **chapter 4**. In this chapter, initial thermal treatment tests were performed to validate the stability of single oxynitride layers in air, showing no degradation at temperatures above 600ºC. A set of individual $AlTi(O_xN_{1-x})$ layers deposited by CVA were analysed in terms of composition, morphology and optical properties. A thoroughly study of the microstructure of the films, as a function of the oxygen content, was found to be key for a comprehensive analysis of the optical properties. A complete multilayer SSC was designed and deposited with optical simulations based on measured optical constants of each of the individual layers. Excellent agreement was found between simulated and experimental reflectance spectra. A solar selective coating with a simulated absorptance of 94.7% and an emittance of 5.6% is designed. To conclude, the thermal stability in air of the complete SSC was analysed by asymmetric and cyclic heating tests. Remarkable stability at temperatures as high as 650ºC after 750 hours of annealing was found for solar selective coatings based on oxynitrides.

Chapter 5 described a novel technology for the *in-situ* characterization of coatings at high temperatures. This characterization is performed at the two materials candidates. In particular, an accurate knowledge of the variation of the dielectric function of thin films with the temperature and its relation to compositional and microstructural changes could help to prevent failures. The methodology employed combines a sequence of analytical techniques. An a-C:TiC thin film was studied first following the described methodology. Then, $AlTi(O_xN_{1-x})$ thin films with different oxygen concentration were investigated in order to understand the influence of the oxygen to nitrogen ratio on the optical properties and their failure mechanisms at high temperatures. No significant changes in optical properties and composition were found when heating oxynitride films in a vacuum atmosphere at temperature above 800ºC, showing excellent high temperature stability. It is worth noting than a worldwide record of *in-situ* RBS measurement at 840ºC was performed in the framework of this thesis.

The main conclusions of the thesis are discussed in **chapter 6**, including a comparative review of the different materials employed for SSC, along with the strengths and weaknesses observed for each one.

.

II. MOTIVACIÓN Y RESUMEN

Aumentar la cuota de energías renovables en el mix energético es fundamental para asegurar el abastecimiento de energía y disminuir las emisiones de gases de efecto invernadero asociadas al uso de combustibles fósiles. El objetivo de la presente tesis es desarrollar nuevos recubrimientos solares selectivos (SSC por sus siglas en inglés), estables a alta temperatura, que supongan una mejora en el rendimiento de las plantas de energía solar de concentración (CSP).

La mayor parte del trabajo descrito en esta tesis se ha llevado a cabo en la compañía Abengoa, que es líder internacional en el desarrollo de plantas CSP. Sin embargo, ha sido fundamental la colaboración con centros de investigación como son el instituto de Ciencia de los Materiales de Sevilla, el Centro Tecnológico Manresa, el centro Helmholtz Zentrum Dresden-Rossendorf, y la compañía Metal Estalki.

El incremento de la eficiencia de las plantas CSP pasa en parte por conseguir un aumento de la temperatura de trabajo del receptor, llegando a una temperatura media máxima de 650ºC en el caso de receptores de vapor sobrecalentado y de sales fundidas. Desde un punto de vista de investigación y desarrollo de materiales ha habido diferentes intentos de sustituir las pinturas comerciales usadas actualmente en los receptores pero que presentan degradación en aire a altas temperaturas. De especial interés es el desarrollo de SSC fabricados usando técnicas de deposición al vacío realizado por diversos grupos en el mundo en los últimos años.

En esta tesis, se han seleccionado dos tipos de materiales para obtener nuevos recubrimientos solares selectivos: i) nanocompuestos de carbono y carburos de metales de transición (a-C:MeC); y ii) oxinitruros de aluminio-titanio ($AlTi(O_xN_{1-x})$).

La metodología que se ha seguido en este trabajo contiene aspectos novedosos en materia de simulación, deposición por arco catódico (CVA) y caracterización avanzada de recubrimientos. Para simular la reflectancia de los distintos recubrimientos se ha empleado el programa de simulación óptica CODE. La validez de los resultados de simulación se ha confirmado mediante la comparación de los espectros de reflectancia simulados con los medidos experimentalmente. La simulación permite predecir el comportamiento óptico de los recubrimientos en función de parámetros tales como el material del que están formados o el grosor de sus distintas capas. Durante este trabajo se ha prestado especial atención a la simulación de las constantes ópticas de los materiales. Se ha demostrado también, que el conocimiento de la microestructura del material es en muchas ocasiones fundamental para el diseño de recubrimientos solares selectivos. La idoneidad de varios modelos ópticos se ha evaluado y descrito en detalle, y como consecuencia, esta tesis supone una valiosa aportación al correcto modelado de las propiedades ópticas de materiales

nanocompuestos y oxinitruros. Utilizando como técnicas de deposición el arco catódico pulsado y filtrado (PFCVA), y el arco catódico no filtrado (CVA), se han depositado numerosos capas finas individuales, y también recubrimientos solares selectivos completos. Sus propiedades se han caracterizado de una manera exhaustiva utilizando un gran número de técnicas de análisis. Las propiedades ópticas de las películas se han caracterizado usando espectrofotómetros UV-Vis-NIR y FT-IR. La composición elemental se obtuvo mediante las siguientes técnicas de análisis de iones: espectrometría retrodispersión de Rutherford (RBS), análisis de reacción nuclear (NRA) y análisis por detección del retroceso elástico (ERD). La estructura cristalina se analizó por difracción de rayos X, y la espectroscopía Raman se usó para determinar el enlace químico en los átomos de carbono presentes en los nanocompuestos. La morfología y la microestructura se estudiaron mediante SEM y HR-TEM. Mediante el sistema de *cluster tool* situado en el centro HZDR, fue posible llevar a cabo una caracterización *in-situ* del comportamiento de los recubrimientos a alta temperatura. Este sistema supone una técnica novedosa para estudiar los procesos de difusión que tienen lugar a alta temperatura en los recubrimientos solares selectivos, permitiendo identificar sus mecanismos de fallo.

En los distintos capítulos que conforman la presente tesis se describen en detalle las simulaciones, deposiciones y caracterizaciones llevadas a cabo en los dos tipos de materiales seleccionados como candidatos para recubrimientos solares selectivos. El **capítulo 1**, que sirve de introducción, comienza con una breve descripción de las ventajas de las películas finas respecto a los materiales en volumen, seguida de un resumen de algunas técnicas de deposición física al vacío (PVD) y los principales mecanismos de crecimiento de las películas finas. Con el objeto de conocer mejorar los principios que determinan las propiedades ópticas de estos recubrimientos, se incluyen en esta introducción algunos aspectos fundamentales de la interacción de la luz con los materiales. El capítulo termina con una revisión del estado del arte de los SSC, incluyendo los distintos mecanismos que han sido empleados para intentar maximizar la absorptancia y disminuir la emitancia de este tipo de recubrimiento.

En el **capítulo 2** se describe en detalle la metodología seguida en la presente tesis para el diseño de un recubrimiento solar selectivo completo. El proceso comienza con la elección de los materiales que van a formar las distintas capas del recubrimiento, seguido de la descripción de los distintos equipos que se van a utilizar para su fabricación. Finalmente, las técnicas de caracterización empleadas así como los procedimientos para testar la durabilidad de los recubrimientos son descritos.

El **capítulo 3** comienza con una descripción de los materiales que forman los nanocompuestos a-C:MeC: el carbono y los carburos de metales de transición. Como se describe en detalle en este capítulo, los nanocompuestos formados por carburos de metales de transición embebidos en una matriz de carbono amorfo presentan una combinación única de propiedades que

los hace ser candidatos muy prometedores para formar la capa absorbedora de un SSC para aplicaciones termosolares. En un primer momento se llevaron a cabo simulaciones ópticas basadas en constantes ópticas obtenidas de la literatura para optimizar el comportamiento de los SSC. Estas simulaciones sirvieron para hacer una primera selección de materiales nanocompuestos que fueron posteriormente depositados y caracterizados. Después de un completo análisis de su microestructura y composición, las simulaciones se retroalimentaron con los datos experimentales obtenidos. Estas simulaciones dieron lugar al diseño de un recubrimiento basado en nanocompuestos de carbono con excelentes propiedades ópticas (a>96% and $\varepsilon_{600ºC}$<14%). Finalmente se fabricó un recubrimiento completo y se sometió a un tratamiento térmico a alta temperatura.

La elección de los oxinitruros de aluminio titanio como candidatos para fabricar recubrimientos solares selectivos está ampliamente justificada en el estado del arte recogido en el **capítulo 4**. El estudio de estos recubrimientos comienza con una prueba de estabilidad inicial que muestra que son estables en aire por 2 horas a temperaturas por encima de 600ºC. Capas individuales de $AlTi(O_xN_{1-x})$ depositadas por CVA se analizaron en términos de composición, morfología y propiedades ópticas. Como se verá en este capítulo, un estudio exhaustivo de la microestructura de las películas ha resultado ser crítico para el análisis de las contantes ópticas de estos materiales. En base a simulaciones que emplean constantes ópticas medidas experimentalmente en capas individuales, se han diseñado y depositado recubrimientos SSC completos, encontrándose una excelente concordancia entre la reflectancia simulada y la medida experimentalmente. Se ha diseñado un recubrimientos solar selectivo basado en oxinitruros de aluminio titanio con una absorbancia simulada del 94.7 % y una emitancia del 5.6%. Finalmente, los recubrimientos depositados se sometieron a distintos tratamientos térmicos, presentando una excelente estabilidad tras un tratamiento térmico con una duración de 750ºC y una temperatura de testado de 650ºC.

El **capítulo 5** describe una novedosa metodología para caracterizar *in-situ* recubrimientos a alta temperatura. Esta caracterización se lleva a cabo en los dos materiales candidatos descritos en los capítulos anteriores. El objetivo de esta caracterización es conocer cómo las constantes ópticas varían con la temperatura y cómo este cambio se relaciona con variaciones de la microestructura para así prevenir posibles mecanismos de fallo. La metodología empleada comprende una serie de técnicas de análisis que se aplican sobre las muestras de manera secuencial. Primero se ha analizado un nancompuesto de a-C:TiC siguiendo la metodología descrita en este capítulo. Tras este análisis, películas de $AlTi(O_xN_{1-x})$ con distintos contenidos de oxígeno se han caracterizado para ver cómo la composición influye en los mecanismos de fallo a alta temperatura. Los recubrimientos de oxinitruros presentaron una excelente estabilidad en vacío a temperaturas por encima de los 800ºC.

También es importante resaltar que en esta tesis se describe el récord mundial de medida de RBS *in-situ* a alta temperatura (840ºC).

Las principales conclusiones se resumen en el **capítulo 6**, que incluye una comparativa de los distintos materiales empleados, así como las ventajas e inconvenientes detectados en el uso de cada uno de ellos como SSC

LIST OF PUBLICATIONS

Scientific publications

1. **I. Heras, M. Krause, G. Abrasonis, A. Pardo, J. L. Endrino, E. Guillén, R. Escobar Galindo.** "Advanced characterization and optical simulation for the design of solar-selective coatings based on carbon: transition metal carbide nanocomposites". Solar Energy Materials & Solar Cells (2016) Under review.

2. **I. Heras, E. Guillén, M. Krause, A. Pardo, J.L. Endrino, R. Escobar Galindo,** "Solar selective coatings based on Carbon:Transition Metal Nanocomposites", in High and Low Concentrator Systems for Solar Energy Applications X, Proceedings of SPIE Vol. 9559 (SPIE, Bellingham, WA 2015), 955908.

3. **E. Guillén, I. Heras, G. Rincón, F. Lungwitz, M. Alcon-Camas, R. Escobar-Galindo,** "Room temperature deposition of highly dense TiO_2 thin films by Filtered Cathodic Vacuum Arc", in Nanostructured Thin Films VIII, Proceedings of SPIE Vol. 9558 (SPIE, Bellingham, WA 2015), 95580S.)

4. **I. Heras, E. Guillén, R. Wenisch, M. Krause, R. Escobar Galindo, J.L. Endrino,** "Comprehensive environmental testing of optical properties in thin films", 3rd International Conference through-life engineering services in Procedia CIRP. 22 (2014) 271–276.

Patents

1. **E. Guillén, R. Escobar, I. Heras, J.L. Endrino, N. Martinez, A. Bello, S. Gemming, F. Lungwitz, M. Krause** "Self-cleaning high temperature resistant solar selective coating", P201431972, 2014.

CHAPTER 1: INTRODUCTION TO SOLAR SELECTIVE COATINGS

This introductory chapter starts in section 1.1 with a brief description of the advantages of thin films and coatings versus their bulk counterparts, followed by a summary of physical vapour deposition (PVD) techniques and the main growing mechanisms of thin films. The main principles of the interaction of light with materials are introduced in section 1.2, in order to get a better understanding of the thin film optical properties. The third part of the chapter (section 1.3) describes the main parts of a concentrated solar power (CSP) plant, with particular interest on the solar selective coatings (SSC) of the receiver tubes. This part is focused on the state of the art of SSC and the mechanisms employed to maximize the absorption of sunlight and to minimize the losses by thermal radiation. Finally, the distribution of the chapters of the thesis is summarized in section 1.4.

1.1. Growth mechanisms of thin films

Thin film materials are key elements of continued technological advances made in the fields of semiconductors [1,2], optics [3,4], wear resistant [5–7], decorative [8], medical [9] or solar energy technologies [10,11] in the last decades. Thin films have distinct advantages over bulk materials. Most processes used to deposit thin films occur in non-equilibrium conditions and hence, the composition of thin films is not constrained by metallurgical phase diagrams. Microstructure, surface morphology, tribological, electrical, and optical properties of the thin film are all controlled by the chosen deposition technique (i.e. sol gel, chemical vapour deposition, thermal evaporation, physical vapour deposition) [12,13].

Physical vapour deposition (PVD) is a well-established technology to synthesize coatings with tailored properties [14]. Optical coatings in particular are mainly produced by magnetron sputtering [15,16]. However, when temperature resistance is also required, as for the thin films studied in this work, highly ionized PVD techniques are more suitable. These techniques include cathodic vacuum arc (CVA), [17,18], ion beam assisted deposition (IBAD) [19] or high power impulse magnetron sputtering (HiPIMS) [20].

Unravelling the atomic-scale mechanisms of thin films deposition proved to be difficult because of the different parameters involved in the process. The growth process of thin films by PVD includes i) nucleation, ii) island growth, iii) coalescence of islands, iv) formation of a connected network with islands and channels, v) development of a continuous structure based on filling and shrinking of channels, and finally, vi) continuous film growth [21,22]. Figure 1.1 (a) illustrates how atoms arrive on the surface and depending on their diffusion energy (E_d), they start to accommodate over the surface. During this process they can encounter other adatoms and form small clusters with the binding energy (E_b) or attach to already existing clusters [23]. Besides, nucleation kinetics is affected by the crystal structure of the substrate material, lattice defects, surface steps and surface contamination. Other atomistic processes like re-evaporation and interdiffusion can also occur during deposition [24].

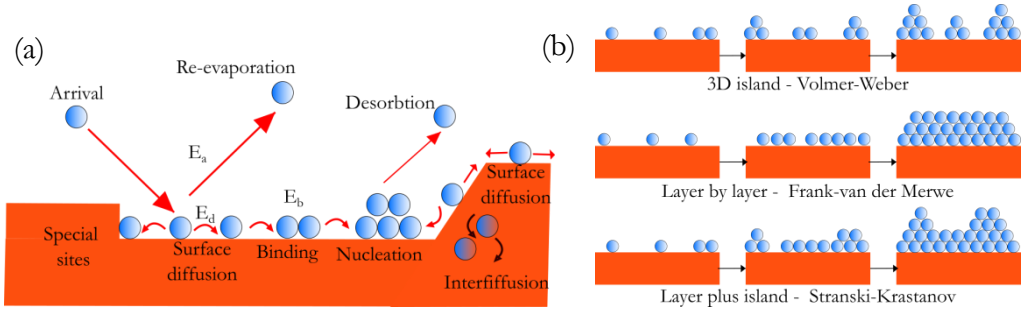

Figure 1.1 – (a) Schematic view of possible atomic processes on a solid surface. (b) Representation of the three basic modes of thin-film growth.

Diffusion and nucleation of atoms give rise to three main growth modes (Figure 1.1 (b)), distinguished in terms of surface and interface energies [21]. The Volmer-Weber mode describes 3D island growth and occurs when the adatoms are more strongly bound to each other than to the substrate. In the opposite case, where the adatoms are more strongly attracted by the substrate than by themselves, layer-by-layer (Frank-van der Merwe) growth arises. Finally, the layer-plus-island or Stranski- Krastanov growth mechanism is an intermediate case, and occurs if, after the formation of one or more monolayers, subsequent layer growth becomes unfavourable and islands are created.

These processes are mainly affected by the substrate temperature and the energy of incoming particles which can be used to manipulate adatom mobility and nucleation rates [25]. At identical deposition rates, the larger mobility will lead to a higher diffusivity, thus allowing a further transport from the original arrival site and earlier coalescence. Hence, higher energies lead to films with larger grains and less defects, while the momentum of the incoming particles can lead to alignment or orientation of the growing crystallites [26]. The description of microstructural evolution during PVD of thin films as function of growth conditions and material composition has attracted much attention over the last years and led to the development of various structure zone models (SZMs) or diagrams. Movchan and Demchishin proposed one of the first SZM in 1969 [27]. In this model, the microstructural evolution of coatings can be systematically represented as a function of only one parameter, the homologous temperature (T_h), defined as film growth temperature normalized by the melting temperature (T_m) of the growing material. More refined SZMs were developed, notably those by Thornton [28], Messier [29], Barna and Adamik [30] or Anders [31]. The latter is shown as an example of extended zone diagram in Figure 1.2, and includes the use of high energy ions.

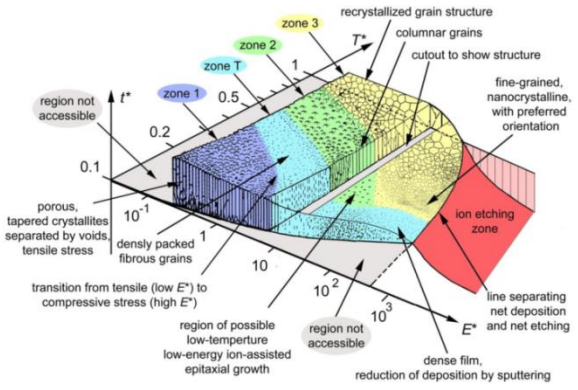

Figure 1.2 – Structure zone diagram applicable to energetic deposition; in function of the generalized temperature (T^*), the normalized energy flux (E^*) and the net thickness (t^*). The numbers on the axes are for orientation only as the values depend on the material and other conditions [31]

Anders proposed to replace T_h by a generalized temperature (T^*) that includes changes in temperature with potential energy of arriving atoms to the surface. He also includes a parameter called normalized energy (E^*), to describe displacement and heating effects caused by the kinetic energy of bombarding particles and a z-axis with for film thickness (t^*). Anders' SZM [32] shows

how fine grained and dense films are typically achieved with high energy ions techniques as CVA. Consequently, in the present work, CVA was selected as deposition technique in order to obtain dense films with improved thermal stability and good adhesion.

The morphology of compound films is significantly more complex than for pure element ones. In these multi-element systems, limited solid solubility of the components can result in a phase separation or the existence of amorphous films. However, the structure zone models are a qualitative way to understand the film microstructure evolution and relate with the deposition parameters employed. As explained in this thesis, the comprehensive study of the thin film microstructure will be crucial to achieve the desired optical properties in solar selective coatings. In this regard, the basics of light interaction with matter are summarized in next sections.

1.2. Interaction of radiation with matter: basic principles

The vibration of electric and magnetic charges creates electromagnetic waves that have both an electric and a magnetic component (Figure 1.3). The electric field, (in red) is perpendicular to the magnetic field, (blue), and the motion direction is given by the cross product vector. Electromagnetic radiations are classified by the wavelength (λ) of their oscillations within the electromagnetic spectrum, which includes (ordered by increasing λ): gamma rays, X-rays, ultraviolet (UV) radiation, visible light (Vis), infrared (IR) radiation, microwaves and radio waves [33].

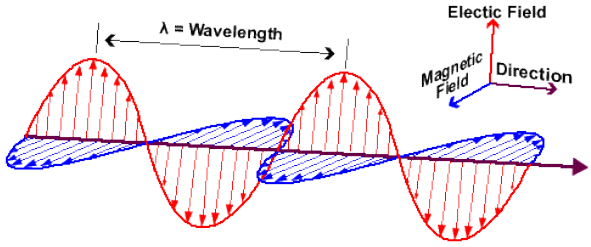

Figure 1.3 –Schematic electric (red) and magnetic (blue) fields that compose an electromagnetic radiation, propagating from left to right.

All materials are constantly emitting electromagnetic radiation, with an intensity and wavelength dependent on its temperature and optical characteristics. For instance, a blackbody is an ideal material that emits the maximum possible radiation for each temperature, whose wavelength distribution ($B(\lambda,T)$) is given by Plank's law [34], as expressed in equation (1.1)

$$B(T,\lambda) = \frac{c_1}{\lambda^5(e^{c_2/\lambda T} - 1)} \qquad (1.1)$$

with c_1 and c_2 Plank's constants (c_1= $3.74 \cdot 10^{-16}$ W m^2; c_2=$1.44 \cdot 10^{-2}$ m K) and T, the temperature in kelvin degrees. The maximum value in the blackbody radiation is displaced toward shorter wavelengths as the temperature increases, following Wien's displacement law , as observed in Figure 1.4 (a), at four selected temperatures.

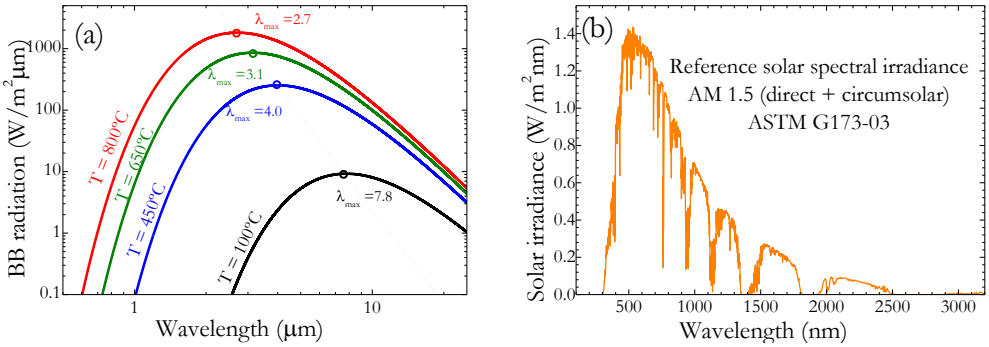

Figure 1.4 – (a) Blackbody radiation spectrum at different temperatures, including the position of the wavelength for the maximum intensity of blackbody radiation at each temperature selected (b) Terrestrial solar spectral irradiance at AM 1.5: Direct + circumsolar for a 37º tilted surface as defined by ASTM-G173-03.

Solar radiation or sunlight is the portion of electromagnetic spectrum emitted by the sun. Figure 1.4 (b) shows the solar spectra irradiance distribution ($G(\lambda)$) that reaches the surface of the Earth, as defined in the American Society for Testing and Materials (ASTM) G173-03 for an air mass 1.5 (AM1.5), at 37º sun facing tilted surface [35]. The solar radiation is limited to the range between 0.3 and 3 μm, i.e. ultraviolet-visible-near infrared (UV/Vis/NIR) wavelengths, so that there is almost no overlap with the blackbody spectra [36], until high temperatures (T> 450ºC) are reached.

When sunlight radiation reaches a surface, part of this incident light is reflected from the surface and the rest enters into the medium. A fraction can be absorbed by the material and the remaining radiation is transmitted, as schematized in Figure 1.5.

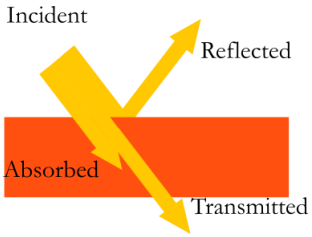

Figure 1.5 – Reflection, absorption and transmission of a light beam incident on a material.

The interaction of an electromagnetic radiation with the material can be quantified by intrinsic parameters of the material. The amount of light that is reflected is determined by the coefficient of reflectance (R) of the surface and is defined as the ratio of intensities of light reflected (I_R) and incident light (I_0). The coefficient of transmission (T) is defined likewise as the ratio of intensities of light transmitted (I_T) and incident light. Application of conservation of energy leads to the statement that the sum of T, R and absorption (A) of the incident flux, for each wavelength, is equal to unity, as expressed in (1.2) [37,38]:

$$R(\lambda) + T(\lambda) + A(\lambda) = 1 \qquad (1.2)$$

The absorption is related with the attenuation of the light intensity (I) when it travels through a material, following Beer-Lambert law (equation (1.3)) [39]:

$$I(z) = I_0 e^{-ad} \tag{1.3}$$

where a is the attenuation coefficient and d the thickness of the film. This coefficient a, is directly proportional to the extinction coefficient of the material (k) that measures how fast light vanishes in a material. If the material is transparent, k is equal to zero (and thus a), and all the radiation will be transmitted through the material. The relation between the speed of light in the material (v) and the speed of light in vacuum ($c \approx 3.00 \cdot 10^8$ m/s) is defined by the refractive index (n), as expressed in (1.4):

$$n = \frac{c_0}{v} \tag{1.4}$$

Both n and k are intrinsic values for each material and depend on the wavelength of the radiation. They can be incorporated into a single quantity called the complex refractive index ($\tilde{n}$), with n the real part and k the imaginary one. This $\tilde{n}$ describes how an electromagnetic radiation propagates through a medium, as the example of shown in Figure 1.6. The relation of the complex refractive index with the dielectric function ($\tilde{\varepsilon}$), derived from Maxwell's equations [40], is defined in equation (1.5)

$$\tilde{n} = n + i\kappa = \sqrt{\tilde{\varepsilon}(\omega)} \tag{1.5}$$

The dielectric function and the complex index of refraction are called optical constants. Real and imaginary parts of the optical constants are not independent and they are mathematically coupled through Kramers-Kronig relationships [41].

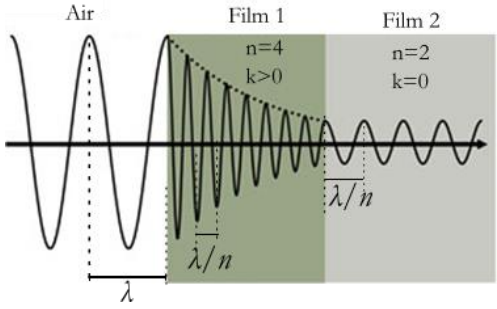

Figure 1.6 – Light wave travels from air (n=1; k=0) into absorbing film 1 (n=4; k>0), and then into the transparent film 2 (n=2; k=0). The phase velocity and wavelength change in each material depending on its complex index of refraction.

Fresnel's equations, describe the behaviour of light when crossing between two materials with differing optical constants [42]. These equations can be used to calculate the previously defined $R(\lambda)$, $A(\lambda)$ and $T(\lambda)$ for each wavelength, as a function of the angle of incidence and polarization of the incident ray, and the complex refractive index of the two materials.

The utilisation of the maximum energy coming from sunlight implies the design of materials with optical constants that absorb in the specific wavelengths of this radiation. Likewise, to avoid losses of the absorbed energy, the material must show poor irradiative properties, opposite to blackbody behaviour. These two conditions (high absorption and low emittance), are generally

competing. However, as they occur in different wavelength regions, they can be fulfilled in the so-called solar selective surfaces as explained in the next section.

1.3. Solar selective coatings for solar thermal energy

The amount of solar energy incident on the Earth's surface per year is about $1.5 \cdot 10^{18}$ kWh, approximately 10000 times the current annual energy consumption in the world [43]. Concentrating solar power (CSP) is a commercial available technology in the field of renewable energies, based on the conversion of concentrated solar energy into heat and subsequently into electrical energy [44]. CSP systems use mirrors to concentrate sunlight onto a receiver that transfers heat to the internal circulating fluid called heat transfer fluid (HTF). From the technological point of view, medium and high temperature CSP plants are distinguished [45]. Medium-temperature CSPs employ parabolic troughs as solar light collectors concentrating the light on vacuum protected receiver tubes. The operational temperature of the receivers is in the range of 150 to 350°C. In high-temperature CSP, solar light is concentrated by large-area mirror fields onto a central receiver that is installed in a solar tower with current operational temperatures of 525°C.

Solar receivers' performance is determined by its solar absorptance (α) and thermal emittance (ε). For opaque materials ($T(\lambda)=0$), solar absorptance is defined as the fraction of incident radiation in the solar wavelength range that is absorbed, as expressed in equation (1.6):

$$\alpha = \frac{\int_{\lambda_1}^{\lambda_2}[1 - R(\lambda)]G(\lambda)d\lambda}{\int_{\lambda_1}^{\lambda_2} G(\lambda)d\lambda} \tag{1.6}$$

where λ_1, λ_2 is the integration interval. In this thesis, the ASTM E903:2012 [46] is employed for α definition with $G(\lambda)$ by ASTM G173:2008 [35] (see Figure 1.4 (b)) and λ_1 - λ_2 = 300 - 2500 nm.

Thermal emittance is defined as the relative ability of a material to emit heat by radiation and it is the ration of the radiance of a surface to the radiance of a blackbody at a temperature. This magnitude is, therefore, dimensionless and ranges from 0 to 1 (the emissivity of a blackbody is 1). The thermal emittance is calculated from its reflectance spectra in the infrared region, applying Kirchoff's law, for each temperature, following equation (1.7):

$$\varepsilon_T = \frac{\int_{\lambda_1}^{\lambda_2}[1 - R(\lambda,T)]B(\lambda,T)d\lambda}{\int_{\lambda_1}^{\lambda_2} B(\lambda,T)d\lambda} \tag{1.7}$$

where $B(\lambda,T)$ is the wavelength distribution of the blackbody [34], temperature T, as expressed above in (1.1). The integration interval selected in this thesis is λ_1 λ_2 = 0.3-2.5 μm, based on EN-673:2011 [47], but with extended wavelength range to include all UV-Vis-IR spectra.

In order to maximize the photothermal conversion efficiency, the receivers need to absorb most of the solar light (high α) and retain the heat energy (low ε) to be carried effectively by HTF. The above conditions of an ideal SSC can be expressed in terms of an ideal spectral reflectance as expressed by equation (1.8) and graphically schematized in Figure 1.7:

$$\begin{aligned} \alpha_{max} &\rightarrow R(\lambda) = 0 \quad for \quad 0.3 < \lambda < \lambda_c\ \mu m \\ \varepsilon_{T,min} &\rightarrow R(\lambda) = 1 \quad for \quad \lambda_c < \lambda < 30\ \mu m \end{aligned} \tag{1.8}$$

where λ_C is a critical wavelength between 2 or 3 μm depending on the operating temperature [38,48]

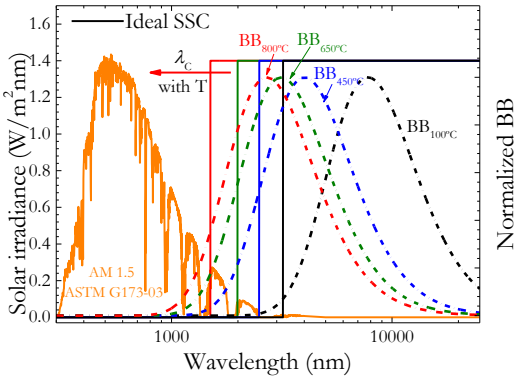

Figure 1.7 – Spectral reflectance of an idealized solar selective coating with different critical wavelength (λ_C) for each temperature. The solar spectral irradiance (ASTM-G173-03) and the normalized Blackbody radiation spectrum at different temperatures are included for a better understanding.

A variety of thin film architectures can be exploited as SSC depending on the physical mechanism for obtaining spectral selectivity. The SSC can be classified in i) intrinsic spectral selective materials, ii) semiconductor -metal tandem, iii) textured surfaces, iv) photonics crystals (PhC), v) solar selective transmitting coating with blackbody-like absorber, vi) dielectric –metal (cermet) composite and vii) multilayer interference stacks. The operating principle together with an example for each system type is reviewed below.

i) Intrinsic spectral selective materials

Intrinsic spectral selective materials are homogeneous films possessing some inherent spectral selectivity, induced by dielectric dispersion as a function of wavelength. Metals generally possess a plasmon wavelength (λ_p), below which absorptivity gradually increases. However, the λ_p of a typical metal in the UV region is below the ideal cut-off wavelength for ideal solar selectivity. There are few materials with intrinsic selective optical properties that show the desired intermediate behaviour between metals and heavily doped semiconductors (Figure 1.8), such as titanium, zirconium, or hafnium metal carbides, oxides, and nitrides (on a highly reflective substrate) [49]

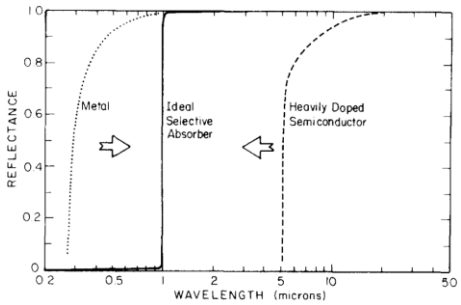

Figure 1.8 – Reflectance of an ideal selective absorber compared to that of a metal and a heavily doped semiconductor [58]

Substoichiometric compounds of TiN_x, ZrN_x, and ZrC_xN_y [50,51] have the best combination of high solar absorptance and low thermal emittance [52]. The IR reflectance of these materials is notable high (ε_{RT}<10%) and the absorption edge is located close to the Vis range [39]. Cr–Cr_2O_3 known as black chrome and Ni–Zn–S (black nickel) are frequent materials employed as intrinsic solar absorbers in solar thermal industry [53–55]. They have to be used over an IR reflectance metallic surface to achieve the desired optical selectivity. In general, these SSC are structurally stable and easy to fabricate. However, it offers less-than-ideal spectral selectivity and therefore this approach has not been particularly fruitful at commercial applications [56].

ii) Semiconductor-metal tandem

The combination of a semiconductor film onto a metal underlay results in a solar selective tandem stack. Semiconductors and doped semiconductors are characterised by their energy band structure, with occupied valence electron states and unoccupied conduction electron states separated by a forbidden energy gap where no allowed electron states exists. Solar photons with shorter λ than the semiconductor bandgap can be absorbed by semiconductor valence electrons, while photons with greater λ will be transmitted unaffected, and get reflected back by the metal layer [48]. Semiconductor materials suitable for this approach include Si, Ge, and PbS [57]. The semiconductors frequently have large refractive indices near the band edge [58], which tend to give strong reflection losses and decrease the final α, implying that a complex antireflection treatment will be necessary. Donnadieu [59] considered Si/Ge tandem absorber placed on a silver reflector with an AR coating in front. Optimization with optical simulation yielded spectrally selectivity of α=89% and $\varepsilon_{300ºC}$ = 3.9%. More recently, Chester *et al.* [60] optimized a Ge on Ag reflector, showing a performance of α=91% and $\varepsilon_{120ºC}$ = 2%, based on optical simulations.

This selective coating can withstand continuous temperatures in excess of 500ºC with good stability. However the optical properties are very sensitive to film thickness and a careful monitoring of the deposition parameters is necessary. Barriers between layers are commonly required to prevent inter-diffusion as well as buffers to reduce thermal or structural mismatch [61]. Many processing challenges appears associated with deposition growth in industry of reliable and

high quality finishes on receivers tubes [48]. Additionally, achieving low emittance can be challenging for semiconductor absorbers, as electron hole pair generation and free carrier emission at high temperatures can lead to large radiated losses [44].

iii) Textured surface

Textured surfaces are studied as SSC due to they can achieve high α by multiples reflections against metal dendrites with sizes in the order of solar wavelengths [62], while the thermal emittance is rather unaffected by this treatment since the relevant wavelengths are much larger than the dendrite separation (Figure 1.9 (a)). The microstructure of the surface, such as the orientation and mean feature height, controls the degree of selectivity.

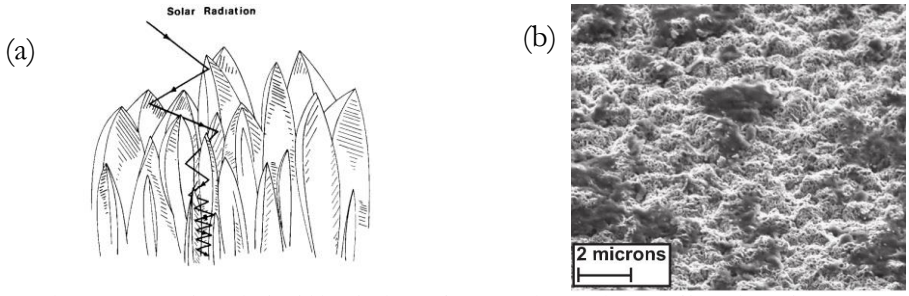

Figure 1.9 – (a) Schematic dendritic selective surfaces [63]. (b) SEM images of laser sintered tungsten [64].

Ideally, surface-textured absorbers should withstand high temperature, and they must be protected from external damages such as contact or abrasion by protective coatings like sol-gels. Selection of surface materials with high absorptivity will further increase the overall efficiency. There are several ways to create surface texturing including unidirectional solidification of eutectic alloys, nanoimprint lithography, ion-exchange reactions between metals, vapour deposition or oxidation of metals at high temperature [57].

For example, dendritic tungsten has been deposited in the form of forests of whiskers whose size and separation are of the same order of magnitude than the sunlight wavelength. Hence, they promote absorption by multiple cavity reflections [65,66]. Recently, Sha *et al.* [64] developed a SSC based on tungsten nano and micro particles (Figure 1.9 (b)) fabricated by laser sintering with a surface roughness from nanoscale to 2 μm that helped to achieve spectral selectivity. The performance obtained was α=92% and ε_{RT} =16%, and relatively the same before and after heat treatment 36 h up to 650ºC in air. The absorptance can be affected by the metallic oxidation in air but few data have been found on durability of texture surfaces due to the elevated cost of producing at industrial scale and the difficulties encountered to obtain high quality coatings

iv) Photonic crystals (PhCs)

The recent advances in the semiconductor processing technology has developed the fabrication of nanostructures with wavelength-scale features, known as photonic crystals (PhCs) [67]. These PhC-based designs, allow a control over the spectral and angular selectivity of the devices, compared to other SSC candidates.

One-dimensional (1D) patterns impact on the optical properties of the surface of the bulk material. This is attributed to surface plasmon resonance induced by the surface patterns. The effects of the geometry of gratings such as periodicity and depth on spectral behaviour have been studied. Recently, Babiek [68] proposed a 1D W complex pattern design (Figure 1.10 (a)). The complex grating is defined by the superposition of two or more 1D grating profiles.

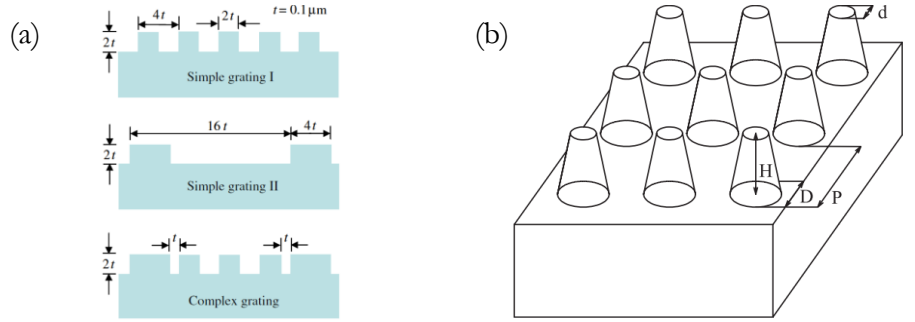

Figure 1.10 – Three W grating designs, two simples and one complex grating formed from superimposing both on top of each other. [68] (b) Schematic diagram of simulated nanocone PhCs [69].

Figure 1.10 (b) shows the simulated 2D Mo PhCs with a square array of nanocones [69]. Mo is stable at high temperature (1000ºC) and shows intrinsic solar selectivity. An optimized Mo nanocone surface can exhibit a = 91.9% and $\varepsilon_{1000ºC}$ = 14.9%.

This emerging area of research is enabled by technological progress in the nanopatterning of surfaces. The manipulation of geometrical rather than material properties, could lead to a new generation of more efficient SSC.

v) Solar selective transmitting coating on a blackbody-like absorber

This concept consists of a two layer stack composed of a selective transmitter on top of a perfect absorber (Figure 1.11). The former has to be transparent in the range of the solar radiation (300 nm – 2000 nm) and reflective in the range of the thermal emission of the system (> 2000 nm), while the latter absorbs in the range of the solar radiation. The emerging heat radiation is reflected at the interface of those two layers and therefore not lost into the environment but used for heating of the transfer fluid below.

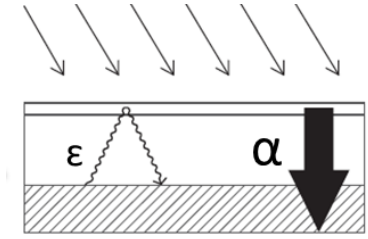

Figure 1.11 – Schematic representation of SSC consisting on a solar transmitting coating (TCO) with a blackbody-like absorber [70].

Materials which have suitable properties for a selective transmitter are mainly the well-known transparent conductive oxides (TCOs) [71–73]. The conductivity in those materials is given by the amount of free charge carriers, which, from an optical point of view, are in principle able to oscillate in resonance with an incoming light wave. At frequencies higher than its plasma frequency, the charge carriers can not follow the excitation and therefore the material is transparent. As the excitation frequency gets lower, the oscillations of the electron plasma are excited and the incoming light waves get reflected. Candidates for such a selective transmitter are *e.g.* SnO_2:Ta and TiO_2:Ta. Furthermore, this combination of a material with high concentration of charge carriers ($n_{e;TiO2:Ta}$ = 10^{21} cm^{-3}) and a material with high charge carrier mobility ($\mu_{e;SnO2:Ta}$ = 20 cm/Vs) may result in a solar selective coating with very good properties [70].

vi) Multilayer interference stack

Multilayer stacks use optical interference effects to promote absorption by alternating dielectric and metal layers (Figure 1.12). The thickness of the films may be selected so that light in the solar region of the spectrum is transmitted through the coating and reflected form the film/metal interface, returning to interference destructively with light reflected from the front surface of the film and thereby, increasing the solar absorptance. As long as the thickness is kept <150 nm, the longwave thermal radiation passes through the films preserving the low emittance properties of the IR layer.

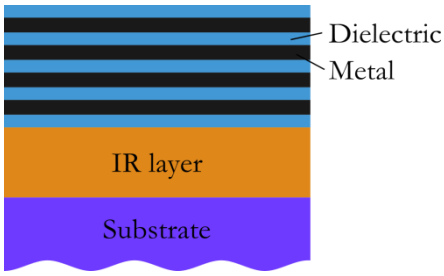

Figure 1.12 – Schematic diagram of a dielectric-metal multilayer interference stack on a IR reflective layer to produce solar selectivity

This interference effect may be optimised by using several thin films to increase the number of multiple reflections and maximize α. The thicknesses and materials of each layer must be chosen carefully to set the electromagnetic amplitude to zero at desired wavelengths. Variations in films thickness due to environmental degradation of differential expansion of the layers can lead

to changes in the optical properties and a subsequent deterioration in the designed performance. Li *et al* [74] designed an aperiodic multilayer structure consisting on SiO_2(105 nm)/Ti(15 nm)/SiO_2(95 nm)/Al(>100 nm), which provides an average $\alpha > 90\%$ and $\varepsilon_{323°C} < 7\%$.

The optical properties in these multilayer stacks are complicated to maintain by the need of interlayers in order to overcome the diffusivity problems between layers at high temperature.

vii) Ceramic – metal (cermet) composite

Ceramic–metal composites, also known as cermets, containing metal nanoparticles embedded in a dielectric or ceramic matrix [75] should have ceramic characteristics in the visible spectrum and metallic properties in the IR. This design offers a large degree of flexibility and the optimization of the spectral selectivity can be made with regard to the choice of constituent materials, film thickness, particle concentration and grading, as well as the shape and orientation of the particles. Smaller particle sizes are beneficial for high absorptance in the visible range meanwhile increasing the particle radius, the number of scattering centres decrease, resulting in lower absorption. The thermal emittance in the IR can be decreased by decreasing the coating thickness and increasing the metal concentration [76].

Stacks formed by a cermet on a metallic layer have been widely reported in literature [77] and successfully commercialized [78–80]. Good candidates for the cermet component are metals with high melting points (Cu, Au, Ni, Mo, Cr, Co, Pt, and W) and dielectrics such as SiO_2, Al_2O_3, AlN, Si_3N_4 or MgO. A single cermet film does not high solar selectivity by itself; hence, more complex structures with increasing metal concentration have also been investigated.

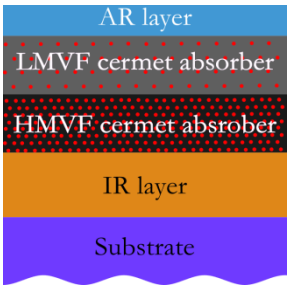

Figure 1.13 – Schematic diagram of a double cermet solar selective coating, consisting in an antireflective layer on the top, low metal volume fraction (LMVF)) cermet, high metal volume fraction (HMVF) cermet and an infrared reflective layer.

To mention a few cermet based SSC, Zhang *et al* developed a double W-AlN cermet solar coatings deposited by reactive DC sputtering [81,82]. Optical simulations based on Bruggeman theory [83] allows a more efficient design obtaining optimized coatings with film structures of AlN/W–AlN (low metal volume fraction (LMVF))/ W–AlN (high metal volume fraction (HMVF))/Al, which schematic is shown in Figure 1.13. This design gives values of $\alpha \geq 95$ % and $\varepsilon_{350°C} \leq 6$ % and stability at 500°C in vacuum. Similar SS-AlN double-cermet solar selective films [84] have high optical selectivity properties. In particular, the Chinese "TurboSun" company

produces SS-AlN double-cermet glass-tubes which are thermally stable between 350°C-500°C in vacuum and lower in cost.

Among the previously described SSC, PVD deposited cermet-based are nowadays successfully employed with high absorptance (α>95%) and low emittance (ε < 10%) for temperatures up to 400ºC in the evacuated tubes of parabolic trough concentrated solar power applications [77]. In medium temperature receiver designs, the surface is protected by a transparent cove which reduces the convective heat losses and provides control to the atmosphere to which the coating is exposed. However, these solutions cannot be directly implemented in central receiver tower plants that are expected to operate in air (without the protective cover) and at higher temperatures (T > 450ºC) to increase the performance [45]. Commercial paints such as Pyromark® are commonly employed as absorber coatings in tower plant central receivers working up to a maximum temperature of 525ºC. Their disadvantages include a poor solar selectivity (ε_{RT} = 86%) and a fast degradation during operation, requiring permanent maintenance [85]. The maximum working temperature in CSP plants is limited by the stability of these paints.

The improvements in efficiencies for solar thermal energy conversions partially implies the increase in the receivers' temperature, aiming to reach up to a maximum temperature of 650ºC for new superheated steam and molten salts receivers [44]. Therefore, the development of SSC durable at high temperature in air is a scientific and technological challenge. SSC must be capable of resisting deterioration and of enduring a lifetime of ~20 years and must be chemically and structurally stable up to the temperature range of the new tower power plants. Moreover, they must withstand thousands of heating and cooling cycles during the operation time of the plant [86]. In an evacuated atmosphere, the principal degradation mechanisms are the interdiffusion between layers or the changes in surface morphology. In air conditions, internal chemical reactions can change the composition, interfacial reactions can lead to loss of adhesion and the SSC may be corrode under high temperatures. Finally, the coatings should be resistant to abrasive wear caused by wind and sand erosion and show good adhesion onto the receiver base material.

In this thesis, the degradation mechanism will be minimized employing refractory metal compounds for the absorber layer and with the addition of an antireflective layer (AR) and an infrared reflection (IR) layer, deposited on a highly stable substrate, as schematized in Figure 1.14 (a). An example of one layer of each type grown for this thesis is shown in Figure 1.14 (b).

The IR layer is situated under the absorber layer to reduce the thermal emittance at high temperatures [48]. Metals, carbides and nitrides are good IR candidates due to their well-known metallic behaviour [50,87]. The IR layer also has to be stable at high temperatures to avoid diffusion of the substrate thorough the rest of the coating and have high melting points. To fulfil these high demanding properties refractory interstitial nitrides (TiN [88], ZrN [50] or VN [58]) are

excellent candidates as they exhibit higher melting points than their host metals (e.g. 2950ºC for TiN and 1660ºC for Ti) [89].).

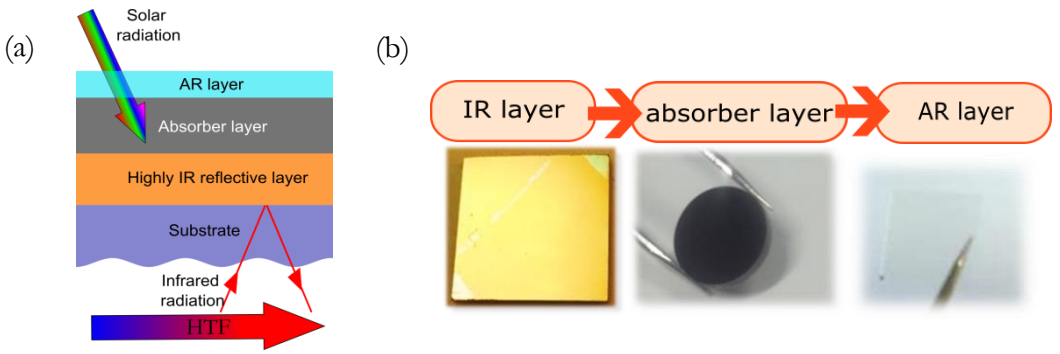

Figure 1.14 – (a) Schematic representation of a complete SSC. (b) CVA deposited thin films for the different layer types that make up the solar selective multilayer stack, including TiN on Si substrate as IR layer, a-C:MoC on inconel substrate as absorber layer and Al_2O_3 on glass as top AR layer.

The AR top layer should reduce the light loss of the solar radiation and also must be thermal stable to reduce the corrosion rate and stabilize the whole coating at high temperatures [90]. The simplest AR coating consists of one transparent layer with a quarter-thickness of the bottom layer and with refractive index (n) the square root of n in the absorber layer. Following this procedure, it is possible to create a destructive interference effect, with decreased reflectance for wavelengths in a broad band around the solar range. Some of the commonly employed materials for AR layer are MgF_2 [91], SiO_2 [92], Al_2O_3 [93] or Si_3N_4 [94].

In this work two candidate materials were proposed as absorber layer, combining the previous spectral selectivity mechanisms. The first approach consist on interstitial metal carbide nanoparticles embedded in an amorphous carbon matrix [95]. This nanocomposite film shows optical selectivity that resembles cermets mechanism and enhanced by both the intrinsic absorptivity of carbon and the spectral selectivity of metal carbides. The other candidate consists on a graded $AlTi(O_xN_{1-x})$ multilayer stack which combines the multilayer interference mechanism with the intrinsic spectral selectivity of this refractory material.

1.4. Description and scope of the thesis

The overall plan of the thesis is summarized in Figure 1.15. The flow diagram shows that there are two common introductory chapters. This chapter 1 explains the interaction of light with materials and the state of the art of previous solar selective coatings (SSC) materials. The methodology for a complete design of SSC is described in chapter 2. This chapter illustrates the different steps followed, starting with the selection of materials, optical simulation, deposition, characterization and thermal treatments.

The research done on the candidate materials selected to be the absorber layer of the SSC has been arranged into two parallel chapters (chapters 3 and 4). In chapter 3, amorphous-carbon: transition metal carbides (a-C:MeC) nanocomposites are employed as solar absorber layer for the SSC. In this chapter, optical simulation based on literature optical constants is employed first for the optimization of complete SSC and for the selection of materials for each layer type. Then, these selected thin films are deposited and comprehensively characterized. The optical simulations are feedback with experimental data and a complete SSC is designed and deposited in order to validate the simulations. A heating test of the deposited multilayer stack is performed to study the failure mechanisms at high temperatures.

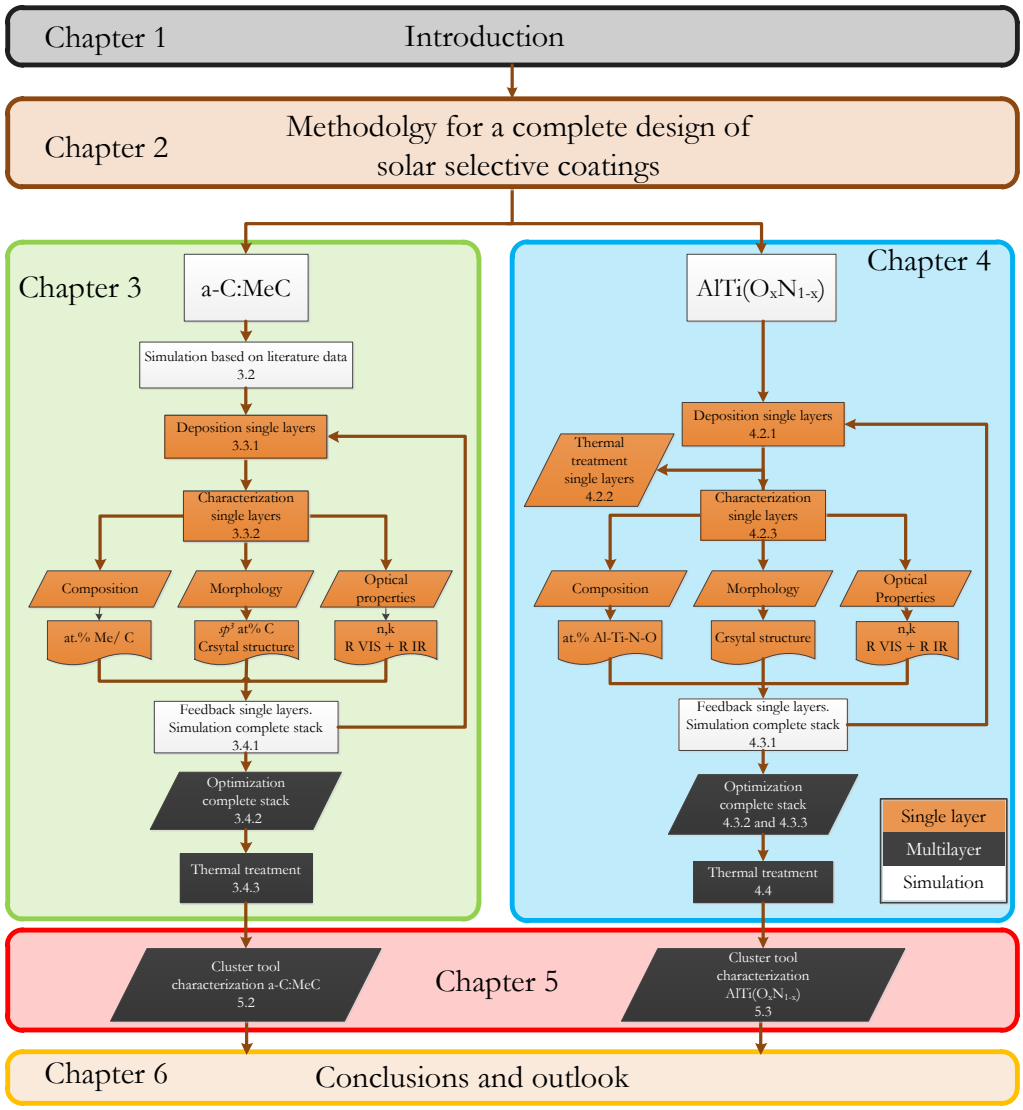

Figure 1.15 - Schematic flow chart of the project procedure.

The experience and capacity acquired on previous chapter, allowed the improvement of the methodology for a complete design of SSC based on aluminium titanium oxynitrides described in chapter 4. The main difference in this from the previous approach is the initial thermal treatment tests performed to validate the stability of single AlTiON layers. A set of individual layers were analysed first, in terms of composition, morphology and optical properties. Then, a complete SSC is designed with optical simulations, based on measured AlTiON optical constants. The optimized multilayers were deposited, and characterized its thermal stability in air.

Chapter 5 describes a novel methodology for high temperature tests that integrates complementary characterization techniques into a single device. The new *cluster tool* situated at Helmholtz-Zentrum Dresden-Rossendorf (HZDR), Germany, includes thin films characterization techniques such as spectroscopic ellipsometry, Raman spectroscopy, and ion beam analysis in several environmental conditions and at different temperatures. The multichamber device has been tested for a-C:MeC and AlTiON single layers. Those samples have been exposed to an *in-situ* heating process while measuring spectroscopic ellipsometry. Before and after heating, the thin films were characterized with Raman spectroscopy and Rutherford Backscattering Spectroscopy (RBS) in order to analyse the compositional and microstructural changes occurred during the heating process.

The conclusions of the different materials employed for SSC, along with the strengths and weaknesses observed for each one are summarized in chapter 6.

1.5. References

[1] C. Kim, J. Garland, H. Abad, P. Raccah, Modeling the optical dielectric function of semiconductors: Extension of the critical-point parabolic-band approximation, Phys. Rev. B. 45 (1992) 11749–11767.

[2] S. Goumri-Said, N. Kanoun-Bouayed, A.H. Reshak, M.B. Kanoun, On the electronic nature of silicon and germanium based oxynitrides and their related mechanical, optical and vibrational properties as obtained from DFT and DFPT, Comput. Mater. Sci. 53 (2012) 158–168.

[3] C.G. Alvarado-Beltrán, J.L. Almaral-Sánchez, R. Ramirez-Bon, Low temperature processing of multilayer dielectrics mirrors by sol–gel method, Mater. Lett. 161 (2015) 523–526.

[4] B.K. Tay, Z.W. Zhao, D.H.C. Chua, Review of metal oxide films deposited by filtered cathodic vacuum arc technique, Mater. Sci. Eng. R Reports. 52 (2006) 1–48..

[5] C. Ducros, C. Cayron, F. Sanchette, Multilayered and nanolayered hard nitride thin films deposited by cathodic arc evaporation. Part 1: Deposition, morphology and microstructure, Surf. Coatings Technol. 201 (2006) 136–142.

[6] J. Nohava, P. Dessarzin, P. Karvankova, M. Morstein, Characterization of tribological behavior and wear mechanisms of novel oxynitride PVD coatings designed for applications at high temperatures, Tribol. Int. 81 (2015) 231–239.

[7] V. Singh, Tribological behavior of nanocomposite DLC based thin films, 2004.

[8] S. Niyomsoan, W. Grant, D.L. Olson, B. Mishra, Variation of color in titanium and zirconium nitride decorative thin films, Thin Solid Films. 415 (2002) 187–194.

[9] B.F. Coll, P. Jacquot, Surface modification of medical implants and surgical devices using TiN layers, Surf. Coatings Technol. 36 (1988) 867–878.

[10] C. Fei Guo, T. Sun, F. Cao, Q. Liu, Z. Ren, Metallic nanostructures for light trapping in energy-harvesting devices, Light Sci. Appl. 3 (2014) e161.

[11] I. Heras, E. Guillén, G. Abrasonis, M. Krause, A. Pardo, J.L. Endrino, et al., Optimizing solar absorption in carbon – transition metal nanocomposite thin films, Sol. Energy Mater. Sol. Cells. (2016).

[12] W. Kern, K.K. Schuegraf, Handbook of Thin Film Deposition Processes and Techniques: Principles, Methods, Equipment and Applications, in: K. Seshan (Ed.), Second Edi, Noyes Publications / William Andrew Publishing, Norwich, NY 13815, 2002.

[13] A. Anders, Handbook of deposition Technologies, Third, William Andrew, Washington, 2009.

[14] K.S. Sree Harsha, Principles of physical vapor deposition of thin films, Elsevie, London, 2006.

[15] H.C. Barshilia, P. Kumar, K.S. Rajam, A. Biswas, Structure and optical properties of Ag–Al2O3 nanocermet solar selective coatings prepared using unbalanced magnetron sputtering, Sol. Energy Mater. Sol. Cells. 95 (2011) 1707–1715.

[16] C. Wang, J. Shi, Z. Geng, X. Ling, Polychromic Al–AlN cermet solar absorber coating with high absorption efficiency and excellent durability, Sol. Energy Mater. Sol. Cells. 144 (2016) 14–22.

[17] K. Valleti, D.M. Krishna, P.M. Reddy, S. V. Joshi, High temperature stable solar selective coatings by cathodic arc PVD for heat collecting elements, Sol. Energy Mater. Sol. Cells. 145 (2016) 447–453.

[18] M.M.M. Bilek, D.R. McKenzie, J. Pigott, P. Denniss, J. Vlcek, Deposition of nanoscale multilayered structures using filtered cathodic vacuum arc plasma beams, in: Emerg. Appl. Vacuum-Arc-Produced Plasma, Ion Electron Beams, Springer, 2002: p. 173.

[19] M. Krause, A. Mücklich, T.W.H. Oates, M. Zschornak, S. Wintz, J. Luis Endrino, et al., Tilting of carbon encapsulated metallic nanocolumns in carbon-nickel nanocomposite films by ion beam assisted deposition, Appl. Phys. Lett. 101 (2012) 053112..

[20] E. Lewin, D. Loch, A. Montagne, A.P. Ehiasarian, J. Patscheider, Comparison of Al-Si-N nanocomposite coatings deposited by HIPIMS and DC magnetron sputtering, Surf. Coatings Technol. 232 (2013) 680–689..

[21] J.M. Albella, Láminas delgadas y recubrimientos: Preparación, propiedades y aplicaciones, C.S.I.C., Madrid, 2003.

[22] M. Ohring, The materials science of thin films: deposition & structure, 2nd editio, Academic Press, San Diego, 2002.

[23] I. Petrov, P.B. Barna, L. Hultman, J.E. Greene, Microstructural evolution during film growth, J. Vac. Sci. Technol. A Vacuum, Surfaces, Film. 21 (2003) S117..

[24] J.A. Venables, Introduction to surface and thin film processes, Cambridge University Press, Arizona State University, 2000.

[25] R.M. Bradley, J.M.E. Harper, D. a. Smith, Theory of thin-film orientation by ion bombardment during deposition, J. Appl. Phys. 60 (1986) 4160–4164.

[26] G.N. Van Wyk, H.J. Smith, Crystalline reorientation due to ion bombardment, Nucl. Instruments Methods. 170 (1980) 433–439.

[27] B.A. Movchan, A. V. Demchishin, 1, Fiz. Met. I Metalloved. 28 (1969) 653–660.

[28] J.A. Thornton, Influence of apparatus geometry and deposition conditions on the structure and topography of thick sputtered coatings, J. Vacumm Sci. Technol. 11 (1974) 666–670.

[29] R. Messier, Revised structure zone model for thin film physical structure, J. Vac. Sci. Technol. A Vacuum, Surfaces, Film. 2 (1984) 500.

[30] P.B. Barna, M. Adamik, Fundamental structure forming phenomena of polycrystalline films and the structure zone models, Thin Solid Films. 317 (1998) 27–33.

[31] A. Anders, A structure zone diagram including plasma-based deposition and ion etching, Thin Solid Films. 518 (2010) 4087–4090.

[32] A. Anders, Cathodic Arcs Fom fractal spots to energetic condensation, Springer Series on, Berkeley, California, 2008.

[33] H. Fujiwara, Spectrsocopic ellispometry, John Wiley & Sons, Tokyo, Japan, 2007.

[34] J.A. Duffie, W.A. Beckman, Solar engineering of thermal processes., 3rd ed., John Wiley & Sons, New York, 2005.

[35] ASTM, ASTM G173: Standard Tables for Reference Solar Spectral Irradiance at Air Mass 1.5: Direct Normal and Hemispherical for a 37 Degree Tilted Surface, US, 2008.

[36] C.G. Granqvist, Solar energy materials: An overview, Appl. Phys. A Solids Surfaces. 52 (1991) 83–93.

[37] R. Joerger, Optical properties of inhomogeneous media, Sol. Energy Mater. Sol. Cells. 54 (1998) 351–361.

[38] C.G. Granqvist, Solar Energy Materials, Adv. Mater. 15 (2003) 1789–1803.

[39] M. Fox, Optical Properties of Solids, Oxford Mas, Oxford Unversity Press, Oxford, 2001.

[40] B. García Olmedo, Fundamentos de Electromagnetismo, Univeridad de Granada, 2005.

[41] W.J. Plieth, K. Naegele, Kramers-Kronig analysis for the determination of the optical constants of thin surface films, Surf. Sci. 50 (1975) 53–63.

[42] E. Hecht, Optics, 4th Editio, Addison-Wesley, 2001.

[43] N. Kannan, D. Vakeesan, Solar energy for future world: - A review, Renew. Sustain. Energy Rev. 62 (2016) 1092–1105.

[44] L.A. Weinstein, J. Loomis, B.B. Bhatia, D.M. Bierman, E.N. Wang, G.G. Chen, Concentrating Solar Power, Chem. Rev. 115 (2015) 12797.

[45] H.L. Zhang, J. Baeyens, J. Degrève, G. Cacères, Concentrated solar power plants: Review and design methodology, Renew. Sustain. Energy Rev. 22 (2013) 466–481.

[46] ASTM: E903-12 Standard Test Method for Solar Absorptance , Reflectance , and Transmittance of Materials Using Integrating Spheres, 2012.

[47] E. Standard, N. Europeenne, UNE-EN 673 Determinación del coeficiente de transmisión térmica, Europe, 2011.

[48] M.G. Hutchins, Spectrally Selective Solar Absorber Coatings, Appl. Energy. 5 (1979) 251.

[49] L. Roux, J. Hanus, J.C. Francois, M. Sigrist, The optical properties of titanium nitrides and carbides: Spectral selectivity and photothermal conversion of solar energy, Sol. Energy Mater. 7 (1982) 299–312.

[50] C.-G. Ribbing, A. Roos, Transition metal nitride films for optical applications, in: R.L. Hall (Ed.), Soc. Photo-Optical Instrum. Eng., Spie. Int. Societiy optical engineering, San Diego, CA, 1997: pp. 148–162.

[51] B. Karlsson, J.-E. Sundgren, B.-O. Johansson, Optical constants and spectral selectivity of titanium carbonitrides, Thin Solid Films. 87 (1982) 181–187.

[52] F. Mammadov, Study of Selective Surface of Solar Heat Receiver, Int. J. Energy Eng. 2 (2012) 138–144.

[53] G.B. Smith, A. Ignatiev, The relative merits of black cobalt and black chrome as high temperature selective absorbers, Sol. Energy Mater. 2 (1980) 461–467.

[54] T. Lee, D. Kim, P. Chungmoo, The optical characteristics of black chrome solar selective films coated by the pulse current electrolysis method, Sol. Energy Mater. Sol. Cells. 29 (1993) 149–161.

[55] M. Valayapetre, O.T. Inal, L.E. Murr, A.E. Torma, A. Rosenthal, Microstructural and mechanical property evaluation of black-chrome coated solar collectors, Sol. Energy Mater. 2 (1979) 177–199.

[56] C. Granqvist, Materials for solar energy conversion: An overview, Sol. Energy Mater. Sol. Cells. 54 (1998) 39–48.

[57] C.E. Kennedy, Review of Mid- to High- Temperature Solar Selective Absorber Materials, (2002).

[58] E.D. Palik, Handbook of Optical Constants of Solids, Academic Press, 1998.

[59] a. Donnadieu, B.O. Seraphin, Optical performance of absorber-reflector combinations for photothermal solar energy conversion, J. Opt. Soc. Am. 68 (1978) 292.

[60] D. Chester, P. Bermel, J.D. Joannopoulos, M. Soljacic, I. Celanovic, Design and global optimization of high-efficiency solar thermal systems with tungsten cermets., Opt. Express. 19 Suppl 3 (2011) A245–57.

[61] B.O. Seraphin, Chemical vapor deposition of thin semiconductor films for solar energy conversion, Thin Solid Films. 39 (1976) 87–94.

[62] G. Pellegrini, Experimental methods for the preparation of selectively absorbing textured surfaces for photothermal solar conversion, Sol. Energy Mater. 3 (1980) 391–404.

[63] C.M. Lampert, Advanced optical materials for energy efficiency and solar conversion, Sol. Wind Technol. 4 (1987) 347–379.

[64] A. a. Shah, C. Ungaro, M.C. Gupta, High temperature spectral selective coatings for solar thermal systems by laser sintering, Sol. Energy Mater. Sol. Cells. 134 (2015) 209–214.

[65] G. Pettit, Cuomo, J.J. Distefano, T. Woodall, Solar absorbing surfaces of anodized dendritic tungsten, IBM J. Res. Dev. 22 (1987) 372– 377.

[66] K.G.T. Hollands, Directional selectivity, emittance, and absorptance properties of vee corrugated specular surfaces, Sol. Energy. 7 (1963) 108–116..

[67] I.E. Khodasevych, L. Wang, A. Mitchell, G. Rosengarten, Micro- and Nanostructured Surfaces for Selective Solar Absorption, Adv. Opt. Mater. (2015)

[68] S.G. Babiker, S. Yong, M.O. Sid-Ahmed, X. Ming, One-dimensional microstructure tungsten gratings for thermo photovoltaic applications, Res. J. Appl. Sci. Eng. Technol. 7 (2014) 2271–2277.

[69] J. Wang, Z. Chen, D. Li, Simulation of two-dimensional Mo photonic crystal surface for high-temperature solar-selective absorber, Phys. Status Solidi Appl. Mater. Sci. 207 (2010) 1988–1992.

[70] E. Guillén, R. Escobar-Galindo, I. Heras, J.L. Endrino, N. Martinez, A. Bello, et al., Self-cleaning high temperature resistant solar selective coating, P201431972, 2014, 2014.

[71] J. Müller, B. Rech, J. Springer, M. Vanecek, TCO and light trapping in silicon thin film solar cells, Sol. Energy. 77 (2004) 917–930.

[72] J. Mun, S.W. Kim, R. Kato, I. Hatta, S.H. Lee, K.H. Kang, Measurement of the thermal conductivity of TiO2 thin films by using the thermo-reflectance method, Thermochim. Acta. 455 (2007) 55–59. doi:10.1016/j.tca.2006.11.018.

[73] G. E., I. Heras, G. Rincón, F. Lungwitz, M. Alcon-Camas, R. Escobar-Galindo, Room temperature deposition of highly dense TiO2 thin films by Filtered Cathodic Vacuum Arc, in: SPIE Opt. + Photonics 2015, 2015.

[74] X.-F. Li, Y.-R. Chen, J. Miao, P. Zhou, Y.-X. Zheng, L.-Y. Chen, et al., High solar absorption of a multilayered thin film structure., Opt. Express. 15 (2007) 1907–12.

[75] C.G. Granqvist, Optical Properties of Cermet Materials, J. Phys. 42 (1981) 247.

[76] F. Cao, K. McEnaney, G. Chen, Z. Ren, Review of Cermet-based Spectrally-Selective Solar Absorbers, Energy Environ. Sci. (2014).

[77] N. Selvakumar, H.C. Barshilia, Review of physical vapor deposited (PVD) spectrally selective coatings for mid- and high-temperature solar thermal applications, Sol. Energy Mater. Sol. Cells. 98 (2012) 1–23.

[78] Q.-C. Zhang, Y.. Shen, High performance W–AlN cermet solar coatings designed by modelling calculations and deposited by DC magnetron sputtering, Sol. Energy Mater. Sol. Cells. 81 (2004) 25–37.

[79] X. Du, C. Wang, T. Wang, B. Chen, L. Zhou, N. Ru, Magnetron sputtering high temperature Mo-Al2O3 cermet solar selective coatings, Mater. Sci. Forum. 546-549 (2007) 1773.

[80] L. Rebouta, A. Sousa, P. Capela, M. Andritschky, P. Santilli, A. Matilainen, et al., Solar selective absorbers based on Al2O3:W cermets and AlSiN/AlSiON layers, Sol. Energy Mater. Sol. Cells. 137 (2015) 93–100.

[81] Q.-C. Zhang, Recent progress in high-temperature solar selective coatings, Sol. Energy Mater. Sol. Cells. 62 (2000) 63–74.

[82] Q.-C. Zhang, Metal-AlN cermet solar selective coatings deposited by direct current magnetron sputtering technology, J. Phys. D. Appl. Phys. 31 (1998) 355–362.

[83] D. Bruggeman, Calculation of various physics constants in heterogenous substances I Dielectricity constants and conductivity of mixed bodies from isotropic substances, Ann. Phys. 24 (1935) 636–664.

[84] Q. Zhang, Stainless-steel–AlN cermet selective surfaces deposited by direct current magnetron sputtering technology, Sol. Energy Mater. Sol. Cells. 52 (1998) 95–106.

[85] S. Wijewardane, D.Y. Goswami, A review on surface control of thermal radiation by paints and coatings for new energy applications, Renew. Sustain. Energy Rev. 16 (2012) 1863–1873.

[86] C. Atkinson, C.L. Sansom, H.J. Almond, C.P. Shaw, Coatings for concentrating solar systems – A review, Renew. Sustain. Energy Rev. 45 (2015) 113–122.

[87] M.A. Signore, D. Valerini, L. Tapfer, G. Caretto, A. Rizzo, Zirconium nitride films deposited in (Ar + N2 + H2) sputtering atmosphere: Optical, structural, and electrical properties, J. Vac. Sci. Technol. A Vacuum, Surfaces, Film. 29 (2011) 061507.

[88] Y. Claesson, M. Georgson, A. Roos, C.-G. Ribbing, Optical characterisation of titanium-nitride-based solar control coatings, Sol. Energy Mater. 20 (1990) 455–465.

[89] H.O. Pierson, Handbook of refractory carbides and nitrides: properties, characteristics, processing, and applications, Noyes Publications, Westwood,New Yersey USA, 1996.

[90] C. Zou, L. Huang, J. Wang, S. Xue, Effects of antireflection layers on the optical and thermal stability properties of a spectrally selective CrAlN–CrAlON based tandem absorber, Sol. Energy Mater. Sol. Cells. 137 (2015) 243–252.

[91] L. Yan, F. Qin Dong, S. Zhao, H. Yan, H. Lv, X. Yuan, Hydrophobic MgF2 antireflective films with enhanced environmental durability by a sol-gel process, Mater. Lett. 129 (2014) 156–158. doi:10.1016/j.matlet.2014.05.036.

[92] W. Dou, P. Wang, D. Zhang, J. Yu, An efficient way to prepare hydrophobic antireflective SiO2 film by sol-gel method, Mater. Lett. 167 (2016) 69–72.

[93] K. Tadanaga, N. Yamaguchi, Y. Uraoka, A. Matsuda, T. Minami, M. Tatsumisago, Anti-reflective properties of nano-structured alumina thin films on poly(methyl methacrylate) substrates by the sol-gel process with hot water treatment, Thin Solid Films. 516 (2008) 4526–4529.

[94] E. Céspedes, M. Wirz, J.A. Sánchez-García, L. Alvarez-Fraga, R. Escobar-Galindo, C. Prieto, Novel Mo–Si3N4 based selective coating for high temperature concentrating solar power applications, Sol. Energy Mater. Sol. Cells. 122 (2014) 217–225. d

[95] G.L. Harding, Absorptance and emittance of metal carbide selective surfaces sputter deposited onto glass tubes, Sol. Energy Mater. 2 (1980) 469–481.

CHAPTER 2: METHODOLOGY FOR A COMPLETE DESIGN OF SOLAR SELECTIVE COATINGS

All the colours make their first appearance about the edge of the circular spot. More explosions make them expand towards the extremity of the space first marked out; while others succeed in their places; till, after thirty of forty explosions, three distinct rings appear, each consisting of all colours.

Joseph Priestley, describing interference colours of oxide coatings on glass by cathodic arcs, 1775.

The methodology followed in this thesis for a complete design of solar selective coatings is fully explained in this chapter. The design process starts with the selection of the material that composes each layer in the multilayer stack, based on optical simulation (section 2.1). Then, the selected thin film candidates are grown by cathodic vacuum arc techniques. The different deposition systems employed are described in section 2.2. The complete characterization of the deposited thin films (section 2.3) was a key element in the validation of the initial simulations and the subsequent optimization of the desired multilayered SSC. Finally, heating tests are performed to analyse the durability of the coatings in air at high temperatures and to predict their service lifetime (section 2.4).

2.1. Optical simulation of multilayer solar selective coatings

The optimization of the optical behaviour of solar selective stacks (i.e. high solar absorptance (a) in the visible range and low thermal emittance (ε_T) in the infrared wavelength), requires an accurate optical simulation. This simulation is a time and money saving matter, reducing the number of necessary thin film depositions and avoiding a try and error optimization strategy. Generally, optical simulation relies on literature data based to obtain the optical constants of the materials. However, in this thesis the microstructure and optical characterization of the samples will be used in order to obtain an optimized simulation. The commercial software CODE (Coatings Design) [1] was employed to carry out these simulations. The input parameters in the software are:

- The **complex refractive index** of materials forming the layer stack. For the initial simulations, the optical constants were extracted from literature data [2–6]. After this preliminary study, the optical constants were obtained experimentally by spectroscopic ellipsometry (SE) measurements on deposited thin films. However, standard SE measurements are limited into the 190-1700 nm wavelength range. Therefore, in order to obtain a proper calculation of the emittance, the optical constants have been extrapolated in the infrared range. This extrapolation is based on the measured reflectance spectra in the infrared range, as detailed in section 2.1.1. In the case of nanocomposite materials, effective medium approximation (EMA) theories were employed (see section 2.1.2), combining the optical constants of the components that form the heterogeneous material.
- **The structure of the multilayer stack**: number of layers, thickness of each layer and roughness of the interface (if scattering losses are expected).
- **The angle of incidence** and **polarization** type of the incident radiation.

2.1.1 Extrapolation of the optical constants in the infrared range

The optical constants (n, k) determined by standard spectroscopic ellipsometry (section 2.3.4) are usually restricted to UV-Vis range. A proper IR extrapolation of the optical constants is crucial for a proper estimation of the thermal emittance of thin films at different temperatures. Infrared ellipsometer devices could determine the optical constants in the infrared range [7,8], however, these systems are scarce and not available in most material science laboratories. Hence, in order to overcome this limitation, an extrapolation of the optical constants measured in the UV-Vis range to the infrared range is necessary. CODE software considers the last experimental value as a constant for the rest of wavelength range of interest (see Figure 2.3 (a)). In this thesis, an alternative approach is proposed. The extrapolation of the optical constants in the IR range is done

studying the measured reflectance in the infrared with an FTIR spectrometer. In the case that no discrete absorption is observed in the measured IR reflectance spectra (associated to vibrational modes as e.g. in doped semiconductor), the real part (n) can be directly calculated by extrapolating the optical model(s) employed to determine the optical constants in the UV-Vis measured range [9]. The optical constants are not independent of each other and the relation between n and k is described by the Kramers-Kronig relations (KKR), whose equations can be found elsewhere [10]. The imaginary part can be subsequently determined by applying KKR and avoiding k negative values in order to obtain physically reasonable models.

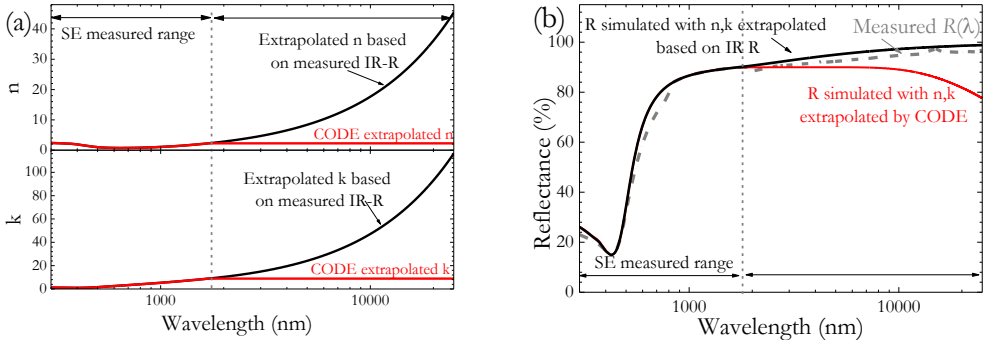

Figure 2.1 – (a) Optical constants of TiN extrapolated in the infrared wavelength region by CODE (black line) and based on the measured infrared reflectance (IR R) spectra employing Drude dispersion model (red line). (b) Experimental reflectance spectrum of TiN (grey dash line) compared to the simulated reflectance using CODE extrapolation in the IR (red) and using optical constants extrapolation applied in this thesis (black).

In Figure 2.1 (b), the simulated reflectance obtained using the two extrapolation methods described above are compared to the experimental reflectance of a TiN film. It can be observed how CODE extrapolation underestimates the reflectance spectrum in the infrared range. On the other hand, the comparison of the simulated and measured spectra reveals that the extrapolation employed in this thesis properly describes the experimental reflectance in the whole wavelength range.

2.1.2 Effective medium approximation (EMA) theories for nanocomposite materials

The complex refractive index of two-phase nanocomposites can be determined by a non-trivial mixing of the optical constants of the individual components by the so-called EMA theories. If the average size of the inhomogeneities or particles is much smaller than the wavelength of the incident radiation, the electric and magnetic fields are almost constant over this length [11], and hence, the composite behaves like quasi-homogeneous material, as represented in Figure 2.2.

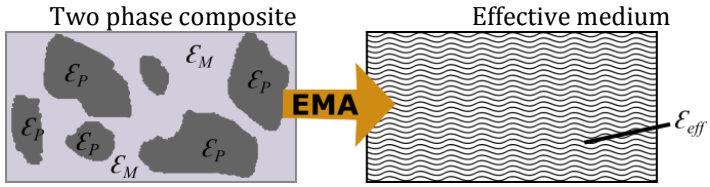

Figure 2.2 - Schematic idea of effective medium approximation theory, where the dielectric behavior of a two-phase nanocomposite can be described by an effective dielectric function (ε_{eff}).

These theories require the optical constants of the embedded particles (ε_P) and the host (matrix) material (ε_M) to determine the effective dielectric function (ε_{eff}) of the composite material. The particle size and distribution in the host matrix are assumed by the volume fraction *f* as defined in equation (2.1).

$$f = \frac{V_{particles}}{V_{total}} \tag{2.1}$$

The simplest EMA theory is the Maxwell-Garnett (MG) theory. This theory considers that the inhomogeneous material has a separated grain structure [12] without particle interactions (no percolation). MG is only applicable to systems of low volume fraction of embedded particles ($f < 0.3$). The MG theory for identical spherical particles is defined in equation (2.2):

$$\frac{\varepsilon_{effMG} - \varepsilon_M}{\varepsilon_{effMG} + 2\,\varepsilon_M} = f\frac{\varepsilon - \varepsilon_M}{\varepsilon + 2\,\varepsilon_M} \tag{2.2}$$

The most commonly used EMA theory was proposed by Bruggeman (BRU) in 1935 [13]. It is applicable to aggregate microstructures where the host matrix and the distributed particles are hardly distinguishable. BRU theory has proven to be adequate for large particle volume fraction ($f \geq 0.3$) and percolated systems. The BRU formula for spherical shaped particles is expressed in equation (2.3)

$$(1-f)\frac{\varepsilon_M - \varepsilon_{effBRU}}{\varepsilon_M + 2\,\varepsilon_{effBRU}} + f\frac{\varepsilon - \varepsilon_{effBRU}}{\varepsilon + 2\,\varepsilon_{effBRU}} = 0 \tag{2.3}$$

For very low volume fraction (f <0.3) BRU is equivalent to MG theory, and no percolation is considered. Above that threshold, the embedded particles are assumed to be partially connected. Both MG and BRU theories have in common that the effective dielectric function does not depend explicitly on the size of the inhomogeneities. This is because the electric dipole term, which is proportional to particle volume, is retained in the series expansion of the amplitude of the electric field scattered by a single particle. However, important discrepancies between experimental and simulation results are found when only volume fraction is taken into account to describe the micro-topology of a nanocomposite material [14].

In 1978, Bergman [15] developed a theory where the microgeometry of the nanocomposite is taken into account by a spectral density function *g(n,f)*. Bergman representation (BER) is described by equation (2.4):

$$\varepsilon_{effBER} = \varepsilon_M(1 - f(G(t))) \quad with \quad G(t) = \int_0^1 \frac{g(n,f)}{t-n} dn \tag{2.4}$$

where t is the reduced dielectric function, that takes real values between 0 and 1, as equation (2.5):

$$t = \frac{\varepsilon_M}{\varepsilon_M - \varepsilon_P} \tag{2.5}$$

The function $g(n,f)$ holds details of the microgeometry. It is a real, non-negative function, normalized in the interval [0,1] with an arbitrary number of points (n) that are used to define the shape of the function by a cubic spline interpolation. Any microgeometry can be represented with a specific $g(n,f)$. However, it cannot be computed analytically for real systems since the topology is too complicated or not even known. If the system has some degree of connectivity between the embedded particles, it is useful to split the spectral density function in a diverging δ function and a continuous part [16] as defined in (2.6):

$$g(n,f) = g_0\delta(n) + g_{cont}(n,f) \tag{2.6}$$

where g_0 is the percolation strength that describes the metallic or dielectric behaviour of the nanocomposite. The parameter g_0 varies between 0 (no percolation) and 1 (total interconnection between the nanoparticles). BER representation parameters are difficult to determine and they are usually calculated by adjusting $g(n,f)$ to experimental data [17]. The effective dielectric function obtained provides additional information related to the shape of the nanoparticles and their degree of percolation. BER theory is especially interesting when the microstructure plays a significant role in the optical properties of the heterogeneous material and it is the approach followed in this work for simulating the nanocomposites. In-depth discussion of the fitting of a measured reflectance spectrum in a a-C:VC nanocomposite thin film using MG, BRU, and BER approximations can be found in chapter 3.

2.2. Thin film deposition

The thin films deposited in this thesis were prepared by Cathodic Vacuum Arc (CVA) as it shows numerous advantages compared to other Physical Vapour Deposition (PVD) techniques [18]. The basics principles of the cathodic arc plasma generation and the three different CVA equipments employed in this these are described below.

2.2.1 Introduction to cathodic vacuum arc deposition

The vacuum arc is an electrical discharge between two metallic electrodes (electrode and cathode) produced in vacuum. The main components of an arc source are shown in Figure 2.3 (a).

The arc is an electrical discharge with a higher ionization degree than other PVD techniques [19], hence, denser, stoichiometric and better adhering coatings are obtained. The discharge is characterized by a low DC or pulsed voltage (typically <30 V) to trigger and sustains an arc plasma with high discharge current (>50 A), concentrated in non-stationary cathode spots. The arc is ignited by contacting the trigger (1 in Figure 2.4 (a)) with the cathode surface (2 in Figure 2.4 (a)) and it is afterwards self-sustained unless the power is cut off. Energetic ion plasma is generated from the source material by explosions at micrometre size cathode spots moving on the cathode surface. In the absence of an external magnetic field, the cathode spots motion has been considered random and with fractals features [20]. Different models based on random walk [21,22] or fractal have been employed to simulate the cathode spots movement.

The vacuum arc plasma is produced at non-stationary cathodic spots with a very high current density of order 10^6 A/cm^2. The high current density is associated with an extremely high power density of ~10^{13} W/m^2 that can provide conditions for the phase transformation of the solid cathode material to a fully ionized dense plasma [23] and expands rapidly into the vacuum chamber. The plasmas can be altered with electric and magnetic fields. In most CVA systems, an external magnetic field is applied in a permanent ring magnet to steer the moving arc spots around the cathode. By doing so, a more efficient material utilization and a more homogeneous distribution of the heat on the cathode is attained.

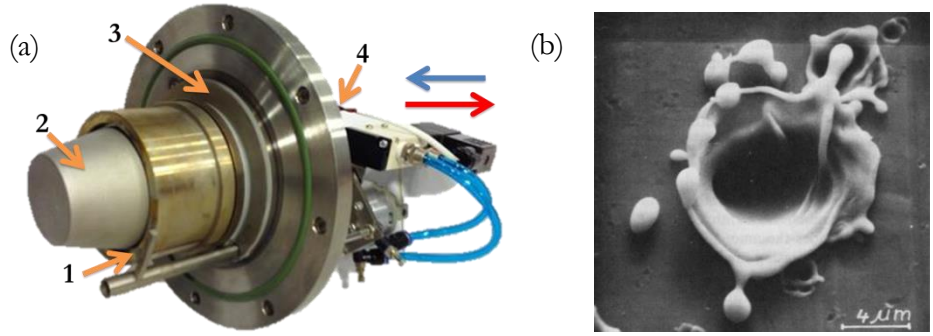

Figure 2.3 – (a) Detail of the arc source: (1) and (2) are the two electrodes where the electrical discharge is created, where (1) is the movable trigger that makes contact with the cathode to start the arc and (2) is the metallic cathode from where the plasma is produced at the cathode spots. (3) Annular grounded anode body that surrounds the cathode and (4) Cooling system to refrigerate the cathode. (b) Crater structure on a cadmium cathode produced by a 4.7-A arc in vacuum [24]

The kinetic and potential energy of the ions created in the cathodic arc can be calculated through the measurement of the ion charge state distribution of the cathode material. The average ion energy plays an important role in the texture, stress or subimplantation depth of the growing thin films [25]. The kinetic energy of the ions can be increased by applying a negative bias voltage (DC or pulsed) to the substrate that also involves obtaining denser deposited films. If the bias voltage is very high, the ions will gain enough energy for ion subimplantation but nevertheless, it

can generate intrinsic stress in the resulting films. Therefore, special attention must be given to stress control, reducing the fraction high energy ions by i.e. pulsed biasing [26].

2.2.2 Filtering of macroparticles

The high energy of the arc can lead to the evaporation of macroparticles or droplets at the cathode spots as the result of the crater formation (see Figure 2.3 (b)) [24], where formed macroparticles can be observed at the boundaries. Hantzsche [21,27] and Jüttner [28] explained the formation of the craters due to incident ion flux on the cathode which applies a pressure on the melted metal, producing micropoints at the crater boundaries and numerous droplets. Several publications have reported the relationship between the macroparticles formation with the temperature, the current, the cathode material and the presence of external magnetic fields [24,29,30]. The authors concluded that the macroparticle generation is independent of the arc current but depends highly on the cathode material. The largest macroparticles are found in materials with low melting points. When a macroparticle reaches the growing film, it could be included in the coating material as shown in Figure 2.4 (a), or cause a hole in the film after the release of macroparticles in the sample (Figure 2.4 (b)). Top view SEM image in Figure 2.4 (c) shows an AlTiN film with a high concentration of macroparticles.

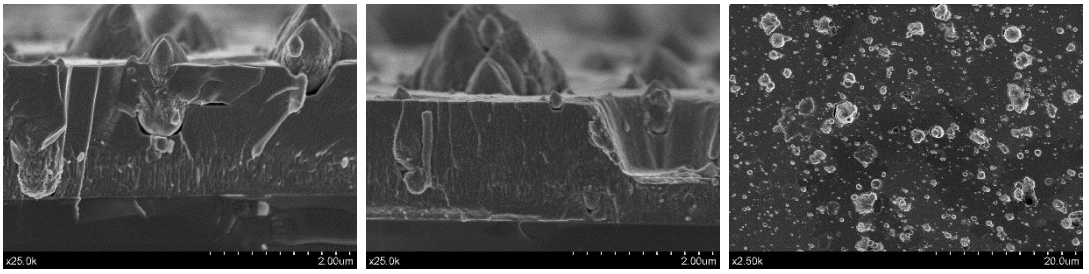

Figure 2.4 – SEM images of AlTiN thin film deposited by unfiltered CVA. (a) Macroparticles incorporated in the growing film at different levels. (b) Hole in the film caused by the loss of a macroparticle as its low adhesion. (c) Top view of the numerous macroparticles with an average size of ~1μm.

The detrimental macro-particles incorporation in the coating can be reduced either by reducing the macroparticle production [31] or by separating the plasma flow from the macroparticles using magnetic filters. The size of macroparticles are reduced by increasing the arc spot velocity by e.g. high current pulsed arcs [32]. Magnetic filters are commonly employed to separate the macroparticles from the plasma generated at cathode spots. The purpose of the coil is to guide the plasma through a duct to the substrate in the deposition chamber. In doing so, the plasma particles (electrons and ions) are separated from the microscopic, but relatively massive neutral droplets. Many different shapes and configurations have been designed for macroparticles filters differing in the bending angles and in the in the plane or out of phase bending [20,33–36]. Some examples are straight magnetic filters, 90º duct filters (Figure 2.5 (a)), knee filters, rectangular

duct filters or freestanding S-filters (Figure 2.5 (b)) among others. The classical 90º duct filter is the one employed in this work.

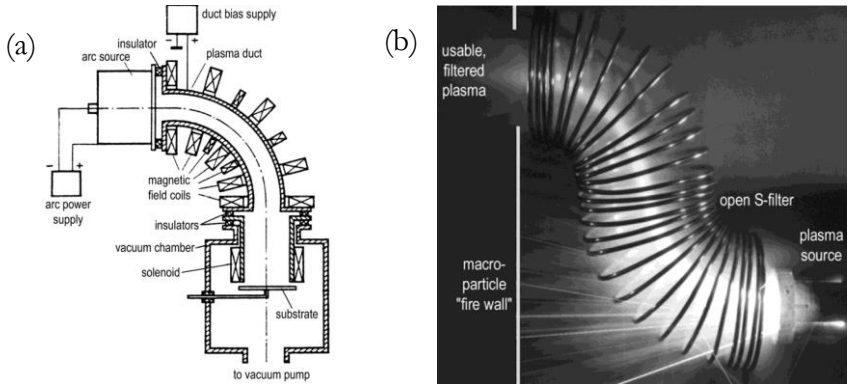

Figure 2.5 – Different macroparticle filter configurations (a) classic 90º duct filter by Aksenov and co-workers (adapted from [34]) and (b) open S-filter [31].

2.2.3 Cathodic vacuum arc deposition systems employed in this thesis

Three different CVA systems were employed in this work, whose main differences are summarized in Table 2.1. A pulsed arc source cathodic vacuum arc (PFCVA) with 90º curved electromagnetic filter was employed for growing the a-C:MeC films described in chapter 3 (Figure 2.6 (a)), sited at "*Centro technologic Manresa*" (CTM) at Manresa, Spain. For the AlTiON films described in chapter 4, a DC unfiltered cathodic vacuum system situated at Metal Estalki S.L (Bilbao, Spain) was employed (Figure 2.6 (b)). Both types of coatings were also deposited in a filtered cathodic vacuum arc DC (FCVA) (Figure 2.6 (c)) situated at Abengoa Research (Sevilla, Spain). Further details of the deposition parameters will be given in Chapter 3 and 4.

Table 2.1 – Comparison of the three different equipments employed in this thesis (a) CVA: cathodic vacuum arc (non-filtered) from Metal Estalki S.L., (b) PFCVA: pulsed filtered cathodic vacuum arc in CTM and (c) FCVA: filtered cathodic vacuum arc in Abengoa Research.

Parameter	(a) PFCVA – CTM	(b) CVA - Metal estalki	(c) FCVA – Abengoa Reseach
Macroparticles filtering	90º duct filter	No	90º duct filter
Arc source	Pulsed DC (3 ms repeated at 7.5Hz)	DC	DC
Cathode size	Cylindrical shape: 30 mm x ø10 mm	331 x 174 mm	Truncated cone: 50mm height x ø50 mm
Number of arc sources	2	1	2
Distance to the substrate	~58 cm	~15 cm	~24 cm
Bias voltage	Max 1000 V pulsed	Max 100V DC	Max 1000 V pulsed + 100V DC
Pulsed biasing	Yes. 0 to 80% at 100KHz	No	Yes. 0 to 80% at 40KHz
Maximum T (ºC)	350ºC	500ºC	350ºC

(a)

(b)

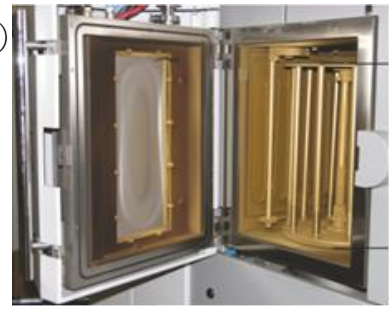

(c)

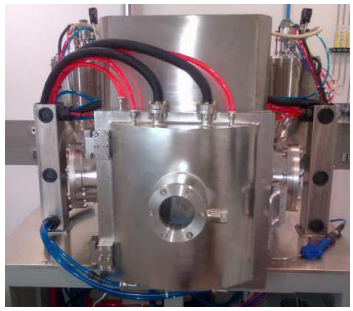

Figure 2.6 – Images of the three different CVA systems employed in this thesis: (a) pulsed filtered cathodic vacuum arc with two arc sources in CTM (b) PL70 Plattitt CVA non-filtered chamber in Metal estalki S.L and (c) filtered cathodic vacuum arc with two arc sources in Abengoa Research.

2.2.4 Substrate preparation

The substrate of a solar selective coating for tower central receivers has to withstand temperatures higher than 700ºC and oxidation damage. Hence, the complete solar selective coatings are deposited on inconel HAYNES 230 or HAYNES 625 ® due to the high oxidation resistance in air (excellent at 1150ºC) [37]. Inconel substrates exhibit as well excellent infrared reflection properties with a thermal emittance of 7 and 13 % at RT and 600ºC, respectively. In addition, Si (100) wafers were used for specific characterization purposes (i.e. XRD, IBA, etc.), and glass substrates were required for measuring the transmittance of the antireflective oxide layers.

All substrate types are subjected to the same chemical cleaning procedure. Before putting into the vacuum chamber, they were cleaned by ultrasonic agitator in distilled water, acetone and ethanol 15 minutes each solvent. Prior to the deposition, substrates were sputter plasma cleaned by ionized argon bombardment for 15 min, employing a pulsed bias discharge of 750V, 80% duty cycle (40 kHz frequency) at ~1.5 Pa pressure.

2.3. Thin film characterization

The characterization techniques employed in this thesis are summarized in Table 2.2, organized by the nature of the input probe and the output signal detected. Thickness and roughness were measured with optical and mechanical profilometers. Film composition and depth

profiles were obtained combining different ion beam analysis (IBA) techniques. For the microstructural analysis, X-ray diffraction (XRD), scanning electron microscopy (SEM) and high resolution transmission electron microscopy (HR-TEM) in combination with selected area electron diffraction (SAED) were employed. Raman spectroscopy was used for structural and chemical analysis of the bonding in the films. The optical constants were determined by spectroscopic ellipsometry (SE) while UV-Vis-NIR and FTIR spectrophotometry was employed for investigating the optical properties, i.e. spectral reflectance.

Table 2.2 – List of characterization techniques employed for complete characterization of the deposited thin films.

Technique	Property analysed	Input probe	Schematic	Output signal detected
Mechanical profilometry	Thickness and roughness	Force		Electrical signal
Confocal microscopy		Photons ((VIS laser λ)	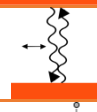	Photons
Rutherford backscattering Spectrometry (RBS)	Film composition, thickness, elemental profiles	High energy light ions	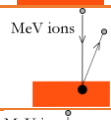	Backscattered light ions
Nuclear reaction analysis (NRA)		High energy ions	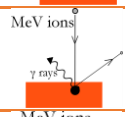	Reactive ions
Elastic Recoil Detection (ERD) analysis		High energy heavy ions	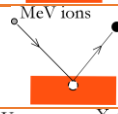	Recoiled light ions
X-ray diffraction (XRD)	Crystal structure	Photons (X-rays)	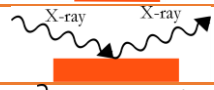	Photons (X-rays)
Raman spectroscopy	Molecular structure	Photons (Vis laser λ)		Photons
Scanning Electron Microscopy (SEM)	Morphology	Electrons	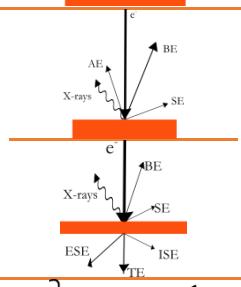	Backscattered electrons (BE), transmitted electrons (TE), elastic/inelastic scattered electrons (ESE, ISE) , secondary electrons (SE), X-rays
Transmission electron microscopy (TEM)				
Spectroscopy ellipsometry (SE)	Optical constants, thickness and roughness	Photons (polarized UV/Vis light)	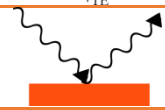	Photons (Polarized UV/Vis light)
UV-Vis-NIR Spectrophotometry	Transmittance and reflectance	Photons (UV-Vis)	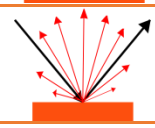	Photons (UV-Vis)
FTIR spectroscopy		Photons (IR)		Photons (IR)

2.3.1 Thickness and roughness

In this study, thickness and roughness have been measured with a mechanical profilometer DektakXT from Bruker. It includes an X-Y auto sample positioning stage that allows 3D mapping along the sample. A diamond-tipped stylus (2 µm radius) with 3 mg force is used for the measurements. An optical profilometer, Confocal Microscope (Plµ 2300, SENSOFAR) with 50x objective was employed too. It is equipped with a laser light source (λ=470nm) and an open-loop z-scan device with a resolution of dz = 0.1 µm. In both equipments, the measurement of the thickness is based on the determination of the step in a marked area in the sample without coating. An example of thickness determination with a confocal microscope is shown in Figure 2.7.

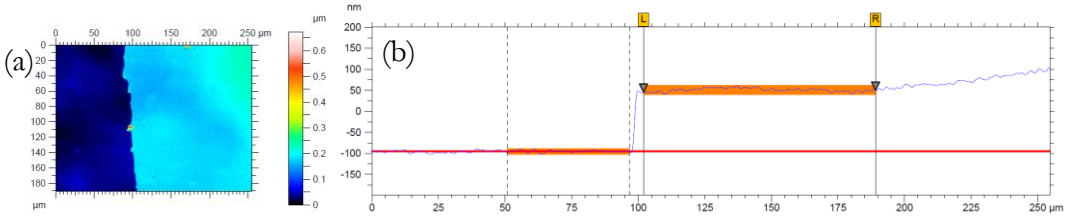

Figure 2.7 - Thickness determination of a-C:MoC sample deposited on inconel substrate with confocal microscope (a) Confocal image and (b) 146 nm step measurement after the leveling, both images from software SensoMap Plus 5.1.1 [38]

To determine the deposition growth rate for each deposited material, single layers have been deposited with three different deposition times, as shown in the example in Figure 2.8 for an AlTiON sample deposited on inconel and silicon substrates.

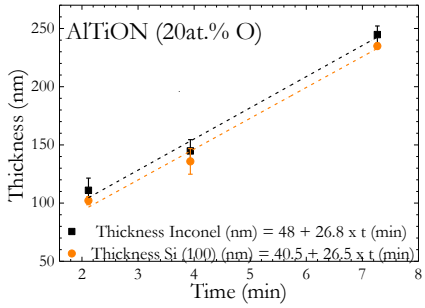

Figure 2.8 – Calculation of the growth rate on AlTiON (20 at.% O) samples deposited on Si and Haynes 230 substrates.

The roughness was analysed following the standard of ISO4287-1997 [39] that defines the parameters to employ for roughness comparison. The two most commonly employed are the arithmetical mean deviation roughness (R_a) and the root mean square roughness (R_q) as defined in equation (2.7):

$$R_a = \frac{1}{n}\sum_{i=1}^{n}|z_i - \langle z\rangle| \quad ; \quad R_q = \frac{1}{n}\sqrt{\sum_{i=1}^{n}(z_i - \langle z\rangle)^2} \qquad (2.7)$$

Where $\langle z\rangle$ is the mean height in a selected evaluation length and n is the defined number of sampling lengths.

2.3.2 Thin film composition by ion beam analysis (IBA).

Ion beam analysis (IBA) techniques are widely employed for identifying the elemental composition of thin films [40]. During the bombardment of a sample with energetic ions, elastic and inelastic scattering, nuclear reactions and/or electromagnetic excitations take place. The advantages of IBA methods are the non-destructiveness, standard free and quantitative interpretation of the experimental results. The three different IBA techniques employed in this thesis are schematized in Figure 2.9: Rutherford backscattered spectroscopy (RBS), nuclear reaction analysis (NRA) and elastic recoil detection (ERD) analysis. All the experiments were performed at the ion beam centre at Helmholtz Zentrum Dresden-Rossendorf (HZDR) in Germany. The following sections further explained the IBA techniques employed in this work

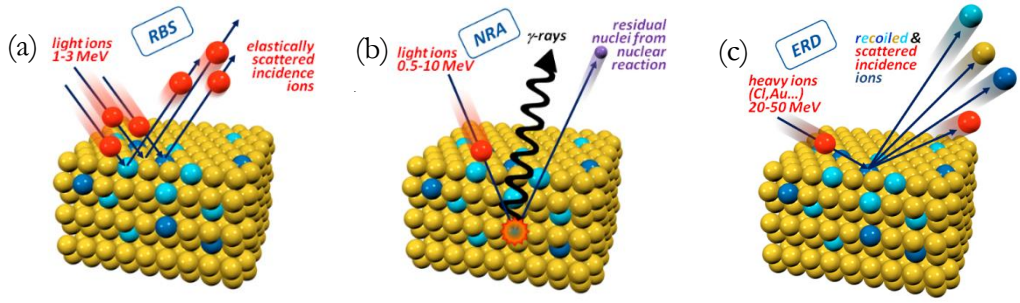

Figure 2.9 - Schematic representation of (a) RBS, (b) NRA and (c) ERD ion beam analysis techniques [41]. The figure depicts the interaction between ions and the material surface in the different IBA techniques.

Rutherford Backscattering Spectrometry (RBS)

RBS is one of the most frequently used techniques for quantitative analysis of composition and depth profiles of thin films up to 1-2 μm depending on the incident energy of the ions [42]. The basic RBS principle is that the energy of an elastically backscattered particle is proportional to: i) the mass of the atoms in the target material and ii) the depth at which the scattering takes place. The ratio between incident energy (E_1) and the energy of the backscattered ions (E_0) is called the kinematic factor ($K=E_1/E_0$), and the energy loss per unit path length is called the stopping power (dE/dx). RBS is best suited for the detection of heavy elements on light substrates and can reach accuracy below 1 at% and a depth resolution of 5-10 nm. However, with RBS technique, light elements in a heavy matrix of the substrate are not detectable.

The cross section in RBS experiments is a known value that depends on the energy of the incident ion, the geometry of the detector and the atomic number of the target atoms. The absolute concentration of atoms (or areal density) in the target material can be determined from the RBS spectra without standards with a depth resolution <5nm and an analysis depth of a few micrometres.

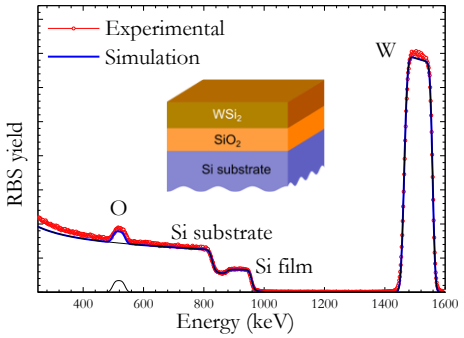

Figure 2.10 – RBS spectrum of WSi2 thin film deposited on silicon substrate thermal oxidized, with $^4He^+$ ions with energy of 1.7 MeV. A schematic of the analysed stack is included

The RBS measurements were carried out at a 2 MeV Van der Graff accelerator by using $^4He^+$ ions with an energy beam of 1.7 MeV. The data were acquired with a silicon barrier detector located at a backscattering angle of 170º, whose energy resolution was 13 keV. As an example, the RBS spectrum of a WSi_2 sample is shown in Figure 2.10 where the tungsten signal can is clearly separated from the Si one. The simulation software SIMNRA [30] version 6.06 was used to extract the metal areal density.

Nuclear reaction analysis (NRA)

NRA is a very useful technique to detect light elements in a heavy matrix or substrate. Once an ion 'a' impinges in an atom 'A', it can induce a nuclear reaction. An intermediate excited nucleus is then formed, which decays to the ground state 'B' by the emission of a particle 'b', normally gamma photons or light particles. The number of reaction products 'b' is proportional to the concentration of the specific element 'A' in the sample. This reaction is described in the abbreviated way A(a,b)B, and it occurs at a characteristic energy. The probability of a NRA is given by the corresponding cross section and depends on the energy, type of projectile and atoms in the target material, and there is no a simple method to predict it. Therefore, NRA is a powerful technique to quantify only a certain element in a sample, but not to probe the composition of an unknown sample, as RBS. A standard sample (reference material with known atom content) is required to determine the absolute concentration of atoms in the target material [43]. The depth resolution of NRA is ~8 nm and the analysis depth is up to 5 μm (depending on the matrix and on the substrate employed), with an accuracy of 0.05 at. %.

NRA is employed in this thesis for an accurate determination of carbon content in the amorphous carbon-metal carbide nanocomposite thin films (Chapter 3). An example of a-C:WC sample measured by NRA is presented in Figure 2.11 (a) and the nuclear reaction is schematized in Figure 2.11 (b).

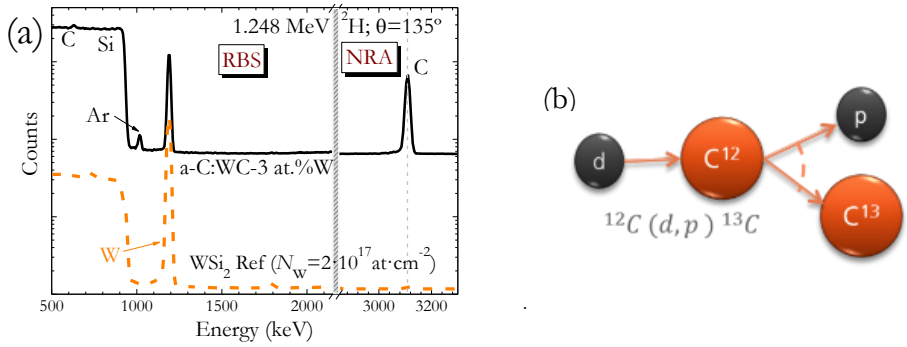

Figure 2.11 – (a) NRA spectrum of WSi_2 as reference sample and a-C:WC samples deposited on a silicon substrate, employing deuterium ions with 1.238MeV. (b) Schematic of the nuclear reaction occurred for cabon.

The NRA measurements were carried out at the 3 MeV Tandem accelerators, by using 1.248 MeV deuterium ions as incident particles at a detection angle of 135º. The nuclear reaction $^{12}C(d,p)^{13}C$ has its maximum cross section at an incident deuterium ion energy of around 1.2 MeV. The intensity of the emitted proton signal is proportional to the carbon concentration in the nanocomposite thin film [44].

Elastic recoil detection (ERD) analysis

ERD analysis is an IBA method based on elastic scattering of ions. The light elements in a heavy matrix or substrate are extracted from the material when a heavy incident ion impinges into the sample. The atoms from the target material are recoiled, and can be quantified. In order to discriminate between the different types of recoiled particles, absorber foils or mass discriminating detectors are employed [45]. The main advantage of ERD over the other IBA techniques is the ability to measure all the elements of the target (including hydrogen) simultaneously and to separate one from each other, avoiding the overlapping as shown in RBS spectra. Figure 2.12 (a) shows ERD measurement for an AlTiN thin film. The areal density and depth profiles are obtained quantitative and without standards from the measurements after fitting the spectra with an accuracy of ~1 at. % (Figure 2.12 (b)). However, due to the usage of heavy ions (i.e. Cl^{+7}), samples can be damaged by the ion beam.

ERD measurements have high detection sensitivity for light elements in a heavy matrix or on a heavy substrate, which is hardly possible using RBS. However, it cannot be used to determine the content of heavy elements in a light matrix. The analysing depth is lower than for the other IBA techniques, <0.75 µm and the depth resolution is ~20 nm.

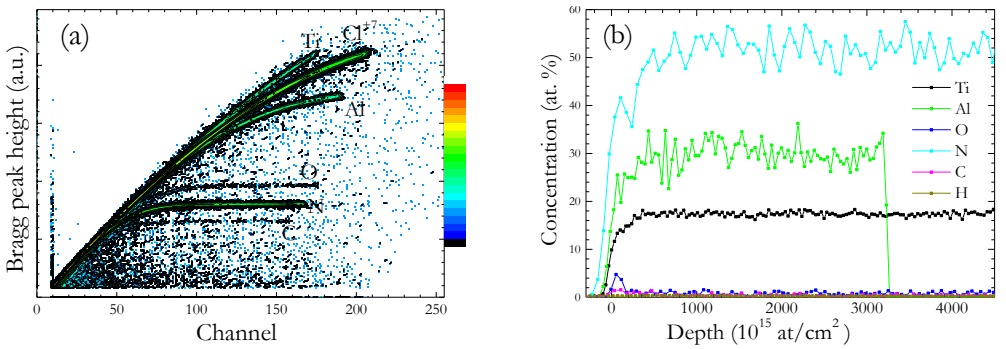

Figure 2.12 - (a) ERDA spectrum of an AlTiN thin film on Si substrate measured with 43 MeV Cl^{7+} ion beam. (b) Resulting depth profile after the fitting of the AlTiN thin film in (a).

ERD measurements in this work were carried out at a 6 MeV tandem accelerator using 43 MeV Cl^{7+} ion beam. The angle between the sample normal and the incoming beam is 75° and the scattering angle is 31°. The analysed area is about 1.5x1.5 mm^2. The recoil ions have been detected with a Bragg ionisation chamber using a full energy detection circuit for the ion energies and a fast timing circuit to obtain a Z-dependent signal to separate ion species. H has been detected with a separate solid state detector at a scattering angle of 41° preceded by an 18 μm Al foil to stop other scattered and recoiled ions. All ERD spectra and the RBS spectrum (Cl^{7+}scattering) were fitted simultaneously using the program NDF v9.3g [46]. For most of the samples, the part of the spectra corresponding to the surface is rounded, what which indicates roughness or thickness variation in the layer. A roughness model has been included in the fitting but it was sometimes not sufficient, resulting in an overestimation of the concentration of the elements.

2.3.3 Microstructural characterization

X-Ray diffraction analysis

X-Ray diffraction is a common method which yields provides crystallographic information of solid materials from s the interaction of a monochromatic X-ray source with the periodic crystal lattice of the sample [47]. Diffraction takes place when the incident X-ray beam satisfies Bragg's law and a constructive interference occurs [43]. Grazing incident geometries have been developed to render X-Ray diffraction more sensitive to the surface,[48], as shown in Figure 2.13 (a). The penetration of the X-rays into the surface is lowered by reducing the incidence angle on the sample surface, and thus limits the depth from where the information is gathered.

In this thesis grazing incident X-ray diffraction (GIXRD) is applied to study the phase structure and crystallinity of the carbide dispersed phase of a-C:MeC nanocomposites (chapter 3) and the phase transformation with oxygen/nitrogen ratio in the different $AlTiO_xN_y$ in chapter 4 as shown in the example of Figure 2.13 (b) for an AlTiN sample.

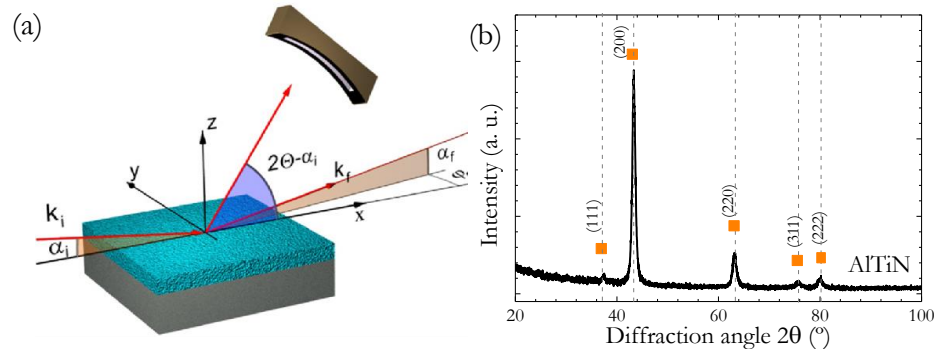

Figure 2.13 – (a) Geometry in grazing incidence diffraction characterized by a small incidence angle (α_i) that is kept constant during the measurement. (b) GIXRD pattern of AlTiN sample on Si substrate. The lines correspond to reference ICDD card of a cubic AlTiN [49].

A PANalytical X'Pert PRO diffractometer with *Cu-K$_a$* radiation (λ=1.542 Å) is employed. The incident angle is 0.4º, and the XRD patterns are measured in the diffraction angle range of 30–100º 2θ angles in steps of 0.05º. All samples were measured additionally by conventional θ-2θ geometry in order to analyse the preferential orientation or texture. the coating peaks were fitted to a pseudo-Voigt function to calculate the integral breadth from the X-ray diffractograms. The crystallite size t is estimated studying the full width at half maximum (FWHM) B of the diffraction peaks in radians, as an average of all the present peaks, following the Scherrer equation [50], as in equation (2.8):

$$t = \frac{k\,\lambda}{B\,(2\theta)\cos\theta_B} \tag{2.8}$$

where k is the shape factor, λ is the wavelength of the X-rays, and θ_B is the angular position of the peak's maximum. A shape factor of 0.94 is employed here, under the assumption that peak broadening is dominated by the small crystalline size. Phase identification was performed using the PANalytical X'Pert High Score Plus software and the ICDD (International Centre for Diffraction Data) PDF-4 database.

Raman spectroscopy

Raman spectroscopy is a non-destructive technique based on the measurement of the light dispersed by matter when a monochromatic light beam impacts on it. The interaction between a photon and a molecule can be elastically or inelastically scattered. In both cases, the molecule will be excited into a virtual state. Raman spectra are specially sensitive to the chemical structure of carbon materials, showing common features [51]. Hence, this technique was employed in chapter 3 to determine the phase structure of the carbon matrix. Raman spectra of samples containing carbon were measured in the wavenumber range 700-2500cm^{-1}, from as the Raman spectra of a a-C:WC samples represented in Figure 2.14.

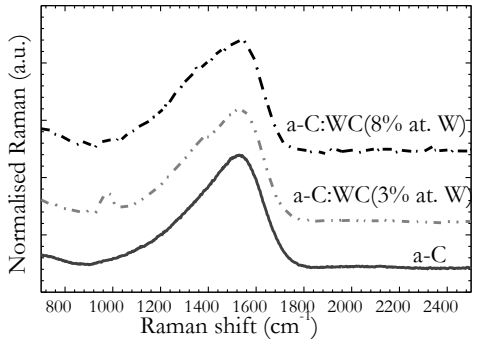

Figure 2.14 – Normalized Raman spectra of a-C:WC samples with 3 and 8at. % W content. The spectrum of the amorphous carbon sample is represented as reference

Micro-Raman spectra were recorded on a LabramHR spectrometer (Horiba), situated at HZDR. The system is equipped with a liquid N_2 cooled charge-coupled device detector and coupled to a BH2 microscope (Olympus). The laser beam of Nd:YAG solid-state laser with a wavelength of 532 nm was focussed to a spot diameter of 1 μm by a 50-fold magnifying objective. The laser power at the sample was 1mW. The scattered light was collected in 180º backscattering geometry and dispersed by a 300 line/mm grating. No sample degradation occurred under these conditions. For the analysis of the Raman line shape, the software PeakFit (version 4.12, Seasolve Software Inc.) was employed.

Scanning electron microscopy (SEM)

In SEM measurements, a focused electron beam is scanned over the surface of the sample. When the electrons strike it, different interactions can occur: emission of backscattered electrons, auger electrons, secondary electrons and X-rays. All these signals can be detected revealing morphology, chemical composition or microstructure information of the sample [52].

A Hitachi S5200 SEM equipped with FEG, located at "Instituto de Ciencia de Materiales de Sevilla" (ICMS) was employed in this study to analyse the microstructure of deposited samples. The cross sections and the top surface of the samples deposited on silicon substrates were measured without metallization in cross-sectional views at 1 and 5 kV electron beam energy. The microscope is dotted with an energy dispersive X-ray (EDX) spectroscopy Bruker X Flash Detector 4010 which allows quantifying the composition of the thin films. A SEM cross section image of a complete multilayer stack is shown in Figure 2.15 (a). As the alumina top layer is an electrically insulating material, it absorbs electrons and accumulate a net negative charge that repels the following electron beam, thereby degrading the image and making the imaging and analysis difficult by SEM if is not properly coated with a conducting film [53].

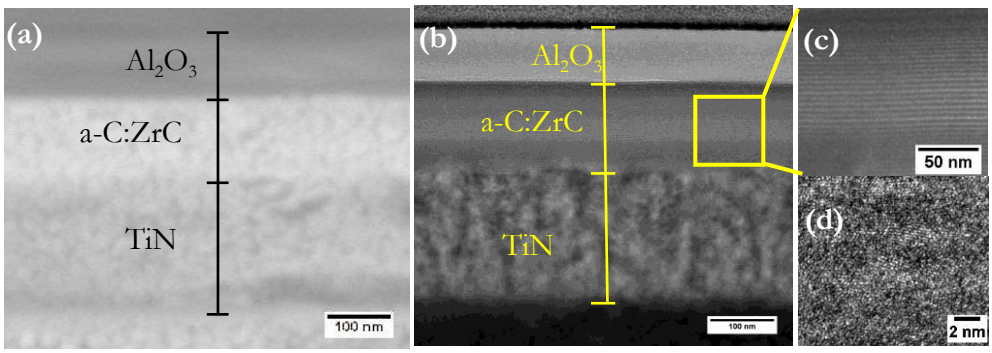

Figure 2.15 – Images of TiN / a-C:ZrC /Al_2O_3 multilayer film deposited by PFCVA. (a) SEM cross section image. (b) HR-TEM cross section image. (c) Higher magnification of the a-C:ZrC layer,of (b) from where a multilayer self-formation can be appreciated. (d) Amplified image of (c) that allows determination of the crystallite size and interplanar distance of the *fcc*-ZrC crystal structures.

High-resolution transmission electron microscopy (HR-TEM)

HR-TEM was employed to investigate the morphology cross-section of the samples[54]. In addition, selected area electron diffraction (SAED) patterns can be recorded which yield information on the nanoparticle phase and the degree of crystallinity of the matrix and the nanoparticles [55].

The HR-TEM TECNAI F30 situated at the "Laboratorio de Microscopía de Avanzada" (LMA) from "Instituto de Nanociencia de Aragón de la Universidad de Zaragoza" (INA-UNIZAR) was employed. The equipment operates at 300kV accelerating voltage is equipped with a Schottky-type field emission gun and an ultra-high resolution pole piece. The HR-TEM is also provided with a scanning transmission electron microscopy with the high angle annular dark field (STEM-HAADF) detector, and EDX analysis has been done to determine the composition of the samples in scanning mode. The cross-section analysis requires the preparation of thin lamellas. Those lamellas were made using a Focused Ion Beam (FIB) Dual Beam Helios 650, consisting of a 30kV Ga focused ion beam combined with a 30kV electron beam placed at 52º between them. The preparation of the lamellas was done with the Omniprobe® manipulator. A protective Platinum thin film was deposited by electron beam deposition from a Pt-organic gas $(CH_3)_3(C_pCH_3)Pt$. As an example, the HR-TEM cross section of a multilayer stack is shown in Figure 2.15 (b). Higher resolution images of the same film (Figure 2.15 (c) and (d)) illustrate the resolution limits.

2.3.4 Optical characterization

Spectroscopic ellipsometry (SE)

SE technique measures the change of the polarization state of the light after reflection on the surface to study [56,57]. The ellipsometric parameters measured are amplitude ratio (ψ) and phase difference (Δ), represented in Figure 2.16 (a). These two parameters are related to the

complex reflection ratio (ρ) between Fresnel reflection coefficients R_p and R_s for parallel and perpendicular polarized light, respectively, relative to the plane of incidence, as defined in (2.9):

$$\rho = \frac{R_p}{R_s} = tan(\psi)e^{i\Delta} \tag{2.9}$$

There exist different configurations of spectroscopic ellipsometer instruments. They all have in common, the presence of a light source and a polarizer on the incident side and an analyser and a detector on the reflection side. Figure 2.16 (b) shows the schematic diagram of the rotating-compensator ellipsometer employed in this thesis.

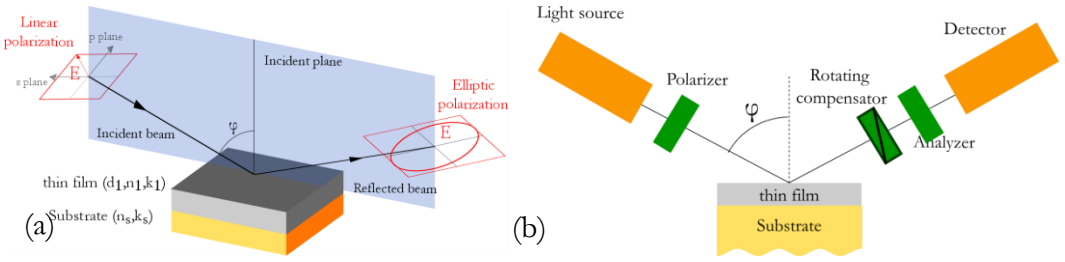

Figure 2.16 – (a) measurement principle of spectroscopic ellipsometry [57] and (b) optical configuration of rotating-compensator ellipsometry.

SE is commonly used to characterize the thickness and optical constants of thin films, i.e. refractive index, n and extinction coefficient k. It is a non-destructive and fast technique with a very high precision (thickness sensitivity ~0.1 Å) that does not require the use of reference samples to obtain quantitative results (see Figure 2.16 (b)). Moreover, ellipsometry can determine other physical properties of thin films such as surface and interfacial roughness, alloy composition, interband transitions (in particular the band gap, E_g), free carrier concentration and carrier mobility (in infrared ellipsometry). On the other hand, the main disadvantage of SE is the need of optical models in order to obtain the physical parameters of the layers from the ellipsometry measured values (ψ and Δ).

The procedure followed to determine the properties of thin films from ellipsometry measurement can be divided into several steps, as shown in the flow chart of Figure 2.17:

i) Measure the sample to obtain the spectral values ψ and Δ.

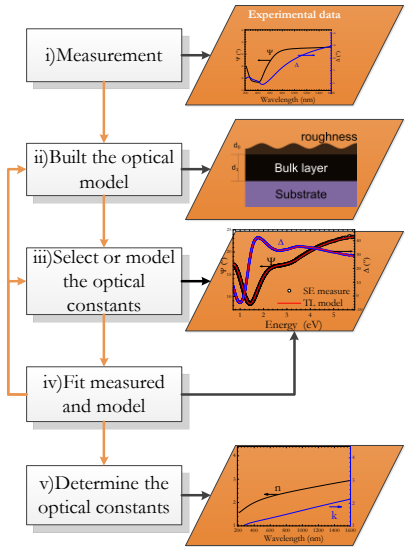

Figure 2.17 – Flow chart of the data analysis procedure in spectroscopic ellipsometry: measurement, optical model, assignation of the dielectric function for each layer on the optical model, fitting the error and determination of the optical constants.

ii) Develop a model based on the measured sample. The multilayer model employed for all the deposited samples assume a structure with ambient / roughness / film(s) / interface /substrate as shown in Figure 2.18. The surface roughness is modelled using BRU EMA, where we suppose a mixture of 50% of voids and 50% film material (see section 2.1.2 and equation (2.3). A crystalline Si substrate with 2 nm of SiO_2 interlayer was employed for the model, with the optical constants taken from measured Si (100) substrate.

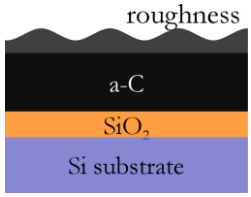

Figure 2.18 - Schematic diagram of a-C samples that consists of four layers including surface roughness, an amorphous carbon layer, native silicon dioxide interlayer and the silicon substrate.

iii) Assign the optical constants for each layer of the optical model. In case that the optical constants are unknown, it is necessary to employ the appropriate mathematical dispersion model(s) according to the optical properties of the sample.

In transparent regions (k~0), at wavelengths lower than the fundamental frequency (λ_0), Cauchy or Sellmeir model can be applied to determine the real dielectric part. The Sellmeier model is employed in this work, with dielectric function values given by equation (2.10):

$$\varepsilon_1 = A + \sum_j \frac{B_j \lambda^2}{\lambda^2 - {\lambda_{0j}}^2} \quad ; \quad \varepsilon_2 = 0 \tag{2.10}$$

where A and B represent analytical parameters used in the data analysis.

Lorentz and Tauc-Lorentz (TL) models [58] have been employed for amorphous materials to express the electric polarization in the UV-Vis region. While in Lorentz model, ε_2 peaks have a symmetric shape, in TL model ε_2 exhibits asymmetric peaks. This imaginary part (ε_2) of the dielectric function is determined by multiplying the Tauc joined density of states in the proximity of the fundamental optical bandgap E_g [59] by the Lorentz oscillator model, as in (2.11):

$$if\ E > E_g \qquad \varepsilon_2(E) = \frac{A\,E_0\,C\,(E-E_g)^2}{(E^2-{E_0}^2)^2 + C^2E^2}\,\frac{1}{E} \qquad (2.11)$$
$$if\ E \le E_g \qquad \varepsilon_2(E) = 0$$

where E_0 is the Penn gap, i.e. the photon energy at which maximum optical absorption occurs, C is the broadening and A the strength of each Lorentz oscillators. The corresponding real part ε_1 is then derived by using the Kramers-Kronig relations [60].

For materials with free electrons like metals or with carrier absorption as in semiconductors, Drude model is employed to examine the infrared behaviour. The complex refractive index (ε_1 and ε_2) with Drude model is defined in equation (2.12):

$$\varepsilon_1 = \varepsilon_\infty - \frac{\omega_p^2}{\omega^2+\Gamma^2} \qquad and \qquad \varepsilon_2 = \frac{\omega_p^2\Gamma}{\omega(\omega^2+\Gamma^2)} \qquad (2.12)$$

where $\omega_p = (4\pi N e^2/m)^{1/2}$ is the plasma frequency, that corresponds to the energy position where $\varepsilon_2 \sim 0$. ε_∞ is the dielectric constant at high frequencies and tends to the unity for high energies. Γ is the collision frequency and the absorption tail increases for higher values.

EMA theories can be applied for composite materials, as explained in section 2.1.2. The dispersion models suitable for each one of the components of the composite material can be merged to calculate the effective refractive index.

iv) Evaluate the fitting error until the optical constants obtained with the dispersion models are optimized, following a linear regression analysis.

v) Determine optical constants and films thicknesses of the analysed samples.

The optical constants of the deposited thin films were determined by SE using a rotating compensator ellipsometer M-2000FI from J. A.Woollam, Inc, situated at HZDR, in the wavelength range of 200 to 1700 nm at an angle of polarized light incidence of 75º The data were acquired and interpreted via modelling using WVASE32 software (J. A. Woollam, Inc) [61].

UV-Vis-NIR and IR reflectance

The solar absorptance (a) and thermal emittance (ε) were calculated by integrating the reflectance measurement following the standards [62,63] as explained in Chapter 1. Specular reflectance ($R(\lambda)$), is defined as the ratio of the radiant flux reflected ($I_r(\lambda)$) on a surface to the incident radiant flux ($I_i(\lambda)$), as equation (2.13):

$$R(\lambda) = \frac{I_r(\lambda)}{I_i(\lambda)} \qquad (2.13)$$

The total reflectance of a surface can be divided into a specular (perpendicular to the incident radiation) and a diffuse (scattered into the entire hemisphere) component. The intensity of each component depends on the on the surface roughness of the sample, as schematized in Figure 2.19.

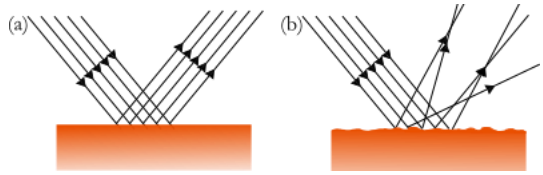

Figure 2.19 –Schematic of types of reflectance of a beam light into a surface. (a) Specular and (b) diffuse reflection.

In order to cover the whole wavelength range of interest (0.3 to 25 μm) is required the separate use of UV-Vis-NIR and IR spectrometers. The reflectance of the deposited samples at room temperature in the UV-Vis-NIR range was measured with two different double beam spectrophotometers:

- The Shimadzu UV-Vis-NIR Solid Spec-3700 spectrophotometer situated in the HZDR was used to measure spectral reflectance in the range 250 to 3300 nm, with a direct detection unit accessory to measure with an incident angle of 5º from the normal. The system is equipped with a Halogen lamp as source and three different detectors for specific wavelength range: PMT for 200 - 870nm, InGaAs 870 – 1650 nm and PbS for 1650 -3300nm to increase the sensitivity in all the analysed range. An aluminium mirror was used as a reference and then corrected the reflectance with a calibrated Al standard. The data were processed with the software UVProbe 2.42 and multiplied by the correction factor.

- The Perkin Elmer spectrophotometer Lambda 1050 sited in Abengoa Research was employed too. It is equipped with a deuterium (175-320 nm) and a tungsten-halogen lamp (320–3300nm). Two accessories were employed to measure specular or diffuse reflectance. The Universal Reflectance Accessory (URA) measures absolute specular reflectance from 8 to 65º as incident angle, without the need of external reference mirrors. There is a silicon detector that covers the UV-visible range and a PbS detector for the NIR range. For rough samples, a 150 mm integrated sphere accessory consisting in two hemispheres coated with Spectralon and equipped with PMT and InGaAs detectors, was employed, shown in Figure 2.20. Spectralon as diffuse material was employed as a reference. The incident angle for the integrated sphere accessory is 8º. The UVWinlab V6 software was used to process the analysed data obtained with the Perkin – Elmer spectrophotometer.

Measurements of the reflectance in the IR were carried out with a Fourier Transform infrared (FTIR) spectrometer Bruker Vertex 70 situated in Abengoa Research. The measurement range was 400 to 4000 cm^{-1} (2.5 to 25 μm), with a resolution of 0.4cm^{-1}. It is equipped with a HeNe laser, a DLaTGS detector and KBr beam splitter. A specular W type accessory is employed to measure reflectance of mirror like samples, employing a gold coated glass as reference. Additionally, the IR reflectance of rough samples was measured by an integrated sphere accessory coated with gold, shown in Figure 2.20. The software OPUS 7.2 was used to process the data.

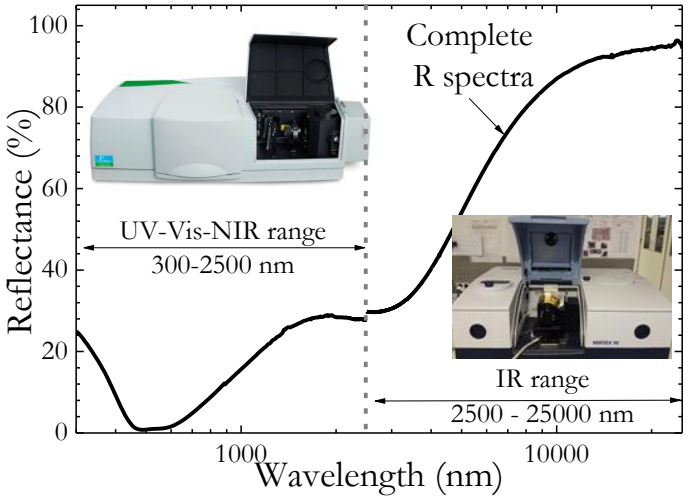

Figure 2.20 –Reflectance spectra of a deposited solar selective coating obtained joining UV-Vis-NIR + IR wavelength ranges. The Perkin Elmer Lambda 1050 spectrophotometer measures from 300 to 2500 nm and the FTIR Vertex70from Bruker, measures the reflectance in the IR range (2500-25000). The inset images show the integrated sphere accessories for both equipments.

2.4. Durability tests of single layers and of complete multilayer stacks

An optimal coating to be used for receivers in a CSP plant needs to show appropriate optical properties as well as thermal and mechanical stability in air at high temperatures. There are numerous publications [64–67] and different standards available, describing durability and accelerated ageing tests of solar thermal collectors. In Europe, the EN 12975 -1:2066+A1:2001 [68] has replaced all national standards. In order to simulate the expected service life time of the coating of 25 years, the International Energy Agency (IEA) in Task X of the Solar Heating and Cooling (SHC) program [69] developed a procedure to estimate the lifetime of solar absorber coatings. In this procedure, the performance criterion (PC) is defined by equation (2.14):

$$\mathrm{PC} = -\Delta\alpha + 0.25\,\Delta\varepsilon_T \quad \begin{cases} PC \leq 5\ PASS \\ PC > 5\ FAIL \end{cases} \tag{2.14}$$

where Δa is the change in the solar absorptance, and $\Delta\varepsilon$ is the change in thermal emittance after and before the test calculated. If PC is ≤0.05, the sample passes the test.

The thermal stability and ageing properties of the designed complete solar selective were investigated by exposing the samples at 450, 650 and 800ºC following three different durability tests: i) asymmetric, ii) cycling and iii) *in-situ* thermal treatment tests.

Asymmetric thermal treatment tests

The asymmetric thermal treatment consists of one heating cycle in which the temperature (450, 650 or 800ºC) is kept constant for 12 hours in an oven at atmospheric conditions. A

programmable heating ramp of 5ºC/min is established for reaching the desired temperature. After 12 hours, the sample cools down to room temperature inside the oven.

The furnace employed for this test was a Nabertherm L9/11 with controller P330, shown in Figure 2.21 (a). It is equipped with SiC rod heating and connected with Ar gas supply. The heating cooling ramps are schematized in Figure 2.21 (b).

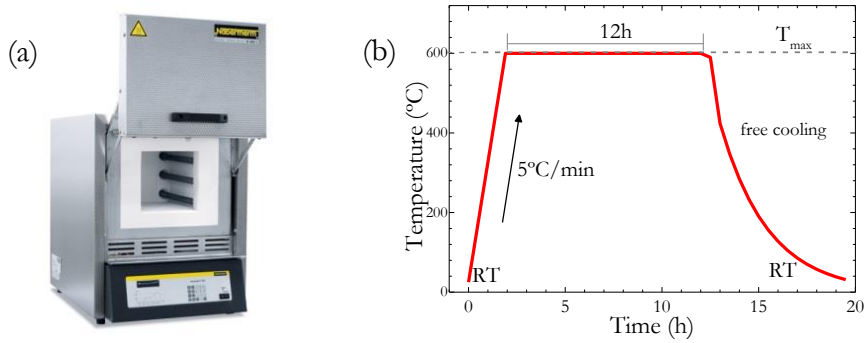

Figure 2.21 – (a) Controllable heating ramp furnace employed for the asymmetric thermal treatments. (b) Schematic of the asymmetric thermal treatment.

Cycling thermal treatment tests

Coatings applied to central receivers do suffer thermal cycling during plant start-up and stop-down and in transitory because of the operation of the power plant or because of the clouds. Previous experience shows that coatings that can withstand high constant temperature, may fail when they are subjected to temperature cycling. Therefore, solar selective were exposed to cyclic symmetric heating test for 250 cycles after the asymmetric thermal treatment.

The samples were introduced into the furnace at atmospheric conditions during 2 hours at each one of the defined temperatures (450, 650 and 800ºC) with a programmable heating ramp of 10ºC/min. Then, the samples were cooled down to 300 ºC, with a cooling ramp of 10ºC/min. The tests are carried out in batches of 250 cycles. However, every 50 cycles, the samples were visually inspected and their optical properties measured.

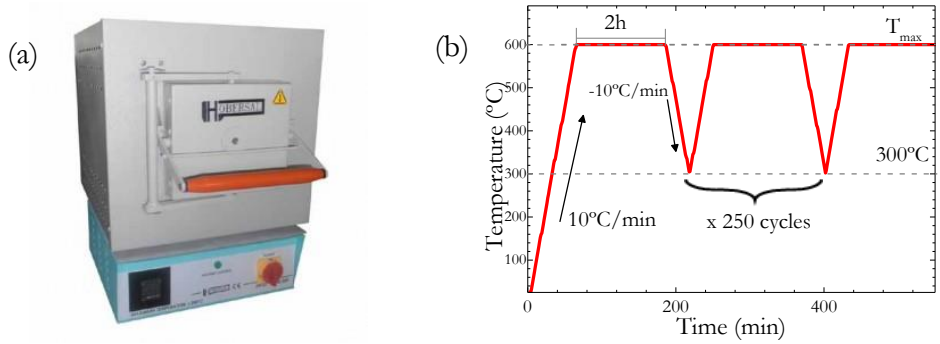

Figure 2.22 – (a) Controllable heating and cooling ramp furnace for the cyclic thermal tests. (b) Schematic of the symmetric cycles for the thermal treatment.

The programmable furnace employed for the symmetric cyclic tests was a Hobersal 13PR/300F (Figure 2.22 (a)) with adjustable cooling and heating ramp by Eurotherm controller. It is equipped with and special chimney with a turbine to allow the cooling. The schematic representation of the cycles employed is show in Figure 2.22 (b).

***In-situ* thermal treatment tests**

Additionally, chapter 5 includes a set of in-situ studies of the high-temperature stability of the coatings performed in a new multi-chamber *cluster tool* developed in collaboration with the Helmholtz Zentrum Dresden-Rossendorf (HZDR). The *cluster tool* includes thin film characterization techniques such as spectroscopic ellipsometry, Raman spectroscopy, and ion beam analysis in several environmental conditions or/and at different temperatures [70]. This methodology will be considered as a fundamental research as is described in the advanced characterization procedure for single layers, to analyse the failure mechanism.

After each thermal treatment, a visual inspection was carried out to evaluate the coating surface's conditions, in which, the lack of homogeneity, changes in the colour or the apparition of cracks in the thin films can be directly detected. The samples that passed the visual inspection were analysed by optical and microstructural characterization in order to evaluate the possible degradation mechanisms.

2.5. References

[1] W. Theiss, CODE Manual. Optical Spectrum Simulation, (2007). http://www.wtheiss.com/.

[2] E.D. Palik, Handbook of Optical Constants of Solids, Academic Press, 1998.

[3] Sopra, Optical data from Sopra SA, (1995). http://www.sspectra.com/sopra.html (accessed October 11, 2013).

[4] M. Polyanskiy, Refractive index, (2008). http://refractiveindex.info/.

[5] S. Adachi, The Handbook on Optical Constants of Metals: In Tables and Figures, World Scientific Publishing Company, 2012.

[6] T. Koide, T. Shidara, H. Fukutani, A. Fujimori, S. Otani, Y. Ishizawa, Optical Constants of TiC 0.95 , VC 0.86 and NbC 0.93 from 0.8 to 80 eV, Jpn. J. Appl. Phys. 32 (1993) 1130–1134. doi:10.1143/JJAP.32.1130.

[7] A. Paone, R. Sanjines, P. Jeanneret, A. Schüler, Temperature-dependent multiangle FTIR NIR-MIR ellipsometry of thermochromic VO2 and V1-xWxO2 films, Sol. Energy. 118 (2015) 107–116. doi:10.1016/j.solener.2015.05.020.

[8] J.H.W.G. Den Boer, Spectroscopic Infrared Ellipsometry: Components,Calibration, and Application, 1996.

[9] M. Fox, Optical Properties of Solids, Oxford Mas, Oxford Unversity Press, Oxford, 2001.

[10] V. Lucarini, J.J. Saarinen, K.-E. Peiponen, E.M. Vartiainen, Kramers-Konig Relations in optical materials research, 2005.

[11] G. Katumba, A. Forbes, Carbon-in-silica composite selective solar absorbers: a determination of composition and dielectric properties, in: B.K. Tsai (Ed.), Soc. Photo-Optical Instrum. Eng., 2009: p. 74100G–74100G–9. doi:10.1117/12.827960.

[12] J.C. Maxwell-Garnett, Colours in Metal Glasses, in Metallic Films, and in Metallic Solutions. II, Philos. Trans. R. Soc. A Math. Phys. Eng. Sci. 205 (1906) 237–288. doi:10.1098/rsta.1906.0007.

[13] D. Bruggeman, Calculation of various physics constants in heterogenous substances I Dielectricity constants and conductivity of mixed bodies from isotropic substances, Ann. Phys. 24 (1935) 636–664.

[14] I. Heras, E. Guillén, G. Abrasonis, M. Krause, A. Pardo, J.L. Endrino, et al., Optimizing solar absorption in carbon – transition metal nanocomposite thin films, Sol. Energy Mater. Sol. Cells. (2016).

[15] D. Bergman, Dielectric - Constant if a Composite material - Problem in classical Physicis, Phys. Reports Rev. Sect. Phys. Lett. 43 (1978) 378–407.

[16] J. Sturm, P. Grosse, W. Theiss, Effective dielectric functions of alkali halide composites and their spectral representation, Zeitschrift Für Phys. B Condens. Matter. 83 (1991) 361–365. doi:10.1007/BF01313406.

[17] W. Theiss, S. Henkel, M. Arntzen, Connecting microscopic and macroscopic properties of porous media: choosing appropriate effective medium concepts, Thin Solid Films. 255 (1995) 177–180.

[18] A. Anders, Energetic deposition using filtered cathodic arc plasmas, Vacuum. 67 (2002) 673–686. doi:10.1016/S0042-207X(02)00260-9.

[19] A. Anders, A review comparing cathodic arcs and high power impulse magnetron sputtering (HiPIMS), Surf. Coatings Technol. 257 (2014) 308–325. doi:10.1016/j.surfcoat.2014.08.043.

[20] A. Anders, Cathodic Arcs Fom fractal spots to energetic condensation, Springer Series on, Berkeley, California, 2008. doi:10.1007/978-0-387-79108-1.

[21] E. Hantzsche, B. Juttner, H. Pursch, On the random walk of arc cathode spots in vacuum, J. Phys. D. Appl. Phys. 16 (1983) L173–L179. doi:10.1088/0022-3727/16/9/002.

[22] J.E. Daalder, Random walk of cathode arc spots in vacuum, J. Appl. Phys. 16 (1983) 16–27.

[23] B. Juttner, Characterization of the Cathode Spot, IEEE Trans. Plasma Sci. 15 (1987) 474–480. doi:10.1109/TPS.1987.4316740.

[24] J.E. Daalder, Cathode spots and vacuum arcs, Phys. B+C. 104 (1981) 91–106. doi:10.1016/0378-4363(81)90040-1.

[25] A. Anders, Atomic scale heating in cathodic arc plasma deposition, Appl. Phys. Lett. 80 (2002) 1100.

[26] J.X. Guo, B.K. Tay, X.W. Sun, X.Z. Ding, D.H.C. Chua, Influence of substrate bias on the mechanical properties of ta-C:Co films prepared by filtered cathodic vacuum arc technique, Surf. Coatings Technol. 169-170 (2003) 393–396. doi:10.1016/S0257-8972(03)00067-7.

[27] E. Hantzsche, B. Juttner, V.F. Puchkarov, W. Rohrbeck, H. Wolff, Erosion of metal cathodes by arcs and breakdowns in vacuum, J. Phys. D. Appl. Phys. 9 (2001) 1771–1781. doi:10.1088/0022-3727/9/12/016.

[28] B. Jüttner, Erosion crater and arc cathode spots in vacuum, Plasmaphysik. 19 (1979) 25.

[29] S. Anders, A. Anders, X.Y. Yao, I.G. Brown, On the macroparticle flux from vacuum arc cathode spots, IEEE Trans. Plasma Sci. 21 (1993) 440–446. doi:10.1109/27.249623.

[30] S. Shalev, R.L. Boxman, S. Goldsmith, Velocities and emission rates of cathode-produced molybdenum macroparticles in a vacuum arc, J. Appl. Phys. 58 (1985) 2503. doi:10.1063/1.335927.

[31] A. Anders, Handbook of deposition Technologies, Third, William Andrew, Washington, 2009.

[32] T. Witke, P. Siemroth, Deposition of droplet-free films by vacuum arc evaporation-results and applications, IEEE Trans. Plasma Sci. 27 (1999) 1039–1044. doi:10.1109/27.782278.

[33] T. Witke, T. Schuelke, B. Schultrich, P. Siemroth, J. Vetter, Comparison of filtered high-current pulsed arc deposition with conventional vacuum arc methods, Surf. Coatings Technol. 126 (2000) 81–88. doi:10.1016/S0257-8972(00)00544-2.

[34] I.I. Aksenov, V.E. Strel'nitskij, V. V. Vasilyev, D.Y. Zaleskij, Efficiency of magnetic plasma filters, Surf. Coatings Technol. 163-164 (2003) 118–127. doi:10.1016/S0257-8972(02)00605-9.

[35] I.I. Aksenov, V. V. Vasilyev, B. Druz, a. a. Luchaninov, a. O. Omarov, V.E. Strel'nitskij, Transport of plasma through the tubular anode and discharge stability in a vacuum arc plasma source, Surf. Coatings Technol. 201 (2007) 6084–6089. doi:10.1016/j.surfcoat.2006.08.114.

[36] A. Anders, Approaches to rid cathodic arc plasmas of macro- and nanoparticles : a review, Surf. Coatings Technol. 120-121 (1999) 319–330.

[37] H. International, HAYNES 230 alloy, (2009) 2.

[38] Sensorfar Metrology, (n.d.). http://www.sensofar.com/metrology/pluapex/software/.

[39] ISO 4287:1997 Geometrical Product Specifications (GPS) - Surface texture: Profile method. Terms, definitions and surface texture parameters, 1997.

[40] Y. Wang, M. Nastasi, Handbook Modern Ion Beam Materials Analysis, 2nd editio, Cambridge University Press, 2010.

[41] J. Dr. von Borany, HZDR, (2014). http://www.hzdr.de/.

[42] R. Escobar Galindo, R. Gago, D. Duday, C. Palacio, Towards nanometric resolution in multilayer depth profiling: a comparative study of RBS, SIMS, XPS and GDOES., Anal. Bioanal. Chem. 396 (2010) 2725–40. doi:10.1007/s00216-009-3339-y.

[43] H. Bubert, H. Jenett, Surface and Thin Film Analysis: Principles, intrumentation, applications, Wiley-VCHVerlag GmgH, 2002.

[44] J.R. Tesmer, M. Nastasi, Handbool of modern ion beam materials analysis, Materials Research Society, Pittsburg, Pennsylvania, 1995.

[45] S. Grigull, U. Kreissig, H. Huber, W. Assmann, Element-dependent ERDA probing depths using different detection systems, Nucl. Instruments Methods Phys. Res. Sect. B Beam Interact. with Mater. Atoms. 132 (1997) 709–717. doi:10.1016/S0168-583X(97)00489-8.

[46] N.P. Barradas, C. Jeynes, R.P. Webb, Simulated annealing analysis of Rutherford backscattering data, Appl. Phys. Lett. 71 (1997) 291. doi:10.1063/1.119524.

[47] B.D. Cullity, S.R. Stock, Elements of X-ray diffraction, Prentice-Hall, 2001.

[48] M. Birkholz, Thin Film Analysis by X-Ray Scattering, Wiley-VCH Verlag GmbH & Co. KGaA, Weinheim, FRG, 2005. doi:10.1002/3527607595.

[49] ICDD Powder Diffraction Data, ICDD Powder Diffraction Data files: 00-037-1140 for fcc AlTiN, (n.d.).

[50] A.L. Patterson, The Scherrer Formula for X-Ray Particle Size Determination, Phys. Rev. 56 (1939) 978.

[51] A.C. Ferrari, J. Robertson, Resonant Raman spectroscopy of disordered, amorphous, and diamondlike carbon, Phys. Rev. B. 64 (2001) 075414. doi:10.1103/PhysRevB.64.075414.

[52] J. Goldstein, D.E. Newbury, D.C. Joy, C.E. Lyman, P. Echlin, E. Lifshin, et al., Scanning Electron Microscopy and X-ray Microanalysis, 3rd editio, Springer, 2003.

[53] W.D. Kingery, H.K. Bowen, D.R. Uhlmann, Introduction to ceramis, 2nd ed., Wiley, New York, 1976.

[54] D.B. Williams, C.B. Carter, Transmission Electron Microscopy, Second, Springer Science & Business Media LLC, 2009.

[55] M. Ohring, The materials science of thin films: deposition & structure, 2nd editio, Academic Press, San Diego, 2002.

[56] H.G. Tompkins, E.A. Irene, C. Hill, N. Carolina, Handbook of ellipsometry, William Andrew, New York, 2005.

[57] H. Fujiwara, Spectrsocopic ellispometry, John Wiley & Sons, Tokyo, Japan, 2007.

[58] G.E. Jellison, F.A. Modine, Parameterization of the optical functions of amorphous materials in the interband region, Appl. Phys. Lett. 69 (1996) 371. doi:10.1063/1.118064.

[59] J. Tauc, Optical properties and electronic structure of amorphous Ge and Si, Mater. Res. Bull. 3 (1968) 37–46. doi:10.1016/0025-5408(68)90023-8.

[60] B. Velický, The use of the kramers-kronig relations in determining optical constants, Czechoslov. J. Phys. 11 (1961) 787–798. doi:10.1007/BF01690042.

[61] J.A. Woollam, B. Johs, C.M. Herzinger, J.N. Hilfiker, R.A. Synowicki, C.L. Bungay, Overview of variable angle spectroscopic ellipsometry, Crit. Rev. Opt. Sci. Technol. CR72 (1999) 3–28.

[62] ASTM: E903-12 Standard Test Method for Solar Absorptance , Reflectance , and Transmittance of Materials Using Integrating Spheres, 2012. doi:10.1520/E0903-12.2.

[63] E. Standard, N. Europeenne, UNE-EN 673 Determinación del coeficiente de transmisión térmica, Europe, 2011.

[64] R. Gampp, P. Oelhafen, P. Gantenbein, S. Brunold, U. Frei, Accelerated aging tests of chromium containing amorphous hydrogenated carbon coatings for solar collectors, Sol. Energy Mater. Sol. Cells. 54 (1998) 369–377. doi:10.1016/S0927-0248(98)00088-9.

[65] B. Carlsson, K. Möller, M. Köhl, U. Frei, S. Brunold, Qualification test procedure for solar absorber surface durability, Sol. Energy Mater. Sol. Cells. 61 (2000) 255–275. doi:10.1016/S0927-0248(99)00111-7.

[66] B. Carlsson, K. Möller, M. Köhl, M. Heck, S. Brunold, U. Frei, et al., The applicability of accelerated life testing for assessment of service life of solar thermal components, Sol. Energy Mater. Sol. Cells. 84 (2004) 255–274. doi:10.1016/j.solmat.2004.01.046.

[67] M. Köhl, M. Heck, S. Brunold, U. Frei, B. Carlsson, K. Möller, Advanced procedure for the assessment of the lifetime of solar absorber coatings, Sol. Energy Mater. Sol. Cells. 84 (2004) 275–289. doi:10.1016/j.solmat.2004.01.041.

[68] Thermal solar systems and components - Solar collectors - Part 1: General requirements, 2011.

[69] B. Carlsson, K. Möller, U. Frei, M. Köhl, Accelerated life testing of solar absorber coatings, in: V. Wittwer, C.G. Granqvist, C.M. Lampert (Eds.), Opt. Mater. Technol. Energy Effic. Sol. Energy Convers. XIII, International Society for Optics and Photonics, 1994: pp. 79–90. doi:10.1117/12.185359.

[70] I. Heras, E. Guillén, R. Wenisch, M. Krause, R. Escobar Galindo, J.L. Endrino, Comprehensive environmental testing of optical properties in thin films, Procedia CIRP. 22 (2014) 271–276.

CHAPTER 3: SOLAR SELECTIVE COATINGS BASED ON CARBON: TRANSITION METAL CARBIDE NANOCOMPOSITES

Nanocomposites are functional advanced materials whose properties cannot be foreseen from those of their individual components. In particular, nanocomposites consisting of nanocrystalline interstitial metal carbide (nc-MeC) embedded in an amorphous carbon (a-C) matrix exhibit a unique combination of properties which makes them very attractive candidates as absorber layer of SSC for thermo-solar applications [1].

In this chapter, the properties of transition-metal carbides and carbon as the individual components of the nanocomposite (a-C:MeC) are introduced in section 3.1. In a first step, optical simulation based on literature optical constants references was employed for optimizing SSC (section 3.2). Sections 3.3 describe the deposition and microstructural characterization performed of the individual thin films. Following a thorough analysis of composition and microstructure of the deposited single layers, the simulations are feedback with experimental data (section 3.4). The simulated complete coating based on these measured properties provides excellent selective optical selective properties (a>96% and $\varepsilon_{600ºC}$<14%). A complete solar selective coating were deposited and analysed in section 3.5 in order to validate the simulations. A heating test of the deposited multilayer stack was performed to study the failure mechanisms at high temperatures.

3.1. Introduction of a-C:MeC as solar absorber layer

The term carbide is applied to a compound between carbon atoms and elements with lower or similar electronegativity [2]. Carbides can be divided in four general categories as shown in Figure 3.1: covalent, salt-like, metallic and interstitial carbides. This carbide formation and classification depends mainly in three atomic characteristics [3]: i) the affinity of the element towards the carbon or difference in electronegativity, ii) the size of the atoms and iii) the bonding characteristic of the atoms.

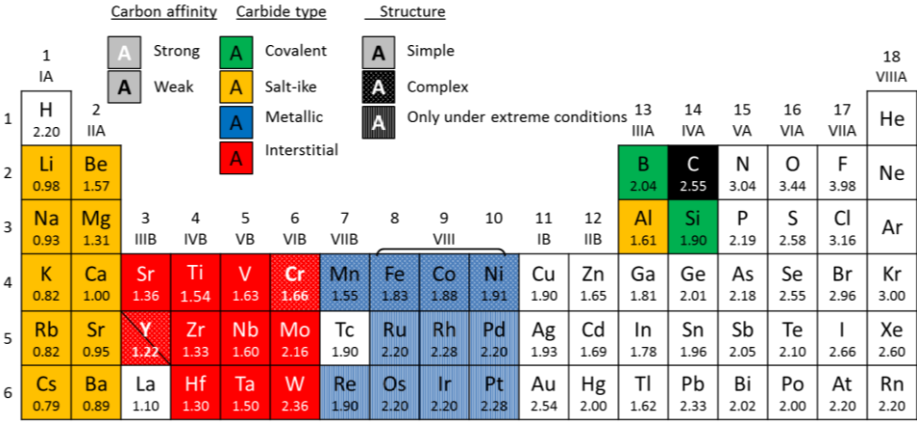

Figure 3.1 - Periodic table with electronegativity values in Pauling scale. Different groups of carbide forming elements have been marked according to their affinity to carbon. Non-carbide forming elements have white background [4]. Lanthanides and elements from period 7 are omitted as they are non-carbide forming.

Among carbides, the most interesting for high temperature applications are carbides formed with transition metals from groups 4, and 6 (with the exception of the chromium) due to their high chemical and thermal stability. This group is named interstitial carbides, and they have a huge difference in electronegativity with respect to the carbon atom. They also have larger atomic radius in comparison to carbon size, allowing the carbon atom to be placed in the interstices of the lattice. Geometrically, the ratio of carbon/metal atomic radius must be less than 0.59 to form an interstitial structure. On the contrary, transition metals of groups 7 to 10, as well as chromium, have an atomic radius small to accommodate the carbon atom in interstitial positions, which provokes distortion in the lattice and chemical instability of the carbides. Table 3.1 shows the atomic radius ratio in metals from groups 4 to 6. In the case of Cr-C, the ratio is higher than the limit for interstitial formation (0.59 following Hägg's rule [5]), so its carbide cannot be considered a metastable.

Table 3.1 – Ratio atomic radii of the components (R_c/R_{Me}) of transition metals from groups 4,5 and 6 [6].

Group 4	Group 5	Group 6
Ti-C 0.551	V-C 0.560	Cr-C 0.615
Zr-C 0.487	Nb-C 0.510	Mo-C 0.543
Hf-C 0.493	Ta-C 0.514	W-C 0.547

Interstitial carbides exhibit a bonding partly covalent, ionic and above all metallic [7]. Therefore, they have similar properties as metals (high electrical and thermal conductivities) and they are hard and chemically inert materials. Moreover, the melting point of interstitial carbides is generally higher than their host metals (e.g. 3160ºC in TiC in compare to 1660ºC in metallic Ti [8]). Other consequence of the metallic bonding in their properties is their high reflectance [9], associated to the large density of free electrons.

The crystal structure in most of the interstitial carbides (TiC, ZrC, HfC, VC, NbC or TaC) is face-centred cubic closed-packed (*fcc*). In this structure, the carbon atom fits into an octahedral site, achieving the highest coordination number, as shown in Figure 3.2 (a). However, metals of group 6, can form simple hexagonal (*hex*) structures where the carbon atoms are in trigonal prismatic sites with the metals atoms in hexagonal arrangement (Figure 3.2 (b)), typically represented by the WC structure. Additionally of these two main crystal structures, Me_2C configurations can be formed in metals from groups 5 or 6, with hexagonal close-packed (*hcp*) crystal structure, as Mo_2C [10].

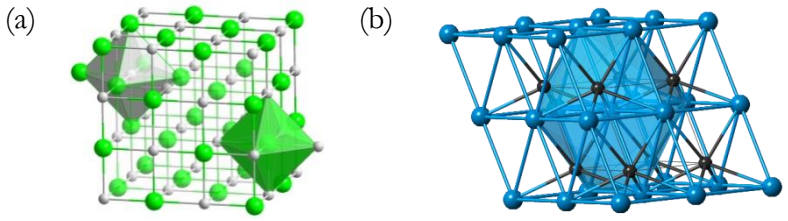

Figure 3.2 - Interstitial carbide crystal structures (a) face-centred cubic (*fcc*) close-packed type and (b) simple hexagonal (*hex*) non-close-packed structure [11]

Remarkably, most of these monocarbides are non-stoichiometric compounds, as not all the possible interstitial sites in the lattice are occupied with carbon atoms. This fact offers a wide range of possible compositions; i.e. ZrC maintain the same NaCl structure from a range from 32 to 50 at.% of carbon ($ZrC_{0.65}$ to $ZrC_{0.99}$), as shown in the binary phase diagram in Figure 3.3 (a). Of particular interest is the complex Mo-C system which has numerous possible monocarbide crystal structures [12] as can be observed in its phase diagram (Figure 3.3 (b)). This diagram shows that among all the only phases thermodynamically stable at room temperature are γ-MoC, and two Mo_2C (β' and β'').

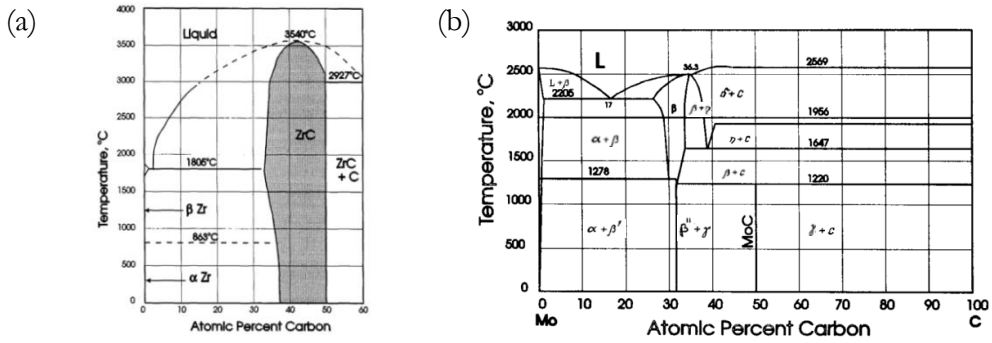

Figure 3.3 - Binary phase diagrams of (a) Zr-C and (b) Mo-C systems. The grey area in (a) is the single phase stable region, whereas white area represents two phase regions [3].

Attending to the previous phase diagrams, over a threshold of carbon content, free carbon atoms can result in different microstructures. Carbon thin films are versatile materials with properties that can be varied over a broad range by controlling the ratio of *sp* hybrid bonds [13] and the degree of clustering in the sp^2 phase. The carbon allotropes can be classified as sp^2 structures (graphitic like), sp^3 structures (diamond like) or fullerenes (Figure 3.4).

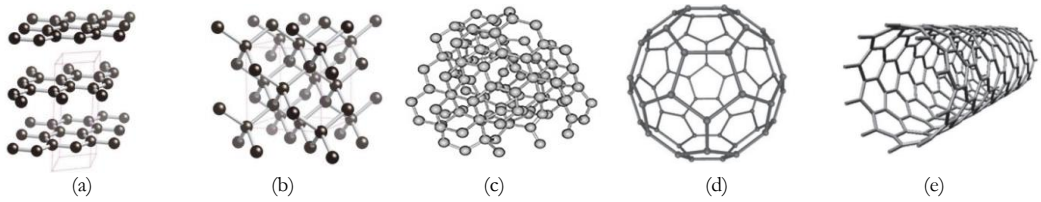

Figure 3.4 - Structures of selected carbon allotropes with different hybridization states of the carbon – carbon bonds (a) graphite, (b) diamond (c) amorphous carbon, (d) fullerene (e) single walled carbon nanotube [14].

Unlike the crystalline counterparts, amorphous carbon (a-C) consists of any mixture of the two bonding types. The mechanical, electrical and in particular optical properties of thin films carbon phase can be controlled by modifying the deposition conditions such as the substrate temperature or the energy of the deposition process. Figure 3.5 shows the differences in the optical constants in selected carbon allotropes.

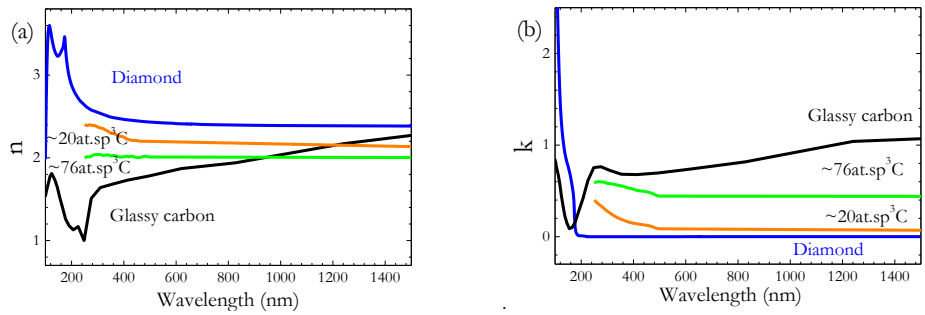

Figure 3.5 – (a) Index of refraction (n) and (b) extinction coefficient (*k*) for pure diamond [15], glassy carbon [16] and a-C with a content of 76 and 20 at.% sp^3 hybrid bonds [17]

While diamond is an isotropic transparent material (with UV absorption at ~291 nm and an absorption band in the 2 to 6 μm in the IR region due to multiphonon processes [15]), graphite has anisotropic hexagonal structure. Graphite exhibits high reflectance in the basal plane (normal incidence reflectance), however it has poor metallic behaviour perpendicular to the plane (along the c-axis) [18]. Glassy carbon is a pure sp^2 C bonding with a structure of very small graphitic crystals, with no orientation between the planes [16].

The sp^3 content can be quantitatively determined by energy electron loss spectroscopy (EELS) [19], nuclear magnetic resonance (NMR) [20] or with optical spectroscopic [21]. In this thesis, Raman spectroscopy was used for the study of the vibrational modes, that allows to distinguish qualitatively between sp^2 and sp^3 C bonding [22] on the a-C:MeC nanocomposites (section 3.3.2).

Generally, the sp^3 content in a-C thin films deposited by PVD techniques can be controlled by the incident energy of the C species. Tetrahedral amorphous carbon (ta-C) is an amorphous carbon with the highest sp^3 hybridized carbon atoms content [22]. It is typically obtained with deposition techniques that generates high ionization ratio such as high power impulse magnetron sputtering (HiPIMS) or cathodic vacuum arc (CVA), where a ~88% sp^3 phase can be achieved [17]. Otherwise, magnetron sputtering or other low energetic deposition techniques produces a-C samples with lower sp^3 content [23]. The optical constants of ~79 and ~20% sp^3 C bonding in a-C samples are also displayed in Figure 3.5. As expected, they show an intermediate behaviour and they can be predicted by employing an Effective Medium Approximation (EMA) and using graphite and diamond as constituents optical constants [17].

Regarding solar applications, a-C with the appropriate sp^3/sp^2 ratio (between ~20 and 50 at.% [17]) can be a good solar absorber material [24]. But nonetheless, a-C has a high thermal emittance showing no optical selective properties. Moreover, at temperatures above 300ºC, the material undergoes a graphitization process, which leads to an increase in sp^2 and decrease in sp^3 bonding structure with the consequent loss of stability.

Combining the advantageous optical and thermo-mechanical properties of amorphous carbon and transition metal carbides, nanocomposites materials can result, with adjustable solar selective properties with high-temperature resistance [25]. Amorphous carbon transition metal carbines (a-C:MeC) nanocomposite thin films have been previously grown by several physical vapour deposition (PVD) techniques such as magnetron sputtering [26], pulsed laser deposition [27], ion beam co-sputtering [28] or filtered cathodic vacuum arc (FCVA) [29]. Different microstructures of the carbon-carbide system have been reported: i) Carbide phases dispersed in a carbon matrix in the form of nanoparticles, with different morphology (globular or elongated [30,31])) and crystal structure (amorphous [32] or crystalline [33]) or ii) self-forming multilayer structures with periodic concentration fluctuations of metal in a-C [19].

Jansson *et al.* described detailed thoughtfully the formation of nanoparticles in the system carbon-carbide when co-deposited by magnetron sputtering at low temperatures. In this deposition conditions, far from the equilibrium, the microstructure evolution of the carbide-based coating in function of the carbon content is represented in Figure 3.6. The increment of carbon involves the formation of two separated phases: carbide nanoparticles embedded in an amorphous carbon matrix, as observed for the Ti-C system [34].

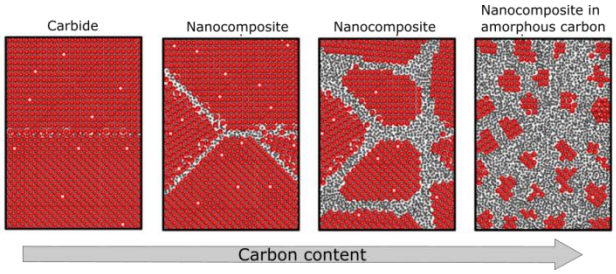

Figure 3.6 - Schematic microstructure evolution in sputter co-deposition of transition metal - carbon when the carbon content increases [4].

If the co-deposition of carbon and a transition metals occurs close from equilibrium conditions due to an increase of the energy of particles during the deposition, the structure can result in a self-organization multilayer sequences of metal-rich and metal-depleted nanolayers [35,36]. The self-assembling layer growth has been explained by many different theories [37,38], associating this phenomenon with high temperature, high energy subimplantation [39], catalytic effect of the metal [40] or effect of the substrate bias [41]. As an example, Figure 3.7 shows the proposed model by Hovsepian [42] for the multilayer self-organization in Cr/C system, attributed to segregation triggered by high-energy ion irradiation during film growth. These multilayer systems can exhibit improved mechanical properties (lower intrinsic compressive stress, improved adherence to the substrate or better wear resistance [20]) compared to dispersed nanoparticles microstructure.

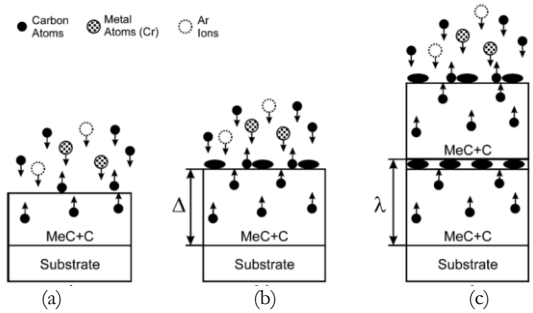

Figure 3.7 - Schematic model for the evolution in self-organization multilayer structure during the growth of the co-deposition of transition metal – carbon. Δ is the critical thickness and λ is the bi-layer thickness [42].

The use of a-C:MeC deposited by PVD techniques as SSC has been previously reported. Harding et al. [43–45] reported that sputter deposited metal carbides (Cr, Fe, Mo, Ni, Ta and W) on copper substrates show good selective properties (α >80% and $\varepsilon_{600ºC}$ ~7%). Gampp developed a multilayer coating based on hydrogenated a-C co-sputtered with Cr or W (a-C:H/Cr and a-C:H/W [46–48]). The reflectance spectra of the coatings at different temperatures are shown in Figure 3.8.

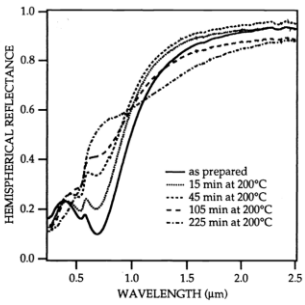

Figure 3.8 - Reflectance spectra of as prepared and aged a-C:H/W (14 at % W) on Cu substrate [46]

However, the optical properties dropped drastically for temperatures higher than 600ºC due to different types of degradation mechanisms: a) undesired interaction between coatings and the metallic bottom layer, and b) degradation due to the intrinsic instability of the coating material itself due to oxidation and changes in the microstructure. At higher temperature, the a-C:H/W films become more transparent in the visible range, and the absorptance decrease sharply due a combination of both failure mechanisms. Moreover, the diffusion along the pores of the deposited absorber layer of Cu from the substrate creates a CuO layer on the top surfaceMore recently, Schüler et al. [49,50] developed a multilayer coating based titanium-containing amorphous hydrogenated carbon (a-C(H):TiC) films adding silicon to increase the durability in air. However, when silicon content is high, the resistance of the layer severely decreases with the humidity.

Those previous published studies of a-C:MeC solar selective coatings show excellent optical performance and high stability in evacuated environments, although they were not stable at high temperatures in air. The main degradation mechanisms can be summarized as follows:

- Diffusion of the substrate or intermediate layers along the absorber layer
- Oxidation of the metal carbide component of the absorber layer what lead to a reduction of the absorptance
- Graphitization or crystallization of the amorphous carbon component.

The goal of the investigations in this chapter is the complete design of a SSC based on a-C:MeC as absorber layer. After the initial optical simulations based on literature data, a-C:VC, a-C:ZrC and a-C:MoC nanocomposite thin films were selected as candidate absorber layer (section 3.2). These a-C:MeC coatings were deposited by pulsed filtered cathodic vacuum arc (PFCVA) and characterised using micro-structural techniques (section 3.3). The element composition was determined using Rutherford Backscattering Spectrometry (RBS) and Nuclear Reaction Analysis (NRA). The microstructure of the a-C:MeC was characterized by Raman spectroscopy, X-ray diffraction (XRD), and high-resolution transmission electron microscopy (HR-TEM). Reflectance spectra were obtained by UV-Vis-NIR spectrophotometry, and the optical constants were measured by spectroscopic ellipsometry (SE). Similar depositions and characterizations were performed to Al_2O_3 and SiO2 (as candidate materials for the AR layer) and TiN and ZrN for the

IR layer, selected in the initial optical simulation. The first optical simulations were feedback with real optical behaviour from deposited single layers (section 3.4) and validated in a complete SSC stack (section 3.5). Bergman representation was found the most suitable EMA for a-C:MeC materials, as it requires a detailed microstructural analysis for an accurate optical simulation. More accurate values were predicted after the complete characterization of each one of the individual layers that forms the SSC, obtaining an outstanding solar absorptance (α) of 96% and an emittance (ε) of 5/15% at 25/600ºC. This is significantly better than the values reported for this class of materials so far, which were an α = 91.0% with ε = 11% at 100ºC for an a-C:TiC/SiO_2 stack on Cu substrate [49,50].

3.2. Optical simulation based on literature optical constants

Simulation of the reflectance spectra allows an optimization of each one of the individual layers (composition, thickness, degree of percolation, etc.). After a definition of the individual layers, a multilayer stack can be designed, where the solar absorbance and the thermal emittance are optimized. In this initial process, all simulations are based only on theoretical optical constants from literature data.

3.2.1 Optical simulations of the a-C:MeC absorber layer.

As discussed in chapter 2, Bergman is the most complete and accurate EMA to simulate optical constants in nanocomposites when the microgeometry of the film is known. However, Bruggeman (BRU) theory was employed in these initial simulations to calculate the effective optical constants of the films as a first approximation previous to deposition and characterization of the thin films. The optical constants of the following carbides are extracted from literature: TiC [51], VC [52], NbC [53], ZrC [54], HfC [55], MoC [56], TaC [57] and WC [58]. Optical constants from an amorphous carbon (a-C) available at CODE database [59] were used for simulation of the carbon matrix.

In order to compare the reflectance of the films as a function of the metal carbide present in the nanocomposite, several nanocomposites were simulated with a fixed volume fraction and thickness. The effective optical constants for the different a-C:MeC are calculated with BRU theory, fixing a volume fraction (VF) content of metal carbide the specular reflectance spectrum of each nanocomposite was simulated using the effective optical constants, as shown in Figure 3.9 for 30% VF and 100 nm thickness. The incidence angle selected for the simulations was 11º for equivalency with the experimental measurements. In order to select the most promising metal

carbide, the solar absorptance was calculated and the results are summarized in Table 3.2 for 10 and 30% VF.

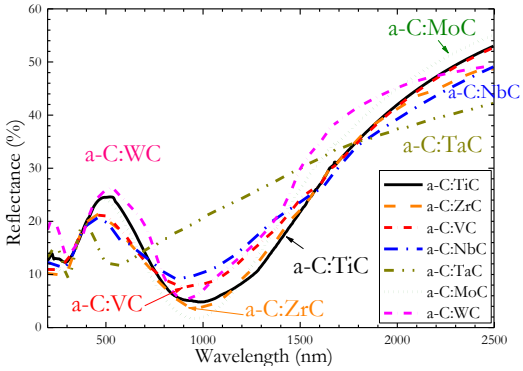

Figure 3.9 - Simulated reflectance spectra of 100 nm a-C:MeC with BRU theory for 30% VF of metal carbide embedded on a-C matrix on inconel substrate.

Table 3.2 – Simulated absorptance of different a-C:MeC with 100 nm thickness on inconel substrate for two volume fractions of metal carbide (30% and 10%), embedded in a-C matrix. The estimated error in the simulation was 0.1%.

Carbide type	TiC	ZrC	VC	NbC	TaC	MoC	WC
α (30% VF MC)	83.1	84.8	85.0	81.3	81.7	83.9	80.4
α (10% VF MC)	73.7	75.5	77.2	77.0	82.5	73.2	73.5

The nanocomposites with the highest *a* (VC ZrC and MoC), were selected for further simulations to study the influence of the carbide volume fraction and thickness of the layer in the solar absorptance. In Figure 3.10 (a), it can be observed how the best *a* values (fixing the thickness to 100 nm) were obtained within a range of ~20 to 30% carbide VF. The maximum values of absorptance for the three pre-selected systems are 85.2 %, 85.6 % and 84.0 % for VC (20% VF), ZrC (25 % VF) and MoC (30 % VF), respectively.

These volume fractions were selected to analyse the solar absorptance dependence on the layer thickness (Figure 3.10 (b)). Solar absorptance increases from 32% (absorptance of the inconel substrate) until it stabilized for thicknesses above ~70-75 nm for the three a-C:MeC with no considerable improvement for larger thicknesses.

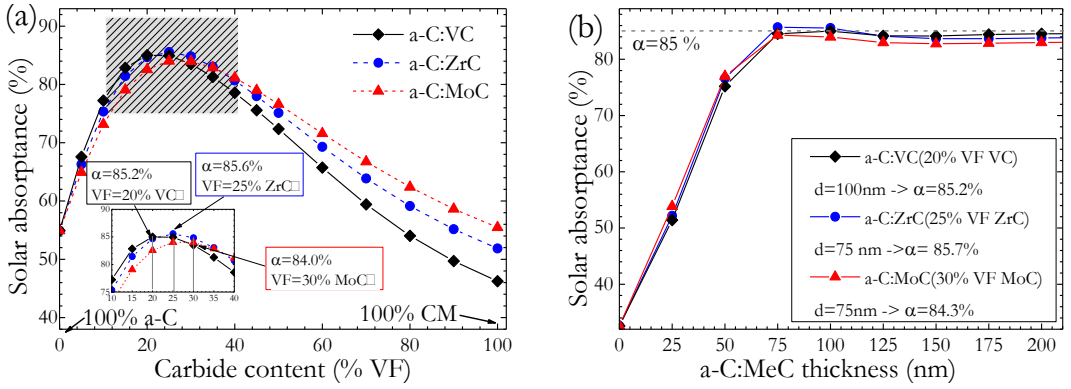

Figure 3.10 – (a) Simulated solar absorptance (α) of a-C:VC, a-C:ZrC and a-C:MoC with thickness of 100nm on inconel substrates with different volume fraction of metal carbide embedded in the a-C matrix. (b) Simulated solar absorbance of a-C:VC, a-C:ZrC and a-C:MoC with 20, 25 and30 % VF, respectively, on inconel substrate as a function of layer thickness (*d*).

Finally, both parameters were optimized simultaneously. The maximum *a* achieved was 91.5 ± 0.1 % for a 82 nm thick a-C:VC single layer with 18 % volume fraction of VC. In the case of the a-C:ZrC system, a maximum absorptance of 89.5 ± 0. % was found for a films with 85 nm and 27% of volume fraction of ZrC and 90.2 ± 0.1 % using a 65 nm of a-C:MoC with 29% VF of MoC.

3.2.2 Optical simulations of the infrared reflective (IR) layer

Four interstitial nitrides (TiN [60], ZrN [61], VN [62] and HfN [63]) were initially selected as potential candidates for IR layer. The simulated reflectance spectra of these nitrides are compared in Figure 3.11 (a), all with a thickness of 300 nm. The plasma frequency in nitrides would vary depending on the deposition conditions, but generally is in UV or Vis wavelength regions. Reflectance above this plasma wavelength is supposed to increase continuously to IR, so the reflectance has in similar values up to the far IR region. TiN, ZrN and HfN give the highest reflectance values (R_{IR} > 92, 91 and 85 % for the TiN, ZrN and HfN, respectively). The variation of thermal emittance of a complete SSC employing an AR layer of Al_2O_3, a-C:ZrC as absorber layer (with the optimized thicknesses and VF form the previous section) and TiN, ZrN or HfN as IR layer is represented in Figure 3.11 (b). From this figure it can be noted that for all the nitrides the emittance decreases with thickness of the IR layer until ~150nm, when it keeps constant. The ε does not further improve for thicknesses higher than 200 nm.

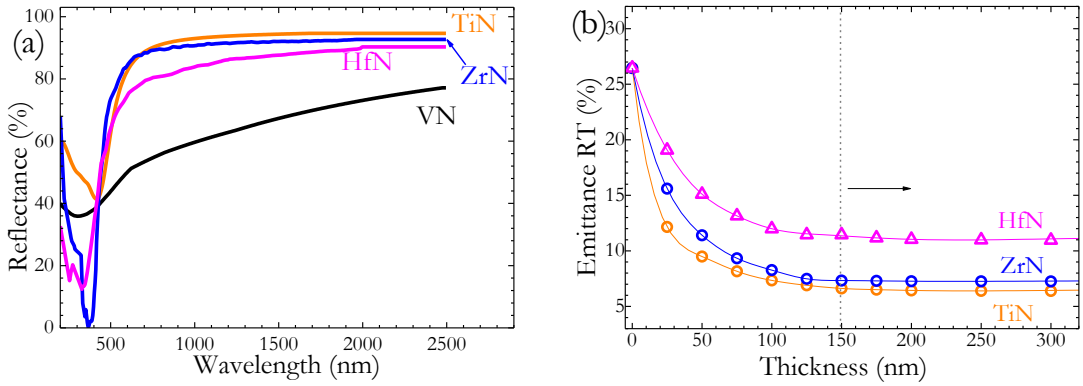

Figure 3.11 - (a) Simulated reflectance spectra for single layer of TiN, HfN, ZrN and VN. (b) RT thermal emittance of simulated SSC (53 nm of Al_2O_3/ 85 nm of a-C:ZrC with 27% VF of ZrC /IR= TiN, ZrN or HfN) for different thicknesses of the IR layer

TiN and ZrN are selected in this work as IR layer candidates due their higher reflectance in compared to the other two studied nitrides. Additionally, TiN and ZrN are thermal oxidation resistance materials at temperatures above 900ºC [64,65] and extensive research has being previously reported of the deposition conditions for those nitrides with FCVA [66–69].

3.2.3 Optical simulations of the antireflective (AR) layer

In order to check the best AR layer, from an optical point of view, a complete SSC was simulated using different candidate materials. Initially, a thickness of 70 nm was fixed. A schematic of the SSC employed for the simulation is represented in Figure 3.12, where the AR top layer was varied for the simulations. The calculated solar absorptance values are presented in Table 3.3, together with the refractive indexes (n) of the different AR layers at λ = 550 nm, extracted from the literature [62,70–72]. All the materials selected as AR, have common optical characteristics such as high transmittance in the visible range (k~0) and n almost constant in the UV-Vis range. They also have infrared vibrational phonon absorption and the band gap in the UV region.

Table 3.3 – Refractive index (n) for different dielectric materials at λ = 550 nm, and simulated solar absorptance (α) for a SSC on inconel substrate, with TiN (300nm) / a-C:ZrC (85nm and 27% VF) / 70 nm of the different AR layer. The estimated error in the simulation was 0.1%.

AR layer	Al_2O_3	MgO	WO_3	ZrO_2	SiO_2	Si_3N_4	MgF_2
***n* (550 nm)**	1.67 [62]	1.84 [62]	2.06 [70]	2.16 [71]	1.44 [62]	2.01 [72]	1.38 [62]
α (%)	93.0	90.5	89.6	90.0	92.5	90.1	92.8

As expected, the materials with the refractive index closer to the square root of the absorber layer (at 550nm, $n_{a\text{-}C:Zr}$=2 → n_{AR} ~1.41) should be the most effective as single AR layer (i.e. SiO_2, MgF_2 or Al_2O_3). Eventually, Al_2O_3 and SiO_2 are selected as candidates materials due to they show the highest simulated solar absorbance (93.0 and 92.5%, respectively), and also inasmuch as they are very stable materials at temperatures up to 1100ºC [73] in comparison with MgO or MgF_2.

By using several layers of low refractive index, it is possible to increase the antireflection effect. However, the absorptance values can only be improved 0.5% so it is not worthwhile the complexity of the 3 layer AR system. This is the reason why the solar selective coating is designed with only one AR layer. The same complete multilayer stacks were simulated with different thicknesses of SiO_2 and Al_2O_3 layer to optimize the thickness of the single AR layer. Figure 3.12 compares the simulated reflectance spectra of the system with and without antireflective layer, employing the optimized thickness for SiO_2 or Al_2O_3 as AR layer.

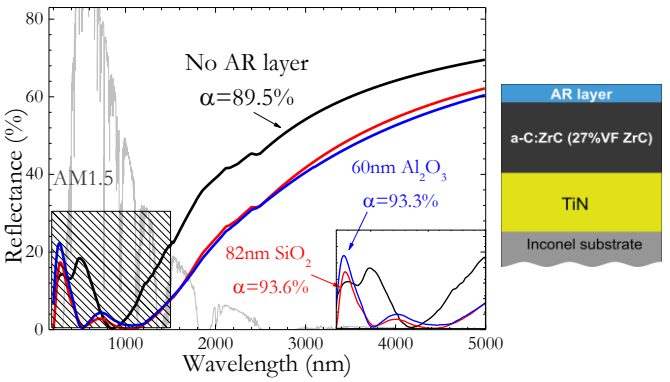

Figure 3.12 –Simulated reflectance of complete SSC without AR layer, with SiO_2 and Al_2O_3 as AR layer with previously optimized thickness and VF. The AM 1.5 solar spectrum from ASTM G173 is also represented. The simulated SSC with AR layer / a-C:ZrC (85 nm and 27% VF of ZrC) / TiN (300nm) on inconel substrate is included.

Both AR layer candidates show quite similar solar absorbance results (α=93.3% for 60 nm of Al_2O_3 and 93.6% for 82 nm of SiO_2) and both have well-known thermal stability at high temperature. Therefore, the decision for the best top layer will be completed once the optical constants and the thermal stability have been experimentally verified.

3.2.4 Optical simulation of the complete solar selective multilayer stack

In this section, the solar absorptance and thermal emittance were optimized simultaneously by CODE for a complete SSC, including TiN as IR layer, an a-C:MeC as absorber layer and Al_2O_3 layer as AR on the top of the coating (Figure 3.13). The optimized parameters of the multilayer stack for the three selected MeC as dispersed nanoparticle in the a-C:MeC absorber layer are represented in the schematic of Figure 3.13.

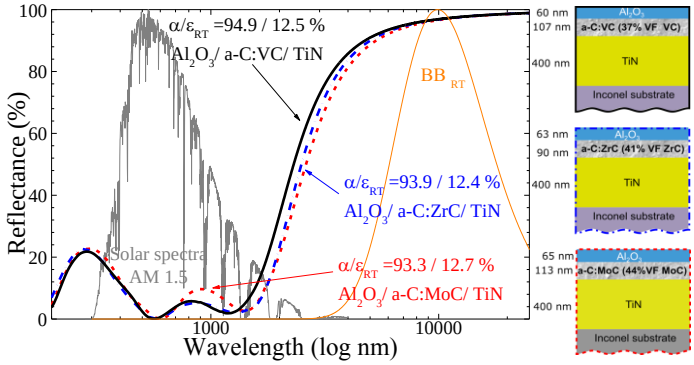

Figure 3.13 - Simulated reflectance spectra of a complete SSC optimizing the thickness of the different layers and the volume fraction in the a-C:ZrC, a-C:VC or a-C:MoC absorber layer.

In order to summarize the different steps followed along this section to achieve this optimized SSC, Table 3.4 includes α values obtained for the three selected carbide candidates for each step. The VF and thickness of the absorber layer are also included in the table. It should also be emphasized that only the last line includes a multilayer SSC with AR and IR layers, and is exclusively for that stack when both α and ε were optimized simultaneously. The TiN thickness was fixed to 400 nm for all the designs. The best solar selectivity α/ε_{RT} achieved was 94.9/12.5 % for a stack composed by Al_2O_3 (60nm)/ a-C:VC (107nm and 37%VF of VC)/TiN(400nm).

Table 3.4 – Simulated solar absorptance (α) obtained in the different optimization steps followed in this work. For the three a-C:MeC (Me = V, Zr, Mo) selected initially the values of the employed volume fraction (VF) and thickness (d) are included. The estimated error in the simulation was 0.1%.

Simulation	a-C:VC			a-C:ZrC			a-C:MoC		
	α	*VF (%)*	*d (nm)*	α	*VF (%)*	*d (nm)*	α	*VF (%)*	*d (nm)*
a-C:MeC (10%VF, *d* = 100 nm)	77.2	10	100	75.5	10	100	73.2	10	100
a-C:MeC (30%VF, *d* = 100 nm)	85.0	30	100	84.8	30	100	83.9	30	100
Optimization VF (fixed *d* = 100 nm)	85.2	20	100	85.6	25	100	84.0	30	100
Optimization *d* (fixed optimized VF)	85.2	20	100	85.7	25	75	84.3	30	75
Optimization VF & *d*	91.5	19	82	89.5	27	85	90.0	29	63
Optimization VF & *d* (complete stack)	94.9	37	107	93.9	41	90	93.3	44	113

The addition of graded films as absorber layer with increasing carbide VF, a/ε ratio has been reported to increase in cermet materials [74]. Figure 3.14 shows the simulated R, the parameters of the SSC and the calculated a/ε using one, two and three a-C:ZrC layers as graded absorber layer. Solar absorptance increases $\Delta\alpha$=+1.7% adding a second absorber layer, but no further improvement is observed for the third a-C:ZrC layer. The thermal emittance slightly increases ($\Delta\varepsilon$= +0.7%) associated with the total higher total thickness. However, this improvement in α does not compensate the increase in complexity and uncertainty of the thickness and VF in the final design of the absorber. Therefore, in this thesis the solar selective coatings will be designed using a single absorber layer.

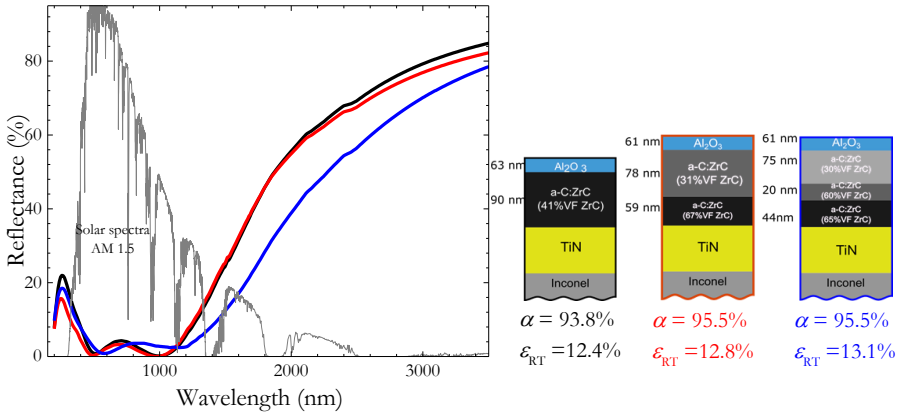

Figure 3.14 - Simulated reflectance spectra of complete absorber selective coatings with one, two and three a-C:ZrC absorber layers. The solar absorptance and thermal emittance at RT are also indicated.

Simulation results from Table 3.4 confirms that, if thicknesses of the different layers and volume fraction of the nanocomposite were optimized, very promising results can be obtained with the combination of materials proposed within this work. These designs significantly improve the solar absorptance from 90.98% reported in previous studies of similar selective coatings [50] (Cu/a-C:TiC/SiO_2) to 94.2% with an emittance at 400ºC of 8.9%.

These simulation based on literature optical constants will be compared in section 3.4 with simulations based on microstructural and optical analysis of deposited layers.

3.3. Deposition and microstructure characterization of SSC individual layers

Taking into account the results obtained with optical simulations, the pre-selected layers which make up the complete SSC were deposited by pulsed filtered cathodic vacuum arc (PFCVA). Their composition, microstructure and morphology were comprehensively analysed in this section.

3.3.1 Deposition of individual SSC single layers

All the samples described in this chapter were deposited in Centre Tecnologic de Manresa (CTM), using a pulsed filtered cathodic vacuum arc (PFCVA) device which schematic diagram is represented in Figure 3.15, and fully explained in chapter 2. The common deposition parameters for all the layer types are sumarized Table 3.5.

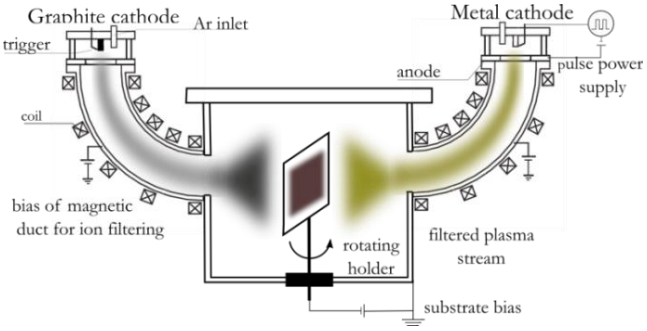

Figure 3.15 - Schematic diagram of the pulsed filtered cathodic vacuum arc (PFVCA) system the two cathodic arc sources.

Table 3.5 – Common deposition conditions for the PFCVA samples

Base pressure	$2.00 \cdot 10^{-3}$ Pa
Operating pressure	0.11 Pa
Argon flow rate	3.5 sccm
Duct bias voltage	-20 V
Duct bias current	15 A
Axial magnetic field	200 G
Cathode diameter	10 mm
Pulse duration of the discharge	3 ms (7.5 Hz frequency)
Bias voltage at deposition stage	- 400 V (100 kHz pulsed)
Duty cycle of the bias	20 %
Rotation speed of the substrate	1.4 rpm
Distance from the filter to the substrate	240 mm

The samples include materials for each layer type (IR, absorber and AR), and they were grown on crystalline silicon (100) and mirror polished inconel HAYNES ® 625 substrates. During film deposition, 3 sccm of Ar gas flow was introduced into the chamber to stabilize the arc.

Deposition of a-C:MeC absorber layers

a-C:MeC nanocomposite thin films (with Me =V, Zr and Mo) were prepared by the co-evaporation of both cathodic arc sources simultaneously. For each metal, two different metal concentrations were deposited, denominated high (h) and low (l) metal content throughout this thesis. The metal content was controlled varying the current applied to each one of the cathodes. The intensity of the carbon arc source was kept constant at 2.5 A, and the metal arc source was varied from 0.6 to 2.5 A for low and high metal content, respectively. A pure carbon reference film was prepared with similar deposition conditions but using only the carbon arc source.

Deposition of infrared reflection (IR) layers

TiN, ZrN layers were deposited in reactive mode employing only one of the arc sources with a metallic cathode and with the adition of 3 sccm of N_2 gas flow. The substrate temperature during the deposition was varied from room temperature to 300ºC.

Deposition of antireflection (AR) layers

Al_2O_3 and SiO_2 layers were deposited employing Al or Si cathodes in a reactive deposition with 3 sccm of O_2 gas flow. Grounded bias was employed to deposit these thin films to lowered the refractive index [75]. Glass substrate was also employed for transmittance measurements.

3.3.2 Composition and microstructural characterization of a-C:MeC thin films as absorber layer

The element concentration was accurately determined using Rutherford Backscattering Spectroscopy (RBS) and Nuclear Reaction Analysis (NRA) ion beam techniques. The structure of the nanocomposite was investigated in detail by Raman spectroscopy, X-ray diffraction (XRD) and high-resolution transmission electron microscopy (HR-TEM).

Film composition and depth profiles

The carbon and metal (V, Zr or Mo) areal densities of films grown in Si substrates as absorber layer were determined by a combination of RBS and NRA measurements. The RBS intensity of backscattered deuterium ions is proportional to the atomic number Z of all elements of the sample. Here it was used for the determination of the metal contents. Since the RBS cross section of carbon is low and the carbon signal is superimposed to that of the Si substrate, NRA measurements were employed to accurately determine carbon areal densities.

In order to calibrate the equivalent areal density for each metal content, data obtained in RBS experiments of samples with the highest V, Zr and Mo content (a-C:VC (h), a-C:ZrC (h), and a-C:MoC (h) samples) were used. The RBS spectra (Figure 3.16 (a) to (c)), shows the V, Zr and Mo metal signals appearing at approximately 1280, 1450 and 1480 keV, respectively. Due to the high Z of the metals, these signals are strong and clearly differentiated from the overlapping signals of the silicon substrate and carbon below 900 keV and at 440 keV, respectively. The weak peak around 1100 keV is caused by the incorporation of less than 4 at.% Ar used to stabilize the arc formation during the deposition. In the case of the Zr-C, less than ~0.5at.% of Ta from the Zr cathode contamination has been found.

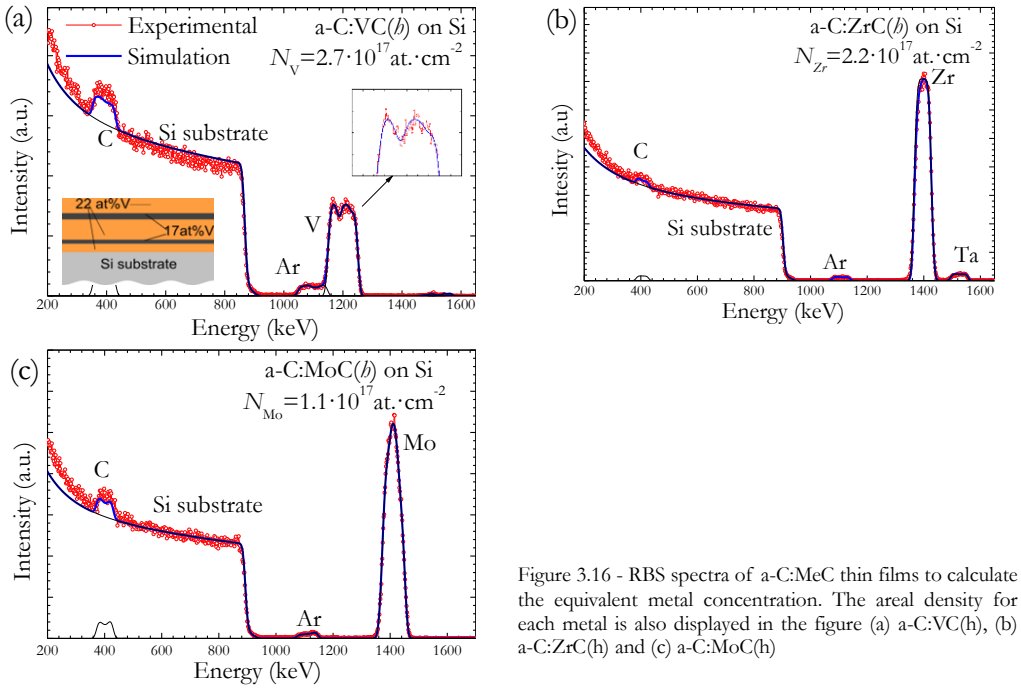

Figure 3.16 - RBS spectra of a-C:MeC thin films to calculate the equivalent metal concentration. The areal density for each metal is also displayed in the figure (a) a-C:VC(h), (b) a-C:ZrC(h) and (c) a-C:MoC(h)

A closer look at the vanadium RBS signal in a-C:VC (h) (inset in Figure 3.16 (a)) reveals an inhomogeneous depth distribution of the metal. In fact, in order to fit the spectrum properly, five different layers with alternating high (22 at.%) and low (17 at.%) vanadium content were taken into account. To a lesser extent, this depth inhomogeneity of the metal concentration is also observed in the a-C:ZrC (h) and a-C:MoC (h) sample. These results will be discussed in detail later in combination with HR-TEM images.

NRA analysis using 1.248 MeV deuterium ions was performed for accurately determination of the carbon and metal content. The equivalent areal density N (total deposited amount per cm^{-2}) for each metal type was extracted from RBS analysis, with, 2.7·10^{17}, 2.2·10^{17}and 1.1·10^{17} atoms cm^{-2} for V, Zr and Mo, respectively.

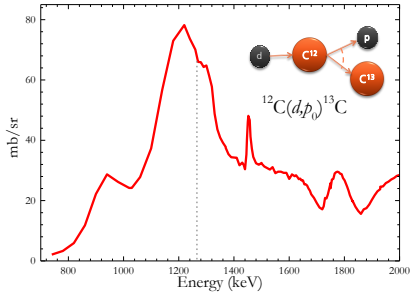

Figure 3.17 – Cross section for the ^{12}C(d,p)^{13}C reaction measured at 135º.

A reference C:Ni sample, with a known areal density of carbon atoms (t_C=5.8·10^{17} C at·cm^{-2}), was measured in the same NRA experiments to determine the total amount of carbon of the carbon-metal samples. The nuclear reaction ^{12}C(d,p_0)^{13}C cross section exhibits its maximum at 1.2-1.4 MeV deuterium ion energy, as shown in Figure 3.17 [76].

The intensity of the emitted proton signal is proportional to the carbon concentration in the nanocomposite thin film [77], while the RBS signal of the scattered deuterium ions is proportional to the atomic number Z of all elements of the sample. The two distinct regions in the spectra obtained are shown in Figure 3.18 (a) to (c) for the different a-C:MeC deposited samples.

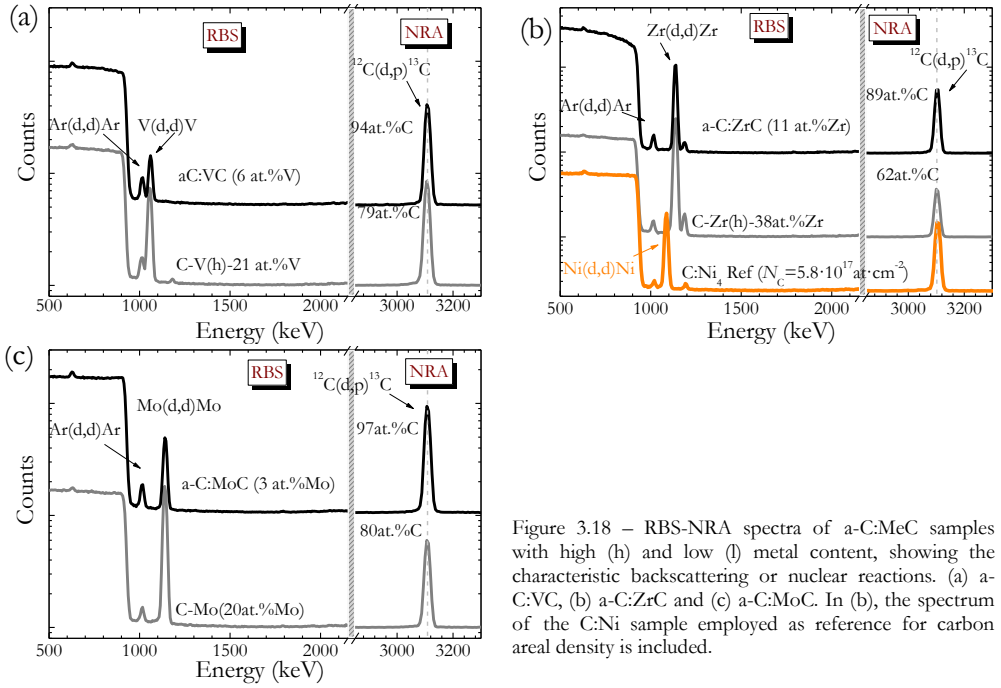

Figure 3.18 – RBS-NRA spectra of a-C:MeC samples with high (h) and low (l) metal content, showing the characteristic backscattering or nuclear reactions. (a) a-C:VC, (b) a-C:ZrC and (c) a-C:MoC. In (b), the spectrum of the C:Ni sample employed as reference for carbon areal density is included.

The carbon and metal film areal densities (t_C and t_{Me} respectively) were determined by integrating the area under the peaks corresponding $^{12}C(d,p)^{13}C$ and Me(*d,d*)Me reactions. To find out the areal density, NRA measurements were performed with both the reference metal (the one measured with RBS) and the unknown one. The areal density is calculated by equation (3.1):

$$t_{Me} = \frac{t_{ref\_Me} x\, I_{Me}}{I_{ref\_Me}} \quad ; \quad t_C = \frac{t_{ref\_C} x\, I_C}{I_{ref\_C}} \tag{3.1}$$

with I_{me} and I_C the integrated are of the unknown metal or carbon, after a proper subtraction of the background. The metal-carbon ratio in metal atomic percentage was calculated as equation (3.2).

$$at.\%(Me) = \frac{t_{Me}}{t_{Me} + t_C} x100\% \tag{3.2}$$

where *Me* can be one of the metals employed (V, Zr and Mo).

The averaged metal contents of the samples are given in Table 3.6. The film density can be estimated from the RBS areal density and film thickness [44]. In the case of a-C:VC (h) sample, the density is ~3.0 g·cm^{-3}, i.e. lower than the density of bulk vanadium carbide (5.7 g·cm^{-3} [45]) and higher than in amorphous carbon (2.1·cm^{-3} [46]) typically obtained with cathodic arc deposition. In the case of the a-C:ZrC(h) sample, the estimated average density e 5.6 g cm^{-3} (in contrast with 6.6 g cm^{-3} of a pure *fcc* ZrC [78]) and 4.8 g cm^{-3} for a-C:MoC (h) film.

In the initial simulations (section 3.2), the ideal metal content of the composite absorber layers, calculated with BRU EMA was around 30-50 at.% VF of MeC in the nanocomposite. For a comparison with the measured concentration values, the content of metal (in at.%) obtained experimentally RBS-NRA was converted into volume fraction (% VF) of metal carbide using the densities of the individual components. MeC o density values of 5.6, 6.6 and 9.5 $g \cdot cm^{-3}$ for VC, ZrC and *γ*-MoC, respectively were obtained from literature data [3,54,79]. The samples deposited with high metal content were in good agreement with the simulated for a-C:VC and a-C:MoC.

Table 3.6 – Relative at.% Me / C content for the a-C:MeC samples with high(h) and low(l) metal content. The estimated error is ± 0.5%. The equivalent %VF of carbide of MeC in a-C is calculated using densities from literature [3,54,79].

Cathodes	a-C: MeC (l)		a-C: MeC (h)	
	at.% Me (l)	%VF MeC (l)	at.% Me (h)	%VF MeC (h)
C-V	6.0	11.7	20.5	40.4
C-Zr	11. 0	27.9	38.0	81.3
C-Mo	3.5	7.0	20.0	40.0

The metal content varies between 3.5 and 11.0 at. % for the low ratio C/Me intensity depositions, and between 20.0 and 38.0 at.% for the high ones. The deposition conditions were the same for all high and for all low metal content, however, the C and Me at.% depend on the metal employed.

X-ray diffraction (XRD) analysis

The phase structure and crystallinity of the a-C:MeC absorber layers grown on Si substrate were investigated by GIXRD (Figure 3.19). It is worth noting that the patterns are intermitted between ~50 and 58º in order to blind the intense peak at ~52º attributed to the (311) peak of crystalline Si substrate. The crystallite size is estimated by Scherrer [80].

The diffraction pattern of the a-C:VC film (20.5 at% V) shows four well-defined Bragg peaks positioned at 2θ =37º, 43º, 63º and 79º (Figure 3.19 (a)). These peaks are assigned to interferences of the (111), (200), (220) and (222) planes of a *fcc* vanadium carbide [81,82], respectively. Applying Bragg's equation the lattice constant (4.13 Å) is obtained in good agreement with the reference value (4.16 Å). A crystallite size of 27 ± 1 nm was estimated by Scherrer. A second set of interferences is observed at 2θ values of 36.7°, 42.7°, 63.0°, and 74.9°. The diffraction angles are slightly smaller than those of the first set, and moreover, the peaks are significantly broader. The diffractogram pattern points to a second *fcc*-VC structure with a lattice constant of 4.25 Å and crystallite size of 7 ± 1 nm. The coexistence of two *fcc*-VC phases can be rationalized by assuming regions with a different V content, what is consistent with the observed fine structure of the RBS signal. The data are in qualitative agreement with those of a recent study on magnetron sputtered a-C:VC films [26]. Similar as in the present study, a slight decrease of the VC lattice constant with increasing V content was reported therein. No significant diffraction peaks were identified in the low metal content a-C:VC sample with 6 at. % V.

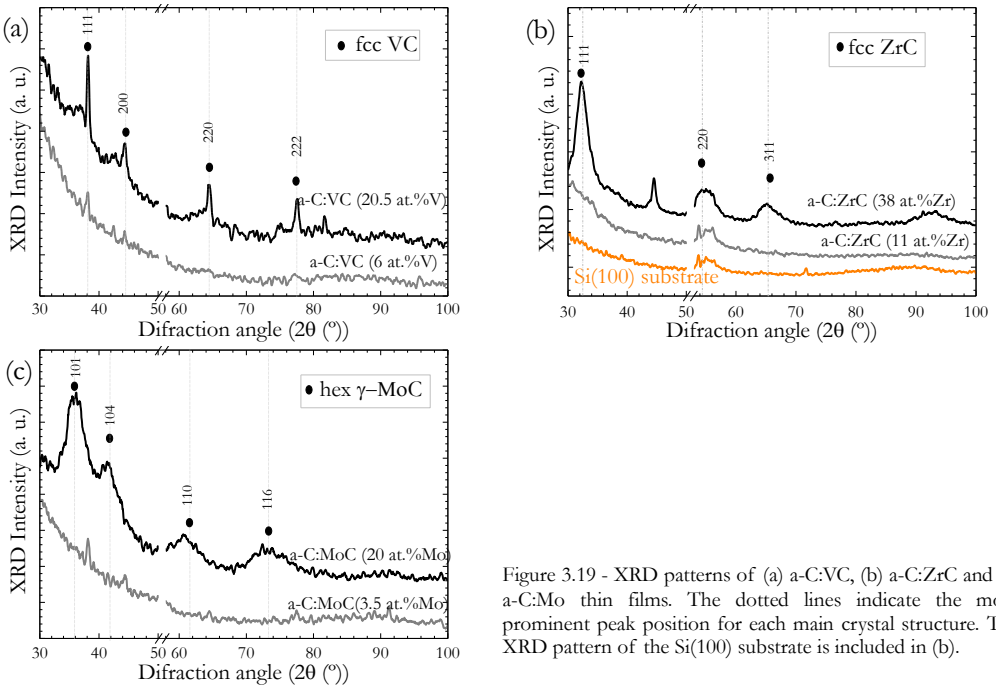

Figure 3.19 - XRD patterns of (a) a-C:VC, (b) a-C:ZrC and (c) a-C:Mo thin films. The dotted lines indicate the more prominent peak position for each main crystal structure. The XRD pattern of the Si(100) substrate is included in (b).

Figure 3.19 (b) represents the X-ray diffraction patterns of the carbon-zirconium samples. The ZrC main peaks are represented in the figure. In the diffraction pattern of a-C:ZrC with low content (11 at.% Zr) not diffraction peaks are observed. Thus this sample can be considered as XRD amorphous [83]. However, in the a-C:ZrC sample with 38 at.% of Zr, the crystallinity increases as revealed by the appearance of one well-defined Bragg peak situated at 2θ ≈ 32º assigned to the (111) plane of ZrC *fcc* structure [81,84]. Other peaks can be observed at 2θ ~54º and ~65º, assigned to the crystal planes (220) and (311) respectively. The estimated average crystal size is 3.0 ± 0.5 nm and the calculated lattice constant is 4.75 Å in excellent agreement with the reference value (4.76 Å).

Table 3.7summarizes the estimated average carbide particle crystal size derived from XRD of the *fcc* MeC crystal stuctures. The crystallite size of VC is around 10 times bigger than for ZrC. Comparing the carbide melting temperatures, VC(2830ºC)< ZrC (3420ºC) [3]. Hence, for lower carbide crystal stability, the temperature at which the metal atoms can leave the surface of carbide particle and diffuse to another particle is lower as well, and following Ostwald ripening process, the carbide grains become bigger [83].

Table 3.7 - Crystallite size of a-C:VC and a-C:ZrC from the XRD patterns of the deposited samples. The average lattice constant (*a*) is also indicated.

Sample	Crystal size (nm)	*a* (Å)
a-C:VC(h)	27 ± 1 (7 ± 1)	4.13 ± 0.01 (4.25± 0.01)
a-C:ZrC(h)	3 ± 0.5	4.75 ± 0.01

Figure 3.19 (c) shows the XRD pattern of the a-C:MoC samples. The diffractogram pattern of a-C:MoC (20.0 at.% Mo) shows four broad diffraction peaks at 2θ = 36º, 41º, 61º and

73º. The pattern closely resembles that of simple hexagonal monocarbide *γ*-MoC [81]. Its main peaks are tabulated at 2θ = ~36º, 42º, 61º and 73º and assigned to the crystal planes (101), (104), (110) and (116), respectively. The main peaks observed here for a-C:MoC (20 at.% Mo) are also close to those of *hcp* *β*-Mo_2C [81]. The Mo-C phase diagram has up to 6 different possible phases [10] (the so-called MoC problem [12,85]), which differs in the stoichiometry and in the order/disorder of the carbon atoms. But, according to the binary phase diagram of Mo and C [86], the thermodynamically stable phase for a Mo content of ≤ 50 at.% is *γ*-MoC with hexagonal simple space group *P6m2*. Therefore we tentatively assign the observed diffractogram of a-C:MoC (19 at.% Mo) to the *γ*-MoC phase. The phase structure of a-C:MoC (20.0 at.% Mo) will be further discussed in the subsequent section about the HR-TEM analysis. Scherrer equation gives a minimum *γ*-MoC crystallite size of 3.5 ± 0.5 nm. For a-C:MoC (3.5 at.% Mo), no significant diffraction peaks were identified. As for a-C:ZrC(11at.% Zr) and a-C:VC (6 at.% V), the low metal content is presumably responsible for a small number of MeC crystals, which moreover are too small in order to provide a sufficiently large volume for coherent scattering of X-rays that is necessary for the observation of diffraction interferences.

In summary, only for high metal content films nanocrystalline carbides are observed. No crystalline phases can be identified for low metal content films. It is plausible that the excess of carbon limits the growth of crystalline carbide grains during deposition [87]. Neither crystalline metal nor graphitic phases are observed. The latter finding is in agreement with the Raman analysis.

Raman spectroscopy analysis.

The Raman spectra of carbons films show common features in the 800–2100 cm^{-1} region, due to sp^2 sites: the *G* peak (or graphite) and *D* peak (disorder-induced). The *G* peak that lies at 1500-1630 cm^{-1} wavenumber is due to the bond stretching vibrations of all pairs of sp^2 carbon atoms (either in -C==C– chains or rings). The *D* peak situated at around 1350 cm^{-1}, is related with the breathing modes of sp^2 carbon atoms in six-foil aromatic rings [22], therefore, only sp^2 sites participating in rings contribute to this mode [88]. As introduced before, the structure of the carbon can be classified with the intensity of the peaks (I_D/I_G ratio), the position and the width of *D* and *G* peaks, and allows distinguishing between graphitic, or disorder carbon.

The Raman spectra depend fundamentally on the degree of clustering of sp^2 sites, the bond disorder, the presence of sp^2 rings or chains and the ratio sp^2/sp^3. Ferrari & Robertson [22] described a three stage model to use visible Raman to describe all carbon films (Figure 3.20 (a), characterized by the evolution of the I_D/I_G ratio of *D* and *G* peaks heights and the position of the *G* peak. The amorphization trajectory consists on i) ordered sp^2 graphite to nanocrystalline graphite with smaller sp^2 groups, ii) nanocrystalline graphite to disordered amorphous carbon in rings configuration and iii) a-C to sp^3 bonded chains of ta-C (as in Figure 3.20 (b)).

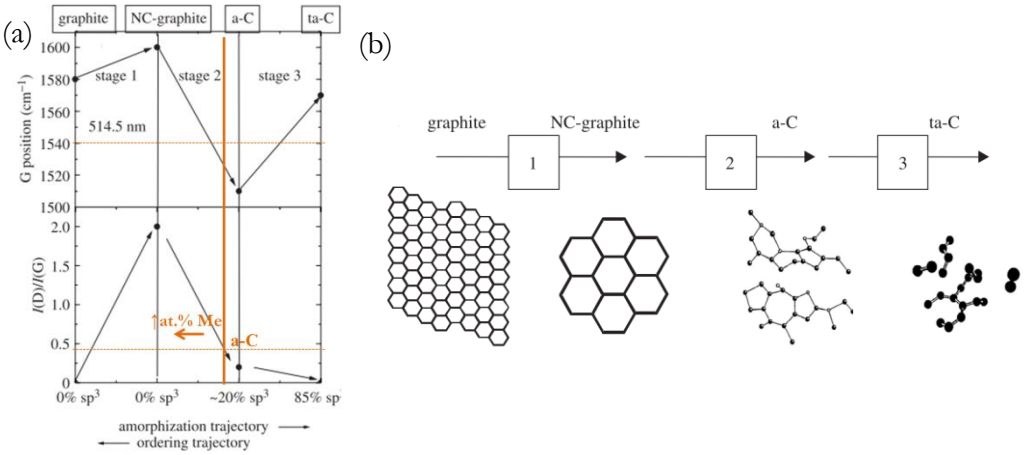

Figure 3.20 – (a) Three-stage model of the variation of the Raman *G* position and the D to G intensity ration I_D/I_G with increasing disorder and (b) variation of the sp^2 configuration on the three amorphization stages [89].

The measured spectra were fitted with a combination of a linear background fixed at the noise level of the spectra at 850 - 2000 cm^{-1}, a symmetric Lorentzian shape for D peak, and an asymmetric Breit-Wigner-Fano (BWF) line for the G peak [26,28,90]. The intensity I as a function of the wavenumber ω for the BWF line shape is described by equation (3.3)

$$I(\omega) = \frac{I_0[1 + 2(\omega - \omega_0)/q\Gamma]^2}{1 + [2(\omega - \omega_0)/\Gamma]^2} \tag{3.3}$$

with the intensity maximum

$$I_{max} = I_0\,[1 + 1/q^2] \tag{3.4}$$

positioned at

$$\omega_{max} = \omega_0 + \Gamma/2q \tag{3.5}$$

where I_0 is the peak intensity, ω_0 the peak position, Γ the FWHM, and q is the BWF coupling coefficient. The Lorentzian line shape corresponds with the limit $q^{-1} \rightarrow 0$. The intensity maximum defined by equation (3.4) will be used to denote the intensity of the *G* and *D* peaks and equation (3.5) to define their wavenumber position.

The a-C:MeC samples are compared with the deposited pure carbon reference sample, which exhibits one peak that is asymmetrically broadened towards smaller Raman shifts (Figure 3.21). This line is attributed to the *G* line of sp^2-C. The *D*-line, which is characteristic for 6-fold aromatic ring clusters, is virtually absent. On the other hand, the Raman line fit is improved by using the 2 line model described in before instead of a single BWF function for the *G* line. Therefore, the phase structure of the carbon reference is attributed to a-C with a small degree of six-fold sp^2-C ring clustering. Hence, the sp^2 atoms are located on chains, and eventually, isolated sp^2 molecules within the sp^3 matrix. The reduced intensity of *D* peak in the Raman spectra is explained by the structural arrangement of sp^2 in pairs [91].

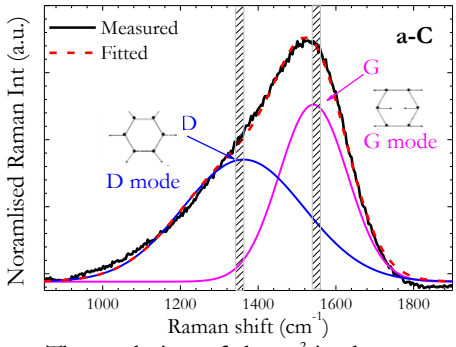

Figure 3.21 – Normalized Raman spectra of pure carbon deposited by PFCVA with *D* and *G* peaks fitted. The schematic vibrational modes of *G* (Graphite) and D (disorder-induced) of the carbon atoms are represented.

The evolution of the sp^2 in the pure carbon varying the substrate temperature was also analysed (not shown here). By increasing the substrate temperature, the sp^2 hybrids cluster in aromatic rings, as indicated by the promotion of the *D* peak [92]. The increase of the I_D/I_G ratio indicates a transition between ta-C to a-C. However the adhesion of the films deteriorates drastically when the deposition temperature increases. The significant worsening of the film adhesion made discard heating the substrate during the PFCVA deposition. The analysis of pure carbon Raman spectrum validates the decision of selecting a-C as matrix material in the nanocomposites employed for the simulations.

The normalized Raman spectra of the a-C:MeC (Me = V, Zr and Mo) nanocomposite thin films together with the a-C deposited under identical conditions are compared in Figure 3.22.

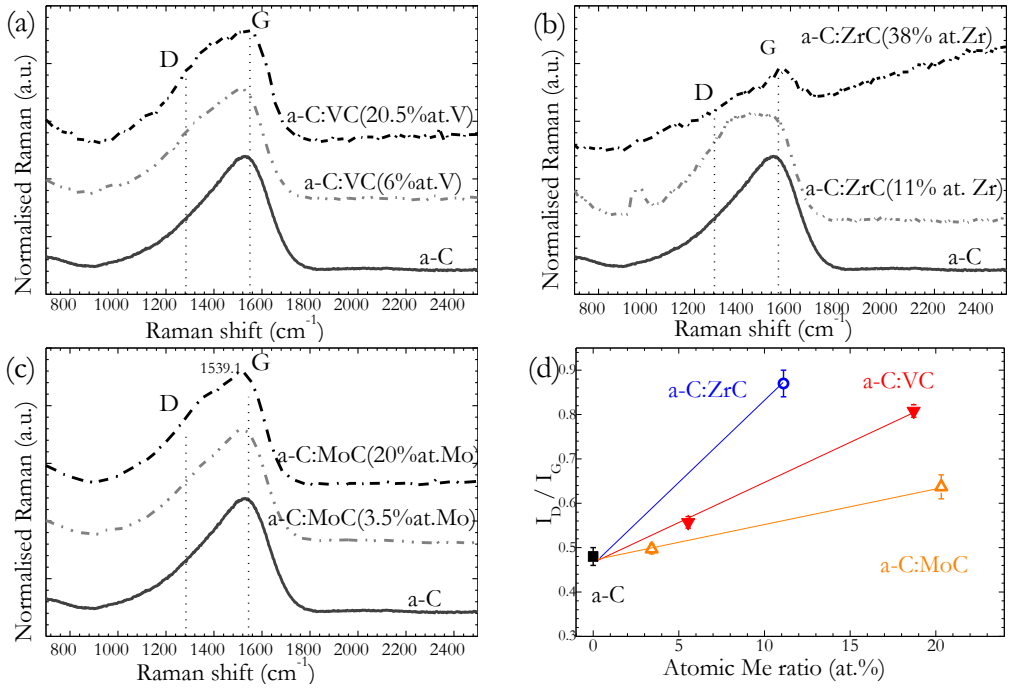

Figure 3.22 - Normalized Raman spectra of (a) a.C:VC, (b) a-C:ZrC and (c) a-C:MoC samples all with high and low metal content. The Raman spectrum of the deposited carbon sample is represented as reference (d) Ratio I_D/I_G and (e) G_{peak} position a-C and a-C:MeC deposited samples. The lines are to guide the eye.

For the sake of completeness, the ratio of the peak intensities I_D/I_G, the peak position and the FWHM have been calculated following the equations (3.3), (3.4) and (3.5), and the obtained values are summarized in Table 3.8.

Table 3.8 - Experimental results from visible Raman spectroscopy of the deposited a-C:MeC thin films.

Sample	*D* band		*G* band		I_D/I_G
	Peak (cm^{-1})	FWHM (cm^{-1})	Peak (cm^{-1})	FWHM (cm^{-1})	
a-C	1392 ± 1	236.5 ± 0.5	1550 ± 1	190.0 ± 0.5	0.48
a-C:VC (20.5 at.%V)	1364 ± 1	238.0 ± 0.5	1545 ± 1	166.5 ± 0.5	0.81
a-C:VC (6 at.%V)	1364 ± 1	227.0 ± 0.5	1539 ± 1	185.0 ± 0.5	0.56
a-C:ZrC (38 at.%Zr)	1389 ± 1	283.0 ± 0.5	1570 ± 1	108.5 ± 0.5	068
a-C:ZrC (11 at.%Zr)	1357 ± 1	237.0 ± 0.5	1534 ± 1	187.5 ± 0.5	0.88
a-C:MoC (20 at.%Mo)	1363 ± 1	231.5 ± 0.5	1539 ± 1	173.0 ± 0.5	0.64
a-C:MoC (3.5 at.%Mo)	1373 ± 1	223.5 ± 0.5	1543 ± 1	183.0 ± 0.5	0.50

In the case of the a-C:ZrC (~38at.%Zr) sample, whose Raman spectra is shown in Figure 3.22 (b), the high metal content reduces the intensity of the Raman spectra. This effect is mainly due to a high percentage of the laser beam reflected with high metal content and the higher fraction of carbon bonded with the metal which no produces Raman signal, as observed by Adelhelm [93]. These combined effects make very difficult a correct measurement of a-C:ZrC (38 at.%) sample, hence this spectrum is not considered for further analysis. The square shaped peak at 950 cm^{-1} in the a-C:ZrC (11at.%Zr), not visible in the other spectra, is due to the second order of Raman from the Si substrate. This peak is a signature of ta-C film, and it indicates high sp^3 content in this sample [94], associated with high optical transparency.

The Raman spectra of a-C:VC, a-C:Zr (11 at.%Zr), and a-C:MoC exhibit similar behaviour with the carbon content. The corresponding sp^3 content of the carbon matrix is in the order of 10 to 15 %, assigned to the second step in view of Ferrari's model (Figure 3.20 (a)). The Raman spectra of the a-C:MeC nanocomposite films exhibit a shoulder in the range of the *D* line and a maximum at the Raman shift of the *G* line of sp^2-C. At first glance, the intensity of the *D* line increases with increasing metal content (Figure 3.22 (d)). The I_D/I_G ratio varies from 0.56 (0.50) for the a-C:VC (a-C:MoC) with lower metal content to 0.8 (0.64) for the higher metal samples up to 0.88 for the a-C:ZrC (11at.%Zr). Together with the position of the *G* line, which is observed nearly unchanged at 1540 cm^{-1} for all samples, the three stage model of Ferrari and Robertson [22] implies a sp^2-C phase consisting of a-C with a higher degree of 6-fold aromatic ring clusters than in the reference sample of pure carbon [22,95].

In summary, the addition of metal increases the ordering of the carbon in the samples, and the carbon of the low metal carbon samples has higher degree of amorphization. The latter finding is in agreement with the XRD analysis.

High resolution transmission electron microscopy (HR-TEM)

The microstructure and film morphology of the a-C:MeC deposited samples were investigated with HR-TEM analysis. Cross-sectional HR-TEM images of the a-C:MeC samples deposited on Inconel substrates are shown in Figure 3.23, Figure 3.24 and Figure 3.25.

In the HR-TEM images of the a-C:VC (20.5 at.% V) sample shown in Figure 3.23, a well-defined multi-layer structure is observed. In total, five regions are found. Three of them exhibit an ordered multilayer pattern with a period of 5 ± 1 nm. In the other two regions, this periodicity is apparently lost (Figure 3.23 (a)). The observed layer sequence is correlated with the different compositional ranges observed in RBS (see Figure 3.16). High-resolution imaging was applied for detailed analysis of the ordered and non-ordered regions of a-C:VC (20.5 at.% V) in Figure 3.23(b). The two different regions are labeled as 1 and 2. The FFT analysis of the non-ordered region 1 reveals only one lattice plane distance of 2.4 Å (Figure 3.23 (c)). This distance is attributed to the (111) planes of *fcc*-VC phase, revealing VC nanocrystals embedded in the a-C matrix. The self-organized multi-layers of region 2 are composed of alternating dark contrast carbide-rich (1 to 1.5 nm thick) and bright contrast carbide-depleted (~ 3-4 nm) nanolayers. The FFT of this region shows three circular intensity maxima (Figure 3.23 (d)). The corresponding lattice plane distances of 1.4, 2.0 and 2.4 Å are in very good agreement with those of *fcc*-VC [96].

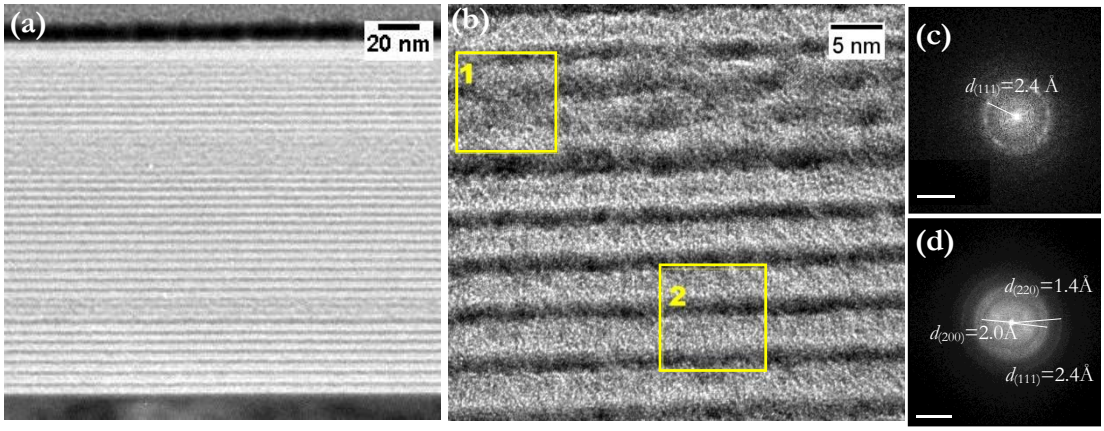

Figure 3.23 – HR-TEM analysis of a-C:VC (20.5 at.%V) deposited on Inconel. (a) Overview image. (b) High resolution image of a representative sample section. (c) and (d) FFTs analysis of selected regions 1 and 2 of (b), respectively.

The periodicity of the layers does not match the rotation speed of the substrate holder. Therefore, the multilayer structure observed for a-C:VC (21 at.% V) cannot be associated with the sample rotation during the deposition. Moreover, it is neither correlated with the pulse sequence during the deposition nor with the lamellae preparation by FIB. In conclusion, the formation of the layered structure is attributed to a self-organization process previously reported in the literature [39–41,97]. In order to support this assumption, an element analysis has been done with energy dispersive X-ray (EDX) spectroscopy with high angle annular dark field detector, along the cross

section (EDX not shown here). The composition analysis reveals how the multilayer alternates bright carbide-rich and dark carbide-depleted zones. Oxygen presence can be detected (at.% O < 5%), with a maximum value in the surface of the sample and decreasing with the depth, attributed to superficial oxidation of the thin films.

The overview TEM image of the a-C:ZrC (~38at.%Zr) sample is shown in Figure 3.24 (a). As in a-C:VC, a multilayer structure can be observed. In this case a total of 28 nanolayers with an individual thickness of about 5-8 nm can be resolved, although they are not as clearly defined as for a-C:VC. In the higher amplification HR-TEM images (Figure 3.24 (b)), it can be observed how the layers are composed of small globular nanocrystals of ZrC carbides, with an average size of ~3 nm, surrounded by amorphous areas. Ordered lattice planes of the ZrC grains can be detected in Figure 3.24 (b1). Fast Fourier Transform (FFT) of the selected area in the HR-TEM image (Figure 3.24 (b2)) shows three clear diffraction rings. Two of them are associated to lattice parameters of 2.7 and 1.7 Å and reveal that the film has randomly oriented crystallites of ZrC *fcc* system. These values are associated to the crystal orientation (111), (220) observed in the XRD pattern. The third interplanar distance of 2.3 Å corresponds to a crystal orientation (200) at 2θ= 38º, that was not detected in the GIXRD difractogram. HR-TEM images of low metal content a-C:ZrC (not shown here) reveals no multilayer self-formation. Moreover, no nanocrystalline structure was found, in concordance with XRD analysis.

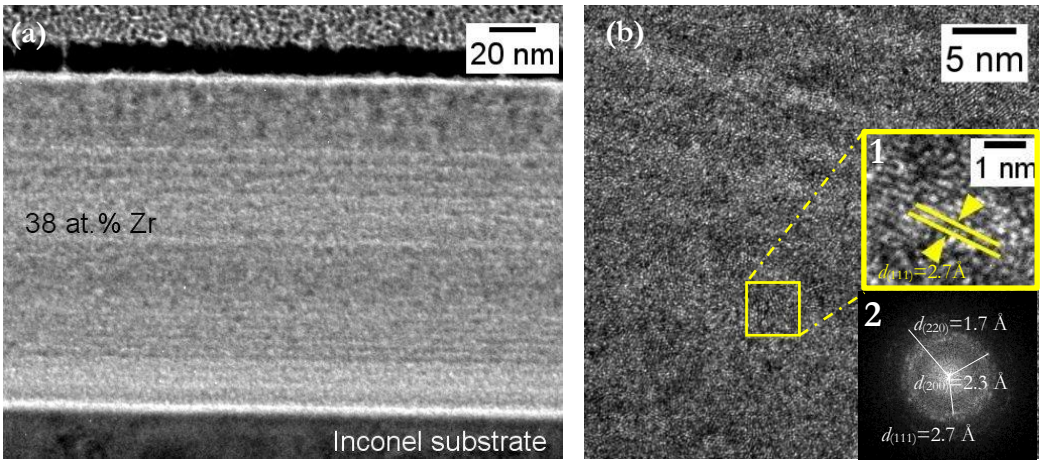

Figure 3.24 – HR-TEM analysis of a-C:ZrC (38 at.%V) deposited on Inconel. (a) Overview image. (b) High resolution image of a representative sample section. (b1) Selected region of (b) in higher magnification. (b2) FFT analysis of sections of (b1) with the different diffraction rings associated to the main lattice spacing of ZrC.

Finally, HR-TEM images of the a-C:MoC (20 at.% Mo) sample reveal that in this case, the sample has not developed a clear multilayer structure (Figure 3.25 (a)), but molybdenum carbide nanoparticles were embedded in a carbon matrix (Figure 3.25 (b)). The main interplanar spacing was calculated and represented in Figure 3.25 (c), and the FFT analysis from this selected area gives three circular intensity maxima associated with lattice parameters of 1.5, 2.1 and 2.5 Å (Figure 3.25

(d)). These interplanar distances are in good agreement with those of the (110), (103) and (101) crystal planes of γ-MoC. Based on the slightly better agreement of the lattice plane distances and the thermodynamics, the carbide phase is attributed to γ-MoC and not to β-Mo_2C.

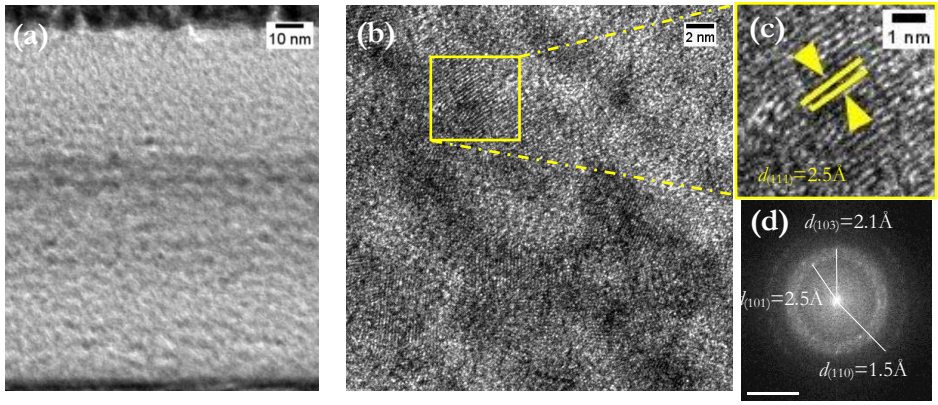

Figure 3.25 - HR-TEM analysis of a-C:MoC (20 at.%Mo) deposited on Inconel (a) Overview image, (b) High resolution image of a representative sample section. (c) Selected region of (b) in higher magnification and (d) FFT analysis of (c).

Conversely, in the a-C:MoC (3.5 at.%Mo) sample, a self-forming multilayer can be observed, as shown in Figure 3.26. In the HR-TEM image the layers are not easily distinguishable due to the low crystallinity exhibited in the sample, as has been shown in XRD analysis. The amorphous character also inhibits the detection of the diffraction rings in the FFT analysis. However, in the STEM image shown in Figure 3.26 (b), the different composition contrast helps to visualize non-homogeneous nanolayers with variable Mo content (from ~1 to 5 at.%. Mo), as verified by EDX analysis. The origin of the self-formation observed for a-C:MoC sample is still under debate.

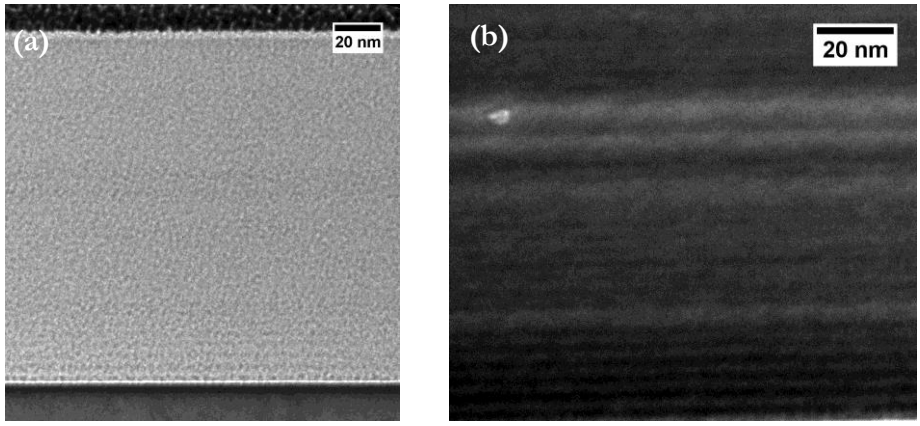

Figure 3.26 – a-C:MoC (3.5 at.%Mo) films deposited on Inconel (a) HR-TEM image and (b) STEM image.

As explained in section 1.1, the growth model for self-organized layer growth is still not clear and different theories have been proposed to explain this phenomenon. The diffusivity of the adatoms on the substrate surface during the film growth, enhanced by the energetic deposition of

the PFCVA deposition technique, as described in previous works [38], [42], can be the best explanation behind this phenomenon.

In summary, the comprehensive characterization gives a consistent scenario of the microstructure evolution of the nanocomposites under study. The formation of nanocomposites structures of dispersed metal carbide crystals embedded in amorphous carbon was confirmed by Raman, XRD and TEM for the samples with high metal content. The phase structure is thermodynamically driven by the immiscibility of the phases which lead to a phase separation. In addition to the generally observed phase separation, a spontaneous formation of ordered multilayers for the cases of the a-C:VC (20.5 at.% V), a-C:ZrC (38 at.% V) and a-C:MoC (3.5 at.% V) thin films are found.

3.3.3 Microstructural characterization of IR and AR layers

The composition of IR layers (TiN and ZrN) deposited at different temperatures were characterized by EDX and by RBS analysis in the case of the AR samples (SiO_2 and Al_2O_3). In both cases the phase and crystal structure were identified by XRD.

Film composition and depth profile

The composition of the IR layer was obtained by EDX analysis (results not shown here). No differences were detected in the compositions of the IR layers between the two different deposited temperatures and stoichiometric TiN and ZrN films were obtained. Oxygen content was detected in all samples, having low content in samples deposited at higher temperature (300ºC). However, it should be noted that EDX is not an accurate method to obtain the composition as it has a low resolution for light elements.

RBS measured spectra for Al_2O_3 and SiO_2 samples deposited on Si substrate (not shown here) indicate that for both AR layers, stoichiometric films were formed (40at.% of Al and 60at% of O in the Al_2O_3 films and 33at.% of Si and 67at.% of Si for the SiO_2) for the deposited conditions.

X-ray diffraction (XRD) analysis

The IR samples were deposited at RT and at 300ºC, and the influence of the deposition temperature is analysed by XRD (Figure 3.27). For both nitrides, stoichiometric NaCl structures were formed with extreme stability, as expected for PVD techniques with high energy of bombarding species. The crystal size of the ZrN and TiN at the two deposition temperatures is shown in Table 3.9.

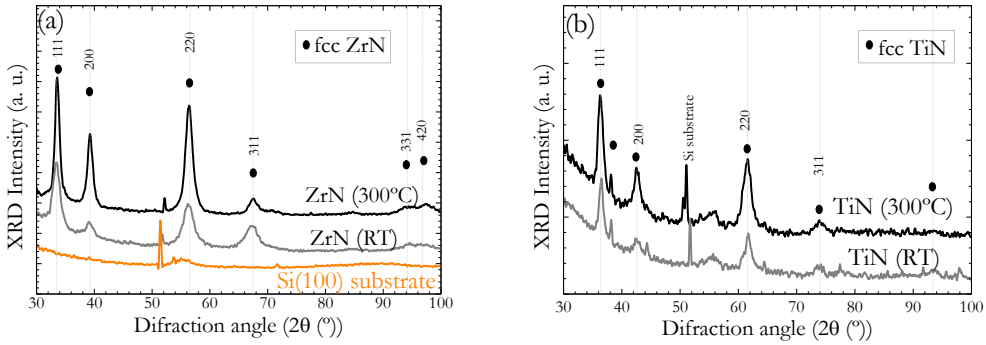

Figure 3.27 - XRD patterns of stoichiometric (a) ZrN and (b) TiN deposited at RT and 300ºC. The symbols represent the position of the XRD peaks taken from the database International Centre for Diffraction Data (cards 00-035-0753 for ZrN and 00-006-0642 for TiN)

As is shown previously in literature, the crystallite size of the nitrides increases with deposition temperature [98], with a post deposition annealing [99,100], increasing the negative bias of the deposition chamber [101,102] or with lower deposition pressure [103]. All those deposition conditions increases the kinetic energy of the ions, resulting in the increment of the crystallite size and the concomitant higher reflectance in the infrared wavelength range, as shown in next section. The deposition of nitrides at high temperature also leads to an improvement of adhesion [104], to a higher lateral homogeneity. These are highly valued properties in IR candidate layers for SSC. The improvement of the quality of the sample was directly verify with a visual inspection of the deposited samples.

Table 3.9: Crystallite size of ZrN, CrN and TiN calculated from the XRD patterns of the deposited samples.

Sample	Crystallite size (nm)	
	RT	300ºC
ZrN	8 ± 1	13 ± 1
TiN	12 ± 1	16± 1

Regarding AR layers, XRD profiles show that the both SiO_2 and Al_2O_3 AR films deposited with identical conditions were XRD amorphous.

This complete microstructural characterization of the different single layers will play a key role in the simulations of the optical properties, as show in the following section. The variety of obtained microstructures and the comprehensive characterization provides the basis for a complete simulation of the optical properties of different layers that form a complete SSC.

3.4. Optical optimization of SSC based on composition and microstructure characterization

The optical characterization of the deposited individual layers for the AR, IR and absorber layer was explained along this section. The optical constants were measured by spectroscopic

ellipsometry (SE) and reflectance spectra by UV-Vis spectrophotometry. The measured reflectance spectra of the individual layers were compared with simulated one, which allow an improvement of the EMA employed for the initial simulations. Based on the microstructural and optical characterization results from the individual layers, a redesign of the complete SSC was performed for each one of the selected a-C:MeC as absorber layer.

3.4.1 Optical characterization and simulation of a-C:MeC absorber layer

Spectroscopic ellipsometry (SE)

The optical constants of a-C:MeC were determined by SE in order to feedback the initial simulation. The measured ellipsometric values (ψ, Δ) of pure carbon sample deposited on silicon can be modelled in different ways. As the properties of the a-C films depend strongly on the sp^2/sp^3 hybrid fraction [24,105], an EMA theory combining sp^2 and sp^3 pure bonded carbon optical constants was employed to determine the optical constants. The excitations of π electrons occurs at lower energy than the σ excitations, therefore sp^3 and sp^2 bonded sites have different optical constants[106]. However, with this EMA approach, no satisfactory results were obtained, due to the lack of good references for the dielectric functions of "pure" sp^2 and sp^3 bonded materials.

In this work, the optical constants of a-C were successfully determined employing only one Tauc-Lorentz (TL) dispersion model [107,108], commonly used to determine dielectric function of amorphous materials (see chapter 2). The ellipsometric measured and modelled values along with the parameters employed for the TL dispersion model are shown in Figure 3.28, and the corresponding optical constants in Figure 3.29 (b).

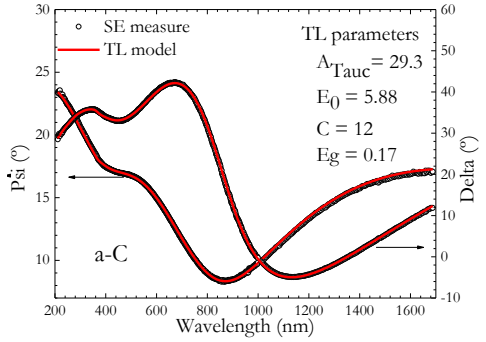

Figure 3.28 – Psi and delta measured and modelled values for the pure carbon sample deposited on silicon substrate. The Tauc Lorentz parameters employed in the model are also icluded in the figure.

In the case of the a-C:MeC samples, in order to merge the metallic behaviour of the MeC with the semi-insulating properties observed for a-C, the fitting of the experimentally SE data includes a combination of Drude [54] and Tauc-Lorentz [72] dispersion models. The separation into contributions from interband transitions and from free-electrons was then analysed.

The complex refraction index of the deposited a-C:MeC samples are represented in Figure 3.31. The three metals selected have similar trend and the main deviations are related to the metal

content. The values of *n* and *k* at λ= 550 and 1500 nm were included in the figure. The real part of the refractive index (*n*) of a-C:VC samples (Figure 3.31 (a)), monotonously increases for both metal contents up to a wavelength ~600 nm. For higher wavelengths, the a-C:VC (h), *n* continues increasing, as expected from the metallic behaviour of the carbides. Meanwhile *n* remains almost constant (*n*~2.3) for the a-C:VC (l) sample. On the other hand, the extinction coefficient (*k*) is substantially different between high and low metal content samples in the whole wavelength range. *k* increases steadily for the a-C:VC(h) since this sample is nearly a pure carbide and follows Drude's free-electron model. On the contrary, for the low metal sample, *k* is close to zero, as expected in dielectric materials. The behaviour of the optical constants in the a-C:ZrC samples (Figure 3.31 (b)), follows the same tendency.

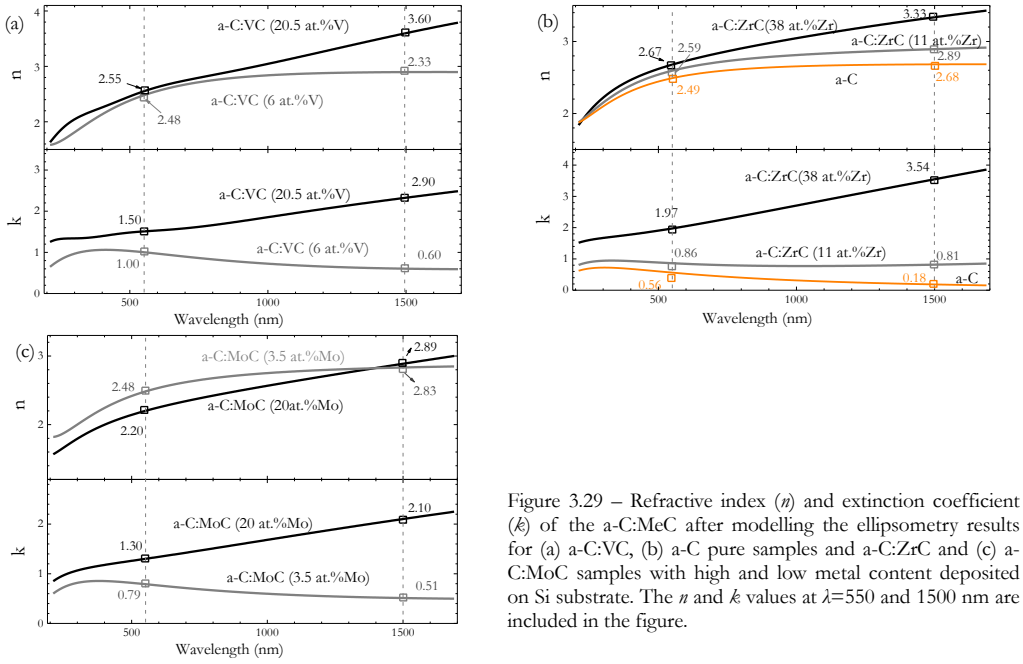

Figure 3.29 – Refractive index (*n*) and extinction coefficient (*k*) of the a-C:MeC after modelling the ellipsometry results for (a) a-C:VC, (b) a-C pure samples and a-C:ZrC and (c) a-C:MoC samples with high and low metal content deposited on Si substrate. The *n* and *k* values at *λ*=550 and 1500 nm are included in the figure.

Contrary to expectations, a-C:MoC(h) has lower *n* than a-C:MoC(l) up to ~1500 nm (Figure 3.29 (c)). This could be assessed to a lower density for the a-C:MoC (h) sample, associated to the nanoparticle morphology observed in the HR-TEM image (Figure 3.25). The extinction coefficient for the a-C:MoC samples shows the same behaviour than for the other two metals.

The analysis of the optical constants shows how the metal content influences in the optical constants modelled for a-C:MeC films. Hence, for an appropriate adjustment of the SE results, Drude's dispersion model must be incorporated together with the Tauc-Lorentz (TL) model employed for pure a-C.

Reflectance spectroscopy of a-CMeC absorber layers and simulation validation.

Reflectance spectra of all deposited samples were measured i) to verify whether the optical constants have been properly calculated and ii) to determine the best EMA model to employ in the case of the a-C:MeC nanocomposites.

The measured reflectance spectra were compared with the simulated ones using the experimental optical constants from Figure 3.29. An appropriate multilayer model (a-C:MeC / SiO_2 / Si) is necessary for an accurate optical simulation (see Figure 2.18). An excellent agreement between simulated and experimental reflectance was obtained. This confirms that the optical constants were correctly calculated.

In order to simulate the optical properties of heterogeneous materials with different volume fractions, it is crucial to find an EMA which accurately describes the combined effect of the nanocomposite components (see chapter 2). Therefore, the measured reflectance spectrum of a selected nanocomposite film, namely a-C:VC (20.5 at.% V), was compared to simulated spectra obtained by using Maxwell-Garnett (MG) [47], Bruggeman (BRU) [48], and Bergman (BER) [49] EMA theories (Figure 3.30). The experimental optical constants of nanocomposite components (a-C matrix and metal carbides) as well as the VF of carbide are required. In this regard, the complete compositional and microstructural analyses performed on the previous sections provide essential information to an accurate simulation of the optical performance of the coatings. Raman analysis confirmed that the nanocomposite matrix was amorphous carbon and its optical constants were estimated from SE. No metallic phases were found in any of the single a-C:MeC layers. Therefore, the MeC was considered to be the particle component of the nanocomposite. The experimental VF according to Table 3.6 was employed for feedback the simulations.

The comparison of simulated and measured spectra reveals that Bergman model properly describes the experimental reflectance of a-C:VC (20.5 at.% V) in the whole wavelength range (Figure 3.30). The differences of the three EMAs are reflected in the solar absorptance (Table 3.10).

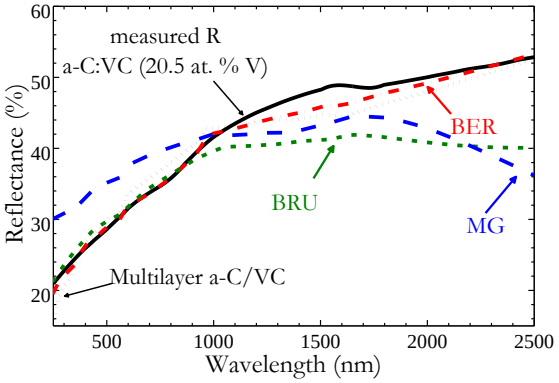

Figure 3.30 - Measured reflectance spectrum of a-C:VC (20.5 at.%), (solid black line) ,simulation obtained for the same composition employing Maxwell-Garnett (MG), Bruggeman (BRU) and Bergman (BER) effective medium approximations with an equivalent 41.3% volume fraction of VC, and simulated reflectance for a 42 layers stack alternating between a-C (5nm) and VC (4nm) nanolayers.

Maxwell-Garnett overestimates the experimental reflectance up to 10% in the visible and underestimates it up to 15% in the near infrared spectral range, giving the largest deviation of the simulated *a* ($\perp a$ = -3.0%) of all the employed EMAs. MG approximation is only applicable to systems with volume fraction below 30% without percolation. The volume fraction of the carbide particles in the a-C:VC (20.5 at.% V) is 41%, hence, a high degree of percolation is expected. This accounts for the strong deviation of MG simulation.

Bruggeman theory is adequate for large particle volume fraction and percolated systems, and it was the one employed in the initial simulations (section 3.2). However, this approach does not properly simulates the experimental reflectance spectra for a-C:VC films (Figure 3.30). This model provided an excellent agreement for the visible range but underestimated the reflectance in the near-infrared range. This results in small deviation of solar absorptance ($\perp a$ = +1.0%), but from deviations in the IR range one could expect misleading thermal emittance values.

Table 3.10: Solar absorptance of deposited a-C:VC (20.5 at.% V) sample compared with the calculated solar absorptance using MG, BRU and BER EMA theories. Results for the the multilayer a-C/VC are also included.

EMA model	Solar absorptance (%)
Maxwell- Garnett (MG)	61.3 ± 0.1
Bruggeman (BRU)	65.3 ± 0.1
Bergman (BER)	63.8 ± 0.1
Multilayer a-C / VC	63.7 ± 0.1
Measured R(λ)	64.3 ± 0.1

As mentioned above, Bergman representation gives the best agreement between the simulated and experimental spectra in the whole wavelength range, with the most accurate value of solar absorptance ($\perp a$ = -0.5%). A tentative explanation for this finding is that this EMA incorporates the shape and degree of percolation of the embedded nanoparticles as additional parameters to the simulation.

In order to clarify whether the multilayer structure of a-C:VC (20.5 at.% V) observed in the HR-TEM images affects the optical film properties, a multilayered structure was also simulated. It is formed of 21 bilayers of pure metal carbide and pure amorphous carbon of 4 and 5 nm thickness, respectively, corresponding to the measured carbide volume fraction (41% VF). No significant differences were observed between the multilayer reflectance simulation (a=63.7%) and BER simulation (a=63.8%) as shown in Table 3.10. This result implies that the film growth mode (self-organized layered structure or dispersed carbide nanoparticles in an a-C matrix) does not affect the optical properties. A similar result has been observed in solar selective coatings based on silicon nitride cermets [109].

Once the appropriateness of the Bergman model to simulate a-C:MeC composites is demonstrated, this EMA was used to simulate reflectance spectra of the rest of nanocomposites. An excellent agreement was obtained for all the studied systems, independently of the metal and the metal carbide content (Figure 3.31(a), (b) and (c)). BER model allows extracting percolation

behaviour according to the metal content in the samples. In the case of nanocomposites with high metal content, the percolation strength (g_0) parameter for a proper fitting was ~1. This is an indication of the interconnection of the embedded carbide particles, pointing to a metallic character of the a-C:MeC(h) films. On the contrary, samples with low metal content exhibit no percolation ($g_0(f)=0$). This is characteristic for a dielectric or insulating behaviour, caused by the missing connection between the carbide particles.

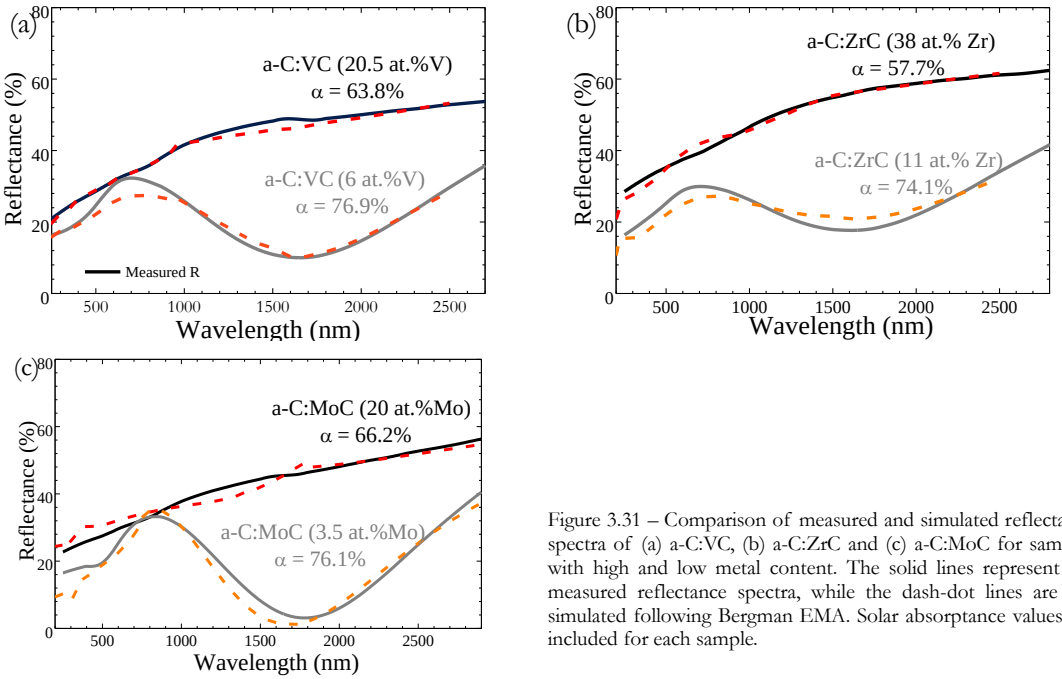

Figure 3.31 – Comparison of measured and simulated reflectance spectra of (a) a-C:VC, (b) a-C:ZrC and (c) a-C:MoC for samples with high and low metal content. The solid lines represent the measured reflectance spectra, while the dash-dot lines are the simulated following Bergman EMA. Solar absorptance values are included for each sample.

On the basis of the BER representation, the *a* was computed as a function of carbide VF and thickness for the a-C:MeC samples on Inconel substrate. As an example, Figure 3.32 shows the *a* dependence on VF and thickness for a-C:VC sample.

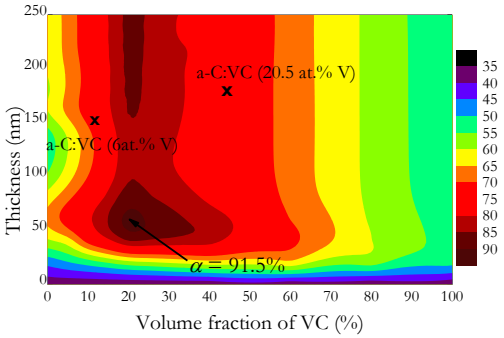

Figure 3.32 – Solar absorptance for different thickness and volume fraction of a- C:VC. The maximum α obtained from simulation, as well as the one obtained experimentally are included in the graph.

The solar absorptance maximum was found in the range of 15 to 40% VF. By variation of the thickness, *a* increases from 36% (absorptance of the inconel substrate) until it reaches a maximum for a thickness of 50 to 70 nm. For thicknesses higher than 150 nm, the absorptance

increases again, reaching a maximum constant value similar to the one in the thinner range. However, increasing the absorber layer thickness can negatively affect to interlayer adherence and/or increase of thermal emittance in a complete solar selective coating.

The maximum α is 91.5 ± 0.5 % for a a-C:VC single layer 62 nm thick a-C:VC single layer with 19 % volume fraction of VC (equivalent to 9.7 at.% of V). In the case of the a-C:ZrC (and a-C:MoC) system, maximum a of 92.0 (90.0) % was found for a film with thickness of 134 (55) nm and 31 (28)% VF of ZrC (MoC).

3.4.2 Optical characterization of IR layers

Optical constants of TiN and ZrN films deposited at 300ºC were modelled employing a Drude dispersion model (Figure 3.33 (a)). The minimum value of k coincides with the plasma wavelength (λ_p) and for both nitrides is located around 400 nm. Above this wavelength, k increases drastically and so does the reflectance. This increase in k is sharper for the TiN, resulting in the highest nitride reflectance, in line with the initial simulations (Figure 3.11).

These experimental optical constants obtained by modelling SE reveal a denser TiN film than the one selected in the initial simulation (section 3.2). Hence, a higher simulated IR reflectance ($R_{IR} \approx 94$ %) was obtained compared with the simulations based on literature data ($R_{IR} \approx 91$ %).

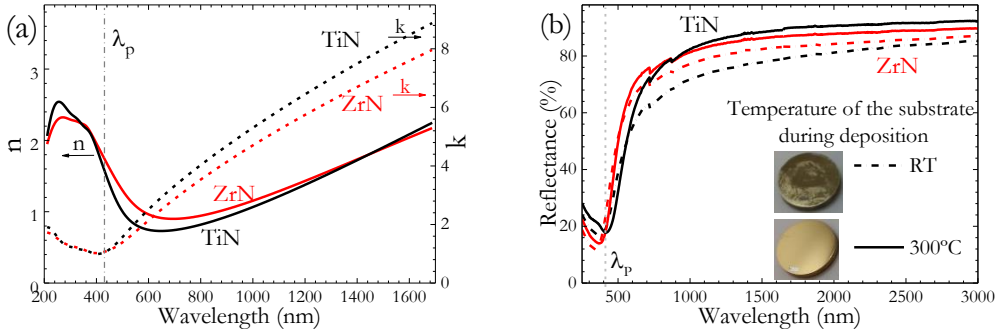

Figure 3.33 – (a) Optical constants determined with data analysis from SE measurements of the 300ºC deposited IR layers TiN and ZrN and (b) measured reflectance spectra of ZrN and TiN. The solid lines represent the samples deposited at RT and the dash-dot line the 300ºC ones. Photographs of TiN samples deposited at RT and at 300ºC are also included.

In Figure 3.33 (b) the experimental reflectances of the IR layers deposited at RT and at 300ºC are represented. As expected from XRD results, samples deposited at higher temperature showed higher R_{IR} ($\Delta R_{RT->300}$ = +2% for ZrN and +5% for the TiN). This improvement is related to the shift of the λ_p to lower values associated to an increase of the concentration of free electrons with bigger crystals [9]. The photographs of TiN samples deposited at the two temperatures are included in Figure 3.33 (b), showing an improvement of the homogeneity, brightness, golden colour and adhesion for the sample deposited at 300ºC.

In summary TiN deposited at 300ºC was selected as the best infrared reflective layer for the complete SSC.

3.4.3 Optical characterization of AR layers

Figure 3.34 (a) shows the modelled optical constants of the dielectric thin films, calculated employing Sellmeier dispersion model, which is shown to be appropriate for transparent materials. The measured wavelength region show transparent behaviour with extinction coefficient k~0, and the Al_2O_3 provided higher refractive index. The measured values are in accordance with the optical constants selected initially for the simulation (Table 3.3), slightly higher in the deposited SiO_2 (measured n_{550nm} = 1.49 compared to 1.44 from the data base), probably due to the different deposition conditions between deposited and reference sample.

The reflectance and transmittance spectra of the deposited AR thin films are represented in Figure 3.34 (b). Both AR layer were transparent in all the UV-Vis-NIR measured range, as expected in stoichiometric amorphous films, without energy loss caused by firm absorption in the Vis-NIR. In general, the transmittance of oxide films would decrease in the UV range if there is oxygen deficiency. This is not observed for both oxide thin films in Figure 3.34 (b). The measured roughness with confocal profilometer indicates a smooth surface with R_q values below 2 nm on Si substrate. This low roughness surface contribute to remove surface light scattering losses, resulting in high transmittance of the films..

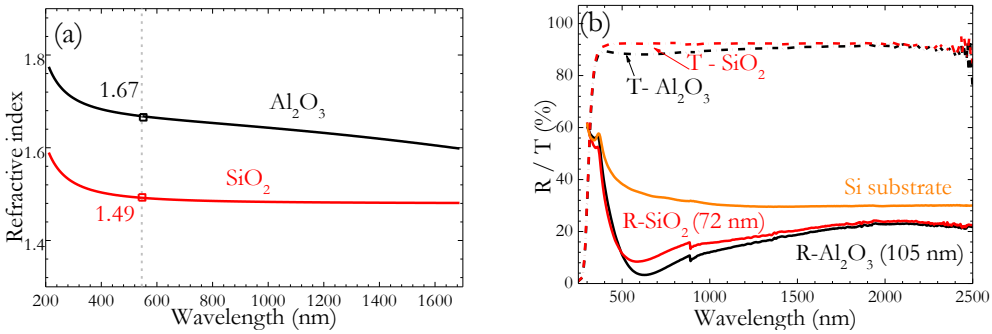

Figure 3.34 – (a) Optical constants determined with data analysis from ellipsometry measurements of the deposited antireflective layers Al_2O_3 and SiO_2. The n values at 550 nm are indicated in the figure. (b) Measured reflectance spectra of Al_2O_3 and SiO_2 deposited on silicon substrate with the measured thickness in brackets and transmittance of Al_2O_3 and SiO_2 deposited on glass substrate. The Si reflectance and glass transmittance spectra are also included.

Alumina and silica are both insulating ceramic material which exhibits excellent chemical inertness, and high optical transparency, and the desired behaviour as effective antireflective layer. Al_2O_3 was selected in this work based on its higher thermal stability (1500 °C) [110,111].

3.4.4 Simulation of the complete stack based on experimental optical constants

Three different complete solar selective coatings where simulated, based in the three a-C:MeC types studied as absorber layers. In the recalculated simulations, the optimized thickness, volume fraction and BER experimental spectral density were employed.

An Al_2O_3 thin film was included above all as AR layer. The analysed TiN films deposited at 300ºC as IR layer was included between the substrate and the absorber layer. Figure 3.35 shows the optimized designed models the three studied carbides. In the optimized complete SSC, the thickness of the AR Al_2O_3 layer varies between 40 to 60 nm according to the thickness and the a-C:MeC selected as absorber layer. The selected thickness of the TiN is independent of the absorber layer, and as analysed in Figure 3.11 (b), it should be higher than 150 nm to an efficient effect as IR layer. Higher thickness would help the effect as thermal barrier coating due to its high stable at high temperatures and avoid possible diffusion of the substrate. However, it should not exceed ~1μm due to residual in FVCA deposited nitrides increases with thickness [112]. Hence, 400 nm was the thickness selected for the TiN in all the multilayer stacks.

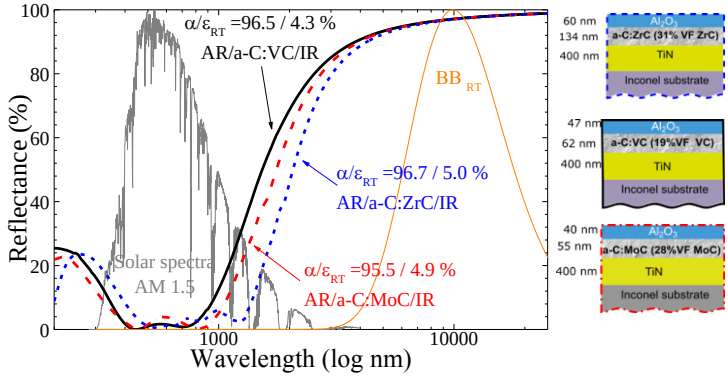

Figure 3.35 - Simulated reflectance spectra of a complete SSC with the optimized a-C:ZrC, a-C:VC and a-C:MoC as absorber layer.

The optimized VF obtained in the simulation has to be converted into metal atomic percentage. This inverse calculation gives a resulted metal content for the optimized absorber layers of 10 at.% of V (a-C:VC with 19% VF of VC), 12 at% of Zr (a-C:ZrC with 31% VF of ZrC) and 14 at.% of Mo for the a-C:MoC with 28% VF of MoC. In all the nanocomposite types, the desired composition has intermediate values between the high and low metal content deposited for the individual layers. This metal content can be obtained with a modulation in the intensity ration between the metal and carbon arc sources.

The best re-simulated complete solar selective coatings provided a selectivity ratio $a/\mathcal{E}_{RT}$ = 96.7/5. When the temperature increases to 600ºC, the emittance worsen to 14.0, 13.5 and 15.8 % for the simulated multilayer stack with a-C:VC, a-C:ZrC and a-C:MoC as absorber layer respectively. The thermal emittance obtained in the simulation with real values is better than the initial calculate, due to as mentioned in the optical characterization of the IR layers, the deposited

nitrides are denser and show higher reflectance in the IR region, and therefore a lower thermal emittance. Those values are significantly better than the values reported for this class of materials so far, which were an a = 91.0% with ε = 11% at 100ºC for an a-C:TiC/SiO_2 stack on Cu substrate [49,50].

3.5. Deposition, characterization and durability test of complete SSC

A first attempt to deposit a complete selective coating by PFCVA was done, based on the excellent results obtained with the improved simulations feedback with the outcomes of the individual layers characterization. a-C:ZrC was selected as absorber layer, as it showed the best simulation performance (Figure 3.35). The deposition parameters employed for each layer are the same than explained for the individual layers in section 3.3.1. The thickness and volume fractions of the individual layers were not optimized in this first approach as the aim of this deposition is the validation of the goodness of fit of the CODE optical simulations.

The HR-TEM cross section image of the complete SSC deposited is represented in Figure 3.36, and the thicknesses of each layer were determined directly from the image. An enlargement of the a-C:ZrC absorber layer is shown in Figure 3.36 (b), where the self-organized multilayer structure was appreciated, as observed for the individual a-C:ZrC (Figure 3.24).

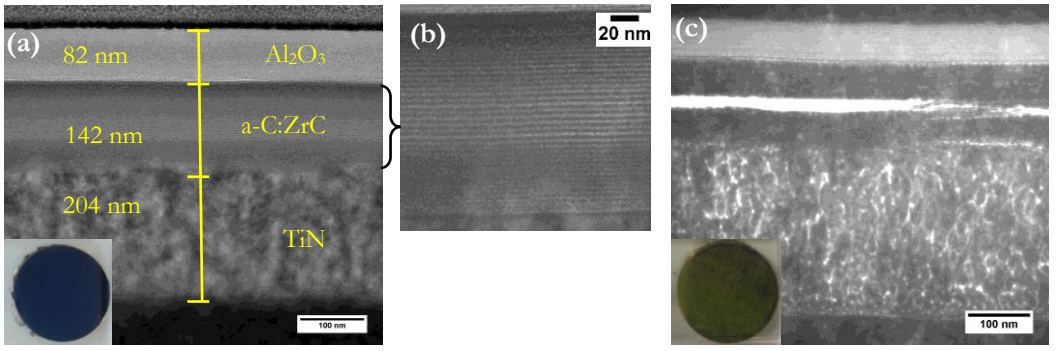

Figure 3.36 - HR-TEM image of the complete SSC deposited multilayer stack. (a) Overview image of the stack with the measured thickness of each one of the individual layers and (b) amplified image of a-C:ZrC absorber layer. (c) HR-TEM images of the same multilayer after heating up to 600ºC 2h. Photographs of the SSC before and after heating are included.

EDX qualitative analysis was carried out in the STEM mode to determine the composition of the different layers along the cross section of the sample. The results indicated in Table 3.11, show reasonable good agreement with the composition analysis performed before. However, oxygen content of ~4 at% was detected in the a-C:ZrC absorber layer. A content of ~10at.% of carbon was observed in both AR and IR layers, not quantified in the composition analysis for the individual layers.

Table 3.11 - EDX elementary composition analysis of the as deposited TiN / a-C: ZrC / Al_2O_3 multilayer coating PFCVA deposited on inconel substrate.

Layer	Al (at.%)	O (at.%)	C (at.%)	Zr (at.%)	Ti (at.%)	N (at.%)
Al_2O_3	44.1	45.7	10.2	-	-	-
a-C:ZrC	-	4.1	68.7	22.1	-	-
TiN	-	-	9.0	-	53.2	37.8-

The measured reflectance spectrum of the multilayer stack is shown in Figure 3.37. A comparison between measured and simulated reflectance spectra was performed, employing the SE optical constants of each one of the single layers that compose the stack, and the thickness from the HR-TEM image. The SE measured range was limited to a 1900 nm maximum wavelength, so simulations based on measured optical constants were only simulated up to this range. The simulated spectrum for λ>1900nm was extrapolated by CODE. The simulated and measured spectra show an excellent fitting in the entire measured wavelength (200 to 2500 nm). Solar absorptance is slightly overestimated (1.5%), due to discrepancy in the visible range. A possible explanation is the increase in the surface roughness of the Al_2O_3 when deposited over the rest of the layers, reducing the antireflective effect when is perfectly smooth.

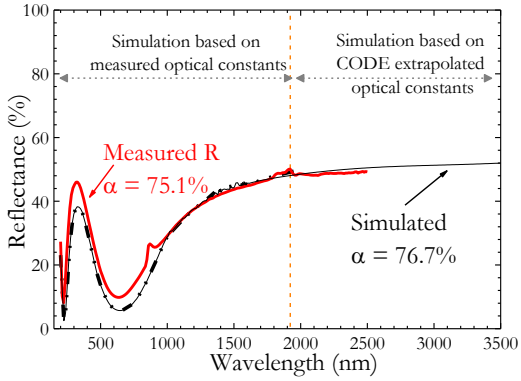

Figure 3.37 - Comparison between measured and simulated reflectance spectra, employing HR-TEM measured thickness and the optical constants experimentally determined for each one of the individual materials. For wavelength higher than 1900 nm, the simulations were done with extrapolated optical constants. Solar absorptance values are included in the figure.

Although the deposition parameters of the complete SSC were not optimized yet, a durability test was performed to test its air stability before continuing with the optimization of the deposition parameters. The complete stack was heated up to 600ºC in air for 2 hours. Figure 3.36 shows the HR-TEM cross section images of the coatings before and after 2 hours of thermal treatment. Figure 3.36 (a) and (c) shows how in the a-C:ZrC absorber layer a crack was developed after the heating test. The failure was directly detected after the durability test with a visual inspection. As observed in the inserted photographs before and after the test, the colour of the sample shifts from a homogeneous dark blue, expected for a solar absorber material, to a non-uniform yellow-brown appearance.

The elementary composition was analysed with EDX-HAADF detector in different points of the cross section of the heated sample, with the STEM mode. Figure 3.38 (a) shows the STEM image of the heated sample, with numbered points associated to the composition values presented in Table 3.12 The number of counts for each element along the cross section is represented in Figure 3.38 (b), with the points indicated from Table 3.12 as well.

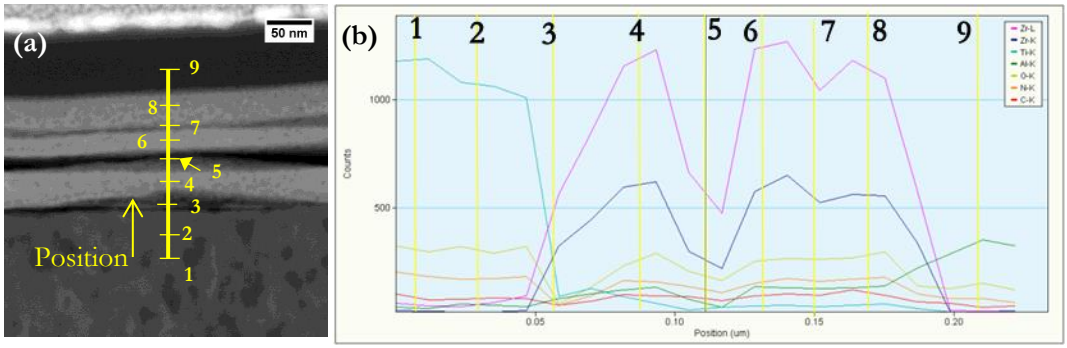

Figure 3.38 – (a) STEM image of complete absorber layer after heating up to 600ºC 2h. (b) EDX counter for the different elements analysed. The points are related to the EDX analysis, which values are shown in Table 3.12.

In STEM mode, the contrast in the image depends on the atomic number (Z-contrast), thus facilitating the detection of light elements. Between the TiN and the a-Z:ZrC layer, a dark region appears, not noticed before. In the IR layer (point 1), the nitrogen content was mostly replaced by oxygen, and there is a delamination observed between the absorber and the IR layer. This incorporation of the oxygen did not come from the diffusion of the substrate due to the N content is higher in point 1 than in point 2. Presumably the O comes from the crack of the absorber layer. The AR layer (point 9), did not show significance differences in the content after heating 600ºC, as its expected good oxidation stability in air.

Table 3.12 - EDX elementary composition analysis of the TiN / a-C: ZrC / Al_2O_3 coating deposited on inconel substrate after heating in air during 2 hours at 600ºC. The position of the points was indicated in Figure 3.38.

Point	Description	Al (at.%)	O (at.%)	C (at.%)	Zr (at.%)	Ti (at.%)	N (at.%)
(1)	TiN layer	-	45.1	-	-	44.4	10.5
(2)	TiN close to a-C:ZrC	-	53.2	-	>0.1	46.8	0
(3)	a-C:ZrC close to TiN	-	49.1	0	0.2	41.9	8.8
(4)	a-C:ZrC	-	12.9	0	78.0	9.1	0
(5)	a-C:ZrC in the crack	-	65.41	0	34.6	0	0
(6)	a-C:ZrC above crack	-	44.4	3.0	52.4	0	0.5
(7)	a-C:ZrC upper crack	-	42.2	0	57.8	0	0
(8)	a-C:ZrC	-	45.8	2.6	51.5	0	0
(9)	Al_2O_3 layer	50.6	49.4	-	-	-	-

However, the absorber layer was divided into different sub-layers, with cracks or breaks in the middle, represented by points 3 to 8 Figure 3.38 (a). In point 3, the part of the absorber layer situated closest to the TiN layer, some diffusion of Ti was observed. While the carbon content was ~69 at % before heating, after 2 hours in air at 600ºC it was replaced by oxygen. Only in the top region without cracks in the a-C:ZrC layer (point 6 and 8), a content of ~3 at% of C can be detected, but almost nothing in the rest of the absorber layer.

Different assumptions were made to explain this break in the absorber layer: i) the crack could result from the elevated stresses of the coating after heating, as has been shown previously in thin films deposited with tis cathodic arc technique [113] ii) the oxygen diffused thorough the AR layer by the porosities. This second reason was not considered due to no oxygen content is

observed in the break. In effect, there was almost no presence of any element in the break. Besides, the oxygen content was drastically increased in the a-C:ZrC layer, achieving ~65 at % O on the broken part (point 5). This oxidation in the carbon – zirconium layer was a sign of the lack of stability of the absorber coating at high temperature.

3.6. Conclusions of solar selective coatings based on a-C:MeC as absorber layer.

Solar selective surfaces have been designed based on carbon transition metal carbide absorber layers. Filtered cathodic arc was used for depositing a-C:MeC films. The main conclusions obtained after the comprehensive characterization are described below.

Optical simulations based on literature data

The initial optical simulations with CODE with materials optical constants from literature database provide a good basis for the selection of the materials to employ for each layer type. The a-C optical constants reported in the literature exhibit wide variations depending mainly on the deposition technique employed, the deposition parameters and the sp^3-C hybrid bonding fraction. The same applies for the metal carbides, whose optical constants depend to a great extent on their stoichiometry and crystal phase formed.

Bruggeman EMA theory was initially employed to simulate the optical constants of the heterogeneous nanocomposite materials, due to the lack of microstructural information. The volume fraction and the thickness of a-C:MeC samples were varied. VC, ZrC and MoC refractory interstitial carbides were selected as the best candidates for solar absorber layer. As AR layer, SiO_2 and Al_2O_3 materials fulfil the double objective required of reducing the solar light reflection in the visible wavelength range and being stable at high temperatures. The reflectance spectra of different interstitial nitrides were simulated to decide the best candidates as IR reflective layer. TiN and ZrN, with thickness higher than 150 nm, exhibit the best performance, obtaining a theoretical thermal emittances below 8% at room temperature.

The thicknesses and volume fractions of the different layers of the complete solar selective stack were optimized in order to maximize the solar absorptance (a) and minimize the thermal emittance (ε). Very promising results were obtained with a proper selection of materials in the initial simulation, obtaining promising values of a = 94.9 % and ε_{RT} = 12.5 for a stack composed by Al_2O_3 (60nm)/ a-C:VC (107nm and 37%VF of VC)/TiN(400nm).

Optimization of the individual layers of the SSC based on a-C:MeC

Pulsed filtered cathodic arc was successfully used for depositing each one of the different layers that form the complete multilayer stack, based on the candidates selected before. A thoughtful analysis of the deposited samples was carried out. The composition of the absorber layers were determined accurately by RBS and NRA. XRD and Raman techniques confirmed the formation of nanocomposites structures of metal carbides particles embedded in an amorphous carbon matrix for samples deposited with higher metal content. In the case of a-C:VC films, a spontaneous arrangement of composite multilayers was found with HR-TEM images. XRD analysis proved that the nitrides employed for IR layer must be deposited at high temperature (300ºC) in order to obtain and homogeneous, smooth, dense and high-reflective IR film. Al_2O_3 film was selected as AR layer according to higher stability criteria and good agreement between the previous simulated results.

Spectroscopic ellipsometry were performed in all layers to determine the real optical constants. The modelled optical constants were validated with spectrophotometry measurements. Reflectance spectra were simulated employing different EMA models using experimentally measured optical constants for a-C. An excellent agreement between simulated and measured reflectance for single a-C:MeC layers was only achieved in the whole wavelength range using a Bergman approach that requires a detailed microstructural analysis.

Optimization of the complete SSC

The simulation of a complete solar selective surface and antireflective and IR mirror layers leads to a solar absorptance higher than 96% with a thermal emittance at room temperature below 5% and 14% at 600ºC. This demonstrates the potential of a-C:MeC as an absorber layer material for high-temperature applications.

Based on the improved simulated results after the feedback with the outcomes of the individual layers characterization, a complete coating with Al_2O_3 / a-C:ZrC (38at.% Zr) / TiN was deposited. The multilayer stack was submitted to an asymmetric thermal test, showing no stability after 2 hours in air at 600ºC.

3.7. References

[1] G.L. Harding, Absorptance and emittance of metal carbide selective surfaces sputter deposited onto glass tubes, Sol. Energy Mater. 2 (1980) 469–481.

[2] A. Earnshaw, N. Greenwood, Chemistry of the Elements, Second Edition, Butterworth-Heinemann, 1997.

[3] H.O. Pierson, Handbook of refractory carbides and nitrides: properties, characteristics, processing, and applications, Noyes Publications, Westwood,New Yersey USA, 1996.

[4] U. Jansson, E. Lewin, Sputter deposition of transition-metal carbide films - A critical review from a chemical perspective, Thin Solid Films. 536 (2013) 1–24.

[5] G. Hägg, Hägg's rules, Zeitschrift Fur Phys. Chemie. 12B (1931) 33.

[6] P. Pyykkö, M. Atsumi, Molecular single-bond covalent radii for elements 1-118., Chem. - A Eur. J. 15 (2008) 186.

[7] K. Schwarz, Band structure and chemical bonding in transition metal carbides and nitrides, Crit. Rev. Solid State Mater. Sci. 13 (1987) 211.

[8] R. Chang, Low-Temperature Elastic Properties of ZrC and TiC, J. Appl. Phys. 37 (1966) 3778.

[9] M. Fox, Optical Properties of Solids, Oxford Mas, Oxford Unversity Press, Oxford, 2001.

[10] K.G.M. Tripathi, C. C. Kumar, M. Kumar, D. Avasthi, D. K. Nair, Low temperature deposition of ultrathin molybdenum carbide films and microstructural characterization, Mater. Sci. Technol. 26 (2010) 5.

[11] D.R. Lide, Handbook of Chemistry and Physics, 87th ed., Boca Raton, FL: CRC Press, Florida, 1998.

[12] J. Lu, H. Hugosson, O. Eriksson, L. Nordström, U. Jansson, Chemical vapour deposition of molybdenum carbides: aspects of phase stability, Thin Solid Films. 370 (2000) 203–212.

[13] J. Robertson, Diamond-like amorphous carbon, Mater. Sci. Eng. R Reports. 37 (2002) 129–281.

[14] A.R. Oganov, R.J. Hemley, R.M. Hazen, A.P. Jones, Structure, Bonding, and Mineralogy of Carbon at Extreme Conditions, Rev. Mineral. Geochemistry. 75 (2013) 47–77.

[15] D.F. Edwards, Cubic Carbon (Diamond), in: E.D. Palik (Ed.), Handb. Opt. Constants Solids, Academic, Boston, 1991: p. 665.

[16] M.W. Williams, Optical properties of glassy carbon from 0 to 82 eV, J. Appl. Phys. 43 (1972) 3460.

[17] J. Lee, R.W. Collins, V.S. Veerasamy, J. Robertson, Analysis of the ellipsometric spectra of amorphous carbon thin films for evaluation of the sp3-bonded carbon content, Diam. Relat. Mater. 7 (1998) 999–1009.

[18] A. Borguesi, G. Guizzetti, Graphite (C), in: E.D. Palik (Ed.), Handb. Opt. Constants Solids, Academic, Boston, 1991: p. 449.

[19] V.S. Veerasamy, G.A.J. Amaratunga, W.I. Milne, P. Hewit, P.J. Fallon, D.R. McKenzie, et al., Optical and electronic properties of amorphous diamond, Diamon. 2 (1993) 782–787.

[20] R.H. Jarman, G.J. Ray, Direct determination of carbon hybridization in amorphous carbon films using 13C n.m.r. spectroscopy, J. Chem. Soc. Chem. Commun. (1985) 1153.

[21] M. Vinnichenko, R. Gago, N. Huang, Y.X. Leng, H. Sun, U. Kreissig, et al., Spectroscopic ellipsometry investigation of amorphous carbon films with different sp3 content: relation with protein adsorption, Thin Solid Films. 455-456 (2004) 530–534.

[22] A. Ferrari, J. Robertson, Interpretation of Raman spectra of disordered and amorphous carbon, Phys. Rev. B. 61 (2000) 14095–14107. doi:10.1103/PhysRevB.61.14095.

[23] S. Logothetidis, M. Gioti, P. Patsalas, C. Charitidis, Insights on the deposition mechanism of sputtered amorphous carbon films, Carbon N. Y. 37 (1999) 765–769.

[24] S. Logothetidis, Optical and electronic properties of amorphous carbon materials, Diam. Relat. Mater. 12 (2003) 141–150.

[25] J.X. Guo, B.K. Tay, X.W. Sun, X.Z. Ding, D.H.C. Chua, Influence of substrate bias on the mechanical properties of ta-C:Co films prepared by filtered cathodic vacuum arc technique, Surf. Coatings Technol. 169-170 (2003) 393–396.

[26] M. Krause, A. Mücklich, C. Wilde, M. Vinnichenko, S. Gemming, G. Abrasonis, Structure , Optical and Mechanical Properties of Direct Current Magnetron Sputtered Carbon: Vanadium Nanocomposite Thin Films, Nanosci. Nanotechnol. Lett. 5 (2013) 94–100.

[27] A.A. Voevodin, J.S. Zabinski, Superhard, functionally gradient, nanolayered and nanocomposite diamond-like carbon coatings for wear protection, Diam. Relat. Mater. 7 (1998) 463–467.

[28] M. Berndt, G. Abrasonis, G.J. Kovács, M. Krause, F. Munnik, R. Heller, et al., Bulk diffusion induced structural modifications of carbon-transition metal nanocomposite films, J. Appl. Phys. 109 (2011) 063503–11.

[29] G. Abrasonis, T.W.H. Oates, G.J. Kovács, J. Grenzer, P.O.A. Persson, K.-H.H. Heinig, et al., Nanoscale precipitation patterns in carbon–nickel nanocomposite thin films: Period and tilt control via ion energy and deposition angle, J. Appl. Phys. 108 (2010) 043503.

[30] K. Sedláčková, P. Lobotka, I. Vávra, G. Radnóczi, Structural, electrical and magnetic properties of carbon–nickel composite thin films, Carbon N. Y. 43 (2005) 2192–2198.

[31] G.J. Kovács, G. Sáfrán, O. Geszti, T. Ujvári, I. Bertóti, G. Radnóczi, Structure and mechanical properties of carbon–nickel and CNx–nickel nanocomposite films, Surf. Coatings Technol. 180 (2004) 331–334.

[32] G. Abrasonis, A.C. Scheinost, S. Zhou, R. Torres, R. Gago, I. Jiménez, et al., X-ray Spectroscopic and Magnetic Investigation of C:Ni Nanocomposite Films Grown by Ion Beam Cosputtering, J. Phys. Chem. C. 112 (2008) 12628–12637. d

[33] K. Sedláčková, T. Ujvári, R. Grasin, P. Lobotka, I. Bertóti, G. Radnóczi, C–Ti nanocomposite thin films: Structure, mechanical and electrical properties, Vacuum. 82 (2007) 214–216.

[34] E. Lewin, O. Wilhelmsson, U. Jansson, Nanocomposite nc-TiC/a-C thin films for electrical contact applications, J. Appl. Phys. 100 (2006) 054303.

[35] L.L. Wang, R.Y. Wang, S.J. Yan, R. Zhang, B. Yang, Z.D. Zhang, et al., Structure and properties of Mo-containing diamond-like carbon films produced by ion source assisted cathodic arc ion-plating, Appl. Surf. Sci. 286 (2013) 109–114. d

[36] C.Q. Chen, Y.T. Pei, K.P. Shaha, J.T.M. De Hosson, Tunable self-organization of nanocomposite multilayers, Appl. Phys. Lett. 96 (2010) 073103..

[37] C. Corbella, E. Bertran, M.C. Polo, E. Pascual, J.L. Andújar, Structural effects of nanocomposite films of amorphous carbon and metal deposited by pulsed-DC reactive magnetron sputtering, Diam. Relat. Mater. 16 (2007) 1828–1834.

[38] I. Gerhards, H. Stillrich, C. Ronning, H. Hofsäss, M. Seibt, Self-organized nanoscale multilayer growth in hyperthermal ion deposition, Phys. Rev. B. 70 (2004) 245418. doi:10.1103/PhysRevB.70.245418.

[39] G. Abrasonis, G.J. Kovács, M.D. Tucker, R. Heller, M. Krause, M.C. Guenette, et al., Sculpting nanoscale precipitation patterns in nanocomposite thin films via hyperthermal ion deposition, Appl. Phys. Lett. 97 (2010) 163108. d.

[40] W.-Y. Wu, J.-M. Ting, Self-assembled alternating nano-scaled layers of carbon and metal, Chem. Phys. Lett. 388 (2004) 312–315.

[41] S. Anders, D.L. Callahan, G.M. Pharr, T.Y. Tsui, C. Singh Bhatia, Multilayers of amorphous carbon prepared by cathodic arc deposition, Surf. Coatings Technol. 94 (1997) 189–194.

[42] P.E. Hovsepian, Y.N. Kok, A.P. Ehiasarian, R. Haasch, J.-G. Wen, I. Petrov, Phase separation and formation of the self-organised layered nanostructure in C/Cr coatings in conditions of high ion irradiation, Surf. Coatings Technol. 200 (2005) 1572–1579..

[43] G.L. Harding, Sputtered metal carbide solar-selective absorbing surfaces, J. Vac. Sci. Technol. 13 (1976) 1070.

[44] G.L. Harding, Magnetron-sputtered metal carbide solar selective absorbing surfaces, J. Vac. Sci. Technol. 16 (1979) 857. d

[45] G.L. Harding, B. Window, Graded metal carbide solar selective surfaces coated onto glass tubes by a magnetron sputtering system, J. Vac. Sci. Technol. 16 (1979) 2101. d

[46] R. Gampp, P. Gantenbein, Y. Kuster, P. Reimann, R. Steiner, P. Oelhafen, et al., Characterization of a-C:H/W and a-C:H/Cr solar selective absorber coatings, in: SPIE Opt. Mater. Technol. Energy Effic. Sol. Energy Convers., Freiburg, Germany, 1994: pp. 92–106.

[47] R. Gampp, P. Gantenbein, Preparation and characterization of chromium containing amorphous hydrogenated carbon films (a-C:H/Cr), in: Film Synth. Growth Using Energ. Beams, Materias research Society, 1995: pp. 305–310.

[48] R. Gampp, P. Oelhafen, P. Gantenbein, S. Brunold, U. Frei, Accelerated aging tests of chromium containing amorphous hydrogenated carbon coatings for solar collectors, Sol. Energy Mater. Sol. Cells. 54 (1998) 369–377.

[49] A. Schüler, I.R. Videnovic, P. Oelhafen, S. Brunold, Titanium-containing amorphous hydrogenated silicon carbon films (a-Si:C:H/Ti) for durable solar absorber coatings, Sol. Energy Mater. Sol. Cells. 69 (2001) 271–284.

[50] D.P. Gruber, G. Engel, H. Sormann, A. Schüler, W. Papousek, Modeling the absorption behavior of solar thermal collector coatings utilizing graded alpha-C:H/TiC layers., Appl. Opt. 48 (2009) 1514–9.

[51] T. Koide, T. Shidara, H. Fukutani, A. Fujimori, T. Miyahara, H. Kato, et al., Optical study of the stoichiometry-dependent electronic structure of TiCx, VCx, and NbCx, Phys. Rev. B. 42 (1990) 4979–4995.

[52] T. Koide, T. Shidara, H. Fukutani, A. Fujimori, S. Otani, Y. Ishizawa, Optical Constants of TiC 0.95 , VC 0.86 and NbC 0.93 from 0.8 to 80 eV, Jpn. J. Appl. Phys. 32 (1993) 1130–1134.

[53] C. Allison, F. Modine, R. French, Optical and electrical properties of niobium carbide, Phys. Rev. B. 35 (1987) 2573–2582.

[54] F. Modine, T. Haywood, C. Allison, Optical and electrical properties of single-crystalline zirconium carbide, Phys. Rev. B. 32 (1985) 7743–7747.

[55] F. Modine, M. Foegelle, C. Finch, C. Allison, Electrical properties of transition-metal carbides of group IV, Phys. Rev. B. 40 (1989) 9558–9564.

[56] G. De Temmerman, M. Ley, J. Boudaden, P. Oelhafen, Study of optical properties of MoxC1−x films, J. Nucl. Mater. 337-339 (2005) 956–959.

[57] F. Modine, R. Major, T. Haywood, G. Gruzalski, D. Smith, Optical properties of tantalum carbide from the infrared to the near ultraviolet, Phys. Rev. B. 29 (1984) 836–841.

[58] M.D. Abad, J.C. Sánchez-López, N. Cusnir, R. Sanjines, WC/a-C nanocomposite thin films: Optical and electrical properties, J. Appl. Phys. 105 (2009) 033510.

[59] W. Theiss, CODE Manual. Optical Spectrum Simulation, (2007). http://www.wtheiss.com/.

[60] Y. Claesson, M. Georgson, A. Roos, C.-G. Ribbing, Optical characterisation of titanium-nitride-based solar control coatings, Sol. Energy Mater. 20 (1990) 455–465.

[61] C.-G. Ribbing, A. Roos, Transition metal nitride films for optical applications, in: R.L. Hall (Ed.), Soc. Photo-Optical Instrum. Eng., Spie. Int. Societiy optical engineering, San Diego, CA, 1997: pp. 148–162.

[62] E.D. Palik, Handbook of Optical Constants of Solids, Academic Press, 1998.

[63] M. Strømme, R. Karmhag, C.G. Ribbing, Optical constants of sputtered hafnium nitride films. Intra- and interband contributions, Opt. Mater. (Amst). 4 (1995) 629–639.

[64] L. Gao, J. Gstöttner, R. Emling, M. Balden, C. Linsmeier, a. Wiltner, et al., Thermal stability of titanium nitride diffusion barrier films for advanced silver interconnects, Microelectron. Eng. 76 (2004) 76–81.

[65] L. Hultman, Thermal stability of nitride thin films, Vacuum. 57 (2000) 1–30.

[66] D.S. Rickerby, A.M. Jones, A.J. Perry, Structure of Titanium Nitride coatings deposited by physical vapour deposition: A unified structure model, Surf. Coatings Technol. 36 (1988) 631–646.

[67] A.J. Perry, M. Georgson, W.D. Sproul, Variations in the reflectance of TiN, ZrN and HfN, Thin Solid Films. 157 (1988) 255–265.

[68] M. Ali, E. Hamzah, M.R. Toff, Friction coefficient and surface roughness of TiN-coated HSS deposited using cathodic arc evaporation PVD technique, Ind. Lubr. Tribol. 60 (2008) 121–130.

[69] S. Niyomsoan, W. Grant, D.L. Olson, B. Mishra, Variation of color in titanium and zirconium nitride decorative thin films, Thin Solid Films. 415 (2002) 187–194.

[70] V. Madhavi, P. Kondaiah, O.M. Hussain, S. Uthanna, Structural, Optical, and Luminescence Properties of Reactive Magnetron Sputtered Tungsten Oxide Thin Films, ISRN Opt. 2012 (2012) 1–8.

[71] S. Venkataraj, O. Kappertz, H. Weis, R. Drese, R. Jayavel, M. Wuttig, Structural and optical properties of thin zirconium oxide films prepared by reactive direct current magnetron sputtering, J. Appl. Phys. 92 (2002) 3599.

[72] G.E. Jellison, Optical functions of GaAs, GaP, and Ge determined by two-channel polarization modulation ellipsometry, Opt. Mater. (Amst). 1 (1992) 151–160.

[73] J. Musil, J. Blažek, P. Zeman, Š. Prokšová, M. Šašek, R. Čerstvý, Thermal stability of alumina thin films containing γ-Al2O3 phase prepared by reactive magnetron sputtering, Appl. Surf. Sci. 257 (2010) 1058–1062.

[74] Q.-C. Zhang, Optimizing analysis of W-AlN cermet solar absorbing coatings, J. Phys. D. Appl. Phys. 34 (2001) 3113–3120.

[75] B.K. Tay, Z.W. Zhao, C.Q. Sun, Effects of substrate bias and growth temperature on properties of aluminium oxide thin films by using filtered cathodic vacuum arc, Surf. Coatings Technol. 198 (2005) 94–97.

[76] L. Csedreki, I. Uzonyi, G.Á. Szíki, Z. Szikszai, G. Gyürky, Á.Z. Kiss, Measurements and assessment of 12C(d,pγ)13C reaction cross sections in the deuteron energy range 740–2000keV for analytical applications, Nucl. Instruments Methods Phys. Res. Sect. B Beam Interact. with Mater. Atoms. 328 (2014) 59–64.

[77] J.R. Tesmer, M. Nastasi, Handbool of modern ion beam materials analysis, Materials Research Society, Pittsburg, Pennsylvania, 1995.

[78] D.R. Lide, Handbook of Chemistry and Physics, 90th ed., CRC, Florida, 2010.

[79] H. Nowotny, E. Parthé, R. Kieffer, F. Benesovsky, Das Dreistoffsystem: Molybdän—Silizium—Kohlenstoff, Phys. Anorg. Und Anal. Chemie. 65 (1954) 255.

[80] B.D. Cullity, S.R. Stock, Elements of X-ray diffraction, Prentice-Hall, 2001.

[81] ICDD Powder Diffraction Data, ICDD Powder Diffraction Data files: 03-065-7885 for fcc VC, 00-008-0384 for hex-MoC , 00-015-0457 for hcp Mo2C, (n.d.).

[82] E. Portolan, C.L.G. Amorim, G.V. Soares, C. Aguzzoli, C.A. Perottoni, I.J.R. Baumvol, et al., Carbon occupancy of interstitial sites in vanadium carbide films deposited by direct current reactive magnetron sputtering, Thin Solid Films. 517 (2009) 6493–6496.

[83] C. Adelhelm, M. Balden, M. Rasinski, S. Lindig, T. Plocinski, E. Welter, et al., Investigation of metal distribution and carbide crystallite formation in metal-doped carbon films (a-C:Me, Me = Ti, V, Zr, W) with low metal content, Surf. Coatings Technol. 205 (2011) 4335–4342.

[84] S. Wei, H.Z. Hua, X. Xiang, Thermodynamic Analysis and Growth of Zirconium Carbide by Chemical Vapor Deposition, Phys. Procedia. 46 (2013) 88–101.

[85] H.W. Hugosson, Theoretical studies of phase stabilities and electronic structure in molybdenum carbide, Uppsala University, 1999.

[86] T. Massalski, Binary alloy phase diagrams, ASM International, Materials Park Ohio, 1990.

[87] G. Abrasonis, M. Berndt, M. Krause, K. Kuepper, F. Munnik, A. Kolitsch, et al., Soft X-ray Absorption and Emission Spectroscopic Investigation of Carbon and Carbon:Transition Metal Composite Films, J. Phys. Chem. C. 112 (2008) 17161–17170.

[88] F. Tuinstra, J.L. Koenig, Raman Spectrum of Graphite, J. Chem. Phys. 53 (1970) 1126.

[89] A.C. Ferrari, J. Robertson, Raman spectroscopy of amorphous, nanostructured, diamond-like carbon, and nanodiamond., Philos. Trans. A. Math. Phys. Eng. Sci. 362 (2004) 2477–512..

[90] G. Abrasonis, M. Krause, A. Mücklich, K. Sedlac˘ková, G. Radnóczi, U. Kreissig, et al., Growth regimes and metal enhanced 6-fold ring clustering of carbon in carbon–nickel composite thin films, Carbon N. Y. 45 (2007) 2995–3006.

[91] N.A. Marks, D.R. McKenzie, B.A. Pailthorpe, M. Bernasconi, M. Parrinello, Ab initio simulations of tetrahedral amorphous carbon, Phys. Rev. B. 54 (1996) 9703–9714.

[92] R. Gago, M. Vinnichenko, H. Jäger, A. Belov, I. Jiménez, N. Huang, et al., Evolution of sp2 networks with substrate temperature in amorphous carbon films: Experiment and theory, Phys. Rev. B. 72 (2005) 014120.

[93] C. Adelhelm, M. Balden, M. Rinke, M. Stueber, Influence of doping (Ti, V, Zr, W) and annealing on the sp carbon structure of amorphous carbon films, J. Appl. Phys. 105 (2009) 033522.

[94] M. Chhowalla, A.C. Ferrari, J. Robertson, G.A.J. Amaratunga, Evolution of sp2 bonding with deposition temperature in tetrahedral amorphous carbon studied by Raman spectroscopy, Appl. Phys. Lett. 76 (2000) 1419.

[95] M. Berndt, M. Krause, G. Abrasonis, A. Mücklich, F. Munnik, A. Kolitsch, et al., Morphology and Structure of C:Co, C:V, and C:Cu Nanocomposite Films, Plasma Process. Polym. 6 (2009) S902–S906.

[96] M. Berndt, Phase separation in carbon : transition metal nanocomposite thin films, Universitat Dresden, 2009.

[97] M. Krause, M. Buljan, M. Arndt, M. Wolfhard, M. Fritzsche, S. Facsko, et al., Compositionally modulated ripples during composite film growth : Three-dimensional pattern formation at the nanoscale, Phys. Rev. B. 89 (2014) 085418.

[98] G. Abadias, Stress and preferred orientation in nitride-based PVD coatings, Surf. Coatings Technol. 202 (2008) 2223–2235.

[99] M. Yuste, R.E. Galindo, S. Carvalho, J.M. Albella, O. Sánchez, Improving the visible transmittance of low-e titanium nitride based coatings for solar thermal applications, Appl. Surf. Sci. 258 (2011) 1784–1788.

[100] A. Tarniowy, R. Mania, M. Rekas, The effect of thermal treatment on the structure, optical and electrical properties of amorphous titanium nitride thin films, Thin Solid Films. 311 (1997) 93–100.

[101] Y. Zhang, P. Yan, Z. Wu, P. Zhang, Influences of deposition parameters on the microstructure and properties of nanostructural TiN films synthesized by filtered cathodic arc plasma, Rare Met. 24 (2005) 370–375.

[102] C. Ducu, S. Moga, D. Negrea, V. Malinovschi, M. Balaceanu, Stress and texture in titanium nitride thin films by X-ray diffraction techniques, J. Optoelectron. Adv. Mater. 12 (2010) 1078–1082.

[103] L.-J. Meng, A. Azevedo, M. dos Santos, Deposition and properties of titanium nitride films produced by dc reactive magnetron sputtering, Vacuum. 46 (1995) 233–239.

[104] V. Merie, M. Pustan, G. Negrea, C. Bîrleanu, Research on titanium nitride thin films deposited by reactive magnetron sputtering for MEMS applications, Appl. Surf. Sci. 358 (2015) 525–532.

[105] S. Xu, L.K. Cheah, B.K. Tay, Spectroscopic ellipsometry studies of tetrahedral amorphous carbon prepared by filtered cathodic vacuum arc technique, Thin Solid Films. 312 (1998) 160–169.

[106] J.N. Hilfiker, R.A. Synowicki, H.G. Tompkins, Spectroscopic Ellipsometry Methods for thin Absorbing Coatings, in: Soc. Vac. Coaters, 2008: p. 856.

[107] H. Fujiwara, Spectroscopic Ellipsometry, John Wiley & Sons, Ltd, Chichester, UK, 2007.

[108] S. Kassavetis, P. Patsalas, S. Logothetidis, J. Robertson, S. Kennou, Dispersion relations and optical properties of amorphous carbons, Diam. Relat. Mater. 16 (2007) 1813–1822.

[109] E. Céspedes, M. Wirz, J.A. Sánchez-García, L. Alvarez-Fraga, R. Escobar-Galindo, C. Prieto, Novel Mo–Si3N4 based selective coating for high temperature concentrating solar power applications, Sol. Energy Mater. Sol. Cells. 122 (2014) 217–225.

[110] W.H. Gitzen, Alumina as a Ceramic Material, John Wiley & Sons, 2006.

[111] V. Edlmayr, M. Moser, C. Walter, C. Mitterer, Thermal stability of sputtered Al2O3 coatings, Surf. Coatings Technol. 204 (2010) 1576–1581.

[112] A.-N. Wang, J.-H. Huang, H.-W. Hsiao, G.-P. Yu, H. Chen, Residual stress measurement on TiN thin films by combing nanoindentation and average X-ray strain (AXS) method, Surf. Coatings Technol. 280 (2015) 43–49.

[113] P.O.A. Persson, L. Ryves, M.D. Tucker, D.R. McKenzie, M.M.M. Bilek, Oriented graphite layer formation in Ti/C and TiC/C multilayers deposited by high current pulsed cathodic arc, J. Appl. Phys. 104 (2008) 074317..

CHAPTER 4: SOLAR SELECTIVE COATINGS BASED ON ALTI(O_XN_{1-X})

Aluminium titanium oxynitrides were selected as candidate materials for solar selective coatings on basis of the state of the art described in section 4.1. The experience and capacity acquired on the previous solar selective coatings based on a-C:MeC (Chapter 3), allowed the improvement of the methodology to follow for a complete design of the coating.

In this chapter, initial thermal treatment tests were performed to validate the stability of single oxynitride layers in air, showing no degradation at temperatures above 650ºC. A set of individual AlTi(O_xN_{1-x}) layers deposited by cathodic vacuum arc (CVA) were analysed in section 4.2 in terms of composition, morphology and optical properties in order to investigate the relationship between their chemical bonding and properties

Once single AlTi(O_xN_{1-x}) thin films were fully characterized, complete solar selective coatings (SSC) were designed with optical simulations, based on measured optical constants of each of the individual layers, providing excellent selective optical selective properties (α=94.7% and ε_{RT}=5.6%). The selected multilayers stacks were CVA deposited, obtaining excellent agreement between simulated and experimental reflectance spectra (section 4.3). In last section (4.4), the thermal stability in air of the complete deposited SSC were analysed by asymmetric and cyclic heating tests, showing no degradation after 750h of cycles in air at 600ºC.

4.1. Introduction

Similar than interstitial carbides explained in chapter 3, interstitial metal nitrides have a complex electronic bonding system which includes metallic, covalent, and ionic components [1], as proposed by Holleck for wear resistant materials [2,3] (Figure 4.1). Interstitial nitrides are formed by the incorporation of nitrogen atoms into the interstitial spaces between metal atoms and they are situated in the middle of the triangle. The incorporation of a third element in the transition metal nitride matrix, i.e. Si or Al, changes the bonding to more covalent character. Covalent bonded materials (e.g. AlN) are characterized for having very high melting points and high hardness [4], however, they normally shows a lack of adherence to metallic substrates due to their brittleness. This adhesion problem does not appear with metallic bonding materials as TiN. Therefore, the combination of metallic and covalent bonding character in ternary compounds results in improvement in the thermal stability at high temperatures.

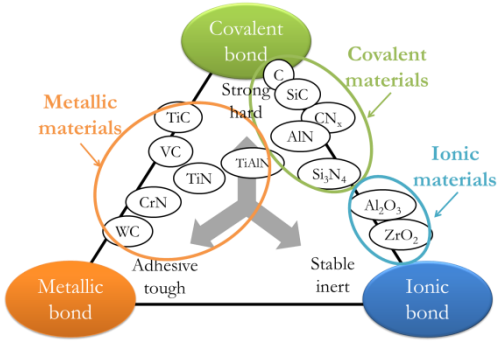

Figure 4.1 – Different materials grouped by their bonding type.

Metal oxynitride (MeON) coatings are a new class of multifunctional materials which allow a transition of the properties of nitride and oxide based coatings [5]. The presence of oxygen and nitrogen allows the tailoring of film properties between those of the metal nitride (MeN) and the correspondent oxide (MeO). MeON have been known for almost a century and their industrial interest keeps growing, not only in the traditional and well-established applications also in new and promising fields such as optoelectronics on solar energy applications.

One of the great advantages of MeON thin films is the possibility of tuning their crystallographic order between the oxide and nitride with a variation of the nitrogen/oxygen content. Hence, the overall set of properties of the metal oxynitride materials (band gap, the electronic conductivity and microstructure) can be tuned by a meticulous control of the O-to-N ratio in the non-metal sublattice. Merging the benefits of both metal nitrides and oxides, MeON have shown excellent physical, chemical and mechanical properties for a wide range of industrial applications with a promising future. Their remarkable properties such as diffusion and corrosion resistance [6], high hardness [7], chemical and thermal stability [8] and electronic properties [9], lead to a wide variety of unexpected uses in many fields. Examples of promising applications of metal

oxynitrides include optoelectronics [10], biocompatible coatings [11], gas barriers films [12] or microelectronics devices [13].

In particular for this thesis, PVD deposited nitrides and oxynitrides coatings are considered to have potential application prospect in high temperature for solar selective coatings (SSC) due to the excellent oxidation resistance and thermal stability. This has been extensively reported in literature. Table 4.1summarizes the multilayer stack, the PVD technique employed and the optical selective characteristics of different solar absorbing coatings prepared by combinations of transition metal nitrides and oxynitrides.

Table 4.1 – Oxynitride based spectrally selective coatings for high temperature, ordered by publication date. The solar absorptance (α) and thermal emittance (ε) values are indicated before/after the stability test indicated. Thermal emittance is calculated at room temperature, unless another temperature is expressed. Duration and temperature of the stability test in air are listed. The substrate(s) employed is expressed in the table being SS = Stainless steel. The SSC based on Al-Ti-O-N materials are highlighted in bold.

Coating	Deposition technique	Substrate	α	ε_{RT}	Stability in air	Ref.
AlTiON / SiO_2	Activated reaction evaporation	Al / Cu	92/85	4/8 at 200ºC	265ºC (19h)	[8,14,15]
TiAlN/TiAlON/Si_3N_4	DC-MS	Cu / SS	96/96	7/7 at 82ºC	525ºC (50h)	[16–18]
NbAlN/NbAlON/Si_3N_4	DC-MS	Cu / Si	94.7/91.9	7/9 at 82ºC	250ºC (350h)	[19]
TiAl/TiAlN/TiAlON/TiAlO	Multi arc ion platting	SS / Cu	90/80	8/18	600ºC 2h	[20]
TiAl/TiN/(TiN-AlN)$_H$/(TiN-AlN)$_L$/AlN	DC and RF – MS	SS	94.3/92	8/16	600ºC (2h)	[21]
TiAlN/TiAlON/AR	DC-MS	Glass / Al	95	9	-	[22]
TiAlSiN/TiAlSiON/SiO_2	DC-MS + PECVD (SiO_2)	Glass/Cu/Al	95/93	6/6 at 100ºC	278ºC (600h)	[23]
NbTiON/SiON	DC-MS	Cu / SS	95/94	7/8 at 80ºC	500ºC (2h)	[24]
TiAlN/TiAlON/SiO_2	DC-MS + PECVD (SiO_2)	Glass/Cu	95.5/95	8/9 at 100ºC	278ºC (600h)	[25]
NbTiON/SiON	DC-MS	Cu / SS	95/94	7/8 at 80ºC	500ºC (2h)	[24]
$Ti_{0.5}Al_{0.5}N/Ti_{0.25}Al_{0.75}N$/AlN	DC and RF – MS	SS /Si	92.2/92	6/5 at 82ºC	475ºC (2h)	[26]
CrMoN (H)/CrMoN(L)/ CrON	DC-MS	SS / Al	92/92	13/14	425ºC(7h)	[27]
Ti/AlTiN/AlTiON/AlTiO	DC-MS	SS	93/91.9	16/16	350ºC (1000h)	[28,29]
TiAlCrN/ TiAlN/ AlSiN	CVA	Cu / SS	88/88	9/9	600ºC (4h)	[30]
Mo/TiZr/TiZrON/SiON	DC and RF – MS	SS thermal oxidized	95/92	8/10 at 80ºC	500ºC vacuum (300h)	[31]
W/AlSiN/AlSiON/AlSiO	DC-MS	SS	94.2/94	8.3/8.9	400ºC (1200h)	[32]
CrAlN/CrAlON	DC-MS	Cu	98.4/91.1	7/21 at 82ºC	600ºC (100h)	[33]
Al/NbMoN/NbMoON/SiO_2	DC-MS	SS	94.8/94	5/5 at 80ºC	400ºC (500h vacuum)	[34]
W/TiAlC/TiAlCN/ TiAlSiCN/ TiAlSiCO/ TiAlSiO	DC-MS	SS	96/<96	7/<7 at 82ºC	325ºC (400h)	[35]
W/TiAlN/TiAlON/ TiAlO	DC-MS	SS	94	8 at 82ºC	325ºC (2h)	[36]
AlMoN(H)/AlMoN(l)	DC-MS	SS / Si	93/93	13/13 at	400ºC (2h)	[37]

				82ºC		
$HfMoN/HfON/Al_2O_3$	DC-MS	SS	95	14	-	[38]
$TiAlN/TiAlSiN/Si_3N_4$	DC-MS	SS	94.5/91	9/10 at 75ºC	500ºC (2h)	[39]
Cr/ TiAlCrN (Grad)/ TiAlN/ AlSiN/ AlSiO	CVA	Cu / SS	95/95	9/18	600ºC (12h)	[40]
$W/WAlN/WAlON/Al_2O_3$	DC and RF – MS	SS	94.8/95	8/11	550ºC (350ºC)	[41]
AlCrSiN/AlCrSiON/AlCrO	CVA ion plating	SS	95/92	15/16	600ºC (600h)	[42]

As can be observed from the summary table, different PVD processes were employed for solar selective coatings in order to synthesize MeON with different oxygen/nitrogen ratio. Among these processes, magnetron sputtering is widely employed for large area depositions and is an attractive way to achieve adjustable chemical compositions and consequently the desired tunable optical properties. Notwithstanding the foregoing, little research attention has been done to the use of the industrially well-established cathodic vacuum arc (CVA) deposition technique. However, CVA is well known for metal nitride and oxynitride deposition for many other applications. For instance, AlTi(O_xN_{1-x}) and AlCr(O_xN_{1-x}) coatings were deposited with rotating cathodes as protective cutting tools [6,7] obtaining excellent wear resistance at temperatures up to 600ºC.Until now, only Valleti *et al.* research group [30,40] in Balapour (India) and Zou et al. (Lingnan, China) [42] are currently employing cathodic arc deposition with cylindrical cathodes to produce different combinations of MeON for SSC. In particular, the former cited group has developed multilayer stack consisting on TiAlCrN/ TiAlN/AlSiN [30] and Cr/TiAlCrN (Grad)/TiAlN/AlSiN/AlSiO [40], in which each layer plays a role (IR reflector / absorber / antireflection) for maximizing the spectral selectivity properties.

In this thesis, CVA technique was employed to growth MeON thin films, as this technique produces dense and uniform films, with excellent adhesion and therefore, perfectly suitable for high-temperature applications. In addition to the previous requirements, the deposition process must be simple to implement involving the minimum deposition steps and the raw materials must be cost effective as the purpose of this work is the design of a coating for subsequent application on an industrial scale. These contrains imply reducing the number of employed metals and to utilise economic ones. Hf, Nb or Ta transition metals have been discarded beforehand due to the high price for large scale production, although Hf and Ta oxynitrides could have higher melting points. A thorough review of the MeON candidate materials was conducted to determine the most suitable materials to serve as an antireflective layer, absorber and IR layer in an industrial scalable process.

Rebouta *et al.* obtained remarkable results in 2012 with $Al_{50}Ti_{50}$ oxynitride multilayer stacks deposited by DC-MS and with a top antireflective layer of SiO_2 (n~1.44) deposited by plasma enhanced chemical vapour deposition (PECVD) in a different coating chamber. The system was thermally stable 600h in air at a temperature up to 278ºC, with no changes in the solar

absorptance of 95% and thermal emittance of 6%. Barshilia's AlTiN/AlTiON multilayer coatings exhibited a 95% and 7% thermal emittance at 82ºC on Cu substrate with Si_3N_4 (n~2.00) as AR layer [17]. They employed an $Al_{50}Ti_{50}$ cathode for the oxynitrides and a second Si cathode for the AR layer. The coatings show no degradation of the optical properties 50h in air at 525ºC. Both multilayer designs require a different cathode (Si) or deposition chamber for the antireflective layer, increasing the complexity of the system.

Lei *et al.* [20] in 2009, developed a multilayer stack deposited with a multi-arc ion plating system, using only one $Al_{50}Ti_{50}$ cathode for the complete stack, including an AlTiO as AR layer. They obtained a solar absorptance around 90%, stable at 650ºC in air with a thermal emittance of below 8%. However, the macroparticles deposited along the coating with this arc ion plating system are pretty large (~0.5µm), and an appropriate system to remove the droplets is needed.

Afterwards, in 2014, Barshilia [28,36] designed a similar stack based on Ti and Al separated cathodes, using a pulsed DC-MS system to control the stoichiometric of each layer independently. This new configuration includes AlTiO (n~1.8) as AR layer and Ti chrome as IR interlayer. This system did not offer same optimal performance as the previous ones (α=93% and $\varepsilon_{82ºC}$=16%), nevertheless, it resulted simpler to implement and clearly more oriented towards industrial applications. Following the same AlTi(O_xN_{1-x}) structure, in 2015 Barshila's group added a W layer between the substrate and the MeON multilayer stack in order to reduce the emittance and avoid diffusion from the substrate to the coating up to 300ºC [36]. Several patents were published by Barshilia employing AlTi oxynitride multilayer stacks (Table 4.2) based on the previous explained results. In 2014, they patented a hybrid system combining pulsed DC-MS AlTi(O_xN_{1-x}) stack with a sol-gel AR top layer of organically modified silica (ormosil) [43].

Table 4.2 – Patents review of solar selective coatings based on AlTi(O_xN_{1-x}) multilayer stacks. The maximum solar absorptance (max α) and the minimum thermal emittance at 82ºC (min $\varepsilon_{82ºC}$) evaluated for each multilayer system are also indicated.

Coating	Deposition technique	Cathodes	Max α	Min $\varepsilon_{82ºC}$	Stability in air	Year	Ref.
AlTiN/AlTiON/Si_3N_4	DC-MS	$Al_{50}Ti_{50}$, Si	95	6	525ºC (50h)	2009	[44]
Ti chrome interlayer/TiAlN/TiAlON/TiAlO	Electroplating + Pulsed DC-MS	Al, Ti	92	17	350ºC (1000h)	2013	[45]
Ti chrome interlayer/TiAlN/TiAlON/TiAlO and ormosil	Electroplating + Pulsed DC-MS + sol gel (ormosil)	Al, Ti	95	11	500ºC (1000h)	2014	[43]

The failure mechanism observed in most of those AlTi(O_xN_{1-x}) SSC follows a similar pattern [46]. At temperatures above 500ºC, the main microstructural modifications include interdiffusion between the AlTi(O_xN_{1-x}) layers to produce new phases and subsequent diffusion of the metal substrate (Cu, SS) into the coating [8]. All those alterations affect the initial optical values, reducing the solar selectivity. In addition, delamination problems were observed at T > 600ºC when coatings are deposited directly on a Cu substrate. The $Al_{50}Ti_{50}N$ layer employed as a thermal barrier would minimize the lack of adhesion; however, the stoichiometric of this layer was not

optimized to the best convenient for high-temperature resistance, as discussed below. The increment of the ε after thermal treatments at high temperature was frequently attributed to the increase of roughness. The uncontrollable formation of oxide layers at the surface of the SSC could be the responsible of this increase of roughness [17]. In order to prevent these failure mechanisms an insight on the microstructural phases in AlTiN and AlTiON systems is required.

Based upon the successful results of AlTiN/AlTiON tandem absorber coating developed by Barshilia [16–18], Lei [20], Zhu [22]or Rebouta [23,25] using magnetron sputtering, this chapter aims to develop cathodic vacuum arc AlTi nitride and oxynitride based solar selective coating. Those systems exhibit the best optical properties (α=95%, ε_{RT}=8%) [16–18] and demonstrate good thermal stability in air. Additionally, Al_xTi_{1-x} alloy cathode has an affordable price for industrial uses and it has been widely employed for different Al/Ti compositions.

The ternary system Al-Ti-N is a well-known industrial hard coating that presents composition variations lying in a ternary diagram, which includes TiN, AlN and Ti_2N [47]. As stated before, AlTiN films can be obtained by pure Al and Ti cathodes or an Al_xTi_{1-x} alloy cathode with a different composition. Previous studies analysed the microstructure of $Al_xTi_{1-x}N$ coatings in function of the Al content [48–53]. As shown in Figure 4.2 (a), the crystal structure is cubic for $x \leq 0.62$, mixed cubic and wurtzite for $x=0.67$, and single phase wurtzite for $x \geq 0.75$ [48]. In the cubic structure range, the lattice parameter decreases monotonically from 4.26 Å for TiN to 4.16 Å in the $(Al_{0.3}Ti_{0.7})N$, due to the substitution of the Ti by Al atoms that have smaller atomic radius [54]. The behaviour after a thermal treatment at high temperature in air also varies according to the Al content. The oxides Al_2O_3 and TiO_2 (as well as Al_2TiO_5 in minor proportion) will appear depending on the Al content, showing the more α-Al_2O_3 content, the higher Al content. The formation of a dense Al_2O_3 top layer is beneficial for the oxidation resistance. Al_2O_3 layer either retards the inward diffusion of O_2 during oxidation and avoids the formation of TiO_2 porous layer associated with compressive stress and crack formation [55]. The oxidation resistance increases with the increment of Al, but until ~65 at. %, while for higher content of Al, the oxidation resistance is reduced and becomes comparable to that of pure AlN [55,56]. Therefore, $Al_{67}Ti_{33}N$ shows the best oxidation resistance due this composition allows the transition from the cubic structure to wurtzite. The maximum hardness is also obtained for this composition being the most common composition employed for hard coatings since the mid-1990s [57].

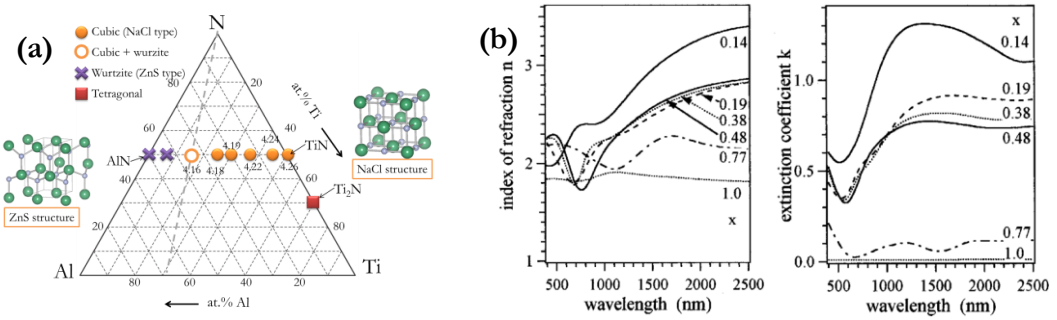

Figure 4.2 – (a) Ternary diagram of the Al-Ti-N system with the different crystal structures observed. The lattice parameter (in Å) of the cubic structures is also included in the figure for the different Al content. (b) Index of refraction *n* and extinction coefficient *k* of $Al_xTi_{1-x}N$ films deposited by magnetron sputtering determined by spectrophotometric data [58].

Regarding the optical properties, the influence of the Al/Ti ratio was analysed by several authors and is directly related to the two possible crystal structures discussed before [25,29,50,58]. While the cubic formed phase ($x \leq 0.62$) is electrically conductive, showing metallic bonding behaviour and thus high reflectance (for $\lambda > \omega_p$), the wurtzite phase observed when Al content is high has dielectric properties, transparent in the visible and insulating behaviour [50]. Figure 4.2 (b) shows the variation of the complex refractive index for $Al_xTi_{1-x}N$ with different Al/Ti contents [58]. The modulation observed in function of the Al content provides the possibility to control the optical constants in order to optimize the desired solar spectral selectivity.

The Ti-Al-O-N phase diagram presents a broad number of mixed phases of (Al,Ti)N-$(Al,Ti)_2O_3$ without any thermodynamically stable quaternary phase reported before [7]. When the oxygen content is low (<~30 at.% [59]), the O atoms can be incorporated in the cubic structure by replacement of N. The incorporation of oxygen into the nitride lattice affects the properties of the compound due to different charges and differences in the nature of metal-anion bonds [60]. Two nitrogen atoms (N^{3-}) need to be replaced by three oxygen atoms (O^{2-}) in order to maintain the electrical neutrality of the network. Whether the O content increases, other binary or ternary phases are expected to be formed. The influence of the N/O ratio in AlON and TiON ternary systems have been thoroughly analysed before [61,62], however, the $AlTi(O_xN_{1-x})$ system includes many possibilities in the microstructural design, very influenced by the deposition technique employed and its conditions. Structural and chemical properties of magnetron sputtered [63] and cathodic vacuum arc [7] $AlTi(O_xN_{1-x})$ were studied, showing the improvement of the thermal resistance and mechanical properties with the addition of a certain oxygen content. A solid understanding of the correlations between bonding type and composition is required to foreseen the final properties in oxynitride materials.

Therefore, the goal in this thesis is to contribute towards the understanding the effect of oxygen incorporation in the morphology and optical properties in Al-Ti-O-N coatings to design a complete SSC based on these materials. For that aim, a set of individual $AlTi(O_xN_{1-x})$ layers grown

by CVA were analysed in terms of composition, morphology and optical properties to investigate the relationship between their growing conditions (oxygen content and deposition pressure) with the final properties (section 4.2).

Once the optical constants of each one of the individual layers were determined, a complete solar selective multilayer stack was first optimized by optical simulations and then deposited by CVA, obtaining excellent agreement between reflectance spectra simulated and experimental (section 4.3). It has been shown that the addition of a dense $(Al,Ti)_2O_3$ top layer [64] increases the diffusion and oxidation resistance of AlTiN, therefore this oxide layer was employed as antireflective top layer.

In last section 4.4, the thermal stability in air of the complete multilayer stacks deposited following the optimized simulated results were analysed by asymmetric and heating – cooling cycles heating tests.

4.2. Optimization of AlTi(O_xN_{1-x}) individual layers

A series of AlTi(O_xN_{1-x}) samples with different nitrogen/oxygen ratio were deposited by CVA. Upon verification of no significant changes in the optical properties after 2 hours annealing in air at temperatures up to 650ºC, the single layers were then fully characterized.

The element concentration and depth profile were determined by elastic recoil detection analysis (ERD), the morphology was analysed by X-ray diffraction (XRD), scanning electron microscope (SEM) and high-resolution transmission electron microscopy (HR-TEM). The optical constants were modelled from spectroscopic ellipsometry (SE) and the optical performance was determined with reflectance spectrophotometry.

4.2.1 Preliminary thermal tests on AlTi(O_xN_{1-x}) layers

As mentioned in the introduction, the decision to pursue AlTi(O_xN_{1-x}) as based materials for SSC was supported by the preliminary stability tests performed at high temperature. AlTiN and AlTiON (20% O_2/O_2+N_2) samples were deposited in Metal Estalki S.L using a CVA device. The deposition parameters employed are explained in next section 4.2.2. These samples were subjected to asymmetric heating tests in air up to 650ºC during 2h. Their optical constants and reflectance spectra were measured after each heating test, and the calculated solar absorptance as a function of annealing temperature is shown in Figure 4.3.

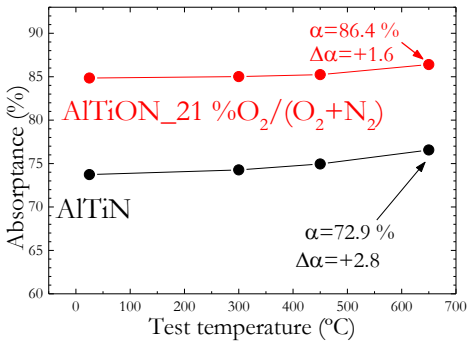

Figure 4.3 – Thermal treatment test for AlTiN and AlTiON ($21\%O_2/(O_2+N_2)$) thin films CVA deposited. Each temperature was maintained 2 hours.

The optical response was preserved and even slightly increased after the heating test in the. At high temperature, a dense Al_2O_3 layer may be formed on the top of the single AlTiN and AlTiON films, as has been reported for the cathode composition employed ($Al_{67}Ti_{33}$) [55]. The growing of this Al_2O_3 layer may also help to improve α, as it behaves as antireflective layer reducing the reflectance radiation in solar wavelength range. A visual inspection of the samples after heating in air show no changes or damages or delamination failure.

After checking the good stability of the samples at high temperatures and the possibility to modulate the optical constants with the different oxygen content, a depth study of $AlTi(O_xN_{1-x})$ thin films as promising materials for solar selective coatings for high-temperature applications was carried out.

4.2.2 Deposition of $AlTi(O_xN_{1-x})$ individual layers with variable O_2/N_2 ratio

A set of $AlTi(O_xN_{1-x})$ thin films were deposited in Metal Estalki S.L., using a direct current (DC) cathodic vacuum arc (CVA) device. Only one rectangular $Al_{67}Ti_{33}$ cathode was employed for all the depositions, varying the O_2 and N_2 gas flow as reactive gases. The CVA system was fully described in chapter 2, and the common deposition parameters applied for the $AlTi(O_xN_{1-x})$ samples are summarized in Table 4.3.

Table 4.3 – Common deposition parameters employed for $AlTi(O_xN_{1-x})$ samples grown by CVA technique.

Base pressure	$2 \cdot 10^{-4}$ Pa
Operating pressure	1.5 Pa
Arc current discharge	125 A
Deposition temperature	450 ºC
Cathode size	331 x 174 mm^2
Cathode material	$Al_{67}Ti_{33}$
Bias voltage at deposition stage	- 75 V
Rotation speed of the substrate	10 rpm
Distance from the filter to the substrate	150 mm

The composition of $AlTi(O_xN_{1-x})$ coatings deposited by CVA can be controlled by a careful adjustment of the kinetic and thermodynamic parameters, i.e. the rate of the metallic atoms arriving at the substrate *versus* the thermodynamic affinity of the reactive gases with the Al and Ti.

Taking into account the available thermochemical data for Al and Ti oxides and nitrides, a complete oxidation of the films would be expected as long as enough oxygen is available, since the formation of a metal-oxygen bond is energetically more favourable [65,66] ($\Delta H_f^o{}_{TiO2}$ =-933.7 kJ/mol and $\Delta H_f^o{}_{Al2O3}$ =-1669.8 kJ/mol) than the one of a metal-nitrogen bond ($\Delta H_f^o{}_{TiN}$ = -338.1 kJ/mol and $\Delta H_f^o{}_{AlN}$ = -317.9 kJ/mol).

Among all the possible parameters that could be selected to change the kinetic *versus* the thermodynamics in CVA deposition (deposition temperature, working pressure, arc current, substrate bias potential or partial pressure of the reactive gases), in this thesis, the partial pressure of O_2 and N_2 reactive gases and the working pressure (varied from 1.5 to 2.1 Pa) were selected. The substrate temperature (450ºC), the arc current (125 A) and the substrate bias (-75 V) were kept as constant parameters, as they have been optimized previously for similar nitride films in this CVA chamber [51,59], obtaining low residual stress and good adhesion samples. Therefore, due to the high affinity of metals towards to O_2 rather than to N_2, the composition of the gas mixture should always contain an excess of nitrogen.

The nitrogen and oxygen flow rate employed for the different AlTi(O_xN_{1-x}) samples are summarized in Table 4.4. Samples #1-6 were deposited at a working pressure of 1.5 Pa while sample #7 (AlTiON_21_HP_w) was deposited at a higher working pressure of 2.1 Pa. Only for the deposition of sample #6 (nitrogen-free), 10 sccm of Ar gas flow was introduced into the chamber to stabilize the arc. Samples #2, #3, #4, #5 and #7 were deposited on top of ~0.5 µm AlTiN in order to improve the adherence. No delamination was observed between the layer and the substrate or between in any of the deposited thin films.

Table 4.4 – Deposition parameters for the different AlTi(O_xN_{1-x}) thin films, including working pressure (P_W), and gas flow.

#	Coating_%O_2/(O_2+N_2)	P_W (Pa)	Ar (sccm)	N_2 (sccm)	O_2 (sccm)	O_2/(O_2+N_2) (%)
1	AlTiN	1.5	0	70	0	0
2	AlTiON_4	1.5	0	72	3	4.0
3	AlTiON_8	1.5	0	61	5	7.6
4	AlTiON_13	1.5	0	52	8	13.3
5	AlTiON_21	1.5	0	46	12	20.7
6	AlTiO	1.5	10	0	50	100.0
7	AlTiON_21_HP_W	2.1	0	64	17	21.0

The films were deposited on Si (100) and mirror polished inconel HAYNES ® 230 substrates. Figure 4.4 shows an image of each sample type on inconel substrate. Under this conditions, a first set of thick samples (d >1.5 µm) were deposited to determine their composition and optical properties. Subsequently, and after initial simulations of a complete SSC based on the modelled optical constants, a new set of samples were grown. This new batch of AlTi(O_xN_{1-x}) films with thickness from ~30 to 500 nm, were subjected to a comprehensive complete characterization that includes XRD, TEM, and optical analysis.

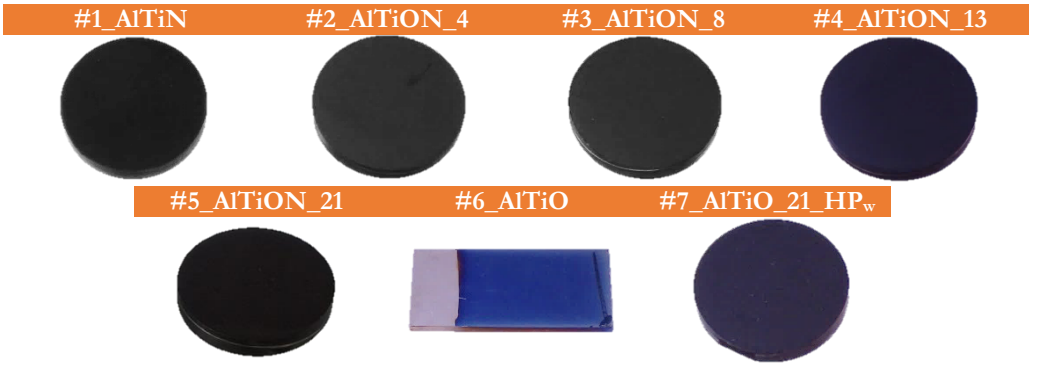

Figure 4.4 – Photos of the deposited samples on inconel substrate for different oxygen – nitrogen ratio.

In a parallel process, equivalent $AlTi(O_xN_{1-x})$ samples were deposited in a filter cathodic vacuum arc (FCVA) situated in Abengoa Research laboratory, also further explained in chapter 2. For the sake of simplicity, the development of these equivalent coatings is not included in this thesis, as the design followed a parallel process.

4.2.3 Morphological characterization of $AlTi(O_xN_{1-x})$ individual layers

Film composition and depth profile

The elemental composition and depth profiles of the $AlTi(O_xN_{1-x})$ samples with different $O_2/(O_2+N_2)$ ratio or reactive gases were analysed by ERD analysis. Glow discharge emission spectrometry (GDOES) and energy dispersive x-ray spectroscopy (EDX) techniques were employed initially to measure the composition of the samples, however, they are not accurate enough to determine quantitatively the content and depth profile of light elements (N, O, C and H) present in the samples. Meanwhile, ERD ion beam analysis technique allows simultaneous measurement of light and heavy (Ti and Al) elements present in the sample. The depth profiles extracted from the measurements are displayed in Figure 4.5 (a) to (g). The thickness in atoms/cm^2 is directly obtained from the measurements and is displayed in the depth profiles. The depth profiles are based on the recoil spectra unless otherwise noted, as for Ti where the depth profiles for both Cl scattering (marked as Ti (RBS)) and the Ti recoils are displayed in order to increase the depth resolution. The analysis depth is different for each element due to limitations in the separation of each recoil ion from the scattered Cl ions and is reached when the profile abruptly drops to zero in the graph.

A roughness model was included in the fit, but sometimes was not sufficient, resulting in an overestimation of the concentration of O. The depth profiles were corrected for the roughness model, but residual rounding is reflected in the profiles. This effect is clearer in sample #5, where the oxygen content in the top of the layer (~100nm) increases up to 35 at.% O, which lead to

decrease the nitrogen content. Sample #6, deposited only with O_2 reactive gas, has a thickness much thinner and is in the only one where the Si substrate is visible (Figure 4.5 (f)).

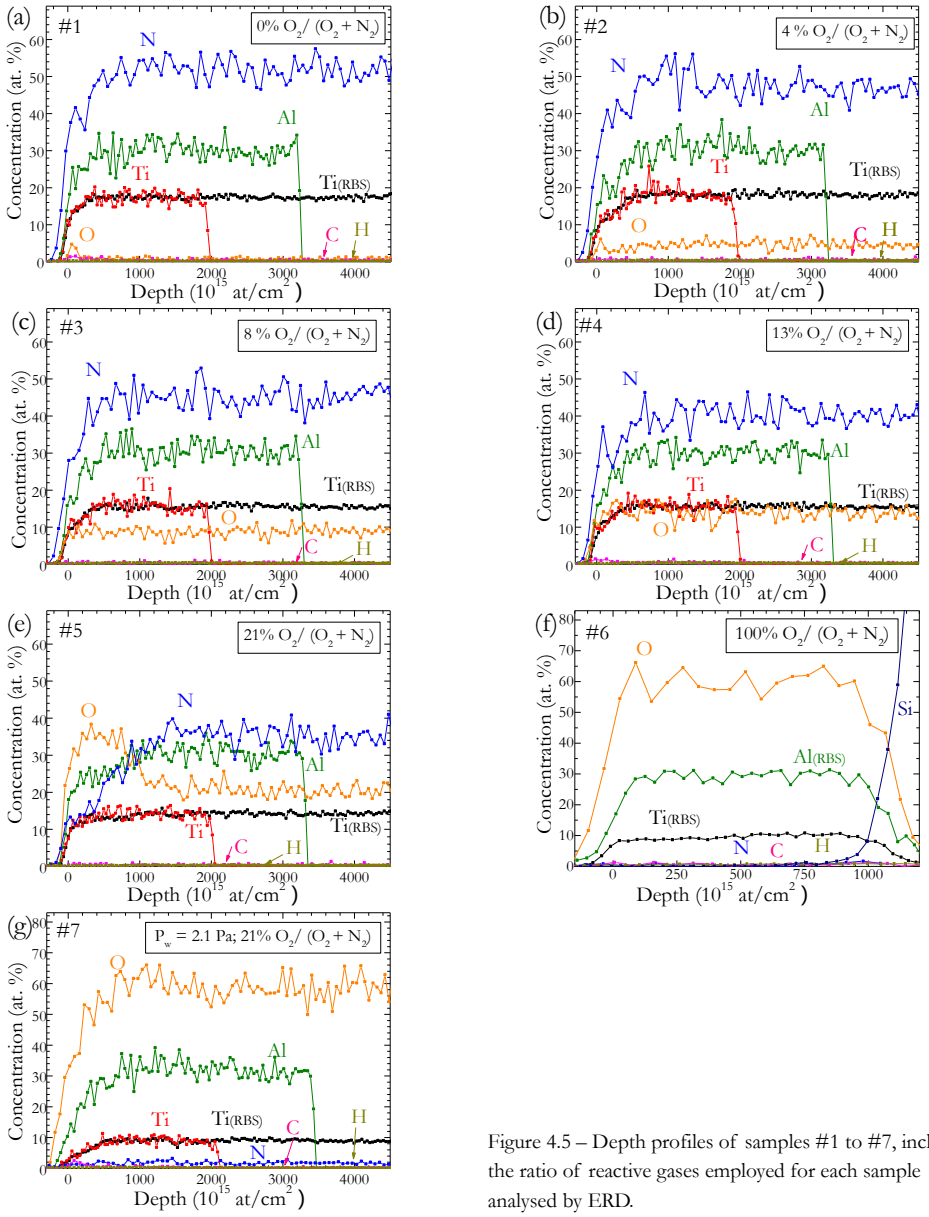

Figure 4.5 – Depth profiles of samples #1 to #7, including the ratio of reactive gases employed for each sample analysed by ERD.

The elemental concentration of the deposited samples measured by ERD analysis is summarized in Table 4.5. These values are valid for the deeper part in the samples with uniform film composition, below the surface region where there are distortions due to roughness.

Table 4.5 – Elemental ERD composition of AlTi(O_xN_{1-x}) thin films. The estimated uncertainty is 1% at. % for concentrations higher than 10 at.%. For concentration smaller than 10at.%, the uncertainty is 10% of the measured value.

#	Coating_%O_2/(O_2+N_2)	Elemental composition (at. %)						(Ti+Al)/ (N+O)	%(Ti+Al)/ (Ti+Al+N+O)	% O/ (N+O)	% Al / (Al+Ti)
		O	N	Ti	Al	C	H				
1	AlTiN	0.5	51	17	31	0.3	0.17	0.95	48.8	0.9	65.1
2	AlTiON_4	4	46	18	30	0.5	0.34	0.96	49.4	8.6	62.6
3	AlTiON_8	9	45	16	30	0.3	0.30	0.86	46.6	16.3	66.1
4	AlTiON_13	14	40	16	30	0.3	0.30	0.85	46.3	25.6	65.8
5	AlTiON_21	20	35	14	30	0.4	0.29	0.82	45.4	37.0	68.2
6	AlTiO	60	0.5	9	28	0.4	0.30	0.65	39.7	99.3	75.1
7	AlTiON_21(HP_W)	58	2	9	31	0.2	0.16	0.68	40.7	97.3	77.7

As observed from Table 4.5, H and C concentration in the AlTi(O_xN_{1-x}) samples are insignificant and independent on the reactive gases ratio or the operating pressure. The low C concentration is close to the detection limit and it could have high uncertainties. The concentration of oxygen (nitrogen) in the films increases (decreases) linearly with the O_2/(N_2+N_2) ratio of reactive gases of samples deposited with the same P_w = 1.5 Pa (#1-5), as shown in Figure 4.6.

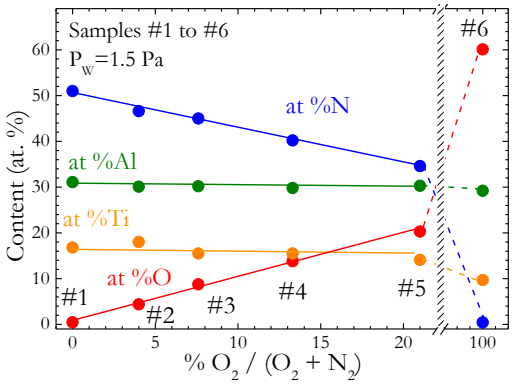

Figure 4.6 – Al, Ti, N and O concentration of AlTi(O_xN_{1-x}) samples deposited at 1.5 Pa for different concentration ratio of O_2 /(O_2 + N_2) reactive gases during the deposition, measured by ERD ion beam analysis.

In samples #1-5 the Al and Ti content remains almost constant, with a slight deviation of the Al:Ti ratio when compared to the cathode composition (67:33). This deviation could be explained by the different degree of ionisation of Al and Ti for CVA depositions [67]. Ti ions arrive with higher energy to the substrate and could penetrate deeper into the surface than Al ions, and might create differences in the composition. The pure nitride sample (#1) had an oxygen impurity level of ~1 at. %O. The ratio metal to nitrogen was approximately 1:1. As the oxygen flow increases, the metallic proportion (i.e. (Ti+Al)/(Ti+Al+N+O)) decrease from 48.8% in sample #1 to 45.4% in sample #5. This reduction was attributed to either the formation of nitrogen vacancies in the cubic lattice or the formation of Al_2O_3 and TiO_2.

The pure oxide film (samples #6) were deposited as AR top layer and to provide integrity and environmental protection at high temperatures [68]. The metallic proportion decreases, practically reaching the stoichiometric $(Al,Ti)_2O_3$ composition, with 40% of metal versus 60at% of oxygen. The Al:Ti ratio differs the initial cathode composition, obtaining approximately 75:25 ratio. Energetically it resulted much more favorable the bonding of O with Al is than with Ti, which can lead the formation of mixed aluminum-titanium oxide in the form $(Al_{0.66}Ti_{0.33})_2O_3$ along with free alumina Al_2O_3.

Sample #7, was deposited with same reactive gases ratio than sample #5. However, the increasing of 40% the working pressure in comparison with rest of samples resulted in a drastic effect in the composition and, as shown in next sections, in the morphology and final optical properties. This sample has a composition nearly equivalent to the pure oxide sample #6, with only a residual content of 2 at.% of N against 58 at% O, although 64 sccm of reactive N_2 were introduced during the deposition. These results will be further discussed with the results obtained in the following characterization techniques.

Film morphology studied by SEM

The cross-section SEM images of AlTiN films deposited with three different thicknesses are shown in Figure 4.7. As clearly observed in Figure 4.7 (a), the 1.6 μm thick film exhibits a dense columnar growth regime, with columns width in the order of ~30 nm. This structure is typical of samples grown under some compressive residual stress and recrystallization grain structure (zone 2 described by Anders model [69]). Additionally, as no filter was employed in the deposition, the film shows numerous macroparticles that can exceed 2 μm. Holes due to the release of these poor adherent macroparticles can also be observed. Conversely, in the other two thinner AlTiN with 0.47 and 0.12 μm thick shown in Figure 4.7 (b) and (c), respectively, no macroparticles are observed although identical non-filtered chamber and deposition parameters were employed. Although some droplets may be generated, their quantity and probability of incorporation into the growing samples increases with the deposition duration. This is of importance because, as the average individual thickness for the designed SSC multilayer stack will be in the order of ~100 nm, no detrimental optical problems associated with the apparition of droplets are expected.

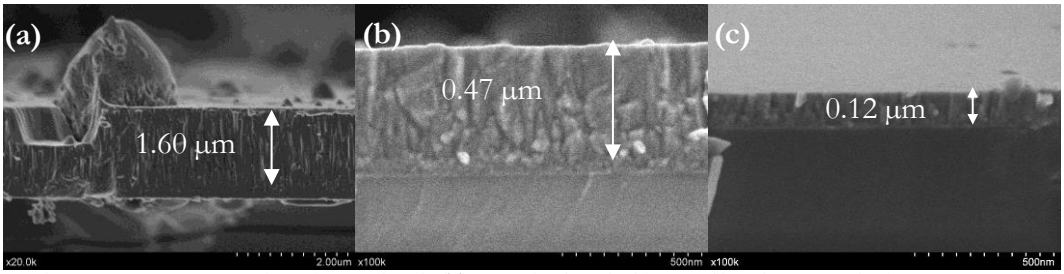

Figure 4.7 – SEM cross-section micrographs of AlTiN samples deposited by non-filtered CVA on Si substrate. (a) 1.6 μm sample with an incrusted macroparticles and a hole as a macroparticle lost, (b) 0.47 μm and (c) 0.12 μm thickness samples. No macroparticles were found in (b) and (c).

SEM analysis of the cross-sectional morphology revealed the dependency of the oxygen content on the coating structure of AlTi(O_xN_{1-x}) (Figure 4.8). As explained above, there is a pronunced dense columnar micrsotructure observed for the oxygen-free AlTiN (sample #1), with the columns extend throughout the whole coating thickness. Samples #2, #3, #4, #5 and #7 (Figure 4.8 (b), (c), (d) (e) and (g)) were grown ot top of a ~0.5 μm thick AlTiN layer. There is a transition region bewteen the AlTiN underlay layer and the upper one where the columnar growing

regime continues. However, when the thickness increases and with the incorporation of more O_2 reactive gas, it resulted in a monotouos width and length shrink of the columns in the AlTi(O_xN_{1-x}) samples, clearly distinguished in samples #2 and #3 with 4.4 and 8.8 at% O content, respectively. Above an oxygen concentration of ca. 9 at.%O (samples #4 and#5), the columnar features are practically absent, indicatting an amorphous or very fine grained film morphology. It is known that small concentration of oxygen can significantly modify the morphology of the film, promoting renucleation during films growth and formation of smaller grains [59].

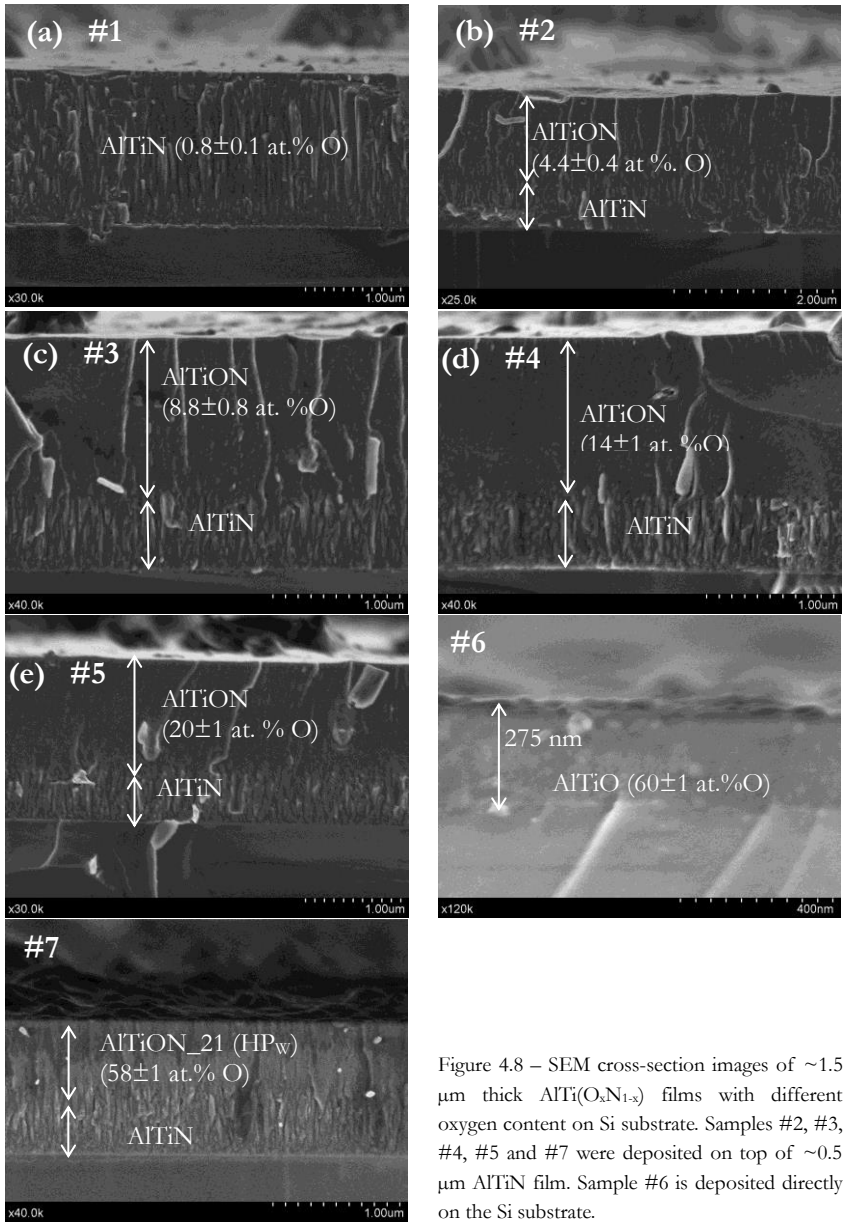

Figure 4.8 – SEM cross-section images of ~1.5 µm thick AlTi(O_xN_{1-x}) films with different oxygen content on Si substrate. Samples #2, #3, #4, #5 and #7 were deposited on top of ~0.5 µm AlTiN film. Sample #6 is deposited directly on the Si substrate.

The pure oxide samples (Figure 4.8 (f)) was not deposited on top on the AlTiN film and it was thinner in comparison with the rest of the samples. No columnar growth is observed in this film. The microstructure of sample #7, (AlTiON_21 (HP_w)), shows as well columnar feature, but it can be appreciated two different regions with non-uniform composition and morphology.

After this initial characterization, the AlTi(O_xN_{1-x}) samples can be classified into three groups according to their microstructure. A first group with well-developed columnar structure (samples #1, #2 and #3). Another group includes samples #4 and #5 and #7 with more diffuse columns structure and higher oxygen content. The third group is in the nitrogen free sample #6.

According to this classification and based on preliminary optical simulations of complete SSC (results not shown here), a more detailed analysis are performed only on selected samples (#1-AlTiN, #4-AlTiON_13, #5-AlTiON_21, #6-AlTiO) as they were the most promising to form a SSC multilayer stack showing clear contrast in their optical properties. Sample #7 was also selected in order to obtain more data about its microstructure. These microstructure, morphology and optical properties of these selected samples will be analysed by XRD, HR-TEM and SE as explained in next sections. After a complete comprehensive analysis, a complete SSC will be designed with optimized optical performance.

4.2.4 Characterization of selected AlTi(O_xN_{1-x}) individual layers

X-ray diffraction (XRD) analysis

The GIXRD patterns of the deposited AlTi(O_xN_{1-x}) films are represented in Figure 4.9. All samples were measured additionally by *θ-2θ* geometry in order to analyse the preferential orientation (XRD patterns not shown). The crystallite sizes were calculated from Scherrer's as an average of all the observed peaks, and they are summarized in Table 4.6 along with the interplanar spacing and the lattice constant.

Table 4.6 – Microstructural data for AlTi(O_xN_{1-x}) thin films on Si substrate obtained from XRD patterns. The interplanar spacing (*d*) and lattice constant (*a*) were deduced from the (200) crystal orientation.

Sample #	X	Pref. orientation	Crystallite size (nm)	*d* (Å)	*a* (Å)
1	0.01	200	11 ± 0.5	2.088	4.176
4	0.26	200	6 ± 0.5	2.087	4.174
5	0.37	200	4.5 ± 0.5	2.086	4.172
6	0.99	No pref.	3.0 ± 0.5	2.011	8.018
7	0.97	No pref.	1.5 ± 0.5	2.035	4.071

A purely cubic B1 osbornite structure, typical for titanium-based nitrides, was observed for the AlTiN coating (#1) in Figure 4.9 (a). Several authors have shown that in the (Ti_yAl_{1-y})N for Al concentrations up to $y<0.6$ a solid solution is formed by incorporation of Al atoms into the NaCl-type lattice of TiN. However, when Al content is approximately $0.6<y<0.75$, the structure consists of a mixture of cubic and hexagonal phase [51,70], or a *h*-AlN incorporated in a cubic

TiAlN matrix [71], as shown in Figure 4.2. No wurtzite structure was observed in the AlTiN sample although the measured Al content was y= 0.63. The observed peaks were displaced to higher angles than the cubic TiN (at 2θ =36.8, 42.8, 61.9º and 74.1º) as the lattice parameter of the AlTiN (4.17 Å) was slightly smaller than TiN (4.23 Å), deposited at the same CVA chamber. This results suggest that titanium atoms in the TiN lattice are substituted by Al atoms with smaller atomic radius [54]. The (200) crystal plane at 2θ=43.3º was the preferential orientation observed for AlTiN. The other peaks identified at 2θ = 37.3, 63.2, 75.6 and 80.0º associated to the crystal orientations (111), (220), (311) and (222), respectively (ICCD card 00-037-1140 for cubic AlTiN) [72]. The dependence of the crystallite size with the thickness was studied by depositing additional AlTiN layers with thicknesses of 100 and 240 nm. There is a dependence on the grain size with the thickness of the layer, correlated to the evolution of the thin film growth. The thinner AlTiN layer (corresponding to the first nanometres of film growth) shows a fine grained structure, with crystallite size of 6 nm. This microstructure evolved into a well-defined columnar structure, with larger crystallite of 11 nm average size. This evolution in the crystallite size was also appreciated in the previous SEM image of the AlTiN film (Figure 4.8 (a)).

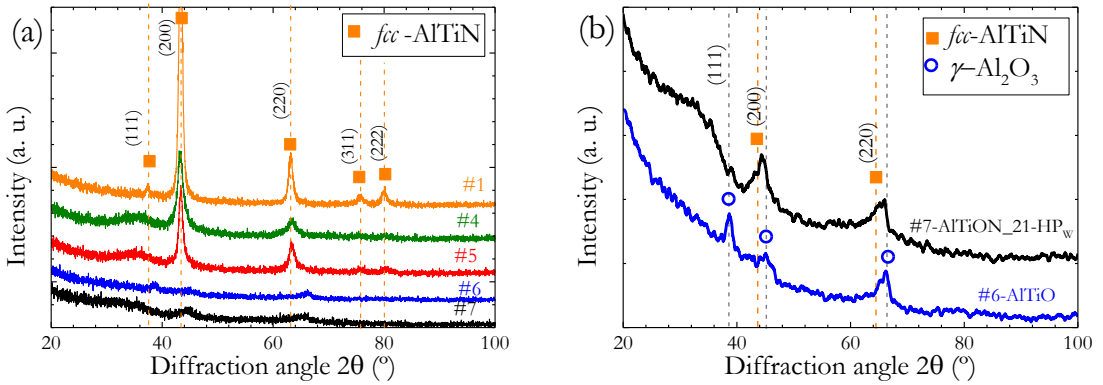

Figure 4.9 – GIXRD patterns of samples on Si(100) substrate (a) AlTi(O_xN_{1-x}) samples with 0; 14; 20; 58 and 60 at.% O content. The vertical lines indicate the peak positions for *fcc*-AlTiN (ICCD card number 00-037-1140) (b) AlTiO and AlTiON_21(HP_w) samples represented with increased intensity resolution. The peak positions of *fcc*-AlTiN and γ-Al_2O_3 (ICCD card number 00-001-1308) are indicated.

The GIXRD diffractograms of the oxynitride films (samples #4 and #5) are qualitatively similar to the oxygen-free AlTiN sample (Figure 4.9 (a)). These samples show again the typical cubic NaCl-type structure, with (200) as preferential orientation at 2θ=43.3º. However, a progressive shift of the (200) diffraction peak toward higher diffraction angles with increasing oxygen concentration can be appreciated. This corresponds to a diminution of the lattice parameter caused by the formation of metal vacancies or replacement of N atoms by smaller O ones. Additionally, this shift is accompanied by a broadening of the peak associated to a decrease in the crystallite size. No crystallite reflections associated to oxide phases were observed in samples #1 to #5. However, a broad peak at 30º<2θ <40º can be appreciated for the high oxygen content

samples #4 (14 at.% O) and #5 (20 at.% O) [73]. This can be related with the formation of amorphous phases in the coating [7] in agreement with the decrease in the (Ti+Al):(N+O) ratio measured by ERD (Table 4.5).

It is also worth mentioning that the observed peaks of al XRD patterns shown in Figure 4.9 could be attributed to *fcc*-AlTi metallic crystals incorporated into the films, in the form of droplets, as has been previously observed [74,75].

The coatings become practically XRD amorphous for samples #6 and #7. However, if they are represented separately with increasing the intensity resolution (Figure 4.9 (b)), small crystallites are revealed. In sample #7 (AlTiON_21 (HP_w)), the *fcc* lattice still appears despite the large proportion of oxygen as confirmed by the two broad diffraction peaks at 2θ = 44 and 65º. These peaks could be associated to (200) and (220) crystal planes, respectively, of the *fcc*-AlTiN NaCl-type structure. The displacement to higher angles observed in these peaks could be explained as the lattice parameter is much smaller in the oxidized sample (4.02 Å) than in the nitride (4.18 Å) and a high value of replacement of N by O in the nitride lattice [59]. The formation of small AlTiN crystallites (1.5 ± 0.5 nm) encapsulated by an amorphous oxide phase has been previously reported [76]. Meanwhile, the pure oxide coating (sample #6) is X-ray amorphous/nanocrystalline having a structure corresponding to metastable cubic γ-Al_2O_3 phase (ICCD card 00-004-0880) [59], with small peaks at 2θ = 38º, 45 and 45º corresponding to (311), (400) and (441), respectively, of the cubic structure. No crystal TiO_2 or Al_2TiO_5 phases were observed, as these crystal structures are associated to higher deposition temperatures (T_s>750ºC) [77,78] than the employed for these samples (T_s=450º). These results, together with the ERD analysis, suggest the formation of an poorly crystalline γ-Al_2O_3 phase embedded in an amorphous TiO_2, Al_2TiO_5 and $(Al,Ti)_2O_3$. HR-TEM images will confirm these results as discussed in the following section.

Film morphology studied by HR-TEM

HR-TEM and electron diffraction (ED) patterns give more accurate information of the crystal structure for the different AlTi(O_xN_{1-x}) samples. In addition, the STEM mode along with the EDX spectroscopy would provide information of the composition for specific selected regions or a profile in the cross section. Cross-sectional HR-TEM and STEM micrographs of samples #1, #5 and #7 deposited on inconel substrate are shown in Figure 4.10, to Figure 4.15.

An overview HR-TEM image of the AlTiN sample #1 (Figure 4.10(a)), shows an initial columnar growing (region 1) of ~150 nm with narrow well-defined columns, and crystallite size of ~ 6nm, in agreement with XRD patterns. This region was followed by a second columnar growth regime (region 2) with wider columns and bigger crystallite size (11 nm). This growth was only interrupted by some defects (indicated in the figure) attributed to the release of a macroparticle and the subsequent growing on the remaining hole.

The corresponding SAED pattern (Figure 4.10 (b)) is constituted of rings, exhibiting some spots originating from the large size of the crystallites in the films. The spots are concentrated into groups, which can suggest certain film texturing. From SAED pattern it could be derived that the phase formed in the films is solid solution *fcc*-AlTiN without phase separation observed. The interplanar distances (*d*) calculated from the ED pattern, closely matches with (111), (200), (220), (311) and (400) planes of the B1 cubic AlTiN (ICCD card 00-037-1140) [72], confirming the results from XRD.

Amplified HR-TEM images were taken to assess microstructural changes in the different growth regimes. Figure 4.10 (c) shows a higher amplification image of the initial region close to the substrate (designated as region 1 in Figure 4.10 (a)), displaying a perfect adherence between substrate and AlTiN film. The differences in this first growing region were attributed to a transition between the amorphous oxidized top layer of the substrate (> 5 nm), and a stable crystallite columnar growth with (200) as preferential orientation plane. In this growing regime, the AlTiN has polycrystalline structure, as revealed by the FFT analysis (inset in Figure 4.10 (c)) that shows three circular intensity maxima corresponding to lattice plane distances of 1.49, 2.07 and 2.37 Å, in good agreement with (220), (200) and (111) of *fcc*-AlTiN [79].

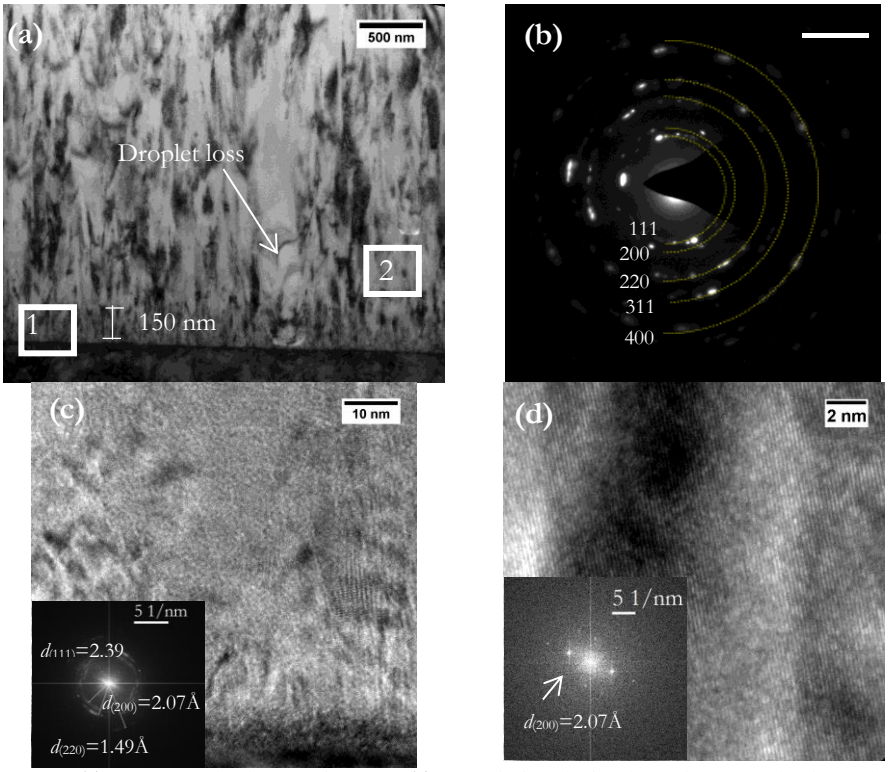

Figure 4.10 – HR-TEM cross-section images of 1.6 µm AlTiN sample deposited on inconel. (a) Overview image, indicating a initical 150 nm growing regime with narrower columns. A deffect assigned to a macroparticle loss is indicated. (b) Selected area electron diffraction pattern. (c) Amplified image of the interface region between AlTiN and the substrate, region 1 in (a). (d) Amplified image of the developed columnar regime, region 2 in (a). The FFT analysis of (c) and (d) are included.

Figure 4.10 (d) shows the amplified HR-TEM image of the upper region 2 of the AlTiN sample (designated as region 2 in Figure 4.10 (a)). The sharp diffraction spots of the FFT (inset in Figure 4.10 (d)) corroborate the crystalline columnar growth of AlTiN cubic structure. The FFT of this region reveals only one lattice plane distance of 2.07 Å, attributed to the (200) crystal planes, the preferential orientation indicated previously. In order to evaluate element content differences in in the region where the macroparticle made a defect, images in STEM mode were obtained (Figure 4.11) (a)). EDX results from regions i and ii in the STEM image of Figure 4.11 (a) were in very good agreement with the composition obtained with ERD. No main differences were found between the selected regions (Figure 4.11 (b)). Similar composition results were obtained as well for the two growing regions 1 and 2 indicated in the previous HR-TEM images (Figure 4.10).

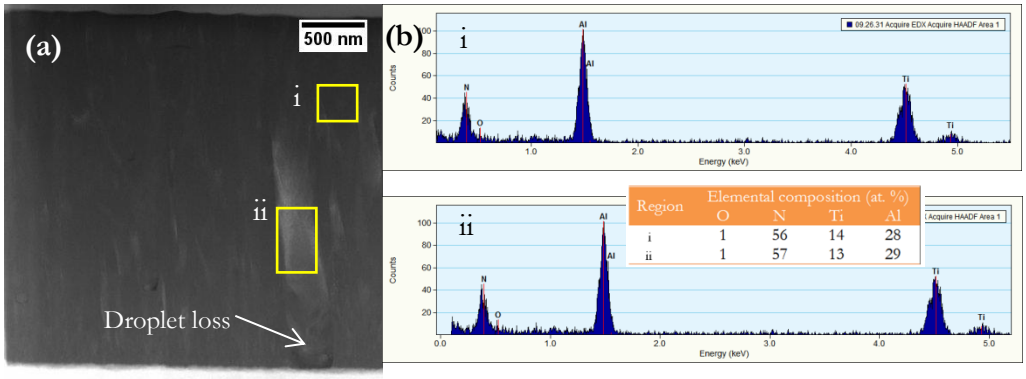

Figure 4.11 –STEM image of AlTiN sample on inconel. A deffect assigned to a macroparticle loss is indicated (b) EDX analysis in selected areas: region (i) corresponds to the developed columnar crystal growth and region (ii) corresponds to the area with a defect in the growth assigned to a macroparticle loss (brigther region).

HR-TEM images of AlTiON sample with 21 at.% O (sample #5) grown on a 0.5 μm of AlTiN are shown in Figure 4.12. As observed from previous SEM images, even small concentration of oxygen can significantly modify the morphology of the film, promoting renucleation during films growth and formation of smaller grains. This can be better appreciated in the overview HR-TEM image (Figure 4.12 (a)) where AlTiN and AlTiON layers are clearly distinguishable. The interface analysis shows that the clear columnar structure in the AlTiN is blurred in the AlTiON region. These not-well defined AlTiON columns grow from the underneath layer, as if the AlTiN serves as a template for promoting pseudomorphic growth of the AlTiON layer [7,64]. The interplanar distances observed in SAED pattern of the AlTiON layer (Figure 4.12 (b)), correspond to *fcc*-AlTiN crystal structure [72], but the presence of diffraction rings varying sharpness indicate very small misoriented crystallites and amorphous regions. As the grains get smaller, less spots are visible in the rings. No evidence of crystalline Al_2O_3 or TiO_2 was observed.

The interface was imaged in higher resolution in Figure 4.12 (c) and (d). The prolongation of the columns from AlTiN to AlTiON was still visible. However, a periodic multilayer structure with periodicity of ~2 nm was now detected in large columnar grains of the AlTiON (Figure 4.12

(e)). Similar multilayer structure with small columnar grains was described by Sjölen for equivalent CVA system [7], associated to rotation of the substrate holder during the deposition. The FFT analysis of this layer (inset in Figure 4.12 (e)) cannot clearly identify single crystallites. This is most probably due to the superposition of several crystallites over the thickness and an amorphous matrix. Two circular intensity maxima were hardly identified, corresponding to lattice plane distances of 1.45 and 2.37 Å, in agreement with (220) and (200) of *fcc*-AlTiN [79], but with smaller lattice parameter than for AlTiN sample.

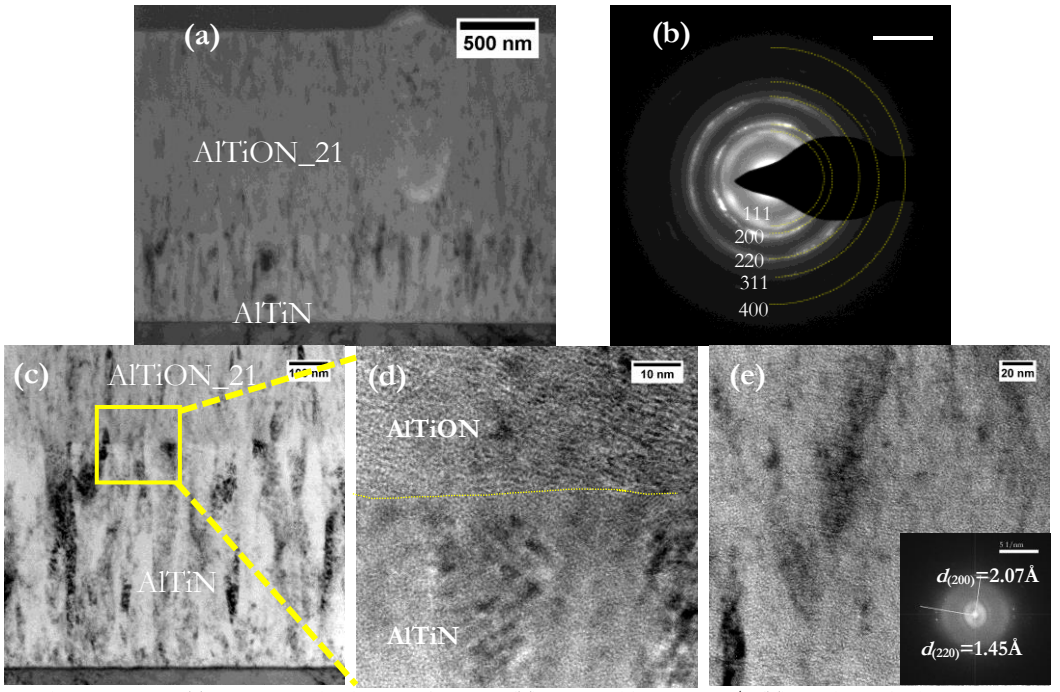

Figure 4.12 – HR-TEM cross-section images of 1.6 µm AlTiON_21 with 20at.% O / AlTiN on inconel substrate (a) Overview image, indicating AlTiON and AlTiN layers. (b) Selected area electron diffraction pattern. (c) and (d) amplified images of the interface region between AlTiN and AlTiON. (e) Amplified image of the AlTiON layer, with the FFT analysis of this region included.

STEM images of the interface between AlTiN and AlTiON (21at.% O) were obtained (Figure 4.13 (a)) to determine the differences elemental concentration of the different layers by EDX analysis. The table inserted in Figure 4.13 (b) shows the composition was in good agreement with the values obtained by ERD (Table 4.5).

Results of STEM image and the corresponding EDX analysis of the multilayer region are shown in Figure 4.13 (c) and (d). The STEM image reveals how the multilayer are likely to be a result of modulation of the films composition, where the bright layers have high metal concentration (i.e. (Ti+Al)/(Ti+Al+N+O)) and dark layers where the reactive gases have high content. The rotation of the sample holder was accounted to be the responsible of this periodic multilayers formation.

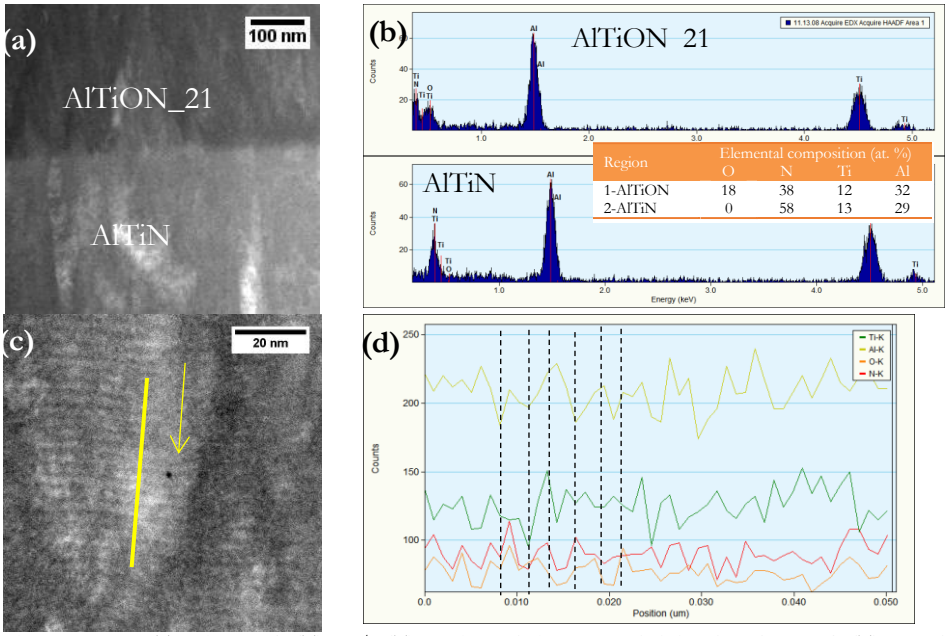

Figure 4.13 – (a) STEM image of AlTiON / AlTiN on inconel. (b) EDX analysis in selected areas of AlTiON and AlTiN layers. (c) Amplified STEM image of AlTiON where multilayers with ~2nm periodicity are distinguishable and (c) EDX analysis of the profile indicated in (c). Vertical lines are included to guide the eye.

Finally, an overview HR-TEM image of the sample #7, AlTiON_21 (HP_w), is shown in Figure 4.14 (a). In the region close to the interface, a periodic multilayer AlTiON structure was observed once more. The periodicity was clearer observed in the enlarged HR-TEM images (Figure 4.14 (b) and (c)) showing equivalent periodicity than in the previous AlTiON (21 at.%O) sample. This region indicate a first epitaxial growth of a cubic *fcc*-AlTiN columnar structure continuing from the AlTiN layer, with an amorphous matrix, as confirmed with the FFT analysis (Figure 4.14 (d)), but distributed in multilayers. The crystalline structure was cubic despite the high levels of oxygen. The continuous deposition at higher pressure supresses gradually the multilayer by an increased renucleation in the upper region and final transformation into an amorphous-fine grained multiphase (Figure 4.14 (e)). The transition is attributed to a progressive increase in the oxygen content and in the pressure, what involves a less conductive surface of the coating, reducing the impact energy of the arriving ions [7]. This could lead to less adatom mobility due to the higher deposition pressure and an increase of the renucleation rate (and reduction in the grain size). Hence, the previous multilayer microstructure is transformed into a solid solution of crystalline nanoparticles embedded in an amorphous matrix (Figure 4.14 (f)). The FFT of a selected grain (Figure 4.14 (g) and (g)) reveals only one lattice plane.

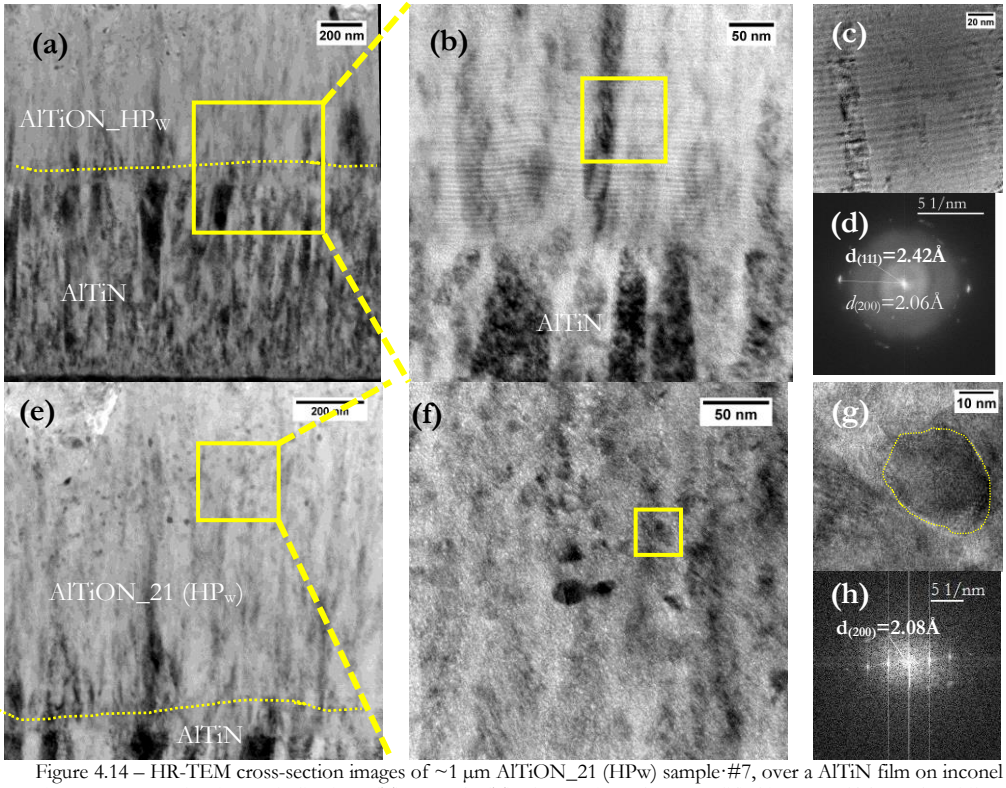

Figure 4.14 – HR-TEM cross-section images of ~1 µm AlTiON_21 (HPw) sample·#7, over a AlTiN film on inconel substrate (a) Overview image, indicating AlTiON and AlTiN layers. (b) and (c) Amplified images self-formed multilayer region with (d) FFT analysis of (c). (e) Overview image, indicating the formation of nanoparticles in the upper region of the AlTiON. (f) and (g) Amplified image of the nanoparticles, and (h) FFT analysis of nanoparticle shown in (g).

In the STEM images shown in Figure 4.15 (a), the two different regions are clearly differentiated. An overall EDX analysis of the multilayer region (Figure 4.15 (b)), show good composition agreement with the previous ERD analysis and only a 3at.% of N was detected. On the other hand, an EDX analysis zoomed on a nanoparticle reveals 14% at. N. this reveals the AlTiN nanoparticles embedded on an oxide amorphous matrix. The EDX analysis of the multilayer structure reveals bright and dark regions associated with the rotations of the sample holder, with high similarity to the previous HR-TEM image in the AlTiON_21 sample.

The multilayer structure observed on the samples, has been observed previously in commercial cathodic vacuum are coatings, which commonly employed a rotatory substrate holder to maximize the number of coatings in the same deposition. However, it is worth highlighting the lack of studies describing in such detail the multilayer composition, as done in this work with high resolution TEM.

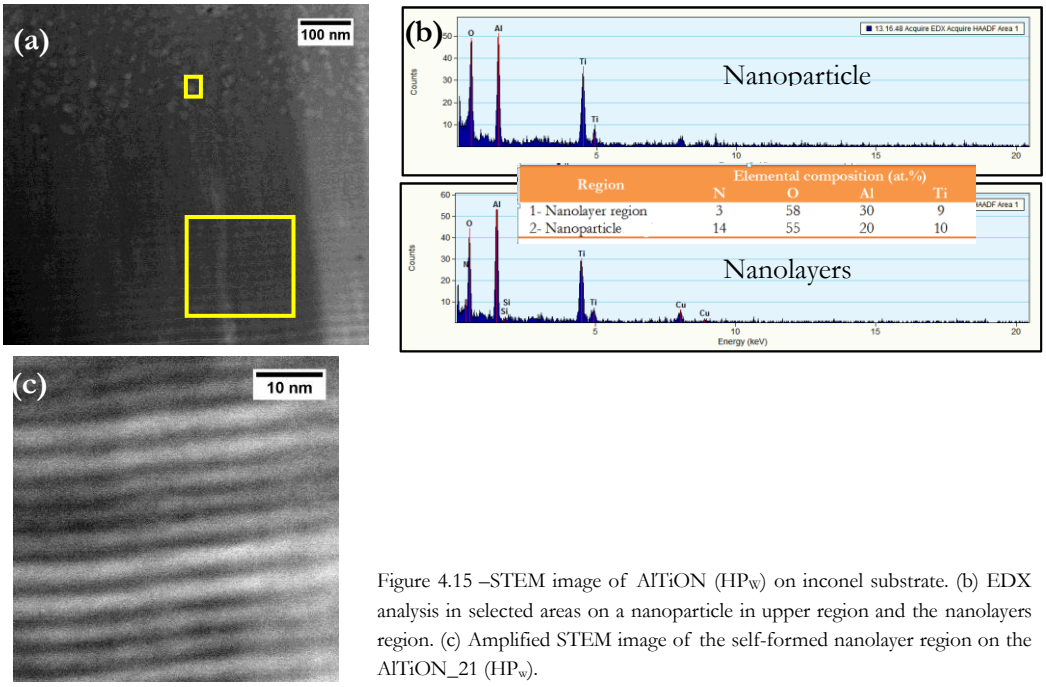

Figure 4.15 –STEM image of AlTiON (HP_W) on inconel substrate. (b) EDX analysis in selected areas on a nanoparticle in upper region and the nanolayers region. (c) Amplified STEM image of the self-formed nanolayer region on the AlTiON_21 (HP_w).

In summary, the microstructural and morphological characterization show the evolution of the Al-Ti-N ternary phases when the oxygen concentration or the pressure was increased. This evolution of the material when increasing the O content was schematized in Figure 4.16 [76].

Figure 4.16 – Stages of the microstructures of Al–Ti-O–N coatings at increasing O concentrations.

There is a pronunced columnar micrsotructure observed for the oxygen-free AlTiN samples, parallel to the preferential (200) crystal orientation of the cubic structure. Increasing the O content resulted in a width and length shringk of the columns, with smaller cristallites embedded on amorphous matrix, as confirmed by XRD, SEM and HR-TEM characterization and previously reported by Petrov *et al* [80]. The higher oxygen content cannot be accommodated into the AlTiN lattice, and amorphous $(Al,Ti)_2O_3$, Al_2O_3 and TiO_2 phases appeared between the grain boundaries, what results in a reduction of the grain size. An initial region of epitaxial growth following columnar AlTiN was detected, despite the fact of the multilayers formed associated with sample rotation. Larger oxygen concentrations (by increasing the deposition working pressure) the epitaxial growth of individual crystals is periodically interrupted by the formation of an amorphous matrix which completely covers the AlTiN nanocrystals embedded in it. The composite film is composed

of three dimensional globular grains separated by an amorphous $(Al,Ti)_2O_3$ phase. At even higher oxygen concentrations (sample #6) amorphous Al,Ti oxide film is formed.

The high solar absorptance expected from graded SSC based on $AlTi(O_xN_{1-x})$ films are attributed to the morphology structure detected in the $AlTi(O_xN_{1-x})$ layers, as schematized at Figure 4.17. The incident light is scattered by the AlTiN nanocrystalline embedded in the amorphous $(Al,Ti)_2O_3$ matrix in the $AlTi(O_xN_{1-x})$ layers and hence, the optical path is enlarged [33].

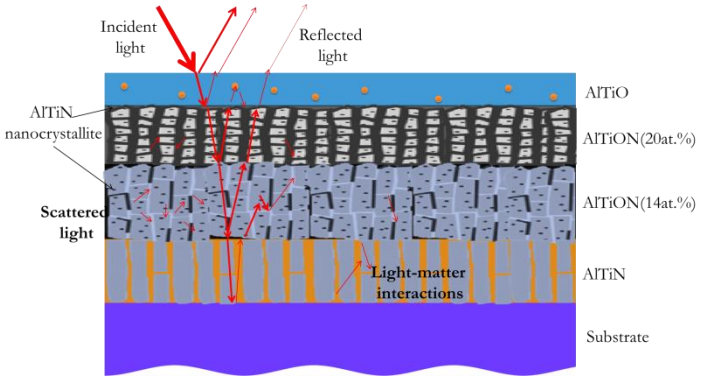

Figure 4.17 – Schematic diagram of the reflectance as interference sum of multiples reflections of the interfaces and multiple scattering effects in AlTiO/AlTiON/AlTiN multilayer SSC stack.

The solar absorption is related to light-matter interaction mechanisms, including photon-induced electronic transitions, and photon-induced collective electron oscillations in the nanoparticles [81]. Moreover, when the particle density is high, the coupling of plasmon between neighbouring particles can occur, which increases the heating and helps transmitting it efficiently to the metallic substrate [82]. This multilayer structure consisting of layers with graded oxygen concentration, is expected to be very efficient for solar selectivity [32,83].

4.2.5 Optical characterization of $AlTi(O_xN_{1-x})$ individual layers

A proper analysis of the optical constants is crucial to success in the design of the multilayer SSC. After a detailed microstructural and morphological analysis, the optical properties of the selected $AlTi(O_xN_{1-x})$ films deposited with different $O_2/(O_2+N_2)$ ratio of reactive gases were analyzed by SE. Then, the reflectance spectra were measured in order to verify the correct modelling of the optical constants, comparing measured and simulated specular reflectance.

Spectroscopic ellipsometry (SE)

Figure 4.18 (a) shows the experimentally measured SE values of the AlTiN sample along with the best fitted theoretical spectrum. In this oxygen free sample (sample #1), Drude model is needed to model the metallic behaviour [25]. The Drude term involves two independent parameters whose relations are described in Chapter 2 and included in Figure 4.18 (a). The unscreened plasma energy (E_{PU}) measures the concentration of conduction electrons in the film

and it can be used to quantify the metallic character. The second parameter is the damping factor (Γ_D) related to the scattering of electrons [50].

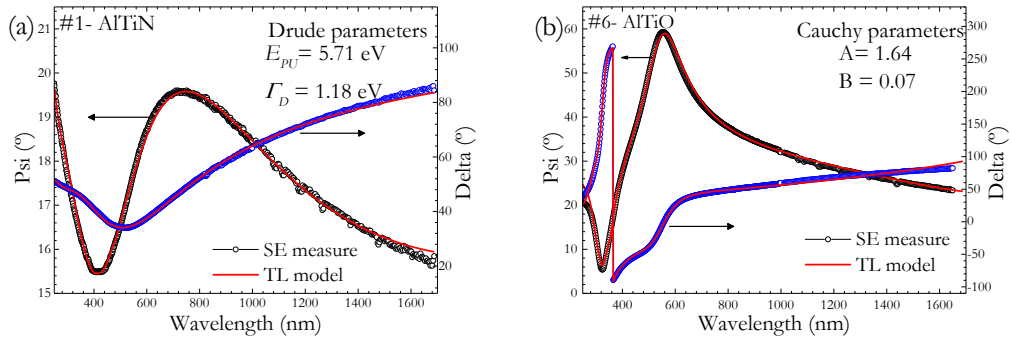

Figure 4.18 – Experimental psi and delta along with fitted values for (a) AlTiN and (b) AlTiO samples deposited on silicon substrate. The parameters employed for each optical model are icluded in the figure.

When the oxygen comes into play, the analysis of SE results gets more complicated. In the case of the pure oxide film (sample #6), the microstructural characterization reveals that the film was almost amorphous. As a semi-transparent dielectric film in the visible, the optical constants were modelled by using Cauchy's dispersion formula, which main parameters employed and the goodness of the fitting are represented in Figure 4.18 (b).

The complex refractive index of the intermediate oxynitride films (samples #4 and #5), was calculated as a contribution of intraband (electronic conductivity) and interband absorptions. As analysed by XRD and HR-TEM, the samples present columns of cubic crystalline structure along with amorphous regions. Therefore, in this thesis the optical constants of these samples were assumed to follow the Drude dispersion model for the contribution of the intraband transitions combined with Tauc-Lorentz (TL) peaks. TL has been previously employed to describe the optical constants in case of amorphous or polycrystalline dielectric materials [84,85], and assuming non-interaction between atoms. Drude parameters required for the modelling of these samples were pretty similar than the employed for the AlTiN, showing no main differences in their metallic behaviour. The best fitting obtaining for AlTi(O_xN_{1-x}) samples with 14 and 20 at.% of O are show at Figure 4.19 (a) and (b), respectively.

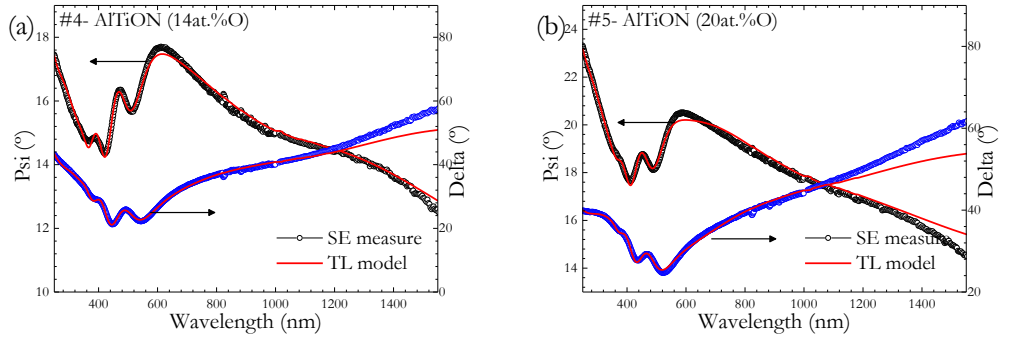

Figure 4.19 – Psi and delta measured and modelled values for (a) sample #4, 14 at.% O and (b) sample #5, 20 at.% O deposited on silicon substrate.

In the case of sample #7, deposited with higher working pressure, their optical constants cannot be modelled following a similar pattern. After the analysis by HR-TEM, the sample shows a solid solution of crystalline nanoparticles embedded in an amorphous matrix (Figure 4.14). The fitting of this sample (Figure 4.20) were successfully performed by a Bruggeman EMA, with inhomogeneous material consisting on an amorphous AlTiO matrix, with a volume fraction of 5% of AlTiN globular particles (depolarization factor 0.55). The employed optical constants for the EMA model were the measured of the AlTiO (sample #6) as matrix component and the AlTiN (sample #1) as the embedded nanoparticles, represented in Figure 4.18.

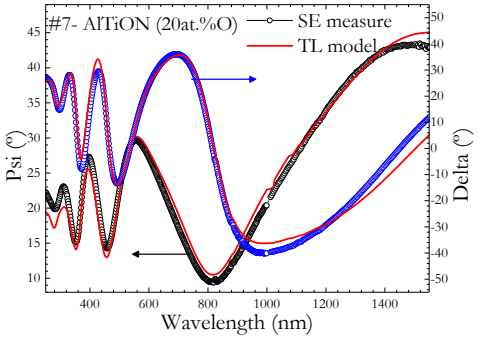

Figure 4.20 – Psi and delta measured and modelled values for sample #7 with 58at% O on silicon substrate.

The refractive index (n) and extinction coefficient (k) as a function of wavelength, for the AlTi(O_xN_{1-x}) samples generated from the best fit parameters of the above described optical models are shown in Figure 4.21.

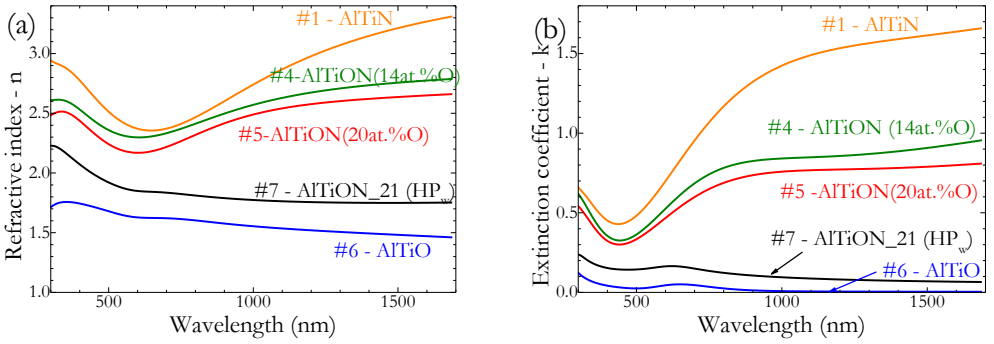

Figure 4.21 – (a) Refractive index (n) and (b) extinction coefficient (k) after modelling the measured SE values of AlTi(O_xN_{1-x}) samples on Si substrate with 0.5, 14, 20 and 60 at.% of O.

The n and k values of AlTiN (sample #1) show a minimum at λ~500 nm and thereafter, increases monotonically with increasing wavelength. This increment with the wavelength indicates the metallic behaviour of AlTiN sample. However, the plasma wavelength of the AlTiN shows a higher value than typical metals, resulting in a possible candidate as intrinsic selective material itself. The absorption coefficient ($a=4\pi k/\lambda$) increases in the visible region and decreases in the IR. Similar trend were observed for the complex refractive index of AlTiON_13 and AlTiON_21 samples [86].

The refractive index of the deposited AlTiN, AlTiON (14 at.% O), AlTiON (20 at.% O) layers were 2.42, 2.31 and 2.21, respectively at a wavelength of 550 nm (Figure 4.22). At the same wavelength, the extinction coefficients of the AlTiN, AlTiON(14 at.% O) and AlTiON(20 at.% O) were 0.58, 0.45 and 0.40, respectively. The refractive index and extinction coefficients of the AlTiN and AlTiON samples are comparable to the values of transition metal nitride and oxynitride films reported elsewhere [25,33,58,87]. The decrease of the *n* and *k* values with higher oxygen concentrations indicate the intermediate character, i.e. a transition between the metallic and the dielectric behaviour, which is in good agreement with the previous morphology and microstructure characterization. It can be concluded how by increasing the oxygen content, there is a clear transition from metallic to dielectric nature. This gradient in the refractive index will enhance the overall absorptance in a designed SSC employing the different AlTi(O_xN_{1-x}) samples [28].

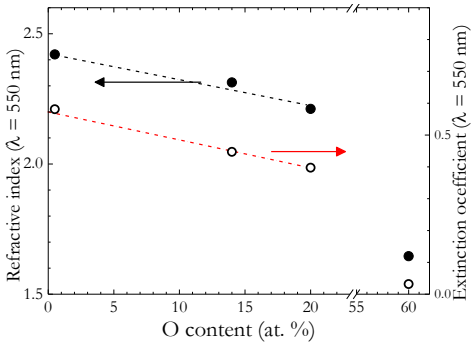

Figure 4.22 – Evolution of the refractive index (*n*) and extinction coefficient (*k*) with the O content.of AlTi(O_xN_{1-x}) coatings deposited at P_w=1.5 Pa.

The abrupt decrease in the extinction coefficient for high oxygen content has been attributed to the loss of percolation between crystalline particles and the appearance of a thick amorphous region around the AlTiN crystallites that separates the crystallites from each other [76]. It has been previously reported a change in the behaviour from metallic to dielectric at oxygen concentrations higher than 25-30 at.% [6,18].

The pure oxide sample #6 is transparent in the Vis-NIR wavelength range and the *n* values decreases with the wavelength, following a *normal* dispersion. The refractive index n_{550nm}=1.64, is similar than the previously measured for Al_2O_3 (n_{550nm} =1.67) in chapter 3. Furthermore, the extinction coefficient values of AlTiO sample was found to be negligible in all wavelength regions, as expected for a dielectric materials. This implies that incident photon loss caused by absorption in the antireflection layers can be neglected. The fundamental band gap, as in the alumina, is situated at λ<~200 nm, and below this wavelength interband transitions are possible and the *k* reaches high values.

Contrary to expectations sample #7 oxide sample shows no dielectric behavior but a high absorption coefficient within the whole wavelength range, with n_{550nm} =1.84 and k_{550nm} =0.15. Such behaviour is typically exhibited by amorphous semiconductors materials, but the polycrystalline

contributions cannot be ruled out, as confirmed by the tiny peaks in the XRD patterns and the HR-TEM images.

Spectral reflectance UV-Vis-NIR + FTIR

The reflectance spectra of the individual single layers were recorded in order to verify the modelling of the previous optical constants. Very good agreement was found between simulated and measured reflectance (Figure 4.23) in the SE measured range.

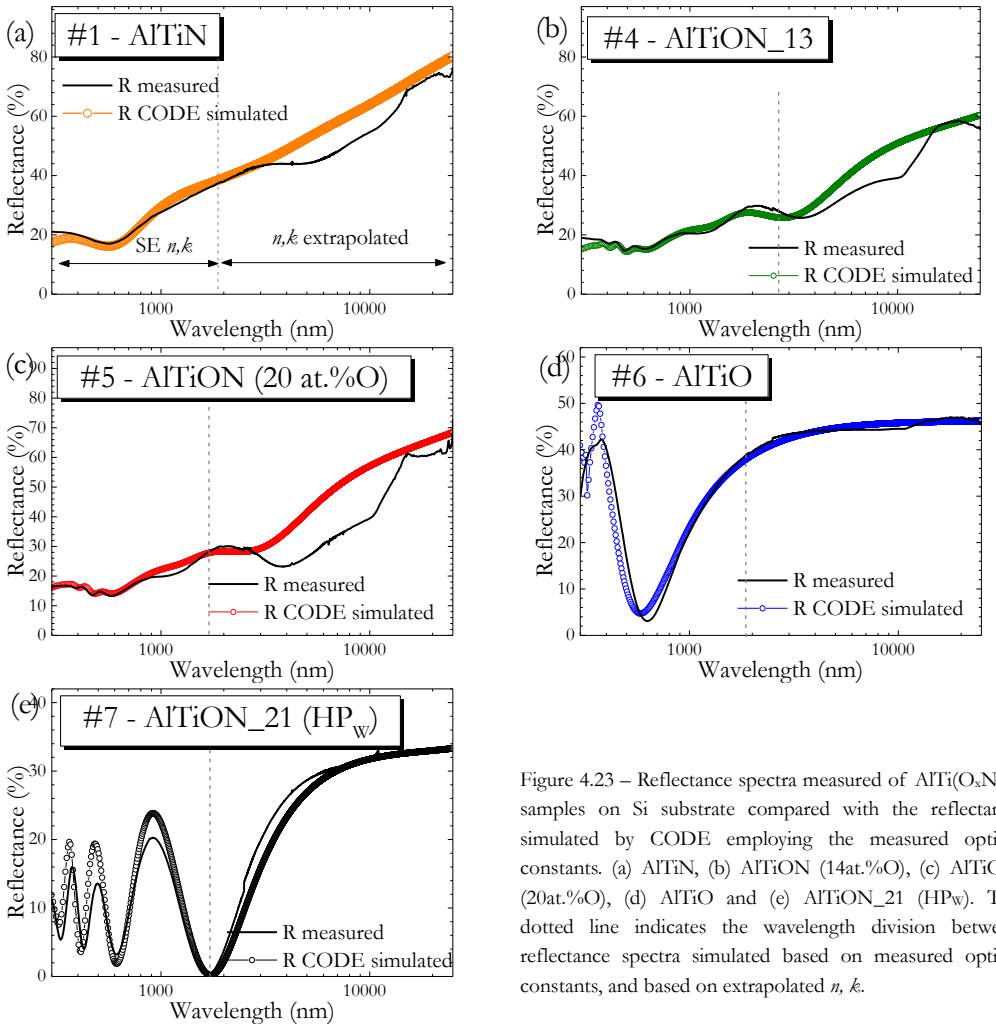

Figure 4.23 – Reflectance spectra measured of AlTi(O_xN_{1-x}) samples on Si substrate compared with the reflectance simulated by CODE employing the measured optical constants. (a) AlTiN, (b) AlTiON (14at.%O), (c) AlTiON (20at.%O), (d) AlTiO and (e) AlTiON_21 (HP_W). The dotted line indicates the wavelength division between reflectance spectra simulated based on measured optical constants, and based on extrapolated *n, k*.

The simulated reflectance spectra includes a pure oxide top layer with a graded composition between air and the final AlTi(O_xN_{1-x}) material for a good fitting along the SE measured wavelength range.

The *n, k* values measured in this work were restricted by the SE device to the 190-1700nm wavelength range. Hence, the optical constants must be extrapolated up to the IR range for a proper estimation of the thermal emittance. Figure 4.23 includes the reflectance measured and

simulated in the complete wavelength range (300 to 25000 nm), with the optical constants extrapolated in the IR following the procedure explained in chapter 2. In samples #1, #4 and #5 a discrete absorption is observed at λ~8000 nm, associated to vibrational modes from the amorphous matrix phase. This vibrational mode cannot be included in the proposed extrapolation model. However, the fitting is completely satisfactory and far better than the extrapolation performed by the simulation software and the one commonly employed in literature [88–90]. This is a proof of the suitability of the optical constants for designing multilayer coatings based on these oxynitrides.

The reflectance spectra measured in the whole wavelength range of interest (0.3 to 25 μm) for the AlTi(O_xN_{1-x}) selected samples on inconel substrate are shown in Figure 4.24. As explained in the SE analysis, AlTiN, AlTiON (14at.%) and AlTiON (20at.%) show intrinsic selective behaviour, with low reflectance in the Vis range, and high IR reflectance. The position of the minimum value of the reflectance curve can be modulated by tuning the film thickness.

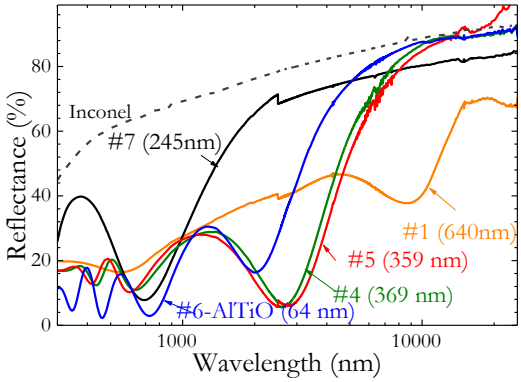

Figure 4.24 – Measured reflectance spectra of AlTi(O_xN_{1-x}) samples on inconel substrate with different thickness, combining UV-Vis-NIR and IR wavelength range. The reflectance spectrum of the inconel substrate is also included in the figure

The nitrogen free sample (AlTiO) is transparent in all the range of interest and does not show interband absorptions in the IR. However, the sample acts as antireflective layer, decreasing the reflectance in the Vis-NIR range and showing the typical modulations of dielectric materials.

AlTiON sample #7 deposited at higher pressure does not exhibit the typical optical response for oxides. This sample shows intrinsic selectivity with a minimum of reflectance at λ=750nm and very high IR reflectance. However, this sample was not employed in the design of the complete SSC, due to its non-homogeneous morphology along the thickness, as observed in the HR-TEM images.

4.3. Optimization of solar selective multilayer stack based on AlTi(O_xN_{1-x})

The design of a complete SSC multilayer based on AlTi(O_xN_{1-x}) materials requires an absorber layer with a gradient composition of AlTi(O_xN_{1-x}) in combination with a dielectric antireflective layer of $(Al,Ti)_2O_3$ and an IR reflective metallic layer. The oxygen/nitrogen ratio and sequence of layers for the simulation of complete SSC were decided once the optical constants of AlTi(O_xN_{1-x}) samples were determined.

Two designed SSC were deposited by CVA, and thereafter, their morphology and optical properties were analysed. In order to verify the temperature resistance, the multilayers were submitted to asymmetric and cyclic thermal stability tests.

4.3.1 Simulation of a complete SSC based on AlTi(O_xN_{1-x})

Using the measured and verified optical constants of the single AlTi(O_xN_{1-x}) layers, complete SSC with different configuration were designed, denominated as Multilayer 1, 2 and 3. The complete stacks were simulated on 2 mm thick Inconel HAYNES@230 whose *n* and *k* were as well experimentally measured. The number of AlTi(O_xN_{1-x}) layers, oxygen concentration and layer thickness were optimized in order to maximize the solar absorptance and minimize the thermal emittance. The simulated reflectance spectra of three configurations, and the parameters employed for each one are schematized in Figure 4.25.

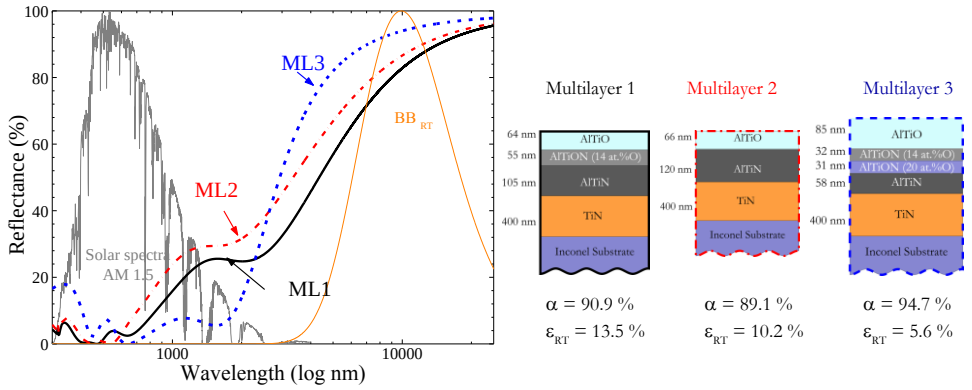

Figure 4.25 – Specular reflectance obtained from CODE simulation of three different configurations: multilayer 1, 2 and 3. The details of the parameters employed and the values for the solar absorptance (α) and thermal emittance (ε) from simulation are included in the figure

The absorptance and thermal emittance are included in Figure 4.25. Multilayer 1 composed of AlTiO/AlTiON (14at.%)/AlTiN/TiN exhibited α = 90.9% and ε_{RT}=13.5%, multilayer 2 (AlTiO/AlTiN/TiN) exhibited slightly lower values for both α = 89.1% and ε_{RT}=10.2%. Multilayer 3 has the best optical performance, employing a design with 5 layers of

AlTiO / AlTiON(14at.%) / AlTiON(20at.%) /AlTiN / TiN with values of α = 94.7% and ε_{RT}=5.6%.

This improvement in the third design may be attributed to the contributions of not only the metallic nanoparticles dispersed in the amorphous matrix but also by the multilayer interference effect. The thicknesses were selected to promote multiple reflexions in the interfaces, returning to interference destructively after the light is reflected from the front surface of the films. The thicknesses of each layer must be carefully chosen to set the electromagnetic amplitude to zero at desired wavelengths and hence, slight variations in film thickness can lead to significant changes in the optical properties.

Due to the technical difficulties associated to an accurate adjustment in the growing thickness for each layer with the rotatory CVA system, and the possible errors in the transition between layers, the designed multilayer 1 and 2 were the selected ones to be deposited and thermal tested, as explained in next section.

4.3.2 Deposition and characterization of complete SSC based on AlTi(O_xN_{1-x})

The simulated multilayers 1 and 2 were deposited by CVA on mirror polished Inconel substrates, employing similar deposition parameters as the explained for the individual layers. The cross sectional morphology of the two multilayers was analysed by SEM (Figure 4.26). From these images it can be observed that there is a good adhesion without delamination problems between the substrate and the TiN IR layer and between layers that comprises the stack. The thicknesses of the different layers are included in the SEM images. As expected for thin layers, no droplets or macroparticles were detected in the cross sections of both complete SSC.

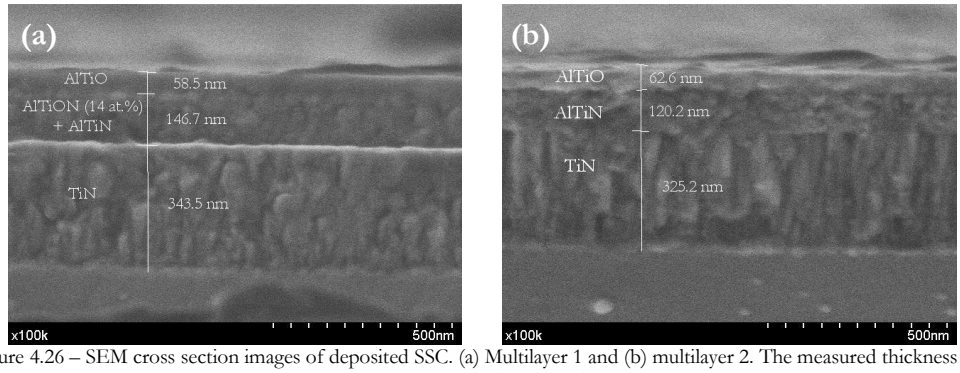

Figure 4.26 – SEM cross section images of deposited SSC. (a) Multilayer 1 and (b) multilayer 2. The measured thickness and layer distribution are indicated in the images.

Only three different layers can be distinguished from the SEM image of the multilayer 1 (Figure 4.26 (a)), where the medium layer corresponds to AlTiON (14at.%) and AlTiN with no differentiated growing regime. The total thickness of these two layer should be 160 nm instead of the 146.7 nm deposited. There was also a slight difference in the AR layer thickness, showing 5.5

nm less than designed. These discrepancies between simulated and deposited thickness may result in differences in the optical outcomes. The deposited thicknesses of Multilayer 2 (Figure 4.26 (b)) were in good agreement with the nominal values.

The spectral reflectance of the multilayer stacks were measured by UV-Vis–NIR and FTIR spectrophotometers in the range of 0.3 – 25 μm. In Figure 4.27, the experimental reflectance is compared with the optical simulated reflectance for the two designed multilayer stacks.

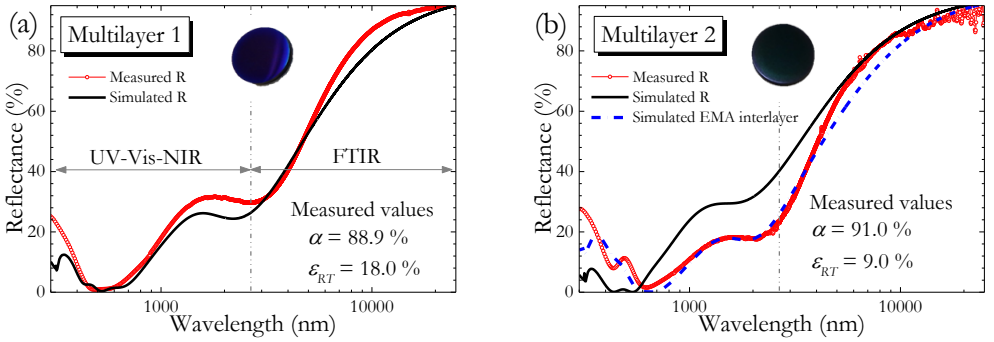

Figure 4.27 –Simulated and experimentally measured reflectance spectra of (a) multilayer 1 and (b) multilayer 2. The solar absorptance and thermal emittance values obtained from the measured curves and the images of the as deposited SSC are also indicated in the figure. An optimized simulated spectra in included in (b)

The absorptance (indicated in Figure 4.27) was 88.9 and 91% for multilayer 1 and multilayer 2, respectively, with a variation $\Delta\alpha$ ±2% in comparison to simulated results. The measured thermal emittance at room temperature also shows a slight difference with regard to the simulated, obtaining ε_{RT} =18 and 9% for multilayer 1 and multilayer 2, respectively. Deposited SSC multilayer 2 shows improved values for α and ε than the simulated, turning into the most promising design.

The fitting of the simulated reflectance of the tandem SSC is not completely satisfactory as the interfaces between AlTiN AlTiON and AlTiO are not sharp and well-defined in the deposited stack. Nonetheless, the behaviour is as a gradient in the optical constants. Hence, a new simulations was performed in multilayer 2 (Figure 4.27 (b)), introducing an EMA interlayer between AlTiN and AlTiO. Thanks to the experience gained in chapter 3 with the different EMA models, a Bergman effective medium was selected, with 33% VF of AlTiN embedded into AlTiO matrix, with percolation degree of 0.66 and a fitted spectral density plot.

Hence, and despite of all these uncertainties an excellent fitting of multilayer 1 was obtaining, and it was significantly improved in multilayer 2 with the incorporation of a Bergman EMA interlayer composed for the upper a lower layers. These results shows once again the strength and validity of the optical simulations performed in this thesis.

4.4. Durability tests of complete SSC based on AlTi(O_xN_{1-x})

In this section, a detailed analysis of the thermal stability of the deposited multilayer stacks was carried out. The thermal stability and ageing properties of the designed complete solar selective were investigated by exposing the samples at asymmetric and cycling thermal treatment tests, described in chapter 2. Their microstructure and optical properties were characterized after each thermal treatment. The performance criterion (PC) from the IEA SHC program task X, as defined in chapter 2, was employed to simulate the expected service life time of the coating of 25 years [91].

4.4.1 Asymmetric thermal treatment test on complete solar selective coatings

The asymmetric thermal treatment consists of heating the complete stack at 450, 650 and 800ºC for 12 hours in air, with a heating ramp of 5ºC/min. Figure 4.28 shows the reflectance spectra of the deposited multilayer after each temperature.

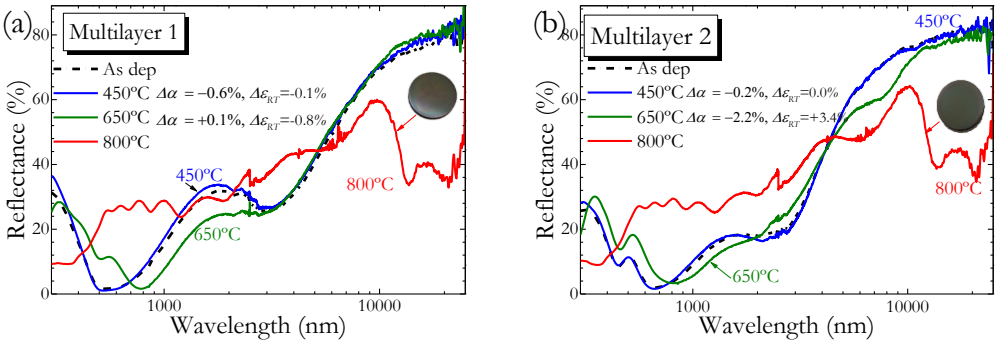

Figure 4.28 – Reflectance of multilayer SSC before and after the asymmetric thermal treatments. (a) Multilayer 1 and (b) multilayer 2. The values of the measured *a* and ε_{RT} after each temperature are tabulated in the figure. The photographs of the degraded SSC after the thermal test at 800ºC are included.

The SSC solar absorptance and thermal emittance did not change significantly after heat treatment up to 650ºC, showing high thermal stability in air, as observed from the values included in Figure 4.28. Minor variations were observed in the solar absorptance (Δa = +0.1 %) and thermal emittance ($\Delta\varepsilon$ = -0.8 %) for multilayer 1, even better than the as deposited values. The changes on multilayer 2 were slightly larger (Δa =-2.2 and $\Delta\varepsilon$ = +3.4%) but they were valid for the performance criteria of thermal stability defined (PC = 3).

The high thermal stability of the multilayers deposited was attributed to several factors. The interdiffusion between AlTiN/AlTiON and AlTiON/AlTiO is expected to be very low up to 650ºC because of the high activation energies needed, the high melting points of materials and the stable microstructures.

However, a drastic failure was observed when the temperature was increased to 800ºC with many defects even visually observed, such as change of colour from dark blue to yellowish-brown (see photo included in Figure 4.28). The annealing in air of the complete SSC may induce

several microstructural modifications such as interdiffusion, reaction between layers to produce new phases, transformation within one or all layers and oxidation. These modifications resulted in changes in the optical properties and the final optical performance. In order to analyse the microstructural evolution with temperature, the heat treated multilayers were analysed by GIXRD (Figure 4.29).

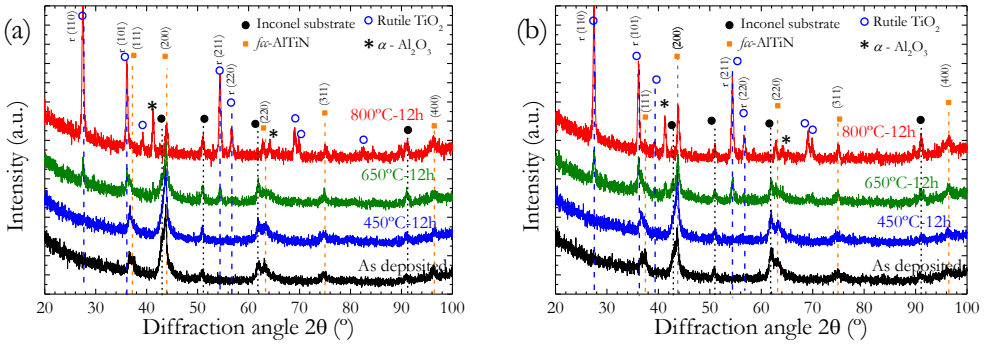

Figure 4.29 –GIXRD patterns of the SSC as deposited and after thermal treatment 12 h at 450ºC, 650ºC and 800ºC of (a) multilayer 1 and (b) multilayer 2.

The GIXRD patterns did not detect significant changes in the crystal microstructure at 450ºC and only the peaks of the cubic AlTiN were observed (2θ =36.8º, 43.7º, 61.8º, 74.9º and 97.0º) [72]. When the temperature increases up to 650ºC, small peaks were detected associated to rutile TiO_2 (ICCD 01-073-2224 for rutile TiO_2 [92]) at 2θ =27.6º, 36.5º, 54.4º and 56.6º. At 800ºC, the TiO_2 peaks become narrower and better defined and additional peaks also appears associated with other crystal oxide phases such as α-Al_2O_3 (ICCD card 00-043-1484) [59] and Al_2TiO_5 in minor proportion, for both multilayers [68]. The metastable cubic γ-Al_2O_3 detected in the as deposited individual AlTiO layers, changes during the thermal treatment and consists of a mixture of rutile TiO_2 and α-Al_2O_3 grains what contributes to a formation of voids along grain boundaries, allowing the external atmosphere (O_2) to penetrate along them [77].

The thermal stability up to 900ºC of the AlTiO top layer deposited by CVA with this stoichiometry has been widely reported previously [6,68]. In the $(Al_{67}Ti_{33})(O_xN_{1-x})$ films, the high temperatures oxidation mechanism expected implies the formation of a beneficial stable corundum α-Al_2O_3 top layer, that retards the inward diffusion of O_2 avoiding the formation of porous TiO_2 [55]. Hence, it is more likely that the titanium of the detected TiO_2 comes from the diffusion of the IR reflective TiN layer instead from the $(AlTi)(O_xN_{1-x})$ layers. This result can also be derived after the visual inspection of the heated multilayers, which show a yellowish coloration more characteristic of TiN [93].

The peaks associated with *fcc*-AlTiN were still detected after heating at 800ºC, although a broadening of only the (200) peak situated at 2θ =36.8º was observed, characteristic feature for spinodal decomposition during annealing of AlTiN films [71,80]. The degradation mechanism

observed include the increase of roughness of the multilayer surface compared to the smooth surface of the as deposited coatings, which correlated to an increase of the emittance [36]. This effect, coupled to the pronounced oxidation of titanium from the TiN make a completely lost of the selective properties.

This failure observed at 800ºC, raise to proceed with accelerated ageing tests at a lower temperature. In particular, cyclic tests will be performed at 600ºC for both deposited SSC.

4.4.2 Cycling thermal treatment test on complete SSC

The multilayer SSCs were exposed to 750 hours of cyclic symmetric heating tests, i.e. 250 cycles heating up to 600ºC for 2 hours in air and cooling down to 300ºC (cyclic test further explained in chapter 2). The reflectance spectra of the deposited multilayers after the symmetric cycles at 600ºC are shown in Figure 4.30. The values of α and ε_{RT} extracted from these spectra for every 50 cycles are included.

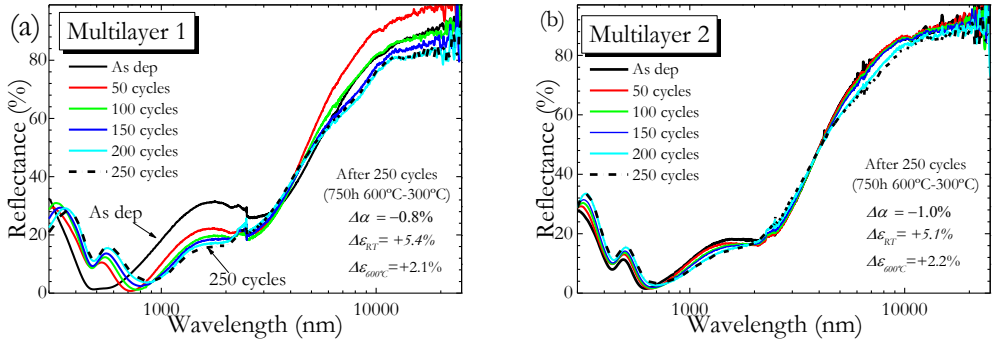

Figure 4.30 –Reflectance of the (a) multilayer 1 and (b) multilayer 2 after 250 cycles at 600ºC during 2 hours with symmetric heating and cooling rams at 10ºC / min. The values of measured α and ε_{RT} for every 50 cycles are tabulated in the figure.

The thermal emittance at 600ºC ($\varepsilon_{600ºC}$) was calculated and plotted together with α and ε_{RT} for every 50 cycles (in Figure 4.31). The resulted values of α and ε_{RT} of the multilayer SSC after 250 cycles at 600ºC (i.e. total 750 hours including heating and cooling ramps) show long term stability at high temperature. Minor variations were observed in the solar absorptance (Δa = -0.8 %) and thermal emittance ($\Delta\varepsilon_{RT}$ = +5.4 % and $\Delta\varepsilon_{600ºC}$ = 2.1 %) for multilayer 1, resulting in a valid accelerated performance criteria (PC= 2.15). Similarly, small changes were also detected in the optical properties of multilayer 2 (Δa =-1.0%, $\Delta\varepsilon_{RT}$=+5.1 % and $\Delta\varepsilon_{600ºC}$ = 2.1 %), showing an excellent optical performance (PC= 2.27).

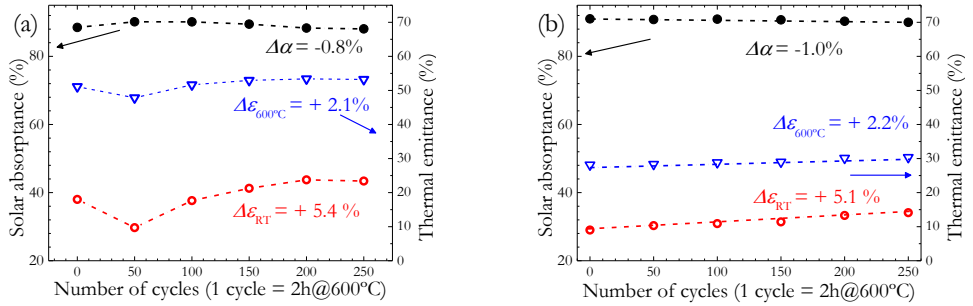

Figure 4.31 – Measured α, ε_{RT} and $\varepsilon_{600ºC}$ for every 50 of the (a) multilayer 1 and (b) multilayer 2 after 250 cycles at 600ºC during 2 hours with symmetric heating and cooling ramps at 10ºC / min

The accelerated life-time tests revealed a very good oxidation resistance after 750 hours of symmetric cycling. The formation of nanocrystalline AlTiN surrounded by the amorphous matrix can protect the coating from oxidation due to increasing diffusion path of oxygen. This concept of AlTiN nanocrystals embedded in an amorphous matrix for high temperature resistance coatings has been widely employed for superhard nanocomposites of AlTiN on a-Si_3N_4 [94,95] mainly deposited by CVA. The principle of self-organization of the nanostructure also observed in the SSC based on AlTi(O_xN_{1-x}) significantly improved the life-time of the coatings at high temperature.

Table 4.7 summarized α and ε_{RT} obtained for multilayer 1 and 2 in the different multilayer SSC design steps, since the initial optical simulated stacks to the deposited, and their variations with the different thermal treatments tests.

Table 4.7 – Simulated and measured solar absorptance (α) and thermal emittance (ε_{RT}) obtained in the different steps followed for the design of a SSC based on AlTi(O_xN_{1-x}) and after the asymmetric and cycling thermal treatment tests.

Maximun T		Multilayer 1			Multilayer 2	
		α	ε		α	ε
Simulated		90.9	13.5		89.1	10.2
As deposited		88.9	18.0		91.0	9.0
	PC	$\Delta\alpha$	$\Delta\varepsilon$	PC	$\Delta\alpha$	$\Delta\varepsilon$
12 h@450ºC	0.6	-0.6	-0.1	0.2	-0.2	0.0
12 h@650ºC	-0.3	+0.1	-0.8	3.0	-2.2	+3.4
250 cycles@600ºC	2.15	-0.8	+5.4	2.27	-1.0	+5.1

Previous experience shows that some of the coatings that can withstand high constant temperature fail when they are subjected to temperature cycling. Very promising results were obtained with a proper design of the multilayer SSC stack, obtaining promising values of α=91.0% and ε_{RT} =9.0 % with no degradation after cycling 750 at 600ºC in air. This is significantly better than thermal stability values reported for this class of SSC so far, wherein AlTiON based stacks deposited by magnetron sputtering shows stability under cyclic heating condition only at 350ºC[28].

4.5. Discussion and conclusions of SSC based on AlTi(O_xN_{1-x})

A systematic, scientifically rigorous and successful study of AlTi(O_xN_{1-x}) single layers was conducted in this chapter. AlTi(O_xN_{1-x}) thin films with different oxygen content were prepared by CVA. After checking the good stability of selected AlTiN and AlTiON (20 at.%O) individual layers at high temperatures and the possibility to modulate the optical constants with the different oxygen content, a depth study of AlTi(O_xN_{1-x}) thin films was carried out.

Deposition and characterization of AlTi(O_xN_{1-x}) individual layers

A first set of samples were deposited to determine their composition and optical properties. Thin films with thickness below ~150nm did not show evidences of macroparticles, and hence, no problems are foreseen for the deposition of a multilayer stack with the non-filtered CVA. After initial simulations a new set of samples were grown including AlTiN, AlTiON (14 at.%), AlTiON (20 at.%), AlTiO and AlTiON deposited at higher P_w. The latter sample has a composition nearly equivalent to a pure oxide, with only a residual content of 2at.% of N.

The microstructural and morphological characterization shows the evolution of the AlTiN ternary phases when the oxygen concentration or the pressure was increased. The deposited AlTiN film exhibits a dense and columnar structure with diameters in the order of 30 nm extended throughout the whole coating thickness and parallel to the preferential (200) crystal orientation of the cubic structure. With the incorporation of O_2 as reactive gas, it resulted in a monotouos width and length shrink of the columns, with smaller cristallites embedded on amorphous matrix, as confirmed by XRD, SEM and HR-TEM. The higher oxygen content cannot be accommodated into the AlTiN lattice, and amorphous $(Al,Ti)_2O_3$, Al_2O_3 and TiO_2 phases appeared between the grain boundaries, what results in a reduction of the grain size. An initial region of epitaxial growth following columnar AlTiN was detected. Amorphous phases in the coating were identified with the incorporation of oxygen. The epitaxial growth of individual crystals is periodically interrupted by the formation of an amorphous matrix which completely covers the AlTiN nanocrystals embedded in it. Pure oxide samples were practically XRD amorphous with tiny peaks associated to the metastable cubic γ-Al_2O_3 phase.

Excellent fitting of the measured spectroscopic ellipsometry data of single AlTi(O_xN_{1-x}) layer was accomplished using a combination of Drude and Tauc-Lorentz dielectric function models. After the analysis of the SE data it can be concluded that there is a transition from metallic to dielectric by increasing the oxygen content. The optical properties of these AlTi(O_xN_{1-x}) films can be controlled in a wide range from metallic to dielectric character by choosing the oxygen

concentration. The results revealed that both the refractive index and the extinction coefficient are decreased when oxygen was introduced.

The optical constants were extrapolated in the whole wavelength range of interest (300-25000 nm) for a proper estimation of the thermal emittance, and their fitting was verified comparing simulated reflectance with UV-Vis-NIR + IR measured one on individual layers, obtaining an excellent agreement.

Deposition and characterization of SSC based on AlTi(O_xN_{1-x})

An exhaustive simulation work was performed in order to obtain trustful models for the reflectance based on optical constant measurements. Once achieved this mastering, simulations of two different SSC multilayers were done, employing the measured optical constants of the individual AlTi(O_xN_{1-x}) and extrapolated in the IR. The SSC composed of AlTiO / AlTiON(20at.%) /AlTiON (14at. %)/ AlTiN / TiN exhibited α = 94.7% and ε_{RT}=5.6%. However, due to the technical difficulties to obtain an accurate adjustment of each layer thickness, two alternative multilayers, which also show good optical selectivity values, were the selected ones to be deposited.

These two simulated SSC were deposited by CVA on mirror polished Inconel substrates. Their reflectance spectra were recorder and compared their α and ε_{RT} obtaining slight differences on the results, attributed to inaccuracies in the determination of the optical constants, which were assigned to the uncertainties in the values obtaining from the SE fitting and furthermore, to the gradient nature of the AlTi(O_xN_{1-x}) coatings, without well-defined interfaces.

The multilayers stacks show good thermal stability up to 650ºC. However, above 800ºC noticeable oxidation was identified which in turn leads to degradation of the optical properties. Ti diffusion through the film from the TiN involves subsequent oxidation to crystalline rutile TiO_2 and the reflectance spectra show how the selectivity properties were completely lost. The formed crystalline oxides affect the solar absorptance.

Preliminary accelerated thermal ageing tests comprise 750 hours in air (250 cycles with 2 hours per cycle at 600ºC and cooling down to 300ºC) showed that the multilayers pass the test with PC value of 2.1 which is below the lower limit of 5.

This results confirm that the designed SSC based on AlTi(O_xN_{1-x}) materials withstand breakdown at 600ºC in air, and therefore, they can be an exciting candidate material for CSP applications at high temperature.

More experimental results are underway to validate the failure mechanism that would include SEM and HR-TEM analysis of the heat treated coatings and *in-situ* evaluation of their microstructure and optical constants on the *cluster tool*, as described further in chapter 5.

4.6. References

[1] S.T. Oyama, The Chemistry of Transition Metal Carbides and Nitrides, Springer, Dordrecht, 1996. doi:10.1007/978-94-009-1565-7.

[2] H. Holleck, V. Schier, Multilayer PVD coatings for wear protection, Surf. Coatings Technol. 76-77 (1995) 328–336. doi:10.1016/0257-8972(95)02555-3.

[3] H. Holleck, Material selection for hard coatings, J. Vac. Sci. Technol. A. 4 (1986) 2661. doi:10.1116/1.573700.

[4] H.O. Pierson, Handbook of refractory carbides and nitrides: properties, characteristics, processing, and applications, Noyes Publications, Westwood,New Yersey USA, 1996.

[5] F. Vaz, N. Martin, M. Fenker, Metallic Oxynitride Thin Films by Reactive Sputtering and Related Deposition Methods. Process, properties and applications, 2014. doi:10.1007/s13398-014-0173-7.2.

[6] J. Nohava, P. Dessarzin, P. Karvankova, M. Morstein, Characterization of tribological behavior and wear mechanisms of novel oxynitride PVD coatings designed for applications at high temperatures, Tribol. Int. 81 (2015) 231–239. doi:10.1016/j.triboint.2014.08.016.

[7] J. Sjölén, L. Karlsson, S. Braun, R. Murdey, A. Hörling, L. Hultman, Structure and mechanical properties of arc evaporated Ti–Al–O–N thin films, Surf. Coatings Technol. 201 (2007) 6392–6403. doi:10.1016/j.surfcoat.2006.12.006.

[8] H. Schellinger, M.P. Lazarov, H. Klank, R. Sizmann, Thermal and Chemical Metallic - Dielectric Transitions of TiNXOY Cu Absorber Tandems, in: C.M. Lampert (Ed.), SPIE's 1993 Int. Symp. Opt. Imaging, Instrum., International Society for Optics and Photonics, 1993: pp. 366–376. doi:10.1117/12.161977.

[9] J. Schmitz, B. Rangarajan, A.Y. Kovalgin, Fabrication and properties of GeSi and SiON layers for above-IC integrated optics, Solid. State. Electron. 108 (2015) 8–12. doi:10.1016/j.sse.2014.12.022.

[10] E. Aubry, S. Weber, A. Billard, N. Martin, Enhanced tunability of the composition in silicon oxynitride thin films by the reactive gas pulsing process, Appl. Surf. Sci. 290 (2014) 148–153. doi:10.1016/j.apsusc.2013.11.018.

[11] J. Probst, U. Gbureck, R. Thull, Binary nitride and oxynitride PVD coatings on titanium for biomedical applications, Surf. Coatings Technol. 148 (2001) 226–233. doi:10.1016/S0257-8972(01)01357-3.

[12] S. Iwamori, Y. Gotoh, K. Moorthi, Characterization of silicon oxynitride gas barrier films, Vacuum. 68 (2002) 113–117. doi:10.1016/S0042-207X(02)00294-4.

[13] S. Goumri-Said, N. Kanoun-Bouayed, A.H. Reshak, M.B. Kanoun, On the electronic nature of silicon and germanium based oxynitrides and their related mechanical, optical and vibrational properties as obtained from DFT and DFPT, Comput. Mater. Sci. 53 (2012) 158–168. doi:10.1016/j.commatsci.2011.09.021.

[14] H. Schellinger, M.P. Lazarov, W. Assmann, B. Bauer, C. Steinhausen, Improved selective properties of SiO2/TiNO/Al tandem absorbers effected by tempering, in: V. Wittwer, C.G. Granqvist, C.M. Lampert (Eds.), Opt. Mater. Technol. Energy Effic. Sol. Energy Convers. XIII, International Society for Optics and Photonics, 1994: pp. 172–181. doi:10.1117/12.185368.

[15] M.P. Lazarov, R. Sizmann, U. Frei, Optimization of SiO2 - TiNxOy - Cu interference absorbers: numerical and experimental results, in: C.M. Lampert (Ed.), SPIE's 1993 Int. Symp. Opt. Imaging, Instrum., International Society for Optics and Photonics, 1993: pp. 345–356. doi:10.1117/12.161975.

[16] H.C. Barshilia, N. Selvakumar, K.S. Rajam, D.V. Sridhara Rao, K. Muraleedharan, Deposition and characterization of TiAlN/TiAlON/Si3N4 tandem absorbers prepared using reactive direct current magnetron sputtering, Thin Solid Films. 516 (2008) 6071–6078. doi:10.1016/j.tsf.2007.10.113.

[17] H.C. Barshilia, N. Selvakumar, K.S. Rajam, Thermal stability of TiAlN/TiAlON/Si3N4 tandem absorbers prepared by reactive direct current magnetron sputtering, J. Vac. Sci. Technol. A Vacuum, Surfaces, Film. 25 (2007) 383. doi:10.1116/1.2699425.

[18] H.C. Barshilia, N. Selvakumar, K.S. Rajam, D. V. Sridhara Rao, K. Muraleedharan, A. Biswas, TiAlN/TiAlON/Si3N4 tandem absorber for high temperature solar selective applications, Appl. Phys. Lett. 89 (2006) 191909. doi:10.1063/1.2387897.

[19] H.C. Barshilia, N. Selvakumar, K.S. Rajam, A. Biswas, Spectrally selective NbAlN/NbAlON/Si3N4 tandem absorber for high-temperature solar applications, Sol. Energy Mater. Sol. Cells. 92 (2008) 495–504. doi:10.1016/j.solmat.2007.11.004.

[20] H. Lei, W. ShuMao, J. LiJun, L. XiaoPeng, L. HuaLing, L. ZhiNian, Preparation and thermal stability on non-vacuum high temperature solar selective absorbing coatings, Chinese Sci. Bull. 54 (2009) 1451–1454. doi:10.1007/s11434-009-0159-6.

[21] H. Lei, D. Miao, L. XiaoPeng, W. ShuMao, J. LiJun, L. Fang, et al., Thermal stability of nitride solar selective absorbing coatings used in high temperature parabolic trough current, Sci. China Technol. Sci. 53 (2010) 1507–1512. doi:10.1007/s11431-010-3176-4.

[22] D. Zhu, S. Zhao, Chromaticity and optical properties of colored and black solar–thermal absorbing coatings, Sol. Energy Mater. Sol. Cells. 94 (2010) 1630–1635. doi:10.1016/j.solmat.2010.05.019.

[23] L. Rebouta, P. Capela, M. Andritschky, A. Matilainen, P. Santilli, K. Pischow, et al., Characterization of TiAlSiN/TiAlSiON/SiO2 optical stack designed by modelling calculations for solar selective applications, Sol. Energy Mater. Sol. Cells. 105 (2012) 202–207. doi:10.1016/j.solmat.2012.06.011.

[24] Y. Liu, C. Wang, Y. Xue, The spectral properties and thermal stability of NbTiON solar selective absorbing coating, Sol. Energy Mater. Sol. Cells. 96 (2012) 131–136. doi:10.1016/j.solmat.2011.09.034.

[25] L. Rebouta, A. Pitães, M. Andritschky, P. Capela, M.F. Cerqueira, A. Matilainen, et al., Optical characterization of TiAlN/TiAlON/SiO2 absorber for solar selective applications, Surf. Coatings Technol. 211 (2012) 41–44. doi:10.1016/j.surfcoat.2011.09.003.

[26] M. Du, X. Liu, L. Hao, X. Wang, J. Mi, L. Jiang, et al., Microstructure and thermal stability of Al/Ti0.5Al0.5N/Ti0.25Al0.75N/AlN solar selective coating, Sol. Energy Mater. Sol. Cells. 111 (2013) 49–56. doi:10.1016/j.solmat.2012.12.010.

[27] N. Selvakumar, S. Santhoshkumar, S. Basu, A. Biswas, H.C. Barshilia, Spectrally selective CrMoN/CrON tandem absorber for mid-temperature solar thermal applications, Sol. Energy Mater. Sol. Cells. 109 (2013) 97–103. doi:10.1016/j.solmat.2012.10.003.

[28] H.C. Barshilia, Growth, characterization and performance evaluation of Ti/AlTiAlTiNON/AlTiO high temperature spectrally selective coatings for solar thermal power applications, Sol. Energy Mater. Sol. Cells. 130 (2014) 322–330. doi:10.1016/j.solmat.2014.07.037.

[29] H.C. Barshilia, N. Selvakumar, K.S. Rajam, A. Biswas, Optical properties and thermal stability of TiAlN/AlON tandem absorber prepared by reactive DC/RF magnetron sputtering, Sol. Energy Mater. Sol. Cells. 92 (2008) 1425–1433. doi:10.1016/j.solmat.2008.06.004.

[30] K. Valleti, D. Murali Krishna, S.V. Joshi, Functional multi-layer nitride coatings for high temperature solar selective applications, Sol. Energy Mater. Sol. Cells. 121 (2014) 14–21. doi:10.1016/j.solmat.2013.10.024.

[31] Y. Liu, Z. Wang, D. Lei, C. Wang, A new solar spectral selective absorbing coating of SS–(Fe3O4)/Mo/TiZrN/TiZrON/SiON for high temperature application, Sol. Energy Mater. Sol. Cells. 127 (2014) 143–146. doi:10.1016/j.solmat.2014.04.014.

[32] L. Rebouta, A. Sousa, P. Capela, M. Andritschky, P. Santilli, A. Matilainen, et al., Solar selective absorbers based on Al2O3:W cermets and AlSiN/AlSiON layers, Sol. Energy Mater. Sol. Cells. 137 (2015) 93–100. doi:10.1016/j.solmat.2015.01.029.

[33] C. Zou, L. Huang, J. Wang, S. Xue, Effects of antireflection layers on the optical and thermal stability properties of a spectrally selective CrAlN–CrAlON based tandem absorber, Sol. Energy Mater. Sol. Cells. 137 (2015) 243–252. doi:10.1016/j.solmat.2015.02.010.

[34] Y. Wu, C. Wang, Y. Sun, Y. Xue, Y. Ning, W. Wang, et al., Optical simulation and experimental optimization of Al/NbMoN/NbMoON/SiO2 solar selective absorbing coatings, Sol. Energy Mater. Sol. Cells. 134 (2015) 373–380. doi:10.1016/j.solmat.2014.12.005.

[35] J. Jyothi, H. Chaliyawala, G. Srinivas, H.S. Nagaraja, H.C. Barshilia, Design and fabrication of spectrally selective TiAlC/TiAlCN/TiAlSiCN/TiAlSiCO/TiAlSiO tandem absorber for high-temperature solar thermal power applications, Sol. Energy Mater. Sol. Cells. 140 (2015) 209–216. doi:10.1016/j.solmat.2015.04.018.

[36] K.P. Sibin, S. John, H.C. Barshilia, Control of thermal emittance of stainless steel using sputtered tungsten thin films for solar thermal power applications, Sol. Energy Mater. Sol. Cells. 133 (2015) 1–7. doi:10.1016/j.solmat.2014.11.002.

[37] N. Selvakumar, K. Rajaguru, G.M. Gouda, H.C. Barshilia, AlMoN based spectrally selective coating with improved thermal stability for high temperature solar thermal applications, Sol. Energy. 119 (2015) 114–121. doi:10.1016/j.solener.2015.06.047.

[38] N. Selvakumar, K. Prajith, A. Biswas, H.C. Barshilia, Optical simulation and fabrication of HfMoN/HfON/Al2O3 spectrally selective coating, Sol. Energy Mater. Sol. Cells. 140 (2015) 328–334. doi:10.1016/j.solmat.2015.04.031.

[39] J. Feng, S. Zhang, Y. Lu, H. Yu, L. Kang, X. Wang, et al., The spectral selective absorbing characteristics and thermal stability of SS/TiAlN/TiAlSiN/Si3N4 tandem absorber prepared by magnetron sputtering, Sol. Energy. 111 (2015) 350–356. doi:10.1016/j.solener.2014.11.005.

[40] K. Valleti, D.M. Krishna, P.M. Reddy, S. V. Joshi, High temperature stable solar selective coatings by cathodic arc PVD for heat collecting elements, Sol. Energy Mater. Sol. Cells. 145 (2016) 447–453. doi:10.1016/j.solmat.2015.11.012.

[41] A. Dan, K. Chattopadhyay, H.C. Barshilia, B. Basu, Angular solar absorptance and thermal stability of W/WAlN/WAlON/Al2O3-based solar selective absorber coating, Appl. Therm. Eng. (2016). doi:10.1016/j.applthermaleng.2016.04.069.

[42] C. Zou, W. Xie, L. Shao, Functional multi-layer solar spectral selective absorbing coatings of AlCrSiN/AlCrSiON/AlCrO for high temperature applications, Sol. Energy Mater. Sol. Cells. 153 (2016) 9–17. doi:10.1016/j.solmat.2013.10.024.

[43] H.C. Barshilia, J.B. Bharathibai, L.V. Ramachandrappa, A hybrid multilayer solar selective coatign for high temperature solar thermal applications and a process for the preparation thereof, WO2014122667A1, 2014.

[44] H.C. Barshilia, V.K.W. Grips, K.S. Rajam, Solar selective coating having higher thermal stability useful for harnessing solar energy and a precess for the preparation thereof, US 7585568 B2, 2009.

[45] H.C. Barshilia, R.C. Dhawan, An improved solar seelctive coating having high thermal stability and a process for the preparation therof, WO20130888451A1, 2013.

[46] X.J. Wang, L.J. Jiang, M. Du, L. Hao, X.P. Liu, Q.H. Yu, The Degradation of Solar Thermal Absorption Coatings, Energy Procedia. 49 (2014) 1747–1755. doi:10.1016/j.egypro.2014.03.185.

[47] T. Leyendecker, O. Lemmer, S. Esser, J. Ebberink, The development of the PVD coating TiAlN as a commercial coating for cutting tools, Surf. Coatings Technol. 48 (1991) 175–178. doi:10.1016/0257-8972(91)90142-J.

[48] L. Chen, J. Paulitsch, Y. Du, P.H. Mayrhofer, Thermal stability and oxidation resistance of Ti-Al-N coatings., Surf. Coat. Technol. 206 (2012) 2954–2960. doi:10.1016/j.surfcoat.2011.12.028.

[49] V. Godinho, D. Philippon, T.C. Rojas, N.N. Novikova, V. a. Yakovlev, E. a. Vinogradov, et al., Characterization of Ti1−xAlxN coatings with selective IR reflectivity, Sol. Energy. 84 (2010) 1397–1401. doi:10.1016/j.solener.2010.04.021.

[50] S. Kassavetis, G. Abadias, G. Vourlias, G. Bantsis, S. Logothetidis, P. Patsalas, Optical properties of TixAl1−xN thin films in the whole compositional range, Surf. Coatings Technol. (2015). doi:10.1016/j.surfcoat.2015.08.049.

[51] J.M. Andersson, J. Vetter, J. Müller, J. Sjölén, Structural effects of energy input during growth of Ti1−xAlxN (0.55≤x≤0.66) coatings by cathodic arc evaporation, Surf. Coatings Technol. 240 (2014) 211–220. doi:10.1016/j.surfcoat.2013.12.018.

[52] C. Århammar, J.L. Endrino, M. Ramzan, D. Horwat, A. Blomqvist, J.-E. Rubensson, et al., Probing temperature-induced ordering in supersaturated Ti1−xAlxN coatings by electronic structure, Surf. Coatings Technol. 242 (2014) 207–213. doi:10.1016/j.surfcoat.2013.10.054.

[53] S. Larpkiattaworn, C. Chokwatvikul, S. Surinphong, C. Busabok, P. Termsuksawad, Properties of (Ti,Al)N film prepared by PVD cathodic arc, Suranare J. Sci. Technol. 20 (2013) 221–226.

[54] T. Ikeda, S. Satoh, Phase formation and characterization of hard coatings in the Ti-Al-N system prepared by the cathodic arc ion plating method, Thin Solid Films. 195 (1991) 99–110. doi:10.1016/0040-6090(91)90262-V.

[55] F. Vaz, L. Rebouta, M. Andritschky, M.F. da Silva, J.C. Soares, Thermal oxidation of Ti1 − xAlxN coatings in air, J. Eur. Ceram. Soc. 17 (1997) 1971–1977. doi:10.1016/S0955-2219(97)00050-2.

[56] J. Vetter, J. Sjoelen, J.M. Andersson, L. Karlsson, J. Müller, Basic properties and industrial applications of AlxTiyN hard coatings with two third at % of Al and one third at % Ti by cathodic vacuum arc evaporation, in: 41nd ICMCTF San Diego 2015, 2015.

[57] J. Vetter, O. Kayser, H.-W. Bieler, AlTiN - a universal coating for different applications: from dry cutting to decorationAlTiN - Die Universal-Beschichtung für eine Vielzahl von Anwendungen: von Trockenzerspanung bis Dekor, Vak. Forsch. Und Prax. 17 (2005) 131–134. doi:10.1002/vipr.200500245.

[58] A. Schuler, P. Reimann, P. Oelhafen, G. Francz, T. Zehnder, M. Duggelin, et al., Structural and optical properties of titanium aluminum nitride films (Ti1-xAlxN), J. Vac. Sci. Technol. A. 19 (2001) 922.

[59] H. Najafi, A. Karimi, P. Dessarzin, M. Morstein, Correlation between anionic substitution and structural properties in AlCr(OxN1−x) coatings deposited by lateral rotating cathode arc PVD, Thin Solid Films. 520 (2011) 1597–1602. doi:10.1016/j.tsf.2011.08.075.

[60] S.G. Ebbinghaus, H.P. Abicht, R. Dronskowski, T. M??ller, A. Reller, A. Weidenkaff, Perovskite-related oxynitrides - Recent developments in synthesis, characterisation and investigations of physical properties, Prog. Solid State Chem. 37 (2009) 173–205. doi:10.1016/j.progsolidstchem.2009.11.003.

[61] C. Nunes, V. Teixeira, M.L. Prates, N.P. Barradas, A.D. Sequeira, Graded selective coatings based on chromium and titanium oxynitride, Thin Solid Films. 442 (2003) 173–178. doi:10.1016/S0040-6090(03)00967-2.

[62] J. Borges, F. Macedo, F.M. Couto, M.S. Rodrigues, C. Lopes, P. Pedrosa, et al., The influence of nitrogen and oxygen additions on the thermal characteristics of aluminium-based thin films, Mater. Chem. Phys. 163 (2015) 569–580. doi:10.1016/j.matchemphys.2015.08.015.

[63] R. Luthier, F. Levy, Magnetron sputtered TiAlON composite thin films. I. Structure and morphology, J. Vac. Sci. Technol. A Vacuum, Surfaces, Film. 9 (1991) 102. doi:10.1116/1.577107.

[64] K. Tönshoff, B. Karpuschewski, A. Mohlfeld, T. Leyendecker, G. Erkens, H.. Fuß, et al., Performance of oxygen-rich TiAlON coatings in dry cutting applications, Surf. Coatings Technol. 108-109 (1998) 535–542. doi:10.1016/S0257-8972(98)00637-9.

[65] J.A. Dean, Langue's handbook of chemistry, 15th ed., McGraw-Hill, New York, 1999.

[66] D.R. Lide, Handbook of Chemistry and Physics, 90th ed., CRC, Florida, 2010. doi:978-1466571143.

[67] A. Anders, Energetic deposition using filtered cathodic arc plasmas, Vacuum. 67 (2002) 673–686. doi:10.1016/S0042-207X(02)00260-9.

[68] H. Najafi, A. Karimi, P. Dessarzin, M. Morstein, Formation of cubic structured (Al1-xCrx)2+O3 and its dynamic transition to corundum phase during cathodic arc evaporation, Surf. Coatings Technol. 214 (2013) 46–52. doi:10.1016/j.surfcoat.2012.10.062.

[69] A. Anders, A structure zone diagram including plasma-based deposition and ion etching, Thin Solid Films. 518 (2010) 4087–4090.

[70] M. Zhou, Y. Makino, M. Nose, K. Nogi, Phase transition and properties of Ti–Al–N thin films prepared by r.f.-plasma assisted magnetron sputtering, Thin Solid Films. 339 (1999) 203–208. doi:10.1016/S0040-6090(98)01364-9.

[71] A. Hörling, L. Hultman, M. Odén, J. Sjölén, L. Karlsson, Thermal stability of arc evaporated high aluminum-content Ti1−xAlxN thin films, J. Vac. Sci. Technol. A Vacuum, Surfaces, Film. 20 (2002) 1815. doi:10.1116/1.1503784.

[72] J.C. Schuster, J. Bauer, The ternary system titanium-aluminum-nitrogen, J. Solid State Chem. 53 (1984) 260–265. doi:10.1016/0022-4596(84)90100-2.

[73] D. Zhu, F. Mao, S. Zhao, The influence of oxygen in TiAlOxNy on the optical properties of colored solar-absorbing coatings, Sol. Energy Mater. Sol. Cells. 98 (2012) 179–184. doi:10.1016/j.solmat.2011.11.001.

[74] J. Ramm, A. Neels, B. Widrig, M. Döbeli, L.D.A. Vieira, A. Dommann, et al., Correlation between target surface and layer nucleation in the synthesis of Al-Cr-O coatings deposited by reactive cathodic arc evaporation, Surf. Coatings Technol. 205 (2010) 1356–1361. doi:10.1016/j.surfcoat.2010.08.152.

[75] M. Pohler, R. Franz, J. Ramm, P. Polcik, C. Mitterer, Cathodic arc deposition of (Al,Cr)2O3: Macroparticles and cathode surface modifications, Surf. Coatings Technol. 206 (2011) 1454–1460. doi:10.1016/j.surfcoat.2011.09.028.

[76] A. Pélisson-Schecker, H.J. Hug, J. Patscheider, Morphology, microstructure evolution and optical properties of Al-Si-N nanocomposite coatings, Surf. Coatings Technol. 257 (2014) 114–120. doi:10.1016/j.surfcoat.2014.08.053.

[77] J. Musil, V. Satava, R. Cerstvy, P. Zeman, T. Tolg, Formation of crystalline Al-Ti-O thin films and their properties, Surf. Coatings Technol. 202 (2008) 6064–6069. doi:10.1016/j.surfcoat.2008.07.012.

[78] J. Musil, J. Blažek, P. Zeman, Š. Prokšová, M. Šašek, R. Čerstvý, Thermal stability of alumina thin films containing γ-Al2O3 phase prepared by reactive magnetron sputtering, Appl. Surf. Sci. 257 (2010) 1058–1062. doi:10.1016/j.apsusc.2010.07.107.

[79] ICDD Powder Diffraction Data, ICDD Powder Diffraction Data files: 00-037-1140 for fcc AlTiN, (n.d.).

[80] I. Petrov, P.B. Barna, L. Hultman, J.E. Greene, Microstructural evolution during film growth, J. Vac. Sci. Technol. A Vacuum, Surfaces, Film. 21 (2003) S117. doi:10.1116/1.1601610.

[81] M. Fox, Optical Properties of Solids, Oxford Mas, Oxford Unversity Press, Oxford, 2001.

[82] R. Perrem, F. Henry, G. Peraudeau, B. Armas, R. Berjoan, E. Beche, An XPS and thermogravimetric study of oxidized AlN and AlN–Si3N4 layers deposited by liquid-phase chemical vapour deposition, J. Mater. Sci. 32 (n.d.) 1305–1312. doi:10.1023/A:1018556606993.

[83] F. Cao, K. McEnaney, G. Chen, Z. Ren, Review of Cermet-based Spectrally-Selective Solar Absorbers, Energy Environ. Sci. (2014). doi:10.1039/c3ee43825b.

[84] J. Price, P.Y. Hung, T. Rhoad, B. Foran, A.C. Diebold, Spectroscopic ellipsometry characterization of HfxSi yOz films using the Cody–Lorentz parameterized model, Appl. Phys. Lett. 85 (2004) 1701. doi:10.1063/1.1784889.

[85] G.E. Jellison, F.A. Modine, Parameterization of the optical functions of amorphous materials in the interband region, Appl. Phys. Lett. 69 (1996) 371. doi:10.1063/1.118064.

[86] R. Joerger, Optical properties of inhomogeneous media, Sol. Energy Mater. Sol. Cells. 54 (1998) 351–361. doi:10.1016/S0927-0248(98)00086-5.

[87] A. Biswas, D. Bhattacharyya, H.C. Barshilia, N. Selvakumar, K.S. Rajam, Spectroscopic ellipsometric characterization of TiAlN/TiAlON/Si3N4 tandem absorber for solar selective applications, Appl. Surf. Sci. 254 (2008) 1694–1699. doi:10.1016/j.apsusc.2007.07.109.

[88] Q.-C. Zhang, Optimizing analysis of W-AlN cermet solar absorbing coatings, J. Phys. D. Appl. Phys. 34 (2001) 3113–3120. doi:10.1088/0022-3727/34/21/303.

[89] J.H. Schön, E. Bucher, Computer modeling of the performance of some metal/dielectric multilayers for high-temperature solar selective absorbers, Sol. Energy Mater. Sol. Cells. 43 (1996) 59–65.

[90] M. Farooq, Z.H. Lee, Computations of the optical properties of metal/insulator-composites for solar selective absorbers, Renew. Energy. 28 (2002) 1421–1431. http://dx.doi.org/10.1016/S0960-1481(02)00033-2 (accessed August 10, 2012).

[91] B. Carlsson, K. Möller, U. Frei, M. Köhl, Accelerated life testing of solar absorber coatings, in: V. Wittwer, C.G. Granqvist, C.M. Lampert (Eds.), Opt. Mater. Technol. Energy Effic. Sol. Energy Convers. XIII, International Society for Optics and Photonics, 1994: pp. 79–90. doi:10.1117/12.185359.

[92] I.P.D. Data, ICDD Powder Diffraction Data files: 01-073-2224 for rutile TiO2, (n.d.).

[93] S. Niyomsoan, W. Grant, D.L. Olson, B. Mishra, Variation of color in titanium and zirconium nitride decorative thin films, Thin Solid Films. 415 (2002) 187–194. doi:10.1016/S0040-6090(02)00530-8.

[94] M. Jilek, T. Cselle, P. Holubar, M. Morstein, S. Veprek, Development of Novel Coating Technology by Vacuum Arc with Rotating Cathodes for Industrial Production of nc- (Al 1 − x Ti x) N / a-Si 3 N 4 Superhard Nanocomposite Coatings for Dry , Hard Machining, Plasma Chem. Plasma Process. 24 (2004) 493–510.

[95] S.Q. Wang, L. Chen, B. Yang, K.K. Chang, Y. Du, J. Li, et al., Effect of Si addition on microstructure and mechanical properties of Ti–Al–N coating, Int. J. Refract. Met. Hard Mater. 28 (2010) 593–596. doi:10.1016/j.ijrmhm.2010.05.001.

CHAPTER 5: COMPREHENSIVE *IN-SITU* CHARACTERIZATION OF THIN FILMS AT HIGH TEMPERATURE

This chapter presents the environmental *in-situ* characterization performed to the two candidate materials proposed in this thesis as absorber layer in a SSC. In particular, an accurate knowledge of the variation of the dielectric function of thin films with the temperature and its relation to compositional and microstructural changes could help to prevent failures.

In the first section 5.1, an introduction to *in-situ* characterization of coatings is given. The capabilities of the cluster tool sited in HZDR and used in this thesis are introduced in section 5.2. A new test procedure for the qualification of solar selective coatings (SSC) at high temperature is proposed in section 5.3, which combines a sequence of analytical techniques in the multi-chamber cluster tool at different environments and temperatures.

An amorphous carbon titanium carbide thin film had been studied (section 5.4) as an example of the described methodology. In next section 5.5, $AlTi(O_xN_{1-x})$ thin films were investigated in order to understand the influence of the oxygen to nitrogen ratio on the optical properties and their failure mechanisms at high temperatures. The analysis was performed first in vacuum inside the multi-chamber cluster tool heating samples from RT to 800°C without sample exposure to undefined atmospheres. In the same way, *ex-situ* annealing in air was performed to compare with the previous results observed when vacuum annealing. The low emittance properties of $AlTi(O_xN_{1-x})$ samples, allowed to perform *in-situ* RBS analysis at temperature above 800ºC. No significant changes in optical properties and composition were found when heating in vacuum atmosphere the films, showing excellent high temperature stability.

5.1. Multichamber cluster tool for SSC coating analysis

Solar selective coatings for CSP plants have to withstand extreme environmental conditions. The improvements in efficiencies for solar thermal energy conversions partially implies the increase in the receivers' temperature, aiming to reach up to a maximum temperature of 650ºC for new superheated steam and molten salts receivers [1]. This requires not only the development of new SSC durable at high temperature in air but also a better understanding of those coatings.

Coatings for high temperature applications require an in-depth study of thin films properties at high temperatures. In some of the CSP designs, the coatings of the central receiver tubes are applied in vacuum (parabolic troughs), but in central power tower plants they are exposed to atmospheric environments. In an evacuated atmosphere, the principal degradation mechanisms are the interdiffusion between layers, diffusion or segregation of some internal layers to the surface, thermal expansion or the changes in surface morphology [2]. In air conditions, internal chemical reactions can change the composition and microstructure, oxide may growth induced by temperature [3,4], interfacial reactions can lead to loss of adhesion and evaporation of volatile components [5]. Finally, the coatings should be resistant to abrasive wear caused by wind and sand erosion and show good adhesion onto the receiver base material.

To understand the failure mechanism at high temperature of the new developed SSC it is crucial to understand how material properties change with temperature. A comprehensive analysis of the failure mechanism in SSC should combine the study of how composition, microstructure and optical constants vary with environment and temperature changes. In order to predict and improve the reliability of the new designed SSC under working conditions in a CSP plant, it is necessary to characterize optical and microstructural properties versus temperature in the same experimental setup.

SSC are designed to be used over a large range of temperatures and hence, the temperature dependence of their optical properties is of great importance. A scan of the literature reveals the scarcity of optical data above room temperature [6]. In addition, the data scatter widely when more than one measurement is reported for the same material. Due to thermal expansion, systematic errors are difficult to minimize, since the surface condition of a sample may change irreversibly. Calculating the thermal emittance from spectral data taken at room temperature assumes that the spectral characteristics do not change with increasing temperature. This is only valid if the material is invariant and does not undergo a phase change, breakdown or oxidation at higher temperatures. It is therefore necessary to measure the optical properties of the solar selective coatings at the temperature at which they will be used.

Real time spectroscopic ellipsometry (SE) has proved to be a powerful tool for investigating optical constants in thin films and it has been used during *in-situ* growth of samples

installed inside a deposition chamber [7], or inside a vacuum chamber in order to study the temperature dependence of optical constants in thin films with thermally tunable optical constants [8,9]. Besides the dependence upon temperature, the optical effects associated with defects in the films, such as vacancies, interstitials, dislocations and grain boundaries, should be determined. Such measurements would require a combination of composition and microstructure analysis. Raman spectroscopy and ion beam analysis techniques have been widely applied to characterize chemical bonding and atomic composition respectively [10], but commonly both techniques are used in different set ups suffering from possible oxygen incorporation when the samples are moved from one characterization device to the other.

In order not to break the vacuum during characterization and to give the possibility of characterizing different properties of materials in a connected multi-chamber device, various approaches have been designed. A cluster tool is namely a device that allows making multi-steps experiments. Some cluster tools with ultra-high vacuum technologies and different characterization chambers have been employed previously. For instance, the cluster tool at Forschungszentrum Jülich GmbH (Germany) is dedicated to the study of magnetism and spintronics within an ultrahigh vacuum (UHV) environment [11]. This cluster tool combines a SEM chamber, a spin polarization detector, and a FIB, as shown in Figure 5.1 (a). Additionally, there is another chamber that houses the low temperature Scanning Tunnelling Microscope (STM) and lastly, a preparation and analysis chamber. A transfer chamber connects the two main units and enables *in-situ* access to all attached preparation and characterization tools without vacuum break.

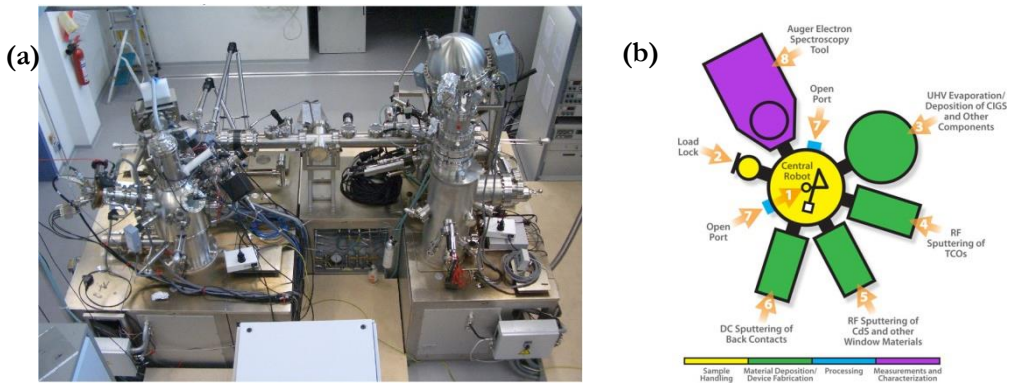

Figure 5.1 - (a) Top view of the Nano-Spintronics-Cluster-Tool at Forschungszentrum in Jüllich (Germany) [13]. (b) Top-view schematic of cluster tool with intra-tool robotic sample transfer [14].

In Princeton University, there is a four chamber UHV cluster tool that allows *in-situ* structural analysis on specific photovoltaic materials [12]. These studied materials can be deposited, processed, measured, and characterized using the process development and integration approach. Another four chamber cluster tool example is situated in the "Process Development & Integration Laboratory" of the National Renewable Energy Laboratory (NREL), in Denver US (Figure 5.1 (b)).

The main tasks are the fabrication and study of a wide range of solar cell technologies by an integrated tool that uses the robotic transfer chamber to connect capabilities: optical, structural, morphological, and chemical compositional techniques.

In all these examples, the samples cannot be exposed to different temperatures and atmospheres, thus making them unsuitable for *in-situ* environmental characterization. Environmental characterization of optical and microstructural properties of thin films continues to be a challenging task, and they have frequently been performed independently. There is an urgent requirement to develop instrumentation to measure the composition, optical and microstructural properties at very high temperatures of solar selective coatings and also to develop a universal test procedure for the performance criterion [15].

5.2. Multichamber cluster tool in HZDR

This chapter presents a novel methodology for environmental high temperature tests that integrates complementary characterization techniques into a single device. The new cluster tool situated at Helmholtz-Zentrum Dresden-Rossendorf (HZDR), Germany, combines the study of the optical constants in an environmental chamber by SE, compositional depth profile analysis using ion beam analysis techniques and microstructural analysis by Raman spectroscopy in several environmental conditions and at temperatures up to 1000 ° C (section 5.3). The main novelty of the proposed methodology is the possibility of performing different measurements sequentially in the same multi-chamber cluster tool, without breaking the vacuum, avoiding the oxygen enrichment of the samples at specific environmental conditions. Other advantages include the possibility of combining optical and structural characterization analysis and the presence of a heatable sample holder in all the chambers, allowing characterization of the samples at different temperatures.

The *in-situ* high vacuum analysis cluster tool consists of three characterization chambers. A general view of the cluster tool is shown in Figure 5.2. The environmental chamber (E-C), the analysis chamber (A-C), and the ion beam analysis chamber (IBA-C) are shown. A central distribution chamber connects all the different units and enables *in-situ* access to the different tools without breaking the vacuum. All experimental chambers offer the possibility of heating the samples through a heatable sample holder which can reach up to 1000ºC.

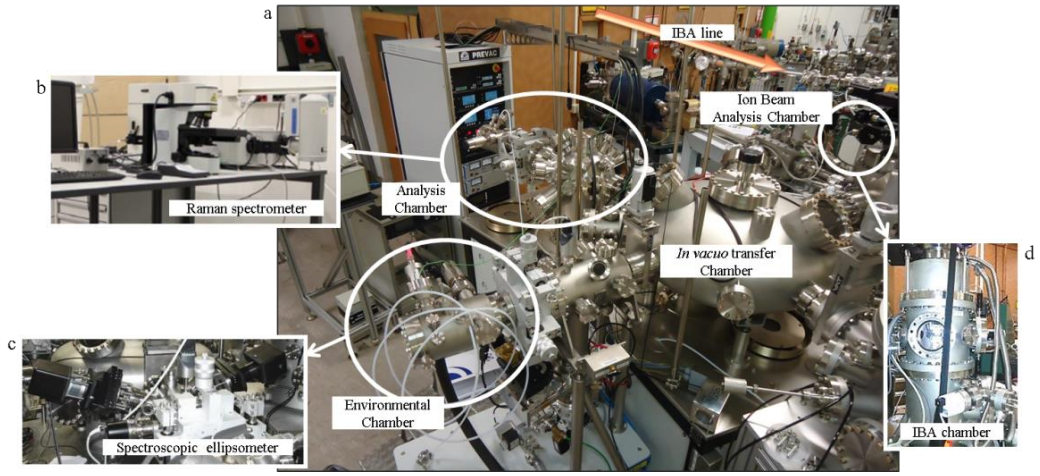

Figure 5.2 - (a) Top view of the cluster tool: the central distribution chamber connects the different units and allows *in-situ* access to all preparation and characterization tools without breaking the vacuum (b) the analysis chamber contains the *in-situ* Raman spectrometer; (c) the environmental chamber houses the real time spectroscopic ellipsometry with different possible simulated environments; (d) the ion beam analysis chamber connected to the 6 MeV accelerator allows characterization of the samples by different IBA techniques (RBS, NRA, ERD).

The E-C houses a real time spectroscopic ellipsometer (SE) and includes the possibility of simulating different environmental conditions, i.e. in vacuum conditions as well as in controlled atmospheres containing O_2, N_2 and Ar, or water vapour. A turbo pump equipped with a butterfly valve helps to limit the gas inlet in environmental operation. There is a heatable sample holder up to 1000°C,that allows the measurement of the optical constants of the samples at different temperatures.

The optical properties of the thin films in the energy range of 370 to 1000 nm at an angle of incidence of 70º can be determined by spectroscopic ellipsometry (SE) using a rotating compensator ellipsometer M-2000FI (J. A. Woolam, Inc.) installed inside the environmental chamber. The acquired data is analysed using WVASE software from J. A. Woolam, Inc.

To determine the variation in the ellipsometry parameters at different temperatures or environments, the integrated area between 450 to 850 nm of measured ellipsometric parameters (Δ, ψ) was evaluated at each temperature (SE_T), as described in equation (5.1). This energy region is selected as it is the region where ⊿ and ψ have higher accuracy and are more relevant for solar applications. The variation of the ellipsometry parameters between two temperatures $\Delta(SE)$ is described by the equation (5.2).

$$SE_T = \int_{450\ nm}^{850\ nm} \psi_T\ dE + \int_{450\ nm}^{850\ nm} \Delta_T\ dE \tag{5.1}$$

$$\Delta(SE) = 100 \times \left| \frac{SE_{T2} - SE_{T1}}{SE_{T1}} \right| \tag{5.2}$$

The IBA-C of the cluster tool is connected to the 6 MV Tandem ion accelerator of the ion beam centre, which can provide ions of different nature and charge state. In this chamber,

$^{4}He^{2+}$ ions up to 4 MeV, $^{2}D^{+}$ up to 1.8 MeV and $^{35}Cl^{7+}$ up to 14MeV energy can be employed to carry out several ion beam analysis techniques. RBS, NRA and ERD ion beam analysis techniques are currently implemented in the IBA-C. The mentioned techniques together allow identification of the overall elements and depth profiles of thin films. The technique, or the combination of techniques, used in each case will depend on the characteristics of the sample [16]. Moreover, the sample holder in the IBA-C is heatable up to 1000°C, allowing a non-destructive compositional analysis of the samples at different temperatures, as well as depth profile composition monitoring. However, only samples with low infrared radiation at high temperatures could be measured due to the incident IR radiation could saturate the semiconducting detector.

The A-C is equipped with a Raman spectrometer. A modular fibre-coupled iHR 550 Raman spectrometer equipped with 3 changeable gratings (1800/mm, 600/mm, 300/mm) is connected to the A-C. Two lasers, green and blue, with laser wavelength of 532 nm and 473 nm, respectively, are available. *In-situ* operation is possible by two fibre-coupled remote Raman heads (one for each wavelength). The incorporation of a TV camera allows a close visualization of the samples inside the vacuum chamber. The back illuminated deep depletion CCD detector with 90% quantum efficiency in the spectral range from 400 nm to 800 nm helps to keep the measurement times at bay. As in the other chamber, the sample holder in the A-C is heatable up to 1000ºC, allowing the study of the variation of the chemical bonding of the samples at different temperatures in a non-destructive manner.

Visual inspection can be also very useful to examine sample deterioration. Depending on the sample and the type of failure, it is possible to detect surface cracks, delamination of the coating, extreme change or colour or the migration of elements to the surface. Therefore, after each heating step, it would be helpful to verify the integrity of the sample before the next heating step. The camera of the A-C allows visual sample evaluation in order to decide whether the characterization procedure needs to be stopped due to a catastrophic failure of the film.

5.3. Qualification test procedure for SSC durability

An optimal SSC needs to show appropriate optical properties as well as thermal and mechanical stability in air at high temperatures. Numerous publications [5,17–19] and standards describes the durability and accelerated ageing tests of solar thermal collectors. However, all these tests are valid only for solar collectors exposed to 200ºC as maximum temperature. The required temperature of the SSC evaluated in this thesis is higher (T>600ºC), and hence, a new test procedure is proposed. This methodology combines a sequence of characterization techniques in

the cluster tool at different environments and temperatures. The steps to follow in a complete thermal characterization process are shown in Figure 5.3.

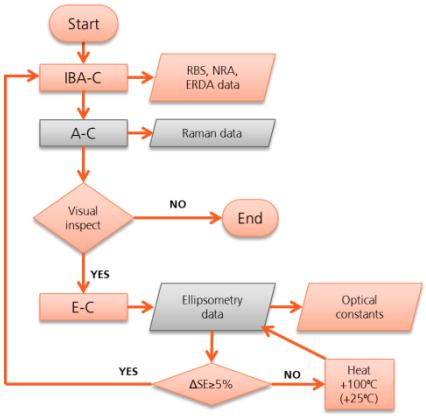

Figure 5.3 - Flow chart of the methodology described for high temperature testing of SSC. The different chambers represented in the diagram: the analysis chamber (A-C), the environmental chamber (E-C) and the ion beam analysis chamber (IBA-C).

1. Installation of the sample in the transfer chamber.
2. Transfer of the sample to the IBA-C to examine its elementary composition and its depth distribution along the thickness. The IBA technique selected depends on the sample type.
3. Sample transfer to the A-C. Measure with Raman spectroscopy if desired.
4. Visual inspection of the state of the sample in the A-C. In the case of sample deterioration, the characterization process is finished. If no visual failure is observed, continue with the next step.
5. Transfer the sample to the environmental E-C. Measure using *in-situ* spectroscopic ellipsometry (SE). Depending on the type of sample and desired study, it is possible to do SE in vacuum or in a controlled environment as described above.
6. Increase the temperature by 100ºC (only until the first changes are measured. upon beginning deterioration round, increase by 25ºC) and measure the ellipsometry parameters (Δ, ψ) at each temperature in the whole energy range.
7. If $\Delta(SE) < 5\%$ (defined in equation (5.2)), go to the previous step increasing the temperature by 100ºC (25ºC after the first changes).
8. If $\Delta(SE) \geq 5$ %, stop heating, and perform final IBA and Raman characterization.

As an example of the versatility and the great potential of the system, the methodology was applied to a carbon-titanium nanocomposite (a-C:TiC) thin film deposited by pulsed filtered cathodic vacuum arc (PFCVA), as explained in section 5.4. The samples were exposed to an *in-situ* heating process while measuring spectroscopic ellipsometry. Before and after heating, the thin films were characterized with Raman spectroscopy and Rutherford Backscattering Spectroscopy (RBS) in order to analyse the compositional and microstructural changes occurred during the heating process. Changes in both chemical bonding and optical constants with increasing temperature were recorded in a single experiment.

In section 5.5, AlTi(O_xN_{1-x}) thin films were investigated in order to understand the influence of the oxygen to nitrogen ratio on the optical properties and their failure mechanisms at high temperatures. The analysis was performed first in vacuum inside the cluster tool heating samples from RT to 800°C and subsequently, annealing in air was performed to compare with the previous results. No significant changes in optical properties and composition were found when heating in vacuum atmosphere the films, showing excellent high temperature stability.

5.4. *In-situ* multichamber characterization of a-C:MeC

Carbon-transition metal nanocomposite films have been studied in chapter 3 as absorber layer of a SSC as they show a combination of remarkable properties, which includes high melting points and spectral selectivity [20,21]. An a-C:TiC sample was selected as an example of the *in-situ* characterization methodology described above. The a-C:TiC sample was grown on silicon (100) substrate by PFCVA (as explained in chapters 2 and 3) by the co-evaporation of carbon and titanium in two different cathodic arc sources [22].

Firstly, a sample was introduced in the IBA-C and the amount of carbon and metal were determined by RBS measurements [23,24]. The elementary areal density and the depth profile can be obtained directly, fitting the spectra with the software SIMNRA [25], as shown in Figure 5.4, where 30 at.% of Ti is found.

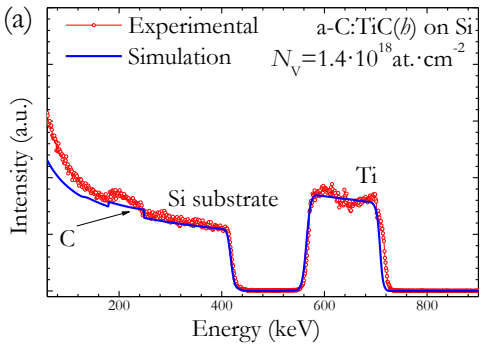

Figure 5.4 - (a) RBS ion beam analysis of carbon - titanium (30 at.% Ti) sample deposited with PFCVA technique on Si (100)

Figure 5.5 shows the Raman spectra of the a-C:TiC thin films as deposited and after heating 650ºC, in the wavenumber range of 800 to 2500 cm^{-1} and measured with 532 nm excitation light. The *D* and *G* peaks can be observed for both temperatures. To obtain quantitative understanding of the temperature dependence structural changes of the films, the Raman spectra were fitted by a combination of an exponential background, a symmetric Lorentzian for the *D* peak and an asymmetric Breit-Wigner-Fano (BWF) shape for the *G* peak [26], as further described in chapter 3. The intensity of the *D* peak is significantly lower than that of the *G* peak region, and this difference increases with temperature. After annealing at 650ºC, the *G* peak is clearly defined and it

shifts towards higher wavenumbers from 1549 to 1579 cm^{-1}, while *D* peak position decreases slightly. The I_D/I_G ratio dispersion decreases with temperature (from 1.21 at RT to 0.876 at 650ºC). The presence of the *D* band indicates the presence of aromatic rings in the sp^2 phase of the carbon, while the I_D/I_G ratio is related with the size of these aromatics clusters in disordered carbons. As reported before [27], in the a-C:TiC deposited thin films, we have 6-fold ring clusters and the average cluster size higher than in pure carbon films. The decrease in the *G* peak at increasing temperature indicated the graphitization of carbon, and the promotion of the nucleation and growth of 6-fold ring clusters by the presence of the Ti. This indicates that the Ti nanoparticles act as nucleation centres of 6-fold rings at low temperatures while at high temperatures the Ti favours the ordering within the clusters [28].

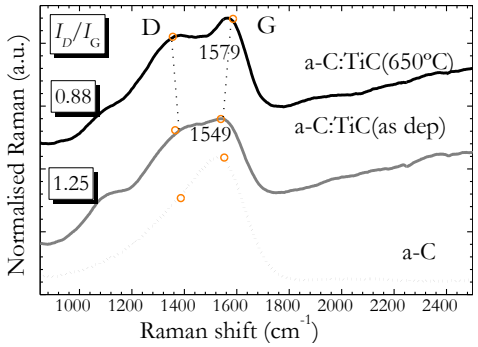

Figure 5.5 - Normalized Raman spectra at different temperatures of a-C:TiC sample on stainless steel substrate

Once the elementary distribution and the chemical bonding were analysed, the sample is transferred to the E-C. The optical constants of the a-C:TiC film were determined by SE using the *in-situ* ellipsometer. The sample was measured during a heating ramp from room temperature up to 650ºC in vacuum, to gauge any changes in the layers with temperature. The ellipsometry data Δ and ψ measured are shown in Figure 5.6 (a).

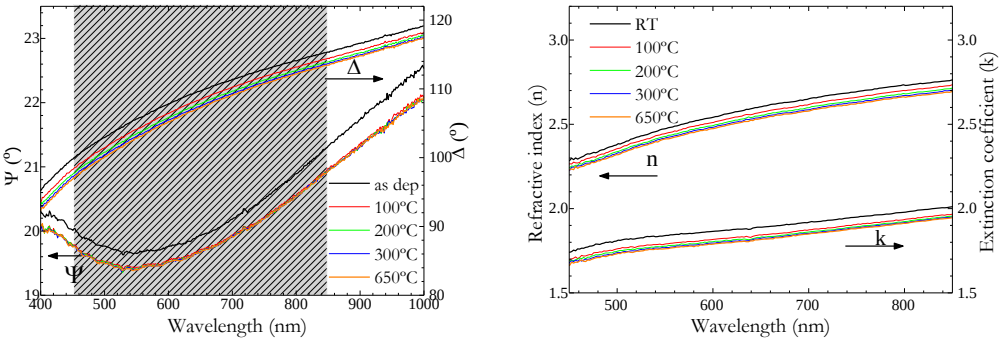

Figure 5.6 - (a) Ellipsometry data at selected temperatures of a-C:TiC sample deposited on Si (100). (b) Complex refractive index (*n, k*) obtained after modelling the ellipsometry data.

The index of refraction (*n*) and extinction coefficient (*k*) were modelled following the optical models employed in chapter 3 for the other a-C:MeC nanocomposites. The fitting of the experimentally SE data includes a combination of Drude [29] and Tauc-Lorentz [30] dispersion

models. The calculated optical constants are shown in Figure 5.6 (b) at selected temperatures employed in the test. Both *n* and *k* decrease with the increment of temperature since the first heating step between RT and 100ºC. Afterward, the optical constants stabilize and no changes were observed at higher temperatures

Although the optical constants of the films did change to some extent up to 650 °C in vacuum, no features appeared in the ellipsometric data that would indicate a change in crystallinity, as the employed models remains without variations. The resulting thickness on the modelling was slightly higher on the heated sample than their non-annealed one. This decrease in the optical constants and the increase on the modelled thickness were attributed to thermal expansion, which is difficult to minimize and may change the sample optical constants irreversibly.

The variation of the ellipsometry parameters were evaluated as described in the methodology, between each heating step, as described in equations (5.1) and (5.2), obtaining the values indicated in Table 5.1. The changes in the defined ellipsometry parameters were below 5% for all the temperature under study.

Table 5.1: Variation of ellipsometry parameters as defined in the proposed methodology.

Temperature interval	*Δ(SE)* (%)
RT-100 ºC	2.4
RT-200 ºC	3.0
RT-300 ºC	3.4
RT-650 ºC	3.7

In summary, the results of the durability procedure reveal that the annealing in vacuum at 650ºC leads an increase in the graphitization degree of the amorphous carbon matrix. This effect was coupled to the promotion of nucleation and 6-fold ring clusters growth. No changes in the composition, and slight decrease of the optical constants associated to the inevitable thermal expansion of the samples. The a-C:TiC sample passes the stability test when heating at temperatures up 650ºC in vacuum. This methodology will be employed for complete SSC, once atmospheric conditions can be introduced in the environmental chamber to simulate real operating conditions.

5.5. Multichamber characterization at high temperature of the solar selective coatings based on AlTiON

$AlTi(O_xN_{1-x})$ thin films were selected as candidate materials for SSC, as explained in chapter 4. Two different $AlTi(O_xN_{1-x})$single layers deposited by CVA on inconel substrates will be analysed in this section in order to understand the influence of the oxygen concentration in the optical and microstructural properties at high temperatures. The selected samples were sample #1

and #5, as defined in chapter 4, i.e. AlTiN and AlTiON (20at.%O), respectively. The analysis was performed first in vacuum heating samples from RT to 800°C without sample exposure to undefined atmospheres. Then, annealing in air was performed to compare with the previous results.

5.5.1 Thermal *in-situ* treatments in vacuum of individual AlTi(O_xN_{1-x}) layers

The stability and microstructural evolution of the samples were *in-situ* tested first in vacuum in the different chambers of the cluster tool.

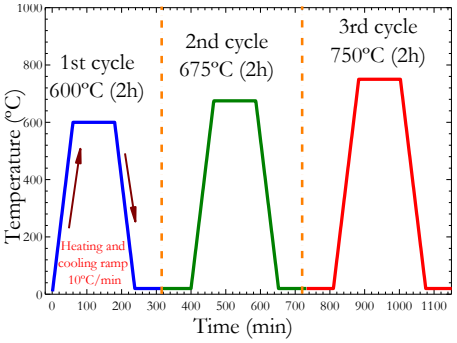

Figure 5.7 – Schematic representation of the symmetric cycles employed in the cluster tool for *in-situ* analysis of the AlTi(O_xN_{1-x}) samples, with a heating and cooling ramp of 10ºC·min^{-1} and maximum temperatures of 600º, 675º and 750ºV.

Firstly, the two oxynitride samples were introduced in the IBA-C in order to examine their composition by RBS measurements. Both AlTiN and AlTiON samples were sample is heated up during three different heating cycles at 600, 675 and 750ºC (as schematized in Figure 5.7) and maintaining that temperature 2 hours. The heating and cooling ramp are controllable and a rate of 10ºC min^{-1} was employed for both ramps.

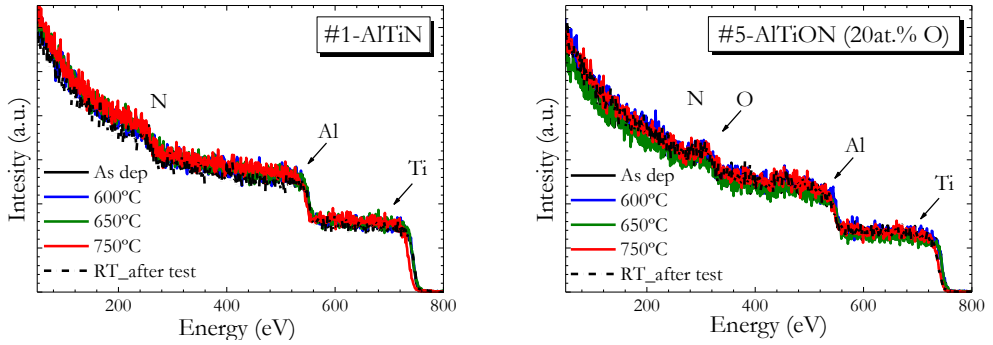

Figure 5.8 – *In-situ* RBS test of samples at different temperature indicated in the graph of (a) AlTiN and (b) AlTiON (20at.% O) samples deposited on inconel Haynes@625 substrate.

No changes in the composition were appreciated thorough the different temperatures, or diffusion of the substrate to the surface in both tested samples, as shown in Figure 5.8. An additional RBS spectrum was recorded after the three heating/cooling cycles, obtaining the same composition when the sample was at high temperature, and when the test started.

The main challenge of this experiment is related to the blinding of the Si diode detector by the infrared radiation that samples emit when exposed to high temperature. In order to avoid this, the sample holder was covered with a Mo radiation shield (Figure 5.9) to reduce the infrared radiation incident on the semiconducting detector. The AlTi(O_xN_{1-x}) samples measured during the test shows low thermal emittance, which implies they resulted ideal candidates to perform this RBS measurement at high temperature. Owing to the aforementioned, it was possible to perform a RBS measurement at 840ºC. After a literature review, it is possible to assure that this is the first time that an *in-situ* RBS has been performed at this high temperature [31,32].

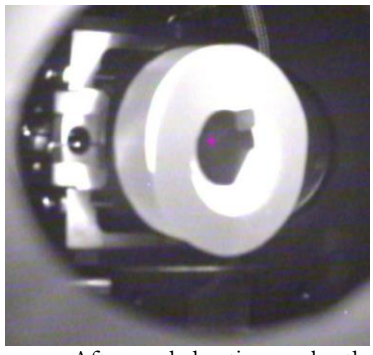

Figure 5.9 – Image of the heated sample inside the ion beam analysis chamber at 840ºC. A cover shield was emplaced around the substrate holder in order to avoid undesired IR emittance from the substrate holder

After each heating cycle, the sample is transferred to the A-C, to measure with Raman spectroscopy to obtain microstructural information of the films at different temperatures. AlTiN and AlTiON were *fcc*-cubic crystalline samples (as shown with GIXRD patterns in chapter 4). In perfect crytal structures, every ion is at a site of inversion symmetry and consequently first-order allowed Raman active phonon vibrations are forbidden.

The spectra of the as-deposited AlTiN and AlTiON films show two broad bands centred at 302 and 630 cm^{-1}, as observed in Figure 5.10 (a) and (b). These bands are originated due to acoustic transitions in the 200–350 cm^{-1} region (LA and TA) by o vibration of Ti and Al ions, and optic modes in the 600–750 cm^{-1} region (LO and TO) of N or O ions vibration.

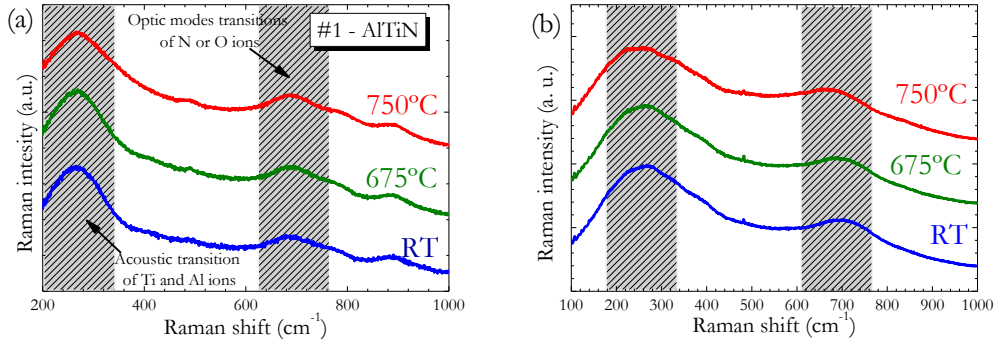

Figure 5.10 – *In-situ* Raman spectroscopy analysis of samples at different temperatures indicated in the graph of (a) AlTiN and (b) AlTiON (20at.% O) deposited on inconel Haynes@626 substrate.

As observed in the HR-TEM images, the samples were not pure crystalline and defects and discontinuities between crystal columns appear, and hence, the effective symmetry is reduced. The Raman spectrum of a perturbed crystal, thus, reflects the presence of impurities/defects in the crystal. In the case of sputter deposited TiAlN or TiAlON coatings, both metal (Ti and Al) ion vacancies and light element (N and O) ion vacancies are present. The Raman spectrum did not change even after heating the sample up to a temperature of 750 °C in vacuum, confirming the stability of the microstructure under vacuum conditions.

The last step includes the determination of the optical constants with temperature. The SE parameters of the samples were recorded at every increment of 100ºC during the three heating and cooling cycles. Figure 5.11 shows the variations in Psi (ψ) and Delta (Δ) with the temperature for an AlTiN thin film deposited on inconel substrate.

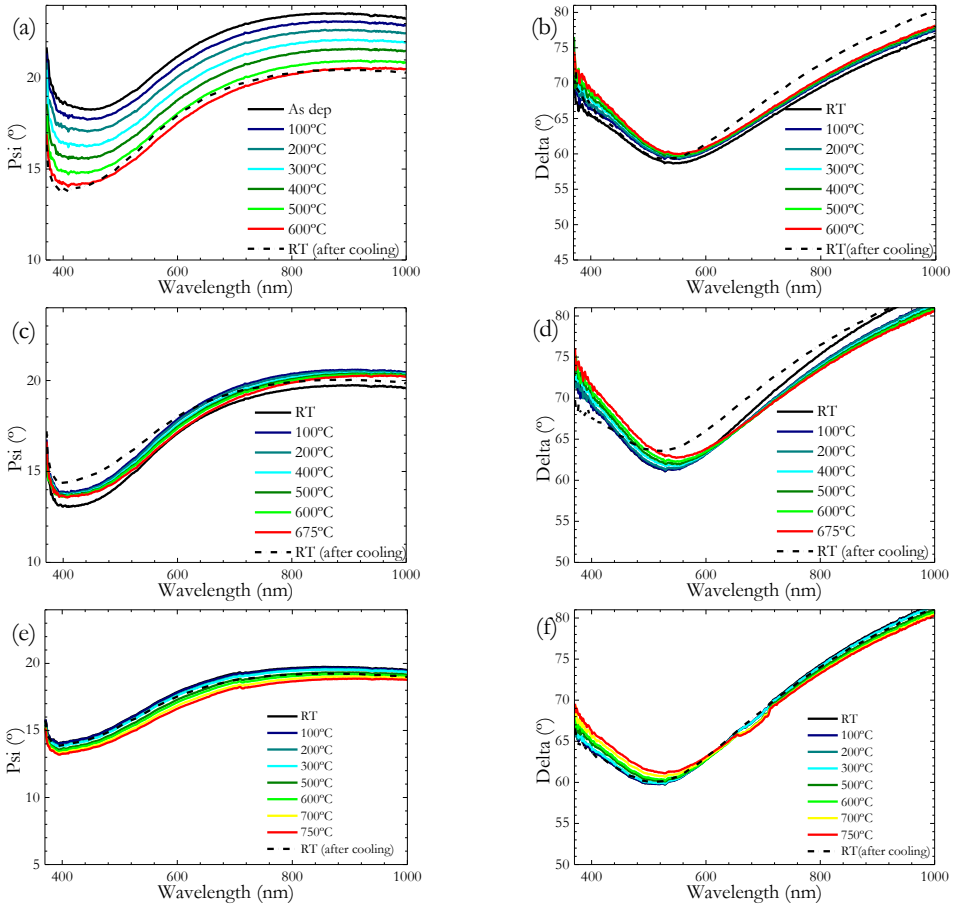

Figure 5.11 - *In-situ* ellipsometry measuremtens of AlTiN sample on inconel Haynes@626 substrate. (a) and (b) represent the ellipsometric parameters ψ and Δ during the first heating cycle from RT – 600 °C ; (c) from RT – 675°C in the second heating cycle and (e) and (f) SE parameters during the third cycle, from RT – 750 °C,

As it can be seen in Figure 5.11, the ellipsometry value ψ changes more than a 10% in the first heating cycle from the initial value. However, in the other cycles, the changes are less than 2%

at it recovers its original values after the heating. Delta value angle conserved their value in almost all the measured wavelength range.

The optical constants of the AlTiN sample were modeled as described in chapter 4, for an equivalent sample. The result of n and k at different temperatures are represented in Figure 5.12. The optical constants change upon heating in almost the whole measured spectral range the refractive index increases by less than 5% of its original value at room temperature. In the near IR this difference gets smaller. On the other hand the extinction coefficient is constant in the region above 3.0 eV but decreases at higher wavelengths about 5% as well during heating up to 800°C.

Similar trend in the optical constant behavior were observed when repeating this asymmetric thermal treatment of AlTiON (20at.%) sample (results not shown here).

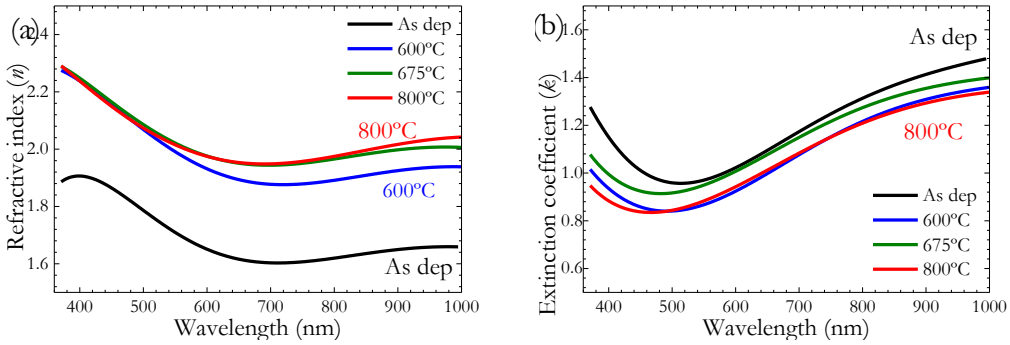

Figure 5.12 – *In-situ* optical constant's measured at different temperatures after modeling the ellipsometry parameters of AlTiN sample on inconel Haynes@626 substrate. (a) Refractive index (*n*)and (b) extinction coefficient (*k*).

Essentially, two major effects of temperature on the optical constants need to be considered. They arise, respectively, from the scattering of electrons from thermally induced disorder, and the changes in the electronic energy levels due to disorder. The phonon contribution to the optical properties has temperature dependence due to multiphonon processes, and frequently extends into the relevant wavelength range at high temperatures. This may be important in connection with composite materials or in multilayer films in which absorbing layers are placed on infrared reflectors [6].

The increase in emittance with rising temperature is very important for the behaviour of selective surfaces. The decrease in performance due to a rise in temperature is necessary for a Drude-type reflector. The optical properties are determined by the plasma frequency, the optical frequency, and the relaxation time of the electrons, which are in turn determined by the electron-phonon collision frequency, suitably averaged over the electron distribution in k space.

No significant changes in compositionand microstructure were found in the films when heating in vacuum, showing excellent high temperature stability.

5.5.2 Thermal *ex-situ* treatments in air of individual AlTi(O_xN_{1-x}) layers

Annealing in air was also performed to compare with the previous results observed in vacuum annealing. The AlTiN and AlTiON (20 at.% O) single layers were heated at 800ºC in air for two hours and their microstructure and elemental composition, chemical bonding and optical properties were analyzed before and after the annealing. In this study, HR-TEM images of the samples were obtained before and after heating.

The atmospheric heating tests were asymmetric as only the heating ramp could be controlled in the furnace. Figure 5.13 and Figure 5.14 show the ERD ion beam analysis results of the samples as deposited and after heated at 450, 650 and 800ºC. HR-TEM images are also included in the figures.

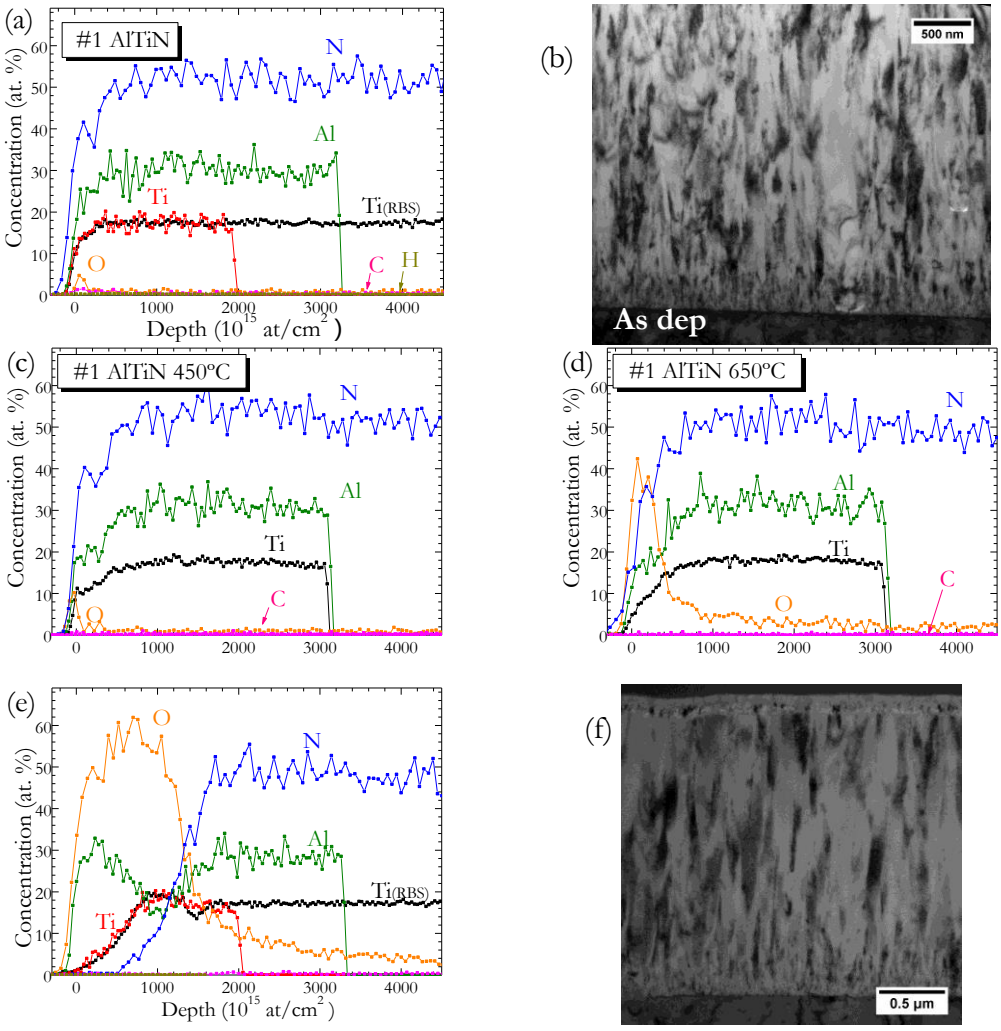

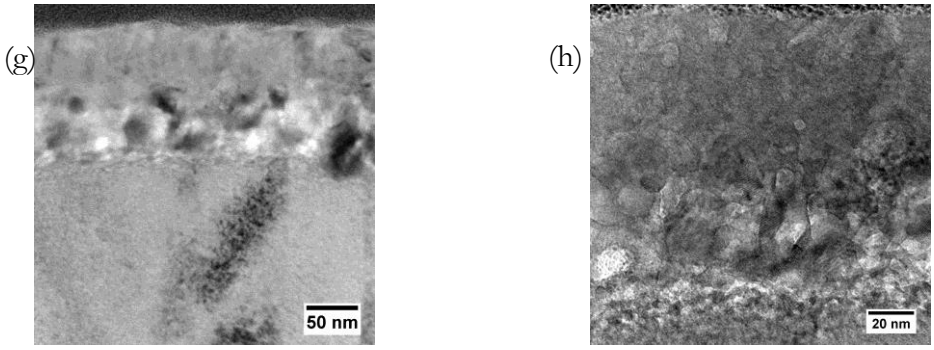

Figure 5.13 - ERD ion beam analysis of AlTiN sample deposited on inconel substrate at (a) RT, (c) after 2h heating in air at 450ºC, (d) after 2h heating in air at 650ºC,and (e) after 2h heating in air at 800ºC. (b) HR-TEM image of AlTiN sample as deposited and (f) HR-TEM image after annealing at 800ºC for two hours. (g) and (h) are high resolution images of the upper oxidized region of the AlTiN films

ERD analysis and HR-TEM images reveal a homogeneous AlTiN layer along the thickness of the sample before the film was subjected to high temperature (Figure 5.13 (a) and (b)). The effect of the temperature is clearly observed when comparing ERD spectra. No changes in the composition are detected at 450ºC (Figure 5.13 (c)) and oxygen appears at 650ºC, as observed in Figure 5.13 (d). After 800ºC annealing the spectrum exhibits a top layer of Al_2O_3 followed by a mixed Al_2O_3 /TiO_2 layer. This oxide scale is shown as a~ 80 nm thick layer grown in the surface in HR-TEM images (Figure 5.13 (f), (g) and (h)).

As deposited ERD spectrum of AlTiON (Figure 5.14 (a)) exhibits a first region with higher amount of oxygen, and then, it shows a constant 20% at. of oxygen. This first region was attributed to roughness in the ERD modeled, and as observed in the HR-TEM image in Figure 5.14 (b), there in not appreciated any oxidized layer on the top. No changes are observed after heating the sample at 450ºC and 650ºC (Figure 5.14 (c) and (d)). The scenario changes after annealing at 800ºC, where three different zones can be clearly distinguished in the ERD spectrum and TEM image (Figure 5.14 (e) and (f)). In the surface (zone 1) a mixed oxide, probably $(Al,Ti)_2O_3$ is formed according to ERD spectrum. This zone is followed by a transition interlayer formed by the mixed aluminum and titanium oxide and oxynitride. Oxygen and nitrogen content are gradually changing along this zone until they reach zone 3, with the previous AlTiON composition before heating. Zones 1 and 2 show a thickness of 300 nm. Higher resolution HR-TEM images of the regions labeled as zone 1, 2 and 3 are presented in Figure 5.14 (h), (i) and (j), respectively

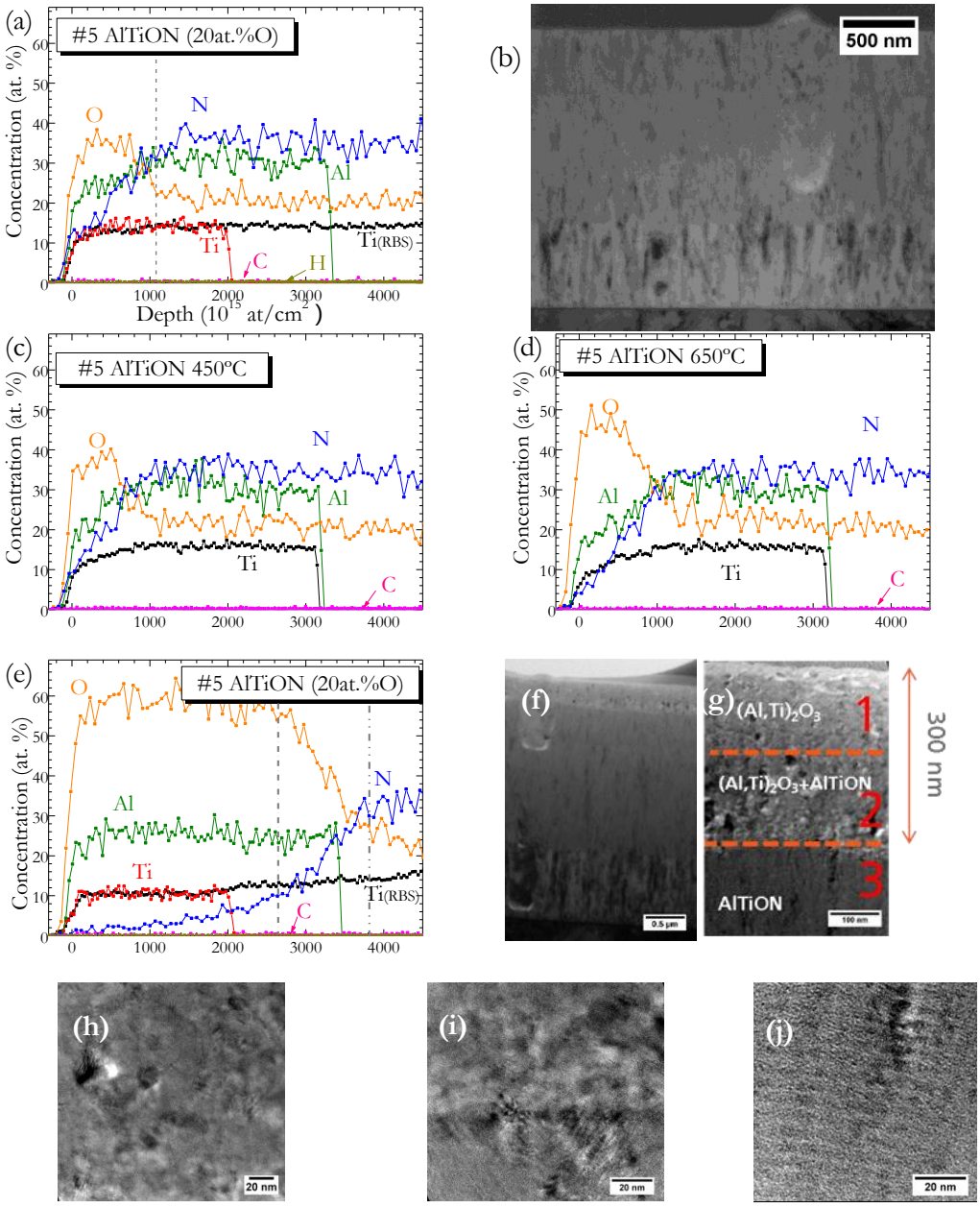

Figure 5.14 - ERD ion beam analysis of AlTiON (20at.% O) sample deposited on inconel substrate at (a) RT, (c) after 2h heating in air at 450ºC, (d) after 2h heating in air at 650ºC and (e) after 2h heating in air at 800ºC. (b) HR-TEM image of AlTiN sample as deposited and (f) HR-TEM image after annealing at 800ºC for two hours and (g) Amplified HR-TEM image of the oxidized region, were three different regions are differentiated. (h), (i) and (j) are high resolution images corresponding to region 1, 2 and 3, respectively.

Raman measurements of AlTiN and AlTiNO samples heated in air are shown in Figure 5.15. As indicated for the previous tests of equivalent samples annealed in vacuum, the Raman spectrum of the as-deposited samples shows two main brad bands originated due to vibration of Ti and Al ions and N or O ions in the second.

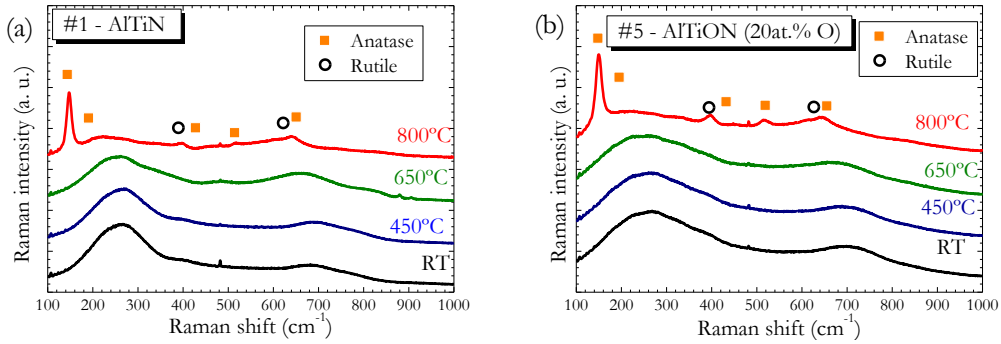

Figure 5.15 - Raman spectroscopy analysis of samples heated 2hours in air at 450, 650 and 800ºC of (a) AlTiN and (b) AlTiON (20at.% O) deposited on inconel Haynes@626 substrate

The Raman spectra of AlTiN and AlTiON samples show no variation in the chemical bonding at 450ºC and 650ºC. However, and in concordance with the ERD and HR-TEM analysis, both samples show peaks centered at 148, 445 and 640cm^{-1} after heating 2 hours in at 800ºC. The well-defined narrow peak at 1458cm^{-1} is characteristic for anatase TiO_2 while 445cm^{-1} peak us due to the formation of rutile TiO_2 [33].

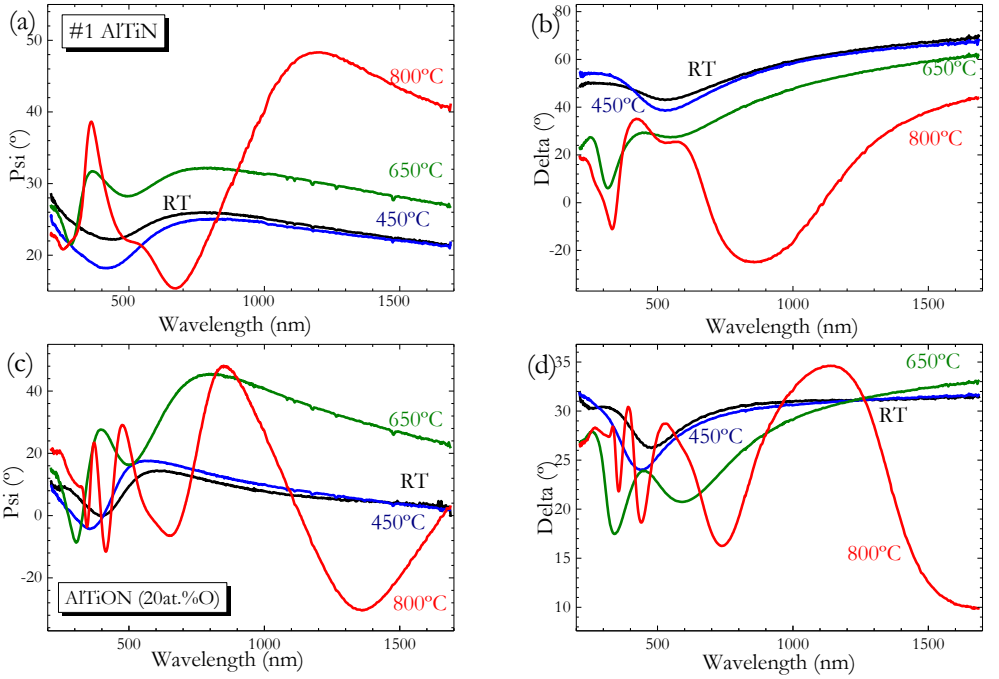

Figure 5.16 – Ellipsometry parameters of samples heated 2 hours in air at 450, 650 and 800ºC of (a) ψ and (b) Δ of AlTiN. (c) ψ and (d) Δ of AlTiON (20at.% O) samples deposited on inconel Haynes@626 substrate.

To complete the thermal treatment in air, the optical response of AlTiN and AlTiON samples were measured by spectroscopic ellipsometry. The ellipsometric parameters ψ and Δ of the films were measured before and after each heating asymmetric cycle at 450, 650 and 800ºC (Figure 5.16). As observed from the previous analysis, no main changes were observed in the samples

heating up to 650ºC. If the temperature was increased up to 800ºC, an oxide layer appears on the top of the coating, with a drastic change in the ellipsometry parameters, and therefore in the optical properties.

5.6. Discussion and conclusions

A novel *in-situ* thermal measurement characterization methodology for thin films has been presented to investigate the compositional, optical and structural changes in a wide range of temperatures and environments. The durability of SSC can be investigated following the presented methodology. The main advantage of the proposed methodology is the possibility of doing different measurements sequentially in the same multi-chamber cluster tool, without breaking the vacuum and the possibility of combining optical and structural characterization analysis. The presence of a heatable sample holder in all the chambers, allows characterization of the samples at different temperatures and environments. With all this capabilities, it is possible to have a better understanding of the failure mechanisms at high temperatures in a wide variety of thin films or coatings.

A new procedure for the qualification of SSC at high temperature was proposed, which combines a sequence of analytical techniques in the multi-chamber cluster tool at different environments and temperatures. As an example of the versatility and the great potential of the system, the methodology was applied to a a-C:TiC thin film. Changes in both chemical bonding and optical constants with increasing temperature were recorded in a single experiment.

The thermal stability of single layers of $AlTi(O_xN_{1-x})$ materials was analysed heating the samples in the multi characterization cluster tool, and in air. The low emittance properties of $AlTi(O_xN_{1-x})$ samples, allowed to perform *in-situ* RBS analysis at temperature above 800ºC. No significant changes in optical properties and composition were found when heating in vacuum atmosphere the films, showing excellent high temperature stability.

The samples *ex-situ* annealed in air showed the good stability of $AlTi(O_xN_{1-x})$ films at temperatures up to 650ºC. After the asymmetric heating test in air at 800ºC, an oxide layer starts to growth in both tested samples. The composition, chemical bonding and optical properties of the oxide layer was comprehensively characterized. This complete analysis improves the understanding of the failure mechanism in SSC based on $AlTi(O_xN_{1-x})$ thin films at high temperatures.

5.7. References

[1] L.A. Weinstein, J. Loomis, B.B. Bhatia, D.M. Bierman, E.N. Wang, G.G. Chen, Concentrating Solar Power, Chem. Rev. 115 (2015) 12797. doi:10.1021/acs.chemrev.5b00397.

[2] C.E. Kennedy, H. Price, Progress in Development of High-Temperature Solar-Selective Coating, Sol. Energy. (2005) 749–755. doi:10.1115/ISEC2005-76039.

[3] H. Schellinger, M.P. Lazarov, H. Klank, R. Sizmann, Thermal and Chemical Metallic - Dielectric Transitions of TiNXOY Cu Absorber Tandems, in: C.M. Lampert (Ed.), SPIE's 1993 Int. Symp. Opt. Imaging, Instrum., International Society for Optics and Photonics, 1993: pp. 366–376. doi:10.1117/12.161977.

[4] A.G. Evans, D.R. Mumm, J.W. Hutchinson, Mechanisms controlling the durability of thermal barrier coatings, Prog. Mater. Sci. 46 (2001) 505–553.

[5] B. Carlsson, K. Möller, M. Köhl, M. Heck, S. Brunold, U. Frei, et al., The applicability of accelerated life testing for assessment of service life of solar thermal components, Sol. Energy Mater. Sol. Cells. 84 (2004) 255–274. doi:10.1016/j.solmat.2004.01.046.

[6] B.O. Seraphin, Spectrally selective surfaces and their impact on photothermal solar energy conversion, in: B.O. Seraphin (Ed.), Top. Appl. Phys., Springer Berlin Heidelberg, Berlin, Heidelberg, 1979. doi:10.1007/3-540-09224-2.

[7] L.R. Dahal, D. Sainju, N.J. Podraza, S. Marsillac, R.W. Collins, Real time spectroscopic ellipsometry of Ag/ZnO and Al/ZnO interfaces for back-reflectors in thin film Si:H photovoltaics, Thin Solid Films. 519 (2011) 2682–2687. doi:10.1016/j.tsf.2010.11.093.

[8] Y. Shim, H. Aoh, J. Sakamoto, K. Wakita, N. Mamedov, Temperature dependence of dielectric function and optical transitions in TlInSe2 and TlGaTe2, Thin Solid Films. 519 (2011) 2852–2854. doi:10.1016/j.tsf.2010.11.077.

[9] J.B. Kana Kana, J.M. Ndjaka, G. Vignaud, a. Gibaud, M. Maaza, Thermally tunable optical constants of vanadium dioxide thin films measured by spectroscopic ellipsometry, Opt. Commun. 284 (2011) 807–812. doi:10.1016/j.optcom.2010.10.009.

[10] M. Berndt, G. Abrasonis, G.J. Kovács, M. Krause, F. Munnik, R. Heller, et al., Bulk diffusion induced structural modifications of carbon-transition metal nanocomposite films, J. Appl. Phys. 109 (2011) 063503–11. doi:10.1063/1.3559302.

[11] J. Mennig, F. Matthes, D.E. Bürgler, C.M. Schneider, Observation and implications of magnetic domains in lateral spin valves, J. Appl. Phys. 111 (2012) 07C504. doi:10.1063/1.3671415.

[12] F. Amy, A.S. Wan, A. Kahn, F.J. Walker, R.A. McKee, Band offsets at heterojunctions between SrTiO[sub 3] and BaTiO[sub 3] and Si(100), J. Appl. Phys. 96 (2004) 1635. doi:10.1063/1.1766417.

[13] Forschungszentrum(Julich), Nano-Spintronics-Cluster-Tool, (n.d.). http://www.fz-juelich.de/pgi/pgi-6/EN/Leistungen/Instrumentierung/TheNanoSpintronicsClusterTool/artikel.html?nn=893062.

[14] NREL, Process Development and Integration Design Features, (n.d.). http://www.nrel.gov/pv/pdil/capabilities.html.

[15] N. Selvakumar, H.C. Barshilia, Review of physical vapor deposited (PVD) spectrally selective coatings for mid- and high-temperature solar thermal applications, Sol. Energy Mater. Sol. Cells. 98 (2012) 1–23. doi:10.1016/j.solmat.2011.10.028.

[16] Y. Wang, M. Nastasi, Handbook Modern Ion Beam Materials Analysis, 2nd editio, Cambridge University Press, 2010.

[17] R. Gampp, P. Oelhafen, P. Gantenbein, S. Brunold, U. Frei, Accelerated aging tests of chromium containing amorphous hydrogenated carbon coatings for solar collectors, Sol. Energy Mater. Sol. Cells. 54 (1998) 369–377. doi:10.1016/S0927-0248(98)00088-9.

[18] B. Carlsson, K. Möller, M. Köhl, U. Frei, S. Brunold, Qualification test procedure for solar absorber surface durability, Sol. Energy Mater. Sol. Cells. 61 (2000) 255–275. doi:10.1016/S0927-0248(99)00111-7.

[19] M. Köhl, M. Heck, S. Brunold, U. Frei, B. Carlsson, K. Möller, Advanced procedure for the assessment of the lifetime of solar absorber coatings, Sol. Energy Mater. Sol. Cells. 84 (2004) 275–289. doi:10.1016/j.solmat.2004.01.041.

[20] A. Schüler, I.R. Videnovic, P. Oelhafen, S. Brunold, Titanium-containing amorphous hydrogenated silicon carbon films (a-Si:C:H/Ti) for durable solar absorber coatings, Sol. Energy Mater. Sol. Cells. 69 (2001) 271–284. doi:10.1016/S0927-0248(00)00396-2.

[21] G. Abrasonis, M. Berndt, M. Krause, K. Kuepper, F. Munnik, A. Kolitsch, et al., Soft X-ray Absorption and Emission Spectroscopic Investigation of Carbon and Carbon:Transition Metal Composite Films, J. Phys. Chem. C. 112 (2008) 17161–17170. doi:10.1021/jp805209r.

[22] A. Pardo, J.G. Buijnsters, J.L. Endrino, C. Gómez-Aleixandre, G. Abrasonis, R. Bonet, et al., Effect of the metal concentration on the structural, mechanical and tribological properties of self-organized a-C:Cu hard nanocomposite coatings, Appl. Surf. Sci. 280 (2013) 791–798. doi:10.1016/j.apsusc.2013.05.063.

[23] G. Abrasonis, T.W.H. Oates, G.J. Kovács, J. Grenzer, P.O.A. Persson, K.-H.H. Heinig, et al., Nanoscale precipitation patterns in carbon–nickel nanocomposite thin films: Period and tilt control via ion energy and deposition angle, J. Appl. Phys. 108 (2010) 043503. doi:10.1063/1.3467521.

[24] W. Jiang, V. Shutthanandan, S. Thevuthasan, D.E. McCready, W.J. Weber, Erratum to: "Carbon analysis using energetic ion beams" [Nucl. Instr. and Meth. B 222 (2004) 538–546], Nucl. Instruments Methods Phys. Res. Sect. B Beam Interact. with Mater. Atoms. 227 (2005) 450–451. doi:10.1016/j.nimb.2004.10.083.

[25] M. Mayer, SIMNRA User ' s Guide, Max-Plank-Institut für Plasmaphysuk, Garching, Germany, 1997.

[26] A. Ferrari, J. Robertson, Interpretation of Raman spectra of disordered and amorphous carbon, Phys. Rev. B. 61 (2000) 14095–14107. doi:10.1103/PhysRevB.61.14095.

[27] B.K. Tay, Y.H. Chenh, S.P. Lau, X. Shi, Carbon nanocomposite thin films prepared by filtered cathodic vacuum arc technique, Int. J. Mod. Phys. B. 16 (2002) 933–945. doi:10.1142/S0217979202010646.

[28] G. Abrasonis, M. Krause, A. Mücklich, K. Sedlac˘ková, G. Radnóczi, U. Kreissig, et al., Growth regimes and metal enhanced 6-fold ring clustering of carbon in carbon–nickel composite thin films, Carbon N. Y. 45 (2007) 2995–3006. doi:10.1016/j.carbon.2007.09.044.

[29] F. Modine, T. Haywood, C. Allison, Optical and electrical properties of single-crystalline zirconium carbide, Phys. Rev. B. 32 (1985) 7743–7747. doi:10.1103/PhysRevB.32.7743.

[30] G.E. Jellison, Optical functions of GaAs, GaP, and Ge determined by two-channel polarization modulation ellipsometry, Opt. Mater. (Amst). 1 (1992) 151–160. doi:10.1016/0925-3467(92)90022-F.

[31] C.C. Chin, T. Morishita, The surface of the (001) SrIiO3 substrate at high temperature, Phys. C. 245 (1995) 77–83.

[32] O.S. Odutemowo, J.B. Malherbe, C.C. Theron, E.G. Njoroge, E. Wendler, In-situ RBS studies of strontium implanted glassy carbon, Vacuum. 126 (2016) 101–105. doi:10.1016/j.vacuum.2016.01.024.

[33] E. Smith, G. Dent, Modern Raman Spectroscopy - A Practical Approach, John Wiley & Sons, Ltd, Chichester, UK, 2005. doi:10.1002/0470011831.

[34] D.J. Gardiner, P.R. Graves, Practical Raman Spectroscopy, Springer-Verlag, 1989.

CHAPTER 6: CONCLUSIONS AND OUTLOOK

The present thesis addresses the design of new solar selective coatings (SSC) for high temperature applications in order to improve the performance of concentrating solar power (CSP) plants. In particular, two new PVD candidate materials are selected as promising materials for SSC and a systematic methodology to design, deposit and characterize this type of coatings is proposed.

The first approach consists on SSC based on **interstitial metal carbide nanoparticles embedded in an amorphous carbon matrix** (a-C:MeC). These nanocomposite materials were selected as their combination of optical and thermo-mechanical properties, with adjustable solar selective properties and high-temperature resistance make them very attractive candidates as absorber layer of SSC. Optical simulations with CODE resulted in a good approach to facilitate the selection of materials to employ for each layer forming the SSC stack (AR layer/ a-C:MeC/IR layer). Particularly challenging was the simulation of optical constants of non-homogeneous materials such as nanocomposites. In a first step, Bruggeman EMA theory was employed to simulate the optical properties of the composite material, based on optical constants reported in the literature for carbon and metal carbides. Using also optical constants from the literature for the IR and AR layers, the reflectance of several complete stacks was simulated. Based on these simulations the best candidates were a-C:VC, a-C:ZrC and a-C:MoC nanocomposites for the absorber layer, SiO_2 and Al_2O_3 films as antireflective (AR) layer and TiN and ZrN as infrared reflective (IR) layer,. In order to maximize the solar absorptance (α) and minimize the thermal emittance (ε), thicknesses of the different layers and volume fraction of the nanocomposites were optimized obtaining promising values of α = 94.9% and ε_{RT} = 12.5% for a stack composed by Al_2O_3 (60 nm)/ a-C:VC (107 nm and 37%VF of VC)/TiN(400 nm).

The different pre-selected layers based on simulation results were deposited by pulsed filtered vacuum cathodic arc (PFCVA) and a thoughtful characterization was carried out

afterwards. This characterization included composition analysis by ion beam analysis techniques (RBS and NRA), that demonstrated how the metal content in the nanocomposite can be tuned varying the intensity ration between the two arc sources available in the deposition chamber. Microstructural and morphological characterization by Raman spectroscopy, XRD and HR-TEM confirmed the formation of nanocomposites of metal carbides particles embedded in an amorphous carbon matrix for samples deposited with the highest metal content. The presence of metal was found to increase the chemical ordering of the carbon in the samples. A spontaneous formation of ordered multilayers for the cases of the a-C:VC (20.5 at.% V), a-C:ZrC (38 at.% V) and a-C:MoC (3.5 at.% V) thin films was observed. The diffusivity of the adatoms on the substrate surface during the film growth, enhanced by the energetic deposition of the PFCVA deposition technique, is proposed as the best explanation behind this phenomenon. However, further research is needed to reach a conclusive assessment about the origin of the self-forming multilayer growth.

Optical constants of the single layers were obtained from spectroscopic ellipsometry measurements. The validity of the optical model was confirmed by spectrophotometry measurements. As expected, the initial optical constants obtained from literature differed from the real one form the deposited materials. This is due to the broad variations in the optical constants depending on the parameters and technique employed during the thin film deposition. Therefore, it is concluded that employing optical constants obtained experimentally (i.e. from SE measurements) from the deposited material is critical in order to get a proper simulation of the optical properties. The limited wavelength range of the experimental SE measurements implies an extrapolation of the results in the IR range. The most common approach, used for example by CODE software, is to keep constant the last SE experimental value as a constant for the rest of wavelength range of interest (2 – 25 μm). However, this extrapolation was not satisfactory for the thermal emittance calculations of the SSC based on a-C:MeC and an alternative approach was needed. The exhaustive microstructural characterization carried out in the samples opened the possibility of using other optical models in addition to Bruggeman to simulate the reflectance of nanocomposite films. Different models were compared and the best agreement between simulated and measured reflectance was obtained with Bergman approach.

The simulation of a complete SSC leads to $\alpha > 96\%$ with a $\varepsilon_{RT} < 5\%$ and $\varepsilon_{600ºC} = 14\%$, showing the potential of a-C:MeC as an absorber layer material. Severe degradation was observed in a multilayer stack formed of Al_2O_3 / a-C:ZrC (38at.% Zr) / TiN after a thermal treatment of 2 hours in air at 600ºC.

The second candidate materials for SSC consists on a **graded AlTi(O_xN_{1-x}) multilayer stack**. Metal oxynitride are refractory materials that have a transition of the properties of nitride and oxide based coatings, and hence, the overall set of properties can be tuned by a meticulous control of the O-to-N ratio in the non-metal sublattice. Based on lessons learned during the design

of a-C:MeC coatings, the methodology followed for a complete design of solar selective coatings was reviewed and improved.

A preliminary annealing test was performed on oxynitrides single films to confirm the potential of this material as SSC. After verifying the stability of optical properties after 2 hours annealing in air at temperatures up to 650ºC, a complete batch of AlTi(O_xN_{1-x}) single layers with different oxygen content were deposited by CVA and then, fully characterized. The accurate composition was determined by ERD ion beam analysis. For samples deposited with same working pressure, the concentration of O (N) in the films increases (decreases) linearly with the $\%O_2/(O_2+N_2)$ ratio of reactive gases. AlTiN films exhibit a dense and columnar structure with diameters in the order of 30 nm extended throughout the whole coating thickness. The incorporation of O_2 as reactive gas resulted in a monotouos width and length shrink of the columns, with smaller cristallites embedded on amorphous matrix, as confirmed by XRD, SEM and HR-TEM analysis. The films with higher oxygen content show amorphous $(Al,Ti)_2O_3$, Al_2TiO_5 and TiO_2 phases between the grain boundaries of the AlTiN crystals. Almost XRD amorphous phases in the coating were identified in pure oxide samples were practically XRD amorphous with tiny peaks associated to metastable cubic γ-Al_2O_3 phase.

Optical constants obtained experimentally from deposited samples were employed in the simulations. Excellent fitting of the measured spectroscopic ellipsometry data was accomplished and a method to extrapolate *n* and *k* in the IR based on measured IR reflectance spectra with FTIR spectrometer was proposed. The validity of the employed optical models was verified by comparing the simulated and the measured reflectance of individual layers, obtaining an excellent agreement in the complete wavelength range of interest. The possibility of controlling the optical properties of AlTi(O_xN_{1-x}) films from metallic to dielectric character by changing the oxygen concentration is proved. Once the optical properties of the oxynitride layers were accurately described, an exhaustive simulation work was performed in order to design the SSC with the best optical performance. An optimized SSC composed of AlTiO / AlTiON(20at.%) / AlTiON(14at.%) / AlTiN / TiN that exhibits an optical performance of α = 94.7% and ε_{RT}=5.6% was obtained. Two alternative multilayers were designed to be deposited by CVA. The fitting of the simulated reflectance of one of the tandem SSC was not completely satisfactory, as the interface between layers was not well-defined and the optical constants act as if there is a gradient. Hence, a new simulation was performed in multilayer 2 introducing a Bergman EMA interlayer between AlTiN and AlTiO, with 33% VF of AlTiN embedded into AlTiO matrix, with percolation degree of 0.66 and a fitted spectral density plot. The fitting was significantly improved in multilayer with the incorporation of a Bergman EMA interlayer. This interlayer can be effectively deposited employing a smooth transition between the nitride and the oxide top layer, and avoids further inaccuracies in the design with optical simulation.

Optical properties of the coatings remained stable after 750 hours of thermal cycling in air at 600 ºC. Good stability was also found after asymmetric testing of 12h at 650ºC. Therefore the designed AlTi(O_xN_{1-x}) multilayer films represent a promising option as solar selective coating for high temperature applications. However, noticeable oxidation was identified at temperatures as high as 800ºC (probably for the TiN interlayer) which leads to the degradation of the optical properties of the films.

There is a lack of a specific durability procedure for solar selective coatings at high temperature. In this thesis, **a new *in-situ* methodology for coatings characterization** at similar conditions than the ones they will be exposed in their lifetime. This methodology can be performed sequentially in a multi chamber *cluster tool* situated in Helmholtz Zentrum Dresden – Rossendorf (Germany). It includes compositional, optical and structural characterization for a better understanding of the failure mechanism at high temperatures. This procedure was satisfactory exemplified within an a-C:TiC thin film. This good assessment of the failure mechanism shows that the proposed methodology can be a routine procedure to evaluate new candidate materials for CSP applications at high temperature. The thermal stability of single layers of AlTi(O_xN_{1-x}) materials was analysed in the cluster tool, and in air. No significant changes were found when heating the samples in vacuum. The *ex-situ* annealing test shows the good stability of the films at temperatures up to 650ºC. However, at temperatures up to 800ºC, an oxide layer starts to growth in both tested samples, as observed for the thermal treated SSC based on AlTi(O_xN_{1-x}) thin films. A complete analysis of this oxide formation helps understanding the failure mechanism in SSC at high temperatures. It is worth noting than a worldwide record of *in-situ* RBS measurement at 840ºC was performed in the framework of this thesis due to the low thermal emittance of the AlTiON films.

In summary, in this work, successful solar selective coating as alternative to the absorber paints currently employed in CSP plants has been designed and tested. Moreover, a detailed and proved methodology for the design of optical coatings for high temperature applications is described. This methodology include a novel method to *in-situ* analyse the mechanisms which lead to failure of materials at high temperatures.

Finally, a list of recommendations for future actions for the optimization of the SSC described in this thesis is given:

- In order to find a balance between the stability and the selective absorption in a-C:MeC, further experimental studies should be carried out, as the optical simulations has demonstrated they exhibit excellent optical performance as absorber layer for SSC.
- More detailed analysis needs to be done to understand the spontaneous formation of ordered multilayers for the a-C:MeC thin films. Some theories have been proposed for

this phenomenon; however, further research is needed to reach a conclusive assessment about the origin of the self-forming multilayer growth.

- a-C:TiC films passes the stability test when heating at temperatures up 650ºC in vacuum. Although this candidate materials shows failure when heating in air, a-C:MeC films could result excellent candidates as absorber layers in SSC for evacuated tubes of parabolic trough in CSP applications.
- The growth of the TiN IR layer has generated several problems that include the diffusion of Ti to the surface forming TiO_2 porous layer and difficulties implicit in the manufacture of SSC at large scales with different cathodes. Therefore, for future SSC multilayer designs, the TiN IR layer should be replaced, although it may imply an increment in the thermal emittance.
- The optimized SSC based on $AlTi(O_xN_{1-x})$ films was not deposit in this study due to technical difficulties associated to an accurate adjustment of the individual layer thickness. The deposition of the films with filtered cathodic vacuum arc reduces the growth rate, and the specific thickness for each layer can be adjusted and avoid macroparticle incorporation. Future depositions of the optimized multilayer could be carried out with this FCVA.
- Al_2O_3 layer employed with the a-C:MeC films yielded good stability and optical behaviour as AR layer. New designs of SSC based on $AlTi(O_xN_{1-x})$ layers with Al_2O_3 as AR could be tested to improve the solar absorptance.
- More experimental work is needed to elucidate the possible failure mechanism in the designed multilayer SSC that would include SEM and HR-TEM analysis of the heat treated coatings and *in-situ* evaluation of their microstructure and optical constants in the cluster tool.
- In this work, the multi-chamber cluster tool was employed only to test SSC under evacuated conditions. However, it is possible to evaluate the stability *in-situ* of the SSC in other environments following the qualification test procedure for SSC durability. New complete tests will be carried out to validate the new designs of complete SSC.